



저작자표시-비영리-동일조건변경허락 2.0 대한민국

이용자는 아래의 조건을 따르는 경우에 한하여 자유롭게

- 이 저작물을 복제, 배포, 전송, 전시, 공연 및 방송할 수 있습니다.
- 이차적 저작물을 작성할 수 있습니다.

다음과 같은 조건을 따라야 합니다:



저작자표시. 귀하는 원저작자를 표시하여야 합니다.



비영리. 귀하는 이 저작물을 영리 목적으로 이용할 수 없습니다.



동일조건변경허락. 귀하가 이 저작물을 개작, 변형 또는 가공했을 경우에는, 이 저작물과 동일한 이용허락조건하에서만 배포할 수 있습니다.

- 귀하는, 이 저작물의 재이용이나 배포의 경우, 이 저작물에 적용된 이용허락조건을 명확하게 나타내어야 합니다.
- 저작권자로부터 별도의 허가를 받으면 이러한 조건들은 적용되지 않습니다.

저작권법에 따른 이용자의 권리는 위의 내용에 의하여 영향을 받지 않습니다.

이것은 [이용허락규약\(Legal Code\)](#)을 이해하기 쉽게 요약한 것입니다.

[Disclaimer](#)

Abstract

Fabrication and Performance of A New-Concept-Energy-Device: BatCap

Hong Soo Choi

Department of Materials Science and Engineering

The Graduate School

Seoul National University

Energy storage technologies have been concerned as the key not only to overcome the energy crisis including global warming, resource exhaustion, and environmental pollution, which problems are originated from the fossil fuel, but also confront the demands for high-performance electrical devices, such as smartphone, tablet, electric vehicles (EVs), etc. Among the many candidate energy storage systems, electrochemical energy storage devices have attracted the significant interests for effective electrical energy storage technology to alternate the fossil fuel-dependent energy system and operate portable electrical devices and EVs. There have been great attention and many researches over the past two decades, however, typical electrochemical energy storage devices

including lithium ion batteries (LIBs) and supercapacitors are required to enhance the electrochemical performances for meeting the needs of new markets and global industries. Therefore, a new energy storage system is required to satisfy the demands for high-performance electrochemical energy storage device which can be an alternative to LIBs and supercapacitors.

In this thesis, a new concept of energy storage devices, BatCap system, is suggested as an alternative to high-performance energy storage technology. The BatCap system is composed of BatCap electrodes consisting of battery and capacitor component hybrids in a single electrode with open porous structure, which gives a synergetic effect on the electrochemical performances of the device. Large amount of storable electrochemical energy from a battery component can improve the energy density of the BatCap system. Also, outstanding charge transport from the capacitor component and 3D open porous structure complement the high rate capability of the battery component with additional storable energy. The aims of this study were to introduce the theoretical approach for the BatCap system with comparison of performance between a typical battery-capacitor hybrid system, design the negative/positive electrode materials for the BatCap system with material characterization, and analyze the electrochemical performances of each material used in the BatCap system.

Part I provides a general introduction of energy storage devices regarding the requirements for the new energy device, BatCap. LIBs and supercapacitors are summarized with energy storage mechanism, performance parameters, and

performance influencing factors of each device. Also, main challenges and issues of the advanced energy storage devices are indicated by means of trade-off on the performances followed by the state of the art analysis. Throughout this part, the aim and scope of this research are introduced, which are theoretical study, synthesis, and characterization of the BatCap electrode materials.

Part II presents a theoretical study of the BatCap system in comparison with the performance between typical hybrid energy storage systems. Various energy storage systems are classified with the symmetry of the electrodes (symmetric/asymmetric), and the types of electrolytes (aqueous/organic). Energy density and power density of each system are theoretically calculated using various factors and coefficients for performance comparison. Then, theoretical modeling for the BatCap system is conducted to indicate the electrochemical performance of this new concept device followed by consideration of ideal structure of the BatCap electrode material. Conclusively, this part successively indicates the performance of each energy storage system depending on the specified conditions and advantages of the BatCap system compared to the typical energy storage systems.

Part III discusses the preparation and characterization of hyper-networked $\text{Li}_4\text{Ti}_5\text{O}_{12}$ /carbon hybrid nanofiber sheets and $\text{Li}_4\text{Ti}_5\text{O}_{12}$ /activated carbon hybrid nanotubes for the negative electrode of the BatCap system. 1D fibrous or tubular structures are chosen as the basic units for 3D open porous structure prepared by electrospinning. Also, $\text{Li}_4\text{Ti}_5\text{O}_{12}$ and carbonaceous materials are

employed as the battery and capacitor components, respectively, due to its great cycle stability and electronic conductivity.

Part IV discusses the preparation and characterization of sulfur-carbon nanosheet hybrids and graphene/carbon nanotube (CNT)-sulfur hybrid aerogel for the positive electrode of the BatCap system. 2D nanoplate structures, obtained by solid-solvothermal reaction for the sulfur-carbon nanosheet hybrids and by hydrothermal reduction for the graphene/CNT-sulfur hybrid aerogel, are employed as the basic units for 3D open porous structure. Cycle stability and rate capability of sulfur, which is capable of storing large amount of energy, are improved by hybridization with carbon nanosheet and graphene/CNT.

BatCap electrode materials in parts III and IV show improved electrochemical behaviors, which the enhancements are attributed to the better charge transfer kinetics through morphology control and hybridization of nanosized battery and capacitor components. They illustrate typical charge/discharge potential profiles of the BatCap electrode shown in part II of theoretical modeling and calculation. The enhanced electrochemical performances compared to typical energy storage systems summarized in part V clearly show the potential of the BatCap system as a new alternative for electrochemical energy device.

Keywords: Electrochemistry; BatCap system; Lithium ion batteries; Supercapacitors; Asymmetric electrode system; Lithium titanium oxide; Sulfur; Graphene; Carbon nanotube

Student number: 2007-22969

Contents

Part I Basic research needs of the new energy storage system

Chapter 1 Introduction	2
1.1 General introduction to energy storage devices	2
1.1.1 Overview of energy storage devices.....	4
1.1.2 Demand for high-performance energy storage devices	4
1.2 Fundamentals of energy storage devices.....	7
1.2.1 Lithium ion batteries and supercapacitors.....	7
1.2.2 Energy storage mechanism of energy storage devices.....	8
1.2.2.1 Working mechanism of LIBs and supercapacitors.....	8
1.2.2.2 Strengths and weaknesses of LIBs and supercapacitors	13
1.2.3 Performance parameters of energy storage devices	16
1.2.3.1 Energy density	16
1.2.3.2 Power density.....	17
1.2.3.3 Cycle stability	18
1.2.4 Factors influencing the performance of energy storage devices	20
1.2.4.1 Charges conductivities	20
1.2.4.2 Quantity of storable charge.....	22

1.2.4.3 Charge/discharge reaction potential.....	23
1.2.4.4 Microstructural change of the active material.....	24
1.3 Main challenges and issues related to advanced energy storage devices.....	
.....	26
1.3.1 Performance trade-off : energy density and power density.....	26
1.3.2 Performance trade-off : the storable charge quantity and cycle stability	
.....	28
1.4 State of the art of advanced energy storage devices.....	30
1.4.1 Approaches to enhance LIBs	30
1.4.1.1 Improving the power density	30
1.4.1.2 Improving the cycle stability	33
1.4.2 Approach to enhance supercapacitors.....	36
1.4.2.1 Improving the energy density	36
1.4.3 Battery-supercapacitor hybridization.....	40
1.4.3.1 Asymmetric electrode system	42
1.4.3.2 Introduction of a Li-ion organic electrolyte.....	44
1.5 Aim and scope of this research	46
1.5.1 Theoretical study of the BatCap system as an advanced energy storage	
device.....	46
1.5.2 Synthesis and characterization of the BatCap electrode materials....	48
1.6 References	49

Part II Fundamental study for the “BatCap” system

Chapter 2 Theoretical approach and prediction of the

BatCap system 57

2.0	Major symbols.....	57
2.1	Introduction.....	63
2.2	Theoretical comparison of typical capacitor systems.....	66
2.2.1	A symmetric capacitor system and an asymmetric capacitor system with an aqueous electrolyte	66
2.2.2	A symmetric capacitor system and an asymmetric capacitor system with an organic electrolyte	82
2.3	New concept of an electrode system: BatCap electrode	91
2.3.1	Concept of the BatCap electrode	91
2.3.2	Theoretical study of the BatCap electrode.....	93
2.3.3	Conditions of the electrode material for the BatCap system	106
2.3.4	Comparison of asymmetric capacitor and BatCap electrode system.....	110
2.4	Conclusions	114
2.5	Appendix	116
2.6	References	124

Part III Negative electrodes for the BatCap system

Chapter 3 Preparation and Electrochemical Performance of Hyper-networked $\text{Li}_4\text{Ti}_5\text{O}_{12}$ /Carbon Hybrid Nanofiber Sheets for a Negative Electrode of the BatCap System

.....	131
3.1 Introduction	131
3.2 Experimental	135
3.2.1 Reagents and chemicals.....	135
3.2.2 Synthesis of LTO/C-HNS	135
3.2.3 Characterization of LTO/C-HNS	136
3.2.4 Electrochemical tests of LTO/C-HNS	136
3.3 Results and discussion.....	139
3.3.1 Morphological, microstructural, and surface characteristics of LTO/C-HNS series.....	139
3.3.2 Electrochemical performance of LTO/C-HNS series	148
3.4 Conclusions	158
3.5 References	159

Chapter 4 Preparation and Electrochemical Performance of $\text{Li}_4\text{Ti}_5\text{O}_{12}$-Activated Carbon Hybrid Nanotubes for a Negative Electrode of the BatCap System	164
4.1 Introduction	164
4.2 Experimental	168
4.2.1 Reagents and chemicals.....	168
4.2.2 Synthesis of LTO-AC hybrid nanotubes	168
4.2.3 Characterization of LTO-AC hybrid nanotubes	169
4.2.4 Electrochemical tests of LTO-AC hybrid nanotubes	169
4.3 Results and discussion.....	172
4.3.1 Microstructural and morphological characteristics of LTO-AC hybrid nanotubes	172
4.3.2 Surface characteristics of LTO-AC hybrid nanotubes	179
4.3.3 Electrochemical performances of LTO-AC hybrid nanotubes..	187
4.4 Conclusions	209
4.5 Appendix	210
4.6 References	220

Part IV Positive electrodes for the BatCap system

Chapter 5 Preparation and Electrochemical Performance of Sulfur-Carbon Nanosheet Hybrids via a Solid Solvothermal Reaction for a Positive Electrode of the BatCap System..... 226

5.1	Introduction	226
5.2	Experimental	229
5.2.1	Reagents and chemicals.....	229
5.2.2	Synthesis of SCNH.....	229
5.2.3	Characterization of SCNH.....	229
5.2.4	Electrochemical tests of SCNH	230
5.3	Results and discussion.....	232
5.3.1	Microstructural and morphological characteristics of SCNH	232
5.3.2	Surface characteristics of SCNH	235
5.3.3	Electrochemical performances of SCNH	240
5.4	Conclusions	250
5.5	References	251

Chapter 6 Preparation and Electrochemical Performance of a Graphene/CNT-Sulfur Hybrid Aerogel via a One-step Hydrothermal Reaction for a Positive Electrode of the BatCap System.....	255
6.1 Introduction	255
6.2 Experimental	259
6.2.1 Reagents and chemicals.....	259
6.2.2 Synthesis of the GCSH aerogel	259
6.2.3 Characterization of the GCSH aerogel	260
6.2.4 Electrochemical tests of the GCSH aerogel	261
6.3 Results and discussion.....	262
6.3.1 Microstructural and morphological characteristics of the GCSH aerogel.....	262
6.3.2 Surface characteristics of the GCSH aerogel	269
6.3.3 Electrochemical performance of the GCSH aerogel	273
6.4 Conclusions	279
6.5 References	280

Part V Conclusions

Chapter 7 Conclusive remarks and the outlook.....	284
--	------------

List of Figures

Figure 1.1. Energy crisis due to the use of fossil fuels

Figure 1.2. Overview of the energy industry

Figure 1.3. Scheme of the Charge and discharge mechanism of LIBs

Figure 1.4. Scheme of the Charge and discharge mechanism of supercapacitors
(left: EDLC; right: pseudocapacitor)

Figure 1.5. Ragone plot of batteries and supercapacitors as described metaphorically schemes

Figure 1.6. Plots of the potential vs. time/charge (left) and cycle property (right) of a typical electrochemical energy storage device

Figure 1.7. Charge transport scheme in an electrochemical energy storage device

Figure 1.8. Specific power vs. specific energy, also called a Ragone plot, for various electrical energy storage devices

Figure 1.9. Storable charge quantity and volume expansion of various anode active materials for LIBs

Figure 1.10. Requirement to improve the power density of LIBs with the related equation

Figure 1.11. Effects of morphological control and the use of a composite with a conductive material on Si at a high rate capability

Figure 1.12. Improving the cycle stability via (A) use of a zero-strain material, (B) confinement of the active material, and (C) control of the storable charges

Figure 1.13. Requirement to improve the energy density of supercapacitors with the related equation

Figure 1.14. Scheme of a hybrid capacitor with an asymmetric electrode system and an organic electrolyte

Figure 1.15. CV profile and Ragone plot of activated carbon nanofiber//graphene-MnO

Figure 1.16. Charge/discharge-potential profile and cycle stability test results for a TiO₂(B)//AC hybrid capacitor with a Li-ion containing organic electrolyte

Figure 1.17. Scheme of the BatCap system consisting of the BatCap electrode for each electrode with a Li-ion containing organic electrolyte

Figure 2.1. Schematic representation of (A) single electrode system and (B) a symmetric capacitor system with an aqueous electrolyte according to the charge-potential profile

Figure 2.2. Schematic representation of an asymmetric capacitor system with an aqueous electrolyte according to the charge-potential profile

Figure 2.3. (A) Plot of the value of the battery-type material-related coefficient, K_{BM} , as a function of the mass and working potential range ratio factors of the battery-type electrode, k_1 and k_2 , respectively. (B) Plot of $K_{BM}=1/2$.

Figure 2.4. Comparison of various capacitor systems using an aqueous electrolyte

Figure 2.5. Plot of the condition for higher values of ED_{as} and PD_{as} compared

to the simultaneous values of ED_s and PD_s

Figure 2.6. Schematic representation of (A) a single electrode system and (B) an asymmetric capacitor system with an organic electrolyte according to the charge-potential profiles

Figure 2.7. (A) Schematic representation of asymmetric capacitor systems containing an aqueous electrolyte and an organic electrolyte according to the charge-potential profiles. (B) Plot of the specified condition $K_E > 1$ as a function of k_3 and k_4

Figure 2.8. Schematic representation of the BatCap electrode system with an organic electrolyte according to the charge-potential profile

Figure 2.9. Scheme of the storable energy of the BatCap system

Figure 2.10. Plot of the value of the BatCap-related coefficient, K_{BC} , as a function of the working potential range ratio factors (k_2 and k_2') and storable electrical charge ratio factor of the capacitor component (k_5) in the BatCap electrode

Figure 2.11. (A) Ideal structure of the BatCap electrode material which resembles (B) the “moisture ant” habitat

Figure 2.12. Specific power density-specific energy density plot of typical commercialized batteries (grey region), an asymmetric capacitor system with an aqueous electrolyte (blue region), an asymmetric capacitor system with an organic electrolyte (green region), and the BatCap system (red region) using various electrode materials

Figure 3.1. Schematic illustration for synthesis of PPy-HNS via electrospinning and vapor polymerization techniques

Figure 3.2. (A) FE-SEM micrographs of electrospun HNS (B) pyrrole vapor polymerized PPy-HNS. (C) LTO/C-HNS after heat treatment of PPy-HNS. The insets show a magnified image of each sample

Figure 3.3. (A) HR-TEM micrograph of LTO/C-HNS, (B) a magnified image of the surface region, and (C) SAED pattern of (B). (D) Typical STEM and EDS images of the LTO/C-HNS surface. The inset graphs of (D) indicate the positions of the line scanning profiles from the EDS images for each atom.

Figure 3.4. X-ray diffractogram of LTO/C-HNS (top) together with JCPDF data for rutile (middle; Card No. 21-1276), and typical $\text{Li}_4\text{Ti}_5\text{O}_{12}$ (bottom; Card No. 49-0207). Diamond symbol indicates the presence of trace amount of rutile TiO_2 impurity.

Figure 3.5. Raman spectra of LTO/C-HNS. The solid lines are the superposition of the D, D', and G bands, shown in red, green, and blue, respectively, fitted by a Lorentzian fitting procedure

Figure 3.6. (A) Thermogravimetric analysis (TGA) of the LTO/C-HNS. Solid line: thermogravimetric curve, dotted line: differential thermogravimetric curve. (B) Nitrogen adsorption/desorption isotherms at 77 K of the LTO/C-HNS (Inset : Pore size distribution of the product, analyzed using the BJH equation.)

Figure 3.7. Cycle performances of the LTO/C-HNS at various charge/discharge rates. The inset shows the potential profiles at a charge/discharge rate of 100 mA g^{-1} .

Figure 3.8. (A) Cycle performances of LTO/C-HNS in the range of 1–2.5 V vs. Li/Li⁺ (Inset : specific capacity ratio over the potential range 1–2.5 V vs. Li/Li⁺ at various charge/discharge rates.) and (B) discharge capacity retention at each charge/discharge rate for LTO/C-HNS and commercial LTO (supported from Umicore Korea).

Figure 3.9. The CV of AC at a 5 mV s⁻¹ sweep rate.

Figure 3.10. Galvanostatic charge/discharge graph of the LTO/C-HNS//AC hybrid BatCap system at C/3 rate (A) and the Ragone plot of the LTO/C-HNS//AC hybrid BatCap system and AC//AC symmetric capacitor at various charge/discharge rates in the working potential range 0–2.5 V (B).

Figure 4.1. XRD patterns of the (A) LTO/AC hybrid nanotubes and (B) typical Li₄Ti₅O₁₂ phase.

Figure 4.2. FE-SEM micrographs of (A) LTO/AC hybrid nanotubes with (B) a magnified image and TEM micrograph of (C) the LTO/AC hybrid nanotubes and (D) a magnified image of the surface region.

Figure 4.3. The thermogravimetric analysis (TGA) of the LTO/C-HNS. The solid line indicates the thermogravimetric curve and the dotted line indicates the differential thermogravimetric curve.

Figure 4.4. (A) Nitrogen adsorption isotherms at 77K of the LTO/AC hybrid nanotubes with the inset showing the pore size distribution and (B) a comparison of the BET specific surface area and amount of residue remaining after heat treatment under ambient conditions.

Figure 4.5. Raman spectrum and curve fitting result for the LTO/AC hybrid nanotubes. Four peaks with peak maxima at 1171, 1337, 1507, and 1604 cm^{-1} were required for the curve description of the Raman spectrum.

Figure 4.6. XPS survey spectrum with the inset showing the Ti2p region (A) and the C1s region (B) of the LTO/AC hybrid nanotubes.

Figure 4.7. (A) Cycle performances of the LTO/AC hybrid nanotubes at various charge/discharge rates. The inset shows the differential capacity vs. cell potential curve at a charge/discharge rate of 100 mA g^{-1} during the second cycle. (B) Retained discharge capacity ratio of the LTO/AC hybrid nanotubes and the pure $\text{Li}_4\text{Ti}_5\text{O}_{12}$, and Coulombic efficiencies at various charge/discharge rates of the LTO/AC hybrid nanotubes.

Figure 4.8. Cycle performances of the LTO/C hybrid nanotubes at various charge/discharge rates in the potential range 1.0-2.5 V vs. Li/Li^+ . The inset shows the discharge capacity of the LTO/AC hybrid nanotubes and LTO/C hybrid nanotubes at various charge/discharge rates.

Figure 4.9. Nyquist impedance spectra of the LTO/AC hybrid nanotubes and pure $\text{Li}_4\text{Ti}_5\text{O}_{12}$. A magnified view of the high frequency region for the LTO/AC hybrid nanotubes is provided in the inset.

Figure 4.10. Experimental and simulated plots for AC impedance spectra of the LTO/AC hybrid nanotubes with equivalent circuit and simulated impedance equation.

Figure 4.11. Normalized capacitance and frequency response for the LTO/AC hybrid nanotubes and pure $\text{Li}_4\text{Ti}_5\text{O}_{12}$ half-cells.

Figure 4.12. The CV of AC at a 5 mV s^{-1} sweep rate over various potential ranges from 1 to 4 V vs. Li/Li⁺.

Figure 4.13. Galvanostatic charge/discharge plot for the LTO/AC hybrid nanotubes//AC hybrid BatCap system at a 4.5 C rate and a 9 C rate in the working potential range of 0.5-3.5 V. The black-colored potential profile indicates the full-cell, the red-colored potential profile indicates the negative electrode of the LTO/AC hybrid nanotubes, and the blue-colored potential profile indicates the positive AC electrode.

Figure 4.14. Ragone plot for the LTO/AC hybrid nanotubes//AC hybrid BatCap system and the AC//AC symmetric capacitor at various charge/discharge rates in the working potential range of 0.5-3.5 V. The data were calculated based on the total mass of both electrodes.

Figure 4.A1. (A) Scheme of LTO-AC simple mixing electrode. (B) Cycle stability and (C) charge/discharge profiles of LTO-AC simple mixing electrode in the half-cell test at various charge/discharge rates

Figure 4.A2. Cycle stability comparison of LTO, LTO-AC simple mixing, and LTO/AC hybrid nanotube electrode in the half-cell test at various charge/discharge rates.

Figure 4.A3. (A) Scheme of LTO//AC asymmetric capacitor with theoretical charge/discharge potential profile and (B) charge/discharge potential profile of LTO//AC asymmetric capacitor at low (left side) and high (right side) rates.

Figure 4.A4. (A) Scheme of LTO-AC simple mixing//AC asymmetric capacitor with theoretical charge/discharge potential profile and (B) charge/discharge

potential profile of LTO-AC simple mixing//AC asymmetric capacitor at low and high rates

Figure 4.A5. Ragone plot for the AC//AC symmetric capacitor, LTO/AC hybrid nanotubes//AC hybrid BatCap system, LTO//AC asymmetric capacitor, and LTO-AC simple mixing//AC asymmetric capacitor at various charge/discharge rates. The data were calculated based on the total mass of both electrodes

Figure 5.1. FE-SEM images of the SCNHs under (A) low and (B) high magnification. (C) TEM and (D) HR-TEM images of the SCNH showing crumpled carbon nanosheet

Figure 5.2. FE-SEM image (A) and TEM images (B) of the CNs showing crumpled carbon nanosheet

Figure 5.3. (A) EDS mapping analysis results of the SCNHs for elements of carbon (green) and sulfur (red) and (B) Powder XRD patterns of the SCNHs (above), elemental sulfur (middle), and the CNs (bottom)

Figure 5.4. XPS (A) and Raman (B) spectrum of the SCNHs. The inset of (A) depicts a magnified view of the the carbon, and a magnified spectrum on the left of (A) indicates XPS of elemental sulfur (top) and SCNHs (bottom). Blue arrow is the amount of chemical shift after hybridization of sulfur and carbon.

Figure 5.5. Electrochemical characterization of the SCNHs: (A) cyclic voltammetry of SCNHs and elemental sulfur in the second cycle at a sweep rate of 5 mV s^{-1} , and (B) cycle performance test results of the SCNHs at various charge/discharge rates. Specific capacities are calculated based on the sulfur

mass. Inset of (B) depicts potential profiles of the SCNHs at various charge/discharge rates.

Figure 5.6. Nyquist impedance spectra of the SCNHs and pure sulfur. The inset shows the equivalent circuit evaluated based on the AC impedance spectra of the SCNHs and pure sulfur.

Figure 5.7. (A) Galvanostatic charge/discharge plot for the AC//SCNH BatCap system at a 10 C rate and a 20 C rate in the working potential range of 0.1-1.8 V. The black-colored potential profile indicates the full-cell, the red-colored potential profile indicates the positive electrode of the AC//SCNH, and the blue-colored potential profile indicates the negative AC electrode. (B) Ragone plot for the AC// AC//SCNH BatCap system at various charge/discharge rates in the working potential range of 0.1-1.8 V. The data were calculated based on the total mass of both electrodes.

Figure 6.1. Photographs of (A) a free-standing GCSH hydrogel after the hydrothermal reaction, (B) a free-standing GCSH aerogel after the freeze-drying process of the hydrogel, and (C) load-bearing capacity of the free-standing GCSH aerogel

Figure 6.2. (A) FE-SEM image with the inset showing a high-resolution image and (B) a HR-TEM image of the free-standing GCSH aerogel

Figure 6.3. (A) EDS analysis and (B) TGA results of the free-standing GCHS aerogel

Figure 6.4. Powder XRD spectrum of the free-standing GCSH aerogel, the GSH aerogel, and pristine GO

Figure 6.5. (A) Nitrogen adsorption isotherms at 77 K of the GCSH aerogel with the inset showing the pore size distribution, and (B) XPS survey spectrum with magnified images of the C1s, O1s, and S2p regions

Figure 6.6. (A) Charge/discharge potential profile of GCSH aerogel at 100 and 500 mA g⁻¹ after 5 cycle (Inset: cycle performances of GCSH aerogel and GSH aerogel at a variety charge/discharge rates.) (B) Cycle performances of GCSH aerogel and MPC-S composite at 100 mA g⁻¹) Specific capacities were calculated based on the total mass of each electrode.

Figure 6.7. (A) Galvanostatic charge/discharge plot for the AC//GCSH aerogel BatCap system at a 2/3 C rate in the working potential range of 0.1-2.5 V. The black-colored potential profile indicates the full-cell, the blue-colored potential profile indicates the positive electrode of the AC//GCSH aerogel, and the red-colored potential profile indicates the negative AC electrode. (B) Ragone plot for the AC//GCSH aerogel BatCap system at various charge/discharge rates in the working potential range of 0.1-2.5 V. The data were calculated based on the total mass of both electrodes.

List of Tables

Table 1.1. Electrochemical performances of supercapacitors and LIBs

Table 1.2. Selected properties of some of the nanostructured carbon materials used in EDLCs

Table 2.1. Theoretical equations to describe the electrochemical performance of each system

Table 2.2. Summary of various electrochemical capacitor systems

Table 3.1. D, D', and G peak parameters, and R of the Raman spectra for LTO/C-HNS

Table 3.2. Pore characteristics determined from the nitrogen adsorption isotherm at 77 K of the LTO/C-HNS

Table 4.1. Residual weight ratios of the LTO/C-HNS series after TGA measurements

Table 4.2. Pore characteristics determined from the nitrogen adsorption isotherm at 77 K of the LTO/AC hybrid nanotubes, LTO/C hybrid nanotubes, and air-heat treated LTO/AC hybrid nanotubes

Table 4.3. Deconvolution of the Raman spectrum of the LTO/AC hybrid nanotubes, as shown in Figure 4.5

Table 4.4. C1s peak deconvolution of the XPS spectrum in the LTO/AC hybrid nanotubes, as shown in Figure 4.6B

Table 4.5. Summary for equivalent circuit with impedance equation from AC impedance spectra of LTO/AC hybrid in Figure 4.10

Table 4.6. Impedance parameters and Li^+ ion diffusion coefficient calculated from the impedance spectra of the LTO/AC hybrid nanotubes and pure $\text{Li}_4\text{Ti}_5\text{O}_{12}$

Table 5.1. Component distribution analysis results by EDS

Table 5.2. Impedance parameters and Li^+ ion diffusion coefficient calculated from the impedance spectra of the SCNHs and pure sulfur

Table 6.1. EDS analysis and EA results for each element of the GCHS aerogel

Table 6.2. Pore characteristics determined from the nitrogen adsorption isotherm at 77 K of the GCSH aerogel

Table 6.3. Peak deconvolutions of the XPS spectra for the GCSH aerogel, as shown in Figure 6.5B

Table 7.1. Summaries of the K-coefficients for each BatCap electrode material

Part I

Basic research needs of the new energy storage system

Chapter 1. Introduction

1.1. General introduction to electrical energy

There is currently a great deal of interest in the finding a solution for the worldwide energy crisis due to the increasing dependence on energy by mankind. Over the past two centuries, fossil fuel has led the energy industry as the most important and widely used energy resource. However, it is now clearly accepted that the production and combustion of fossil fuels are the main causes of grave problems with the environment, such as global warming, ecological problems, and resource exhaustion, as shown in Figure 1.1 [1]. As a solution of this issue, electric energy is increasingly considered as an alternative to fossil fuels due to its clean and useful form. Thus, there is tremendous interest in the development of clean and economic electrical energy resources (e.g. solar energy, wave energy, geothermal energy) as well as high-performance electrical energy storage devices.

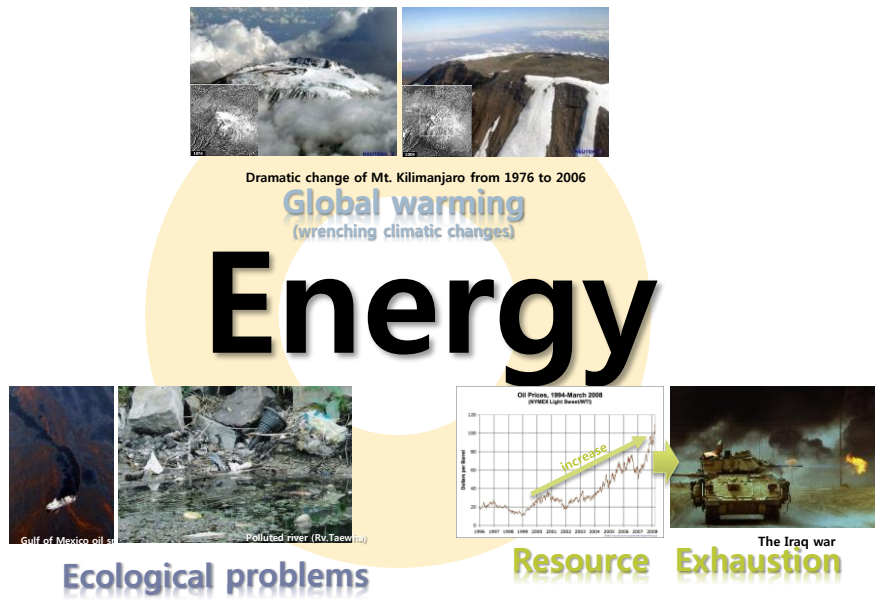


Figure 1.1. Energy crisis due to the use of fossil fuels

1.1.1. Overview of energy storage devices

The energy industry is involved in energy resource production, electrical energy conversion, electrical energy storage, and electrical energy or fossil fuel consumption, as shown in Figure 2. Generally, electrical energy produced by plants can be directly used or can be stored in energy storage devices for specific purposes. Because electrical energy converted from energy resources, such as fossil fuel, should be utilized at the moment it is produced, electrical energy storage devices that use the converted energy efficiently are necessary. An energy storage device is a utility that allows freedom in terms of time- and space-regarding the use of electrical energy by connecting electrical energy production and energy consumption.

1.1.2. Demands for high-performance energy storage devices

As mentioned above regarding the energy crisis, the current energy industry based on fossil fuel is not sustainable. Also, it cannot be easily achieved to supply the strong growth of required energy demand of the entire world for the future, if there is no breakthrough on the energy saving from efficiency increase, according to the US electricity generation scenario [2]. Moreover, the explosive development of high-performance portable devices and electrical vehicles into vehicles which consume alternates to fossil fuel requires greater electrical power and higher energy densities. Therefore, it is necessary to develop high-

performance and more efficient energy storage devices to deal with the demands from the electrical energy industry.

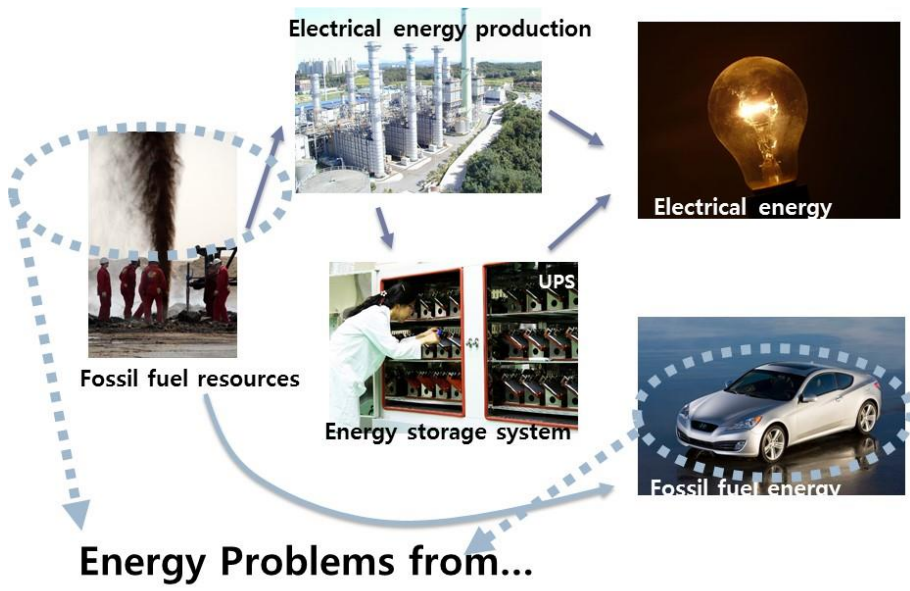


Figure 1.2. Overview of the energy industry

1.2. Fundamentals of energy storage devices

1.2.1. Lithium ion batteries and supercapacitors

Electrochemical energy storage devices are the most important systems to store the electrical energy efficiently. Lithium ion batteries (referred to here as LIBs) and supercapacitors, developed over the past two decades, are the most widely used energy storage devices due to their rechargeability and better electrochemical performance compared to other types of devices [3-5]. LIBs are one of the most popular solid-state batteries due to their superior characteristics, such as no memory effect, a high specific energy, and low loss of charge in an the open-circuit state. After their first suggestion by Whittingham et al. in 1970s [6] and subsequent breakthroughs by researches of Goodenough et al., LIBs were commercialized by Sony in 1991. Regarding the supercapacitor, Conway et al. developed the extensive fundamentals of this advanced energy storage devices between 1975 and 1980 [7]. Numerous scientific and technological studies have been reported since the 1990s [8] related to the storage and release of electrical energy at a short time with great cycle stability. Both LIBs and supercapacitor have been widely studied and produced over the past twenty years given the increase in the market for portable electrical devices.

1.2.2. Energy storage mechanism of energy storage devices

Fundamentally, LIBs and supercapacitors, which mainly consist of electrodes, electrolyte and separator, are based on the electrochemical reaction between electrode and electrolyte. In contrast to basic electrochemistry, these two types of energy storage devices show clearly different operating mechanisms, which are redox reaction and electrostatic charge storage for LIBs and supercapacitors, respectively.

1.2.2.1. Working mechanisms of LIBs and supercapacitors

LIBs operate as electrochemical energy storage devices via redox reaction between the active material in the electrode and Li-ions in the electrolyte. This can be described as a half-cell reaction, as shown by equation 1.1 [9],



where v_{O} and v_{R} represent the stoichiometric coefficients of the oxidant and reductant, respectively. Also, the electrochemical energy of this equation is determined by the passed charge multiplied by the reversible potential difference in an equilibrium state. This is expressed by the equation below.

$$\Delta G = -nFE \quad (1.2)$$

Here, ΔG is the Gibbs free energy of the redox reaction, n is the number of passed electrons per related Li atom, F denotes the charge of the mole of electron (about 96500 C), and E is the electromotive force (EMF) of the electrode reaction. Based the equation 2, the half-cell potential of LIBs is given by equation 1.3, which is known as the Nernst equation,

$$E_{\text{electrode}} = E_{\text{electrode}}^0 - \frac{RT}{nF} \ln \frac{a_{\text{anodic}}}{a_{\text{cathodic}}} \quad (1.3)$$

where $E_{\text{electrode}}$, $E_{\text{electrode}}^0$, R , a_{anodic} , and a_{cathodic} are the electrode half-cell potential, standard half-cell potential, ideal gas constant ($8.314 \text{ J mol}^{-1}\text{K}^{-1}$), anodic reaction chemical activity, and cathodic reaction chemical activity, respectively. The charge/discharge process of LIBs, which can be described by the Nernst equation, includes a redox reaction on the surface of the electrode and a charge transfer process, as shown in Figure 1.3. Therefore, the electrochemical performances of LIBs are related to the redox reaction and charge transfer kinetics.

On the other hand, supercapacitors store electrochemical energy on the surface of the electrode materials, which can be classified as an electric double layer capacitor (denoted as EDLC) and a pseudocapacitor using non-faradaic and faradaic reactions, respectively [8]. Essentially, in the case of EDLC, electrochemical energy is charged and discharged by means of ion separation coupling with electrons by the electrostatic force between electrodes, as

described on the left side in Figure 1.4. In contrast, the pseudocapacitor is charged and discharged with a charge transfer reaction, i.e., a faradaic reaction between the active material and the electrolyte. An example is the doping and undoping process of polymer active materials, such as polypyrrole or polyaniline, as described on the right side in Figure 1.4. Because the amount of storable charge of the supercapacitors depends on the potential difference between the negative and positive electrodes, it can be defined as “the storable charges per potential change” in the following equation;

$$C = \frac{dq}{dV} \quad (1.4)$$

where q is the amount of charge and V is the cell potential. Compared to the EDLC, which has a constant and potential-independent specific capacitance, pseudocapacitor has partially potential-dependent specific capacitance due to the charge transfer reaction on the surface of the electrode. Hence, specific capacitance of this type of supercapacitor is described by average capacitance calculated by equation 1.5;

$$C_{\text{average}} = \frac{q_{\text{total}}}{V_{\text{total}}} \quad (1.5)$$

where the q_{total} and V_{total} are total charge and potential change, respectively.

As mentioned above, supercapacitors store electrons and ions on the surface of the electrode. Therefore, the electrochemical performances of the supercapacitors are hardly dependent on the surface area and pore structure of the electrode.

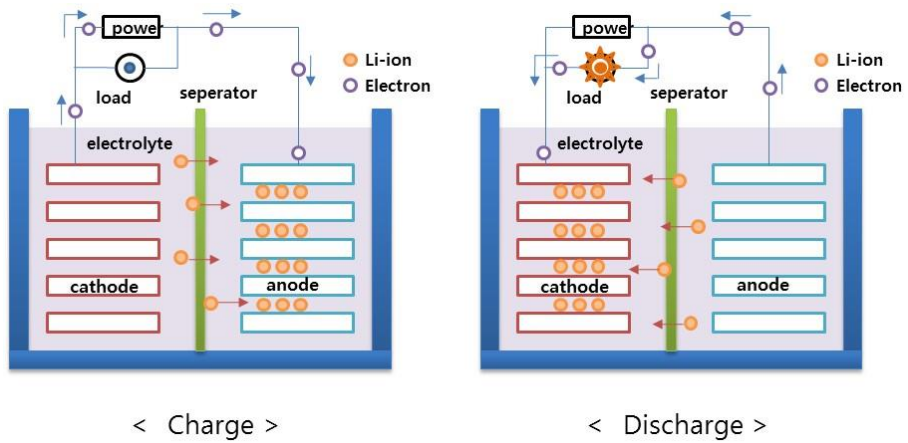


Figure 1.3. Scheme of the Charge and discharge mechanism of LIBs

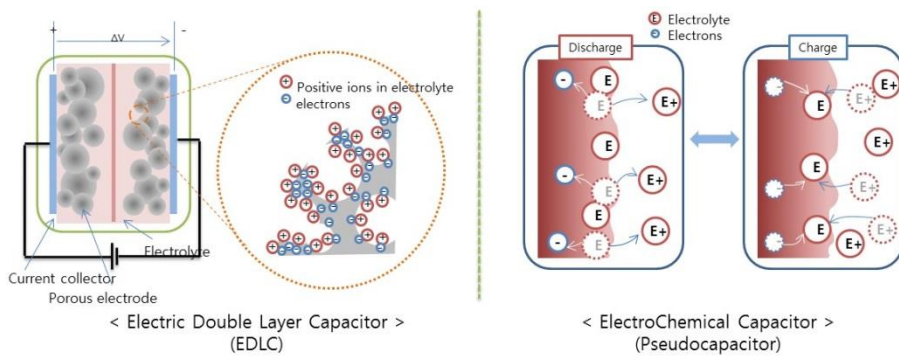


Figure 1.4. Scheme of the Charge and discharge mechanism of supercapacitors

(left: EDLC; right: pseudocapacitor)

1.2.2.2. Strengths and weaknesses of LIBs and supercapacitors

Figure 1.5 and Table 1.1 describe the general performance characteristics of LIBs and supercapacitors. LIBs have higher energy density than supercapacitors due to energy storage mechanism using redox reaction. However, LIBs show poor cycle stability and short service lifetimes. On the other hand, supercapacitors have great cycle stability up to million times of rechargeability with a high power density. The strengths and weaknesses of each energy storage device can be represented metaphorically using two different types of water tanks, one with a large volume, a small nozzle, and damaged surface for LIBs and the other with a small volume and a large size for supercapacitors, as shown in Figure 1.5. Therefore, most studies on LIBs have focused on enhancing the cycle stability and power density. Moreover, supercapacitors were developed to increase the energy density while retaining good cycle stability and high power density.

Table 1.1. Electrochemical performances of supercapacitors and LIBs [10]

PERFORMANCES	SUPERCAPACITOR	LIBS
Discharging time	1 ~ 30 sec	0.5 ~ 3 hrs
Charging time	1 ~ 30 sec	1 ~ 5 hrs
Energy density (Wh kg⁻¹)	5 ~ 10	30 ~ 200
Power density (W kg⁻¹)	2,000 ~ 5,000	50 ~ 200
Working temp. (°C)	-40 ~ 70	-10 ~ 50
Cycle life	> 1,000,000	500 ~ 2,000
Service life	> 10 yrs	2~3 yrs

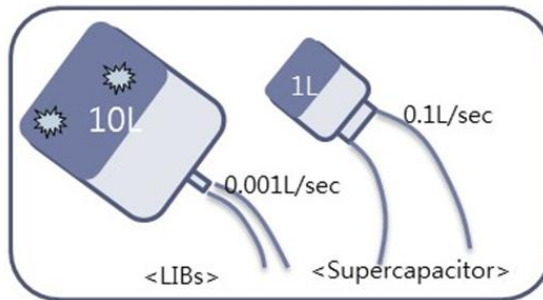
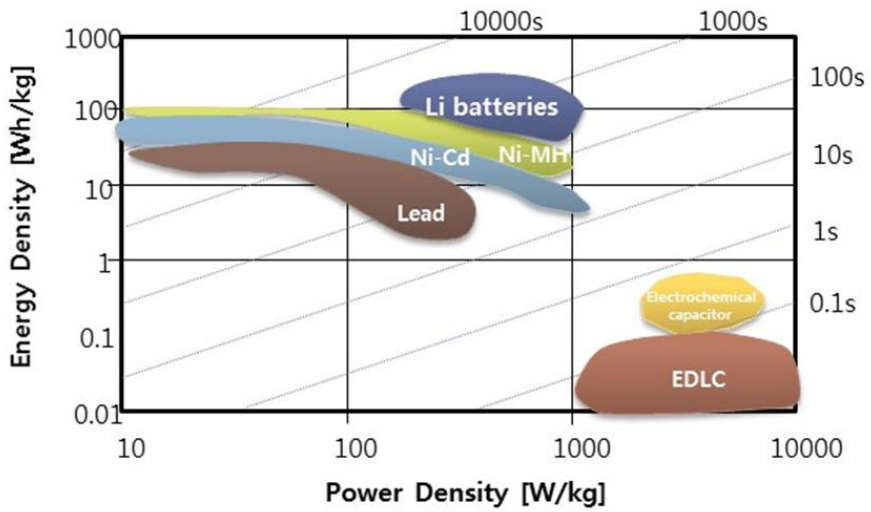


Figure 1.5. Ragone plot of batteries and supercapacitors as described metaphorically

1.2.3. Performance parameters of energy storage devices

As indicated in Table 1.1, there are various parameters to describe the electrochemical performances of energy storage systems, LIBs and supercapacitors. However, among these parameters, there are important and generally considered performance parameters that show the properties of each types of energy storage device. These are the energy density, power density, and cycle stability.

1.2.3.1. Energy density

Energy density is the performance parameter which indicates the amount of electrochemical energy that can be stored in the material. The energy density can be described by the amount of storable energy for an hour per unit volume or mass, of which the units are Wh kg⁻¹ or Wh L⁻¹ for the specific energy density, as described in equation 1.6:

$$E = \int qdV$$
$$ED = \frac{\int qdV}{m} \cdot \frac{1}{3600} \quad (1.6)$$

where E and ED are the amount of energy and the specific energy density of the unit mass. Therefore, the energy density can be obtained from the area of a plot of the potential and time/charge graph, as shown in Figure 1.6 (the region in red).

1.2.3.2. Power density

The power density refers to how much energy can be discharged at one time.

The power density can be expressed as the amount of dischargeable energy at a second per unit volume or mass, of which the units are W kg^{-1} or W L^{-1} for the specific power density in equation 1.7:

$$\begin{aligned} P &= V \cdot \frac{dq}{dt} \\ PD &= \frac{V \cdot \frac{dq}{dt}}{m} \end{aligned} \quad (1.7)$$

where P and PD are the power and the specific power density for the unit mass.

Because the power density can effectively represent the instant available power of energy storage devices, it can be described by the area shown as the region of blue in Figure 1.6.

1.2.3.3. Cycle stability

The cycle stability is a useful parameter to show the renewable ability of an energy storage device. The Coulombic efficiency and capacity retention rate [11] are defined in equation 1.8. A higher value of the Coulombic efficiency (the small green area in Figure 1.6) and a lower value of the capacity retention rate (the green arrow in Figure 1.6) mean better cycle stability.

$$\begin{aligned} \text{Coulombic efficiency}(\%) &= \frac{\text{capacity}_{\text{discharge}}}{\text{capacity}_{\text{charge}}} \times 100 \\ \text{Capacity retention rate} &= \frac{\text{capacity retention}}{\text{cycle}} \end{aligned} \quad (1.8)$$

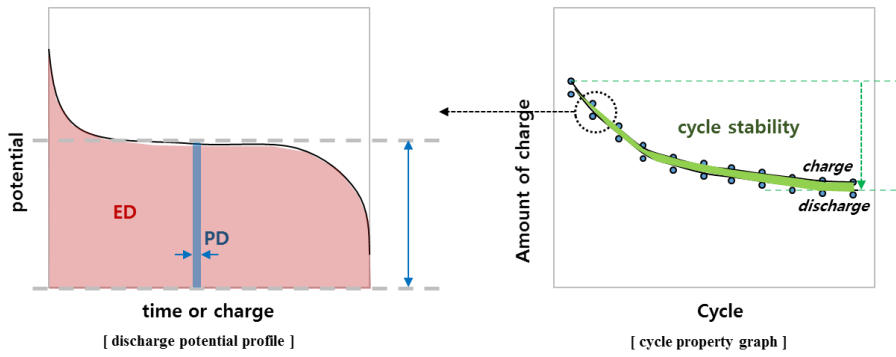


Figure 1.6. Plots of the potential vs. time/charge (left) and cycle property (right) of a typical electrochemical energy storage device.

1.2.4. Performance influencing factors of the energy storage devices

Electrochemical performances described by the aforementioned performance parameters are determined by performance influencing factors, which are charge conductivities, quantity of storable charges, the charge/discharge reaction potential, and the microstructural changes of the active material. It is clear that performance influencing parameters are related to the electrochemical performances in a complex manner, therefore, they will be dealt with here separately.

1.2.4.1. Charges conductivities

There are two different types of charges involved in the electrochemical reaction, i.e., those of electrons and ions. Because the entire electrochemical reaction in the energy storage device is fundamentally influenced by charge transport kinetics, the conductivities of the charges, mainly related to the power density, are important performance influencing factors. The electron conductivity is influenced by the following three steps:

- (1) Electron transport from current collector to the active material
- (2) Electron transport between each active material
- (3) Electron transport in each active material

illustrated in Figure 1.7.

The ion conductivity is determined by two steps, as also shown in Figure 1.7.

(4) Ion transport from electrolyte to the active material in the electrode

(5) Ion transport in each active material

Also, the charges conductivities can influence not only the power density but also the energy density and cycle stability.

1.2.4.2. Quantity of storable charge

The amount of storable energy, i.e., the energy density, is directly related to the quantities of storable charges of all electrons in the electrode, i.e., storable Li-ions for LIBs and electrolyte ions for supercapacitors. This influencing factor is determined by various intrinsic properties of the active material of the electrode and solvent or ions in the electrolyte. Examples are the surface area, redox reaction with Li-ions, and the electrolyte ion size, etc.

1.2.4.3. Charge/discharge reaction potential

Each electron charged in the electrode has some amount of energy which is reflected in the potential (called the voltage). The charge/discharge reaction in the energy storage device is the redox reaction and each the redox reaction indicating a phase transition in the electrode occurs at a specified redox reaction potential. Also, a potential change arises during the operation of the EDLC controlling the electrostatic force. The reaction potential in the energy storage device determines the stored energy of the charges in the electrode. Because the energy density and power density are defined using the reaction potential, the charge/discharge reaction potential is one of the influencing factor on the electrochemical performance in energy storage devices.

1.2.4.4. Microstructural change of the active material

In the charge/discharge process of energy storage devices, a storable space is required to store the charges in the electrodes. Therefore, the amount of storable charge is proportional to the size of the space for the ions of the electrolyte. When the ions are charged in the electrode, a mechanical load is accompanied by a volume expansion from the stored ions causing a microstructural change of the active material. This phenomenon has an influence on the reversibility of the charge transfer reaction of (6) in Figure 1.7. Therefore, the microstructural change of the active material is influencing factor on the cycle stability of the redox reaction in an energy storage devices. Otherwise, there is little microstructural change of the active material during the EDLC operating process due to the energy storage mechanism using electrostatic force between the surfaces of the electrodes. This indicates the great cycle stability of the EDLC compared to LIB or pseudocapacitor.

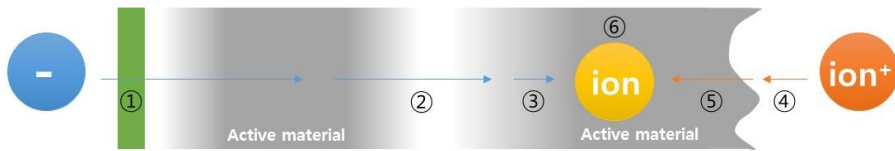


Figure 1.7. Charge transport scheme in an electrochemical energy storage device.

1.3. Main challenges and issues related to advanced energy storage devices

In spite of wide range of studies on all whole aspects of LIBs and supercapacitors, there is great demand for advanced energy storage devices due to the emergence of applications requiring high-performance, such as electric vehicles and the many new types of portable electronic devices. There have been many studies to enhance the electrochemical performance of each type of device. In brief, approaches to enhance the performance of energy storage device have focused on the overcoming performance trade-off problems, specifically “energy density vs. power density” and “the storable charge quantity vs. cycle stability”.

1.3.1. Performance trade-off : energy density and power density

Figure 1.8 illustrates the specific power density and energy density of various energy storage devices. According to Figure 1.8, as shown by the green circle, it is clear that the energy density and power density exist in an inverse proportion relationship. This can be understood in terms of the energy storage mechanisms used with each type of device. Therefore, most studies at present focus on increasing the power density of advanced LIBs and on improving the energy density of advanced supercapacitors.

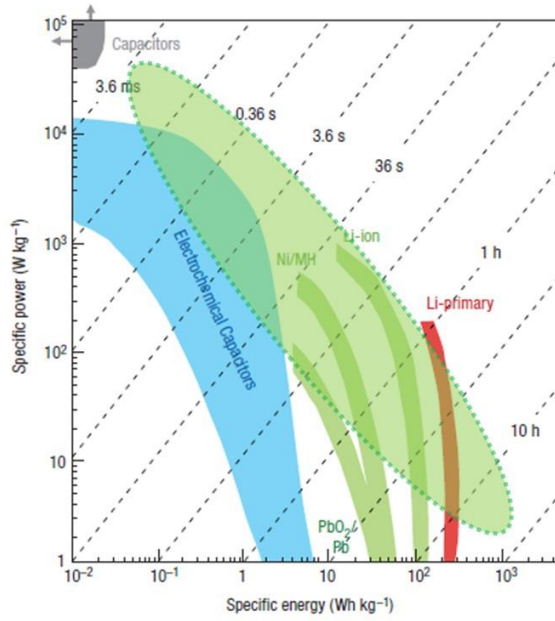


Figure 1.8. Specific power vs. specific energy, also called a Ragone plot, for various electrical energy storage devices [5]

1.3.2. Performance trade-off : the storable charge quantity and cycle stability

Another performance trade-off problem is the storable charge quantity vs. the cycle stability. This problem mainly arises in LIBs or pseudocapacitors which use a redox reaction to store electrochemical energy. As mentioned above, the storage of the charge induces a volume expansion of the electrode: that is, the storable charge quantity is proportional to the volume expansion. For instance, not only carbonaceous material (grey circles) but also various metal oxides (colored circles) exist in a linear relationship between the storable charge quantity and the volume expansion of the anode material of LIBs, as shown in Figure 1.9. Due to the mechanical load followed by the volume expansion, the reversibility of the charge/discharge process is deteriorated as the increase of stored charges. Therefore, numerous studies have attempted to enhance the cycle stability of redox reaction-involving energy storage devices by depressing the volume expansion while minimizing the capacity loss.

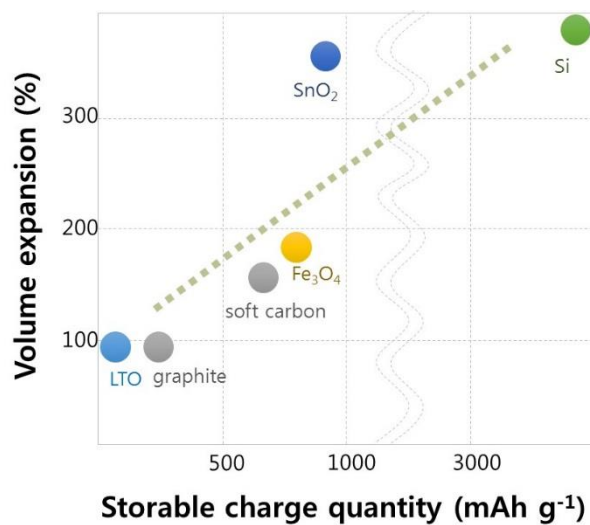


Figure 1.9. Storable charge quantity and volume expansion of various anode active materials for LIBs.

1.4. State of the art of the advanced energy storage devices

1.4.1. Approaches to enhance LIBs

Of course, increasing the energy density of LIBs is an important line of research related to LIBs, and there have been two main issues pertaining to advanced LIBs to improve the power density and cycle stability of devices.

1.4.1.1. Improving the power density

The power density of LIBs is influenced by the potential and amount of charge per unit time as defined in equation 1.7. Hence, improving the power density of LIBs can be categorized as control of the potential and the current, dq/dt , as illustrated in Figure 1.10.

To improve the power density of LIBs by controlling the working potential, V , the combination of a cathode with a higher redox potential and an anode with a lower redox potential is an effective means of increasing the working potential range, as V is calculated according to the potential difference between the two electrodes. Goodenough et al. showed that increasing V in LIBs is associated with formidable challenges in two areas, non-aqueous electrolyte of large V and proper electrode material [12]. There have been various types of organic electrolytes studied for particular LIB applications, involving mainly carbonates containing Li-salt [13-15], ionic liquids [16, 17], polymers [18, 19], solid-state electrolytes [20, 21], and hybrid of electrolytes [22-24]. In particular, ionic liquids have been recently considered as potential alternatives to

carbonate electrolytes (with a reduction potential of 1 V and an oxidation potential of 4.7 V). These are considered as high-V electrolytes due to the high oxidation potential that exceeds 5 V vs. Li/Li⁺ with non-flammability and low toxicity. In spite of the challenges related to high-V electrolytes, unsolved problems, such as a high cost, toxicity, and low viscosity remain to be solved.

Another approach to improve the power density of LIBs is an enhancement of the charge conductivity, i.e., an increase of the electronic and ionic conductivities directly influencing the value of dq/dt in equation 1.7. This can be simply categorized as a type of morphology control, surface modification, and a creation of a composite with conductive materials. There has been much effort to increase the charge transport kinetics via control of the morphology [25-33], which is a general strategy to guarantee the charge pathways, as shown in Figure 1.11. Also, coating [34-38] and doping [39-42] methods for the active materials of LIBs have been widely studied to enhance the electronic conductivity. In general, to prepare a composite to enhance conductivity, carbonaceous materials [43-50] or metals have been introduced to improve poor electron transport kinetics.

Despite the extensive work that has been done thus far, the power density of LIBs has not increased much since their commercialization due to the limitations of the charge transfer reaction kinetics on the surfaces of the active materials, which is an intrinsic property of LIBs using redox reactions for energy storage.

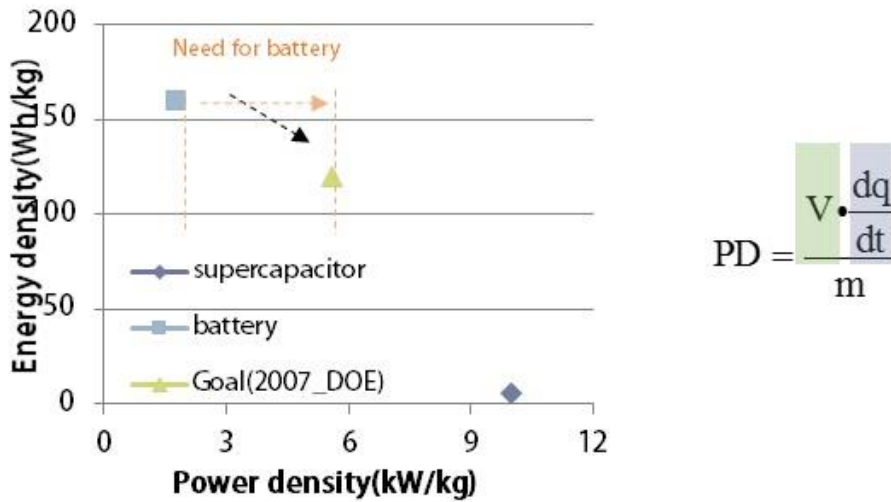


Figure 1.10. Requirement to improve the power density of LIBs with the related equation

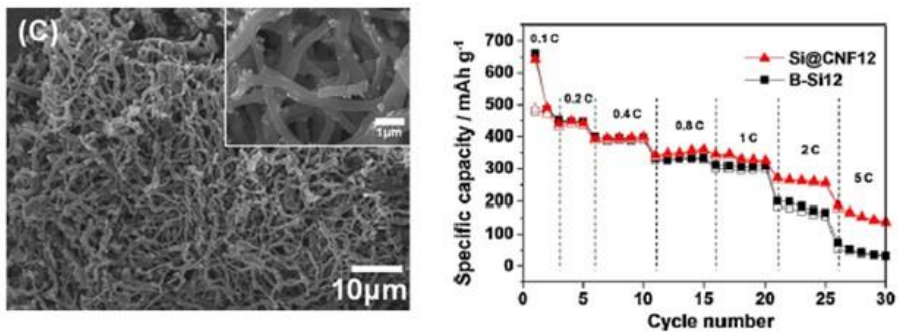


Figure 1.11. Effects of morphological control and the preparation of a composite with a conductive material on Si at a high rate capability [51].

1.4.1.2. Improving the cycle stability

It is apparent that depressing the volume expansion during the charge/discharge process is a key-factor to improve the cycle stability of LIBs. Specifically, because anodic materials can generally store a large amount of Li-ions during operation, there has been much effort to enhance the cycle stability of the anode as compared to the cathode in LIBs.

The introduction of zero- or low-strain active materials has been investigated as an approach to decrease the mechanical load, which cause cycle deterioration via a volume expansion. $\text{Li}_4\text{Ti}_5\text{O}_{12}$ (in Figure 1.12A) and TiO_2 for the anode and LiMn_2O_4 with substitution of Co, Ni, Cr, Fe, and Ti for the cathode are typical active materials which have a stable spinel structure [4, 52]. Also, the introduction of an intermetallic compound for the anode can effectively depress the volume expansion. Candidates for this are SnSb, CuSb, and CuSn [46, 49]. The confinement of active materials is another means of improving the cycle stability of LIBs. Confinement using various materials, such as polymers, carbonaceous materials, carbon nitride, and metal oxides, is advantageous for enhancing the cycle stability due to the depressing effect of a volume expansion, microstructure changes, and dissolution of the active material. Recently, Li-sulfur batteries using sulfur as a cathode have been widely studied to overcome the active material dissolution problem, known as the ‘shuttle reaction’, using mesoporous carbon or conducting polymers as the confinement materials [53-56].

On the other hand, control of the storable charge of the active material may decrease the mechanical load caused by a volume expansion and thus improve the cycle stability of LIBs, especially regarding the anode materials. However, this strategy is affected by the limited amount of storable charge, leading to a decrease of the energy density of the device.

The long-term research and development activities as part of the effort to improve the cycle stability have achieved great progress to realize better performance of LIBs. However, current results do not guarantee the full utilization of LIBs in high-performance electronic device, such as full EVs.

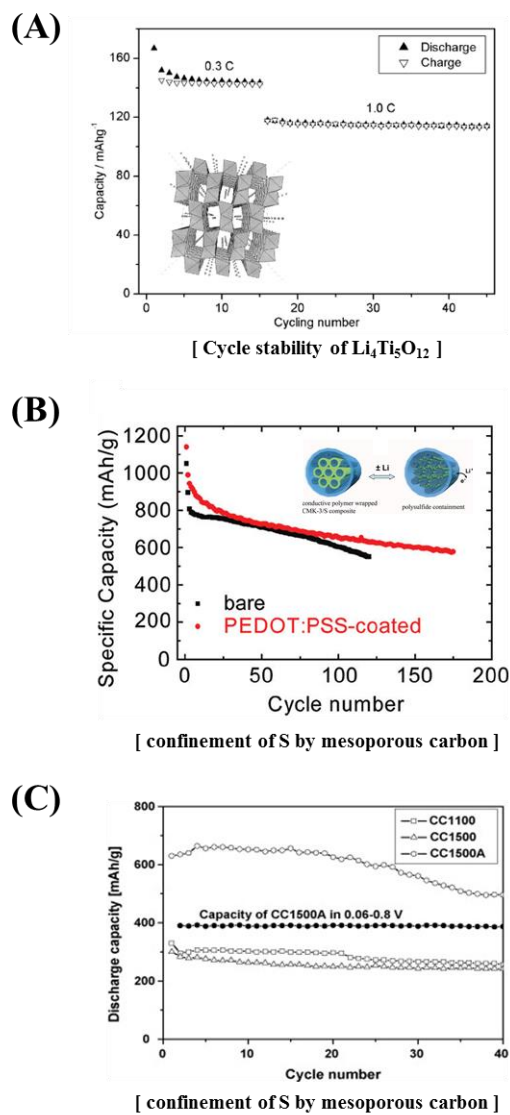


Figure 1.12. Improving the cycle stability via (A) use of a zero-strain material [57], (B) confinement of the active material [55], and (C) control of the storable charges [58].

1.4.2. Approach to enhance supercapacitors

In contrast with LIBs, most approaches to enhance supercapacitors have mainly focused on increasing the storable electrochemical energy due to the overly low energy density for installation into devices which require high levels of energy.

1.4.2.1. Improving the energy density

In the case of supercapacitors, q and ΔV , representing the amount of the storable charge and the working potential window, respectively, are proportional to the energy density due to energy storage mechanism. Thus, most studies have concentrated on increases of q and ΔV to improve the energy density of supercapacitors, as shown in Figure 1.13 in the green and purple squares, respectively. Relevant strategies include an increase of the surface area of the active material, the introduction of pseudocapacitance, and control of the working potential window via an electrolyte.

One of the typical methods to enhance the energy density of supercapacitors is to increase the surface area of active material. This approach is effective for an increase of the storable charge, q , due to an increase in the charge storage space in the active material. There have been various suggestions of materials with a high surface area and a porous structure for supercapacitors, especially carbonaceous materials for the EDLC, such as activated carbon, and nanostructured carbonaceous materials with various morphologies (carbon nanoparticles, carbon nanotubes or graphene), as listed in Table 1.2. In spite of the increase of the surface area, because a proper pore structure (e.g., pore size,

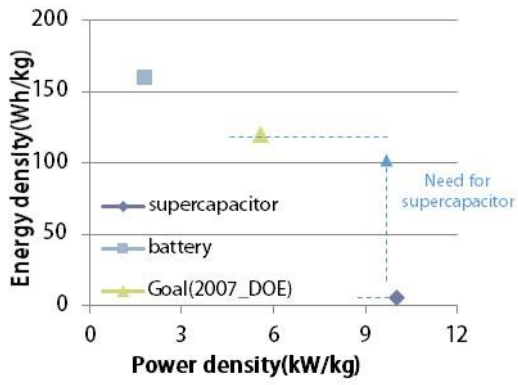
volume, and opened status) related to the electrolyte accessibility is also important, this approach is limited when used to increase the energy density.

Table 1.2. Selected properties of some of the nanostructured carbon materials used in EDLCs [4]

carbon electrode material	BET surface area (m² g⁻¹)	Capacitance in organic and ionic liquid electrolytes (F g⁻¹)	Capacitance in aqueous electrolytes (F g⁻¹)
activated carbon (ac)	800–3500	50–300	50–300
carbide-derived carbon (cdc)	600-2800	70-180	60-220
zeolite-templated carbon (ztc)	1000-3600	80-190	150-340
carbon nanotube (cnt)	400-1200	15-100	15-210
graphene	300-3100	100-240	40-220
onion-like carbon (olc)	400-650	20-60	15-504
carbon aerogel	100-1000	7-80	20-190

Pseudocapacitance originates from a quick faradaic charge transfer reaction on the surface of the active material for a supercapacitor: therefore, the storable charge can be very large [8]. Metal oxides (RuO₂, MnO₂) [59, 60] or conducting polymers (polythiophene, polyaniline) [61, 62] allow pseudocapacitance of a supercapacitor via the faradaic process. In spite of the high energy density from a high q, most pseudocapacitor materials are very expensive and indicate poor cycle stability.

To increase the energy density of supercapacitors via an increase of the working potential window, ΔV , control of the reduction and oxidation potential for the electrolyte is a key-factor, because square proportion of ΔV to the energy density as shown in the equation in Figure 1.13. In an aqueous electrolyte, various water-soluble salts have been used to depress H^+ reduction, OH^- oxidation and water decomposition with a working potential window of 1.2 V, for example KCl, KOH, and HCl [63, 64]. Compared to an aqueous electrolyte, an organic electrolyte is more functional for an increase in ΔV and is more sustainable at a higher operation voltage up to 2.7 V in a symmetric system, such as various systems that use salt-containing acetonitrile [65]. However, a range of problems related to an organic electrolyte should be solved to alternate an aqueous electrolyte, for example flammable property or performance deterioration upon exposure to air or water.



$$ED = \frac{1/2 \cdot q \Delta V}{m} \cdot \frac{1}{3600}$$

$$= \frac{1/2 \cdot C \Delta V^2}{m} \cdot \frac{1}{3600}$$

Figure 1.13. Requirement to improve the energy density of supercapacitors with the related equation

1.4.3. Battery-supercapacitor hybridization

In recent years, intensive efforts have been devoted to develop an advanced electrochemical energy storage device with hybridization of the battery and supercapacitor electrode. These devices are generally called “hybrid capacitors” or “asymmetric capacitors” [66-69]. They are particularly beneficial for an increase in the energy density of supercapacitors. Amatucci et al. and Beguin et al. are pioneers in this research area [70-72]. Battery-supercapacitor hybridization is mainly composed of an asymmetric electrode system and et al. introduction of a Li-ion salt-containing electrolyte.

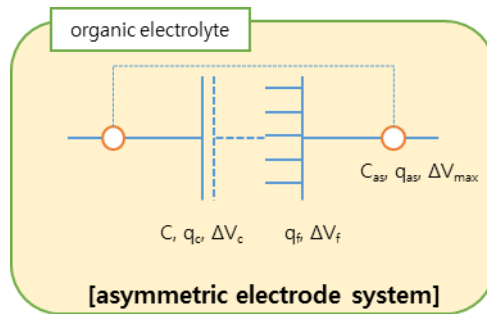


Figure 1.14. Scheme of a hybrid capacitor with an asymmetric electrode system and an organic electrolyte.

1.4.3.1. Asymmetric electrode system

A hybrid capacitor consists of two different types of electrodes, a battery and a supercapacitor electrode, which can be defined as an asymmetric electrode system, as shown in Figure 1.13. In comparison with the symmetric electrode system of a typical supercapacitor, one of electrodes is a LIB-type electrode which can store energy with the typical redox reaction of LIBs. Hence, it can store more electrochemical energy compared to a typical symmetric capacitor. Generally, a carbonaceous material, such as graphite or $\text{Li}_4\text{Ti}_5\text{O}_{12}$ [70, 72], as well as a metal oxide, such as MnO_2 [73, 74] are introduced as a counter electrode for typical activated carbon electrodes in a hybrid capacitor, as illustrated in Figure 1.15. However, despite the better energy density, hybrid capacitors have not been able to overcome completely the low energy density at a high power density due to the poor charge transfer kinetics of the battery-type electrode.

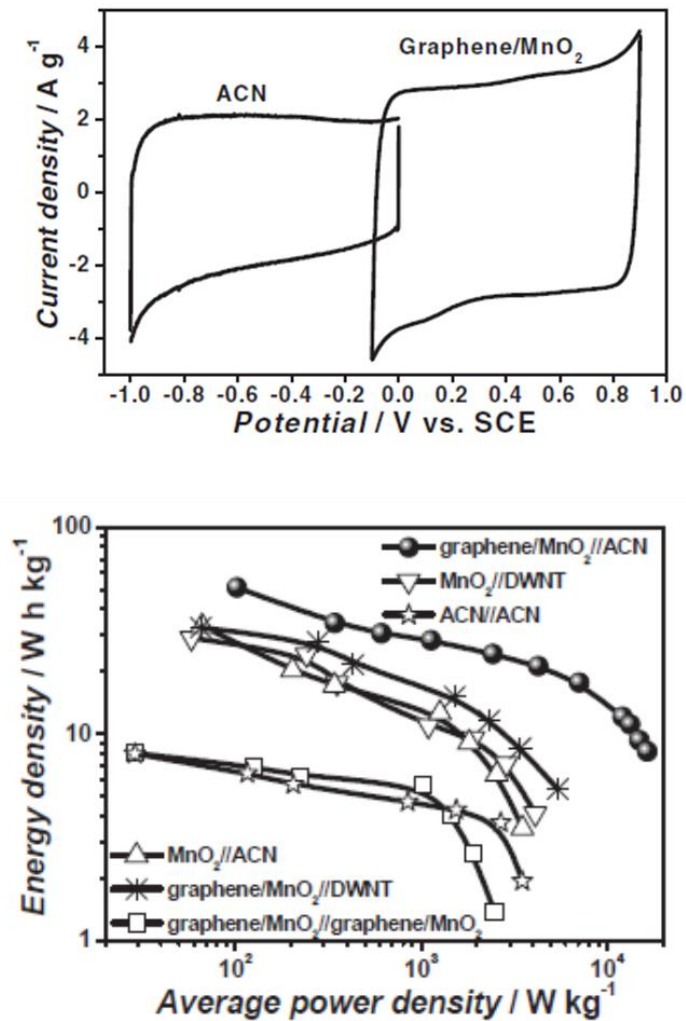


Figure 1.15. CV profile and Ragone plot of activated carbon nanofiber//graphene-MnO₂ [75]

1.4.3.2. Introduction of a Li-ion organic electrolyte

Another important requisite for battery-supercapacitor hybridization is the use of a Li-ion containing organic electrolyte which can be used in LIBs. Owing to the best performance of the LIB-type electrode and the larger working potential window, an organic electrolyte for LIBs is required to realize better electrochemical performance in battery-supercapacitor hybridization schemes.

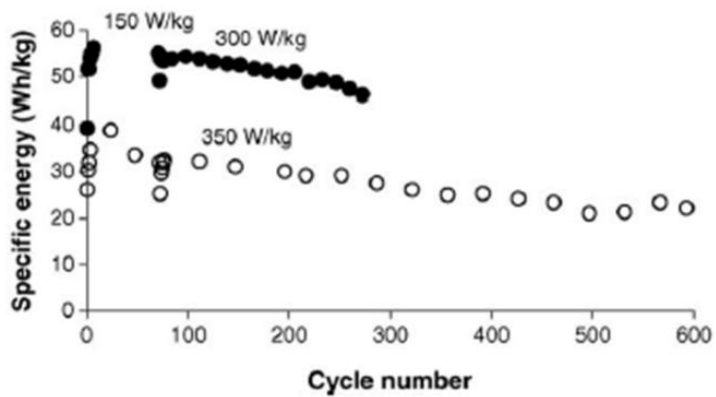
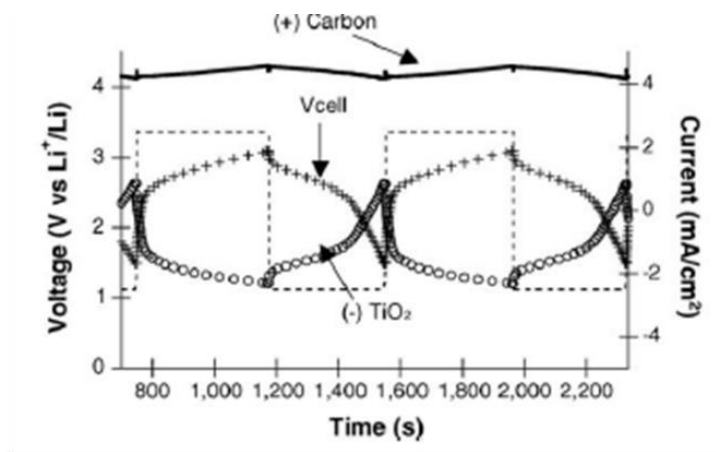


Figure 1.16. Charge/discharge potential profile and cycle stability test results for a $\text{TiO}_2(\text{B})//\text{AC}$ hybrid capacitor with a Li-ion containing organic electrolyte [72]

1.5. Aim and scope of this research

This study aims to develop a new concept-energy device, termed a “BatCap”, by the hybridization of a battery and a supercapacitor in a single electrode to overcome the trade-off performance issues of electrochemical energy devices. Figure 1.17 shows the scheme of the BatCap system.

1.5.1. Theoretical study of the BatCap system as an advanced energy storage device

The theoretical approach for the BatCap system will be discussed in chapter 2. First, the introduction of the new concept of an energy storage system is considered with the theoretical modeling of the BatCap system. Also theoretical calculations for typical capacitor systems will be carried out for comparisons with that of the BatCap system. Through this theoretical study, an ideal structure and ideal conditions for the BatCap system will be proposed.

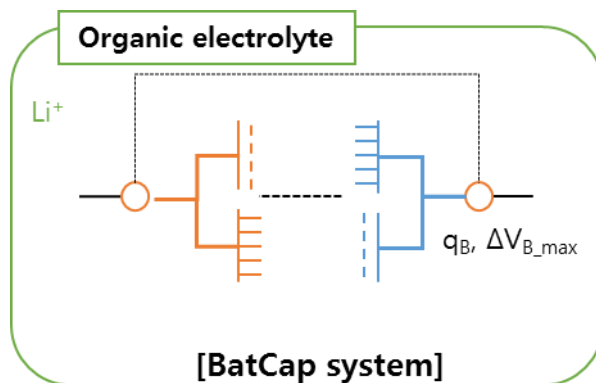


Figure 1.17. Scheme of the BatCap system consisting of the BatCap electrode for each electrode with a Li-ion containing organic electrolyte.

1.5.2. Synthesis and characterization of the BatCap electrode materials

As discussed in chapter 2, battery-supercapacitor hybrid materials will be considered with various preparation methods for the BatCap electrode material. Chapters 3 and 4 describe the synthesis of the negative electrode materials including $\text{Li}_4\text{Ti}_5\text{O}_{12}$ as the battery component and carbonaceous material as the capacitor component with morphology control for the BatCap system. Then, chapters 5 and 6 detail the synthesis of the positive electrode material containing sulfur as the battery component and a carbonaceous material as capacitor component with control of the chemical state and morphology of the BatCap system. Also, material characterization and an electrochemical performance test are conducted using various analytic methods and electrochemical test, respectively, in each chapter to discern the properties and electrochemical performances of the BatCap-tailing materials. Finally, the discussion will be extended to a performance comparison of each device and the requirements to improve the BatCap system in future applications in chapter 7.

1.6. References

- [1] R.A. Huggins, *Advanced Batteries: Materials Science Aspects*, 1 ed., Springer Science, New York, 2008.
- [2] D. Reicher, *Clean energy 2030*, Google Energy Team, 2008, <http://googleblog.blogspot.kr/2008/10/clean-energy-2030.html>.
- [3] M. Armand, J.M. Tarascon, *Nature*, 451 (2008) 652-657.
- [4] N.-S. Choi, Z. Chen, S.A. Freunberger, X. Ji, Y.-K. Sun, K. Amine, G. Yushin, L.F. Nazar, J. Cho, P.G. Bruce, *Angewandte Chemie International Edition*, 51 (2012) 9994-10024.
- [5] P. Simon, Y. Gogotsi, *Nature Materials*, 7 (2008) 845-854.
- [6] M.S. WHITTINGHAM, *Science*, 192 (1976) 1126-1127.
- [7] W.G. Pell, B.E. Conway, *Journal of Power Sources*, 136 (2004) 334-345.
- [8] B.E. Conway, *Electrochemical Supercapacitors—Scientific Fundamentals and Technological Applications*, Kluwer, New York, 1999.
- [9] A.J. Bard, L.R. Faulkner, *Electrochemical Methods : Fundamentals and Applications*, second ed., John Wiley & Sons, Inc., Austin, 2001.
- [10] D. Howell, *Progress Report for Energy Storage Research and Development*, U.S. Department of Energy, 2008, http://www1.eere.energy.gov/vehiclesandfuels/pdfs/program/2008_energy_storage.pdf.
- [11] H.S. Choi, J.H. Im, T. Kim, J.H. Park, C.R. Park, *Journal of Materials Chemistry*, 22 (2012) 16986-16993.
- [12] J.B. Goodenough, Y. Kim, *Chemistry of Materials*, 22 (2009) 587-603.

- [13] K. Hayashi, Y. Nemoto, S.-i. Tobishima, J.-i. Yamaki, *Electrochimica Acta*, 44 (1999) 2337-2344.
- [14] R. Imhof, P. Novák, *Journal of The Electrochemical Society*, 146 (1999) 1702-1706.
- [15] M. Egashira, H. Takahashi, S. Okada, J.-i. Yamaki, *Journal of Power Sources*, 92 (2001) 267-271.
- [16] B. Garcia, S. Lavallée, G. Perron, C. Michot, M. Armand, *Electrochimica Acta*, 49 (2004) 4583-4588.
- [17] E. Markevich, V. Baranchugov, D. Aurbach, *Electrochemistry Communications*, 8 (2006) 1331-1334.
- [18] A. Nishimoto, M. Watanabe, Y. Ikeda, S. Kohjiya, *Electrochimica Acta*, 43 (1998) 1177-1184.
- [19] F. Croce, R. Curini, A. Martinelli, L. Persi, F. Ronci, B. Scrosati, R. Caminiti, *The Journal of Physical Chemistry B*, 103 (1999) 10632-10638.
- [20] A. Pradel, M. Ribes, *Materials Chemistry and Physics*, 23 (1989) 121-142.
- [21] T. Minami, A. Hayashi, M. Tatsumisago, *Solid State Ionics*, 177 (2006) 2715-2720.
- [22] J. Cho, M. Liu, *Electrochimica Acta*, 42 (1997) 1481-1488.
- [23] H. Ye, J. Huang, J.J. Xu, A. Khalfan, S.G. Greenbaum, *Journal of The Electrochemical Society*, 154 (2007) A1048-A1057.
- [24] C. Sirisopanaporn, A. Farnicola, B. Scrosati, *Journal of Power Sources*, 186 (2009) 490-495.

- [25] Y.N. Xia, P.D. Yang, Y.G. Sun, Y.Y. Wu, B. Mayers, B. Gates, Y.D. Yin, F. Kim, Y.Q. Yan, *Advanced Materials*, 15 (2003) 353-389.
- [26] J.W. Long, B. Dunn, D.R. Rolison, H.S. White, *Chemical Reviews*, 104 (2004) 4463-4492.
- [27] C. Kim, K.S. Yang, M. Kojima, K. Yoshida, Y.J. Kim, Y.A. Kim, M. Endo, *Advanced Functional Materials*, 16 (2006) 2393-2397.
- [28] J. Xiang, W. Lu, Y.J. Hu, Y. Wu, H. Yan, C.M. Lieber, *Nature*, 441 (2006) 489-493.
- [29] H.G. Cho, Y.J. Kim, Y.E. Sung, C.R. Park, *Electrochimica Acta*, 53 (2007) 944-950.
- [30] Y.-S. Hu, P. Adelhelm, B.M. Smarsly, S. Hore, M. Antonietti, J. Maier, *Advanced Functional Materials*, 17 (2007) 1873-1878.
- [31] M.-S. Park, G.-X. Wang, Y.-M. Kang, D. Wexler, S.-X. Dou, H.-K. Liu, *Angewandte Chemie International Edition*, 46 (2007) 750-753.
- [32] C.K. Chan, H.L. Peng, G. Liu, K. McIlwrath, X.F. Zhang, R.A. Huggins, Y. Cui, *Nature Nanotechnology*, 3 (2008) 31-35.
- [33] H.T. Fang, M. Liu, D.W. Wang, T. Sun, D.S. Guan, F. Li, J.G. Zhou, T.K. Sham, H.M. Cheng, *Nanotechnology*, 20 (2009) -.
- [34] K. Guo, Q. Pan, L. Wang, S. Fang, *Journal of Applied Electrochemistry*, 32 (2002) 679-685.
- [35] N. Sharma, K.M. Shaju, G.V. Subba Rao, B.V.R. Chowdari, Z.L. Dong, T.J. White, *Chemistry of Materials*, 16 (2003) 504-512.

- [36] Y.-G. Guo, Y.-S. Hu, W. Sigle, J. Maier, *Advanced Materials*, 19 (2007) 2087-2091.
- [37] W.-M. Zhang, X.-L. Wu, J.-S. Hu, Y.-G. Guo, L.-J. Wan, *Advanced Functional Materials*, 18 (2008) 3941-3946.
- [38] X.W. Lou, C.M. Li, L.A. Archer, *Advanced Materials*, 21 (2009) 2536-2539.
- [39] S. Huang, Z. Wen, Z. Gu, X. Zhu, *Electrochimica Acta*, 50 (2005) 4057-4062.
- [40] M. Miyachi, H. Yamamoto, H. Kawai, *Journal of The Electrochemical Society*, 154 (2007) A376-A380.
- [41] K.S. Park, A. Benayad, D.J. Kang, S.G. Doo, *Journal of the American Chemical Society*, 130 (2008) 14930-+.
- [42] X. Li, M. Qu, Z. Yu, *Journal of Alloys and Compounds*, In Press, Corrected Proof (2009).
- [43] C.-M. Park, S. Yoon, S.-I. Lee, J.-H. Kim, J.-H. Jung, H.-J. Sohn, *Journal of The Electrochemical Society*, 154 (2007) A917-A920.
- [44] L. Wang, Y. Yu, P.C. Chen, D.W. Zhang, C.H. Chen, *Journal of Power Sources*, 183 (2008) 717-723.
- [45] Z.-M. Cui, L.-Y. Jiang, W.-G. Song, Y.-G. Guo, *Chemistry of Materials*, 21 (2009) 1162-1166.
- [46] C.-M. Park, H.-J. Sohn, *Electrochimica Acta*, 54 (2009) 6367-6373.
- [47] S. Yoon, B.H. Ka, C. Lee, M. Park, S.M. Oh, *Electrochemical and Solid-State Letters*, 12 (2009) A28-A32.

- [48] J.T. Yin, M. Wada, S. Tanase, T. Sakai, *Journal of The Electrochemical Society*, 151 (2004) A583-A589.
- [49] H. Guo, H. Zhao, X. Jia, X. Li, W. Qiu, *Electrochimica Acta*, 52 (2007) 4853-4857.
- [50] S. Huang, Z. Wen, B. Lin, J. Han, X. Xu, *Journal of Alloys and Compounds*, 457 (2008) 400-403.
- [51] H.S. Choi, J.G. Lee, H.Y. Lee, S.W. Kim, C.R. Park, *Electrochimica Acta*, 56 (2010) 790-796.
- [52] B.L. Ellis, K.T. Lee, L.F. Nazar, *Chemistry of Materials*, 22 (2010) 691-714.
- [53] N. Jayaprakash, J. Shen, S.S. Moganty, A. Corona, L.A. Archer, *Angewandte Chemie International Edition*, 50 (2011) 5904-5908.
- [54] L. Xiao, Y. Cao, J. Xiao, B. Schwenzer, M.H. Engelhard, L.V. Saraf, Z. Nie, G.J. Exarhos, J. Liu, *Advanced Materials*, 24 (2012) 1176-1181.
- [55] Y. Yang, G. Yu, J.J. Cha, H. Wu, M. Vosgueritchian, Y. Yao, Z. Bao, Y. Cui, *ACS Nano*, 5 (2011) 9187-9193.
- [56] G. Zheng, Y. Yang, J.J. Cha, S.S. Hong, Y. Cui, *Nano Letters*, 11 (2011) 4462-4467.
- [57] R.K.B. Gover, J.R. Tolchard, H. Tukamoto, T. Murai, J.T.S. Irvine, *Journal of The Electrochemical Society*, 146 (1999) 4348-4353.
- [58] H.G. Cho, S.W. Kim, H.J. Lim, C.H. Yun, H.S. Lee, C.R. Park, *Carbon*, 47 (2009) 3544-3549.

- [59] T. Brousse, M. Toupin, R. Dugas, L. Athouël, O. Crosnier, D. Bélanger, *Journal of The Electrochemical Society*, 153 (2006) A2171-A2180.
- [60] N.-L. Wu, *Materials Chemistry and Physics*, 75 (2002) 6-11.
- [61] A. Rudge, J. Davey, I. Raistrick, S. Gottesfeld, J.P. Ferraris, *Journal of Power Sources*, 47 (1994) 89-107.
- [62] A. Laforgue, P. Simon, J.-F. Fauvarque, *Synthetic Metals*, 123 (2001) 311-319.
- [63] H.Y. Lee, J.B. Goodenough, *Journal of Solid State Chemistry*, 144 (1999) 220-223.
- [64] A.G. Pandolfo, A.F. Hollenkamp, *Journal of Power Sources*, 157 (2006) 11-27.
- [65] P. Azaïs, L. Duclaux, P. Florian, D. Massiot, M.-A. Lillo-Rodenas, A. Linares-Solano, J.-P. Peres, C. Jehoulet, F. Béguin, *Journal of Power Sources*, 171 (2007) 1046-1053.
- [66] G.G. Amatucci, F. Badway, A.D. Pasquier, T. Zheng, *Journal of The Electrochemical Society*, 148 (2001) A930-A939.
- [67] A.D. Pasquier, I. Plitz, S. Menocal, G. Amatucci, *Journal of Power Sources*, 115 (2003) 171-178.
- [68] S. Nohara, A.A. Toshihide, H. Wada, N. Furukawa, H. Inoue, N. Sugoh, H. Iwasaki, C. Iwakura, *Journal of Power Sources*, 157 (2006) 605-609.
- [69] M. Mastragostino, F. Soavi, *Journal of Power Sources*, 174 (2007) 89-93.
- [70] A. Du Pasquier, A. Laforgue, P. Simon, G.G. Amatucci, J.-F. Fauvarque, *Journal of The Electrochemical Society*, 149 (2002) A302-A306.

- [71] A. Du Pasquier, I. Plitz, S. Menocal, G. Amatucci, *Journal of Power Sources*, 115 (2003) 171-178.
- [72] V. Khomenko, E. Raymundo-Piñero, F. Béguin, *Journal of Power Sources*, 177 (2008) 643-651.
- [73] Z.-S. Wu, W. Ren, D.-W. Wang, F. Li, B. Liu, H.-M. Cheng, *ACS Nano*, 4 (2010) 5835-5842.
- [74] G. Yu, L. Hu, M. Vosgueritchian, H. Wang, X. Xie, J.R. McDonough, X. Cui, Y. Cui, Z. Bao, *Nano Letters*, 11 (2011) 2905-2911.
- [75] Z. Fan, J. Yan, T. Wei, L. Zhi, G. Ning, T. Li, F. Wei, *Advanced Functional Materials*, 21 (2011) 2366-2375.

Part II

Fundamental study for the “BatCap” system

Chapter 2. Theoretical Approach and Prediction of the BatCap System

2.0. Major symbols

2.0.1. Electrical charge

q_1 : storable electrical charge for a single capacitor electrode with an aqueous electrolyte

q_s : storable electrical charge for the symmetric capacitor with an aqueous electrolyte

q_{as} : storable electrical charge for the asymmetric capacitor with an aqueous electrolyte

q_{o_1} : storable electrical charge for a single electrode with an organic electrolyte

$q_{o_{as}}$: storable electrical charge for the asymmetric capacitor with an organic electrolyte

q_B : storable electrical charge for the BatCap system

q_{B_c} : storable electrical charge for the capacitor-type electrode in the BatCap system

q_{B_B} : storable electrical charge for the BatCap electrode in the BatCap system

$q_{B_{Bb}}$: storable electrical charge for the battery component in the BatCap electrode in the BatCap system

q_{B_Bc} : storable electrical charge for capacitor component in the BatCap electrode in the BatCap system

2.0.2. Capacitance

C_1 : capacitance of a single capacitor electrode with an aqueous electrolyte

C_s : capacitance of a symmetric capacitor with an aqueous electrolyte

C_c : capacitance of the capacitor-type electrode of an asymmetric capacitor with an aqueous electrolyte

C_{o_1} : capacitance of a single capacitor electrode with an organic electrolyte

C_{o_c} : capacitance of the capacitor-type electrode of an asymmetric capacitor with an organic electrolyte

C_{B_c} : capacitance of the capacitor-type electrode of the BatCap system

C_{B_Bc} : capacitance of the battery-type component of the BatCap electrode of the BatCap system

2.0.3. Working potential range

ΔV_{max} : maximum working potential range (= maximum potential difference between two electrodes) with an aqueous electrolyte

ΔV_s : working potential range for each electrode of a symmetric capacitor with an aqueous electrolyte

ΔV_b : working potential range for the battery-type electrode of an asymmetric capacitor with an aqueous electrolyte

ΔV_c : working potential range for the capacitor-type electrode of an asymmetric capacitor with an aqueous electrolyte

ΔV_{o_max} : maximum working potential range (= maximum potential difference between two electrodes) with an organic electrolyte

ΔV_{o_b} : working potential range for the battery-type electrode of an asymmetric capacitor with an organic electrolyte

ΔV_{o_c} : working potential range for the capacitor-type electrode of an asymmetric capacitor with an organic electrolyte

ΔV_{B_max} : maximum working potential range (= maximum potential difference between two electrodes) of the BatCap system

ΔV_{B_B} : working potential range for the BatCap electrode of the BatCap system

$$(\Delta V_{B_B} = \Delta V_{B_Bc} + V_{B_Bb})$$

ΔV_{B_Bc} : working potential range for the capacitor-type component in the BatCap electrode

ΔV_{B_Bb} : working potential range for the battery-type component in the BatCap electrode

ΔV_{B_c} : working potential range for the capacitor-type electrode of the BatCap system

2.0.4. Mass

m_1 : mass of a single capacitor electrode

m_s : mass of a single electrode for a symmetric capacitor

m_{as} : mass of both electrodes for an asymmetric capacitor ($m_{as} = m_b + m_c$)

m_b : mass of the battery-type electrode

m_c : mass of the capacitor-type electrode

m_B : mass of both electrodes for an asymmetric capacitor ($m_B = m_{B_B} + m_{B_c}$)

m_{B_B} : mass of the BatCap electrode ($m_{B_B} = m_{B_Bb} + m_{B_Bc}$)

m_{B_Bb} : mass of the battery-type component in the BatCap electrode

m_{B_Bc} : mass of the battery-type component in the BatCap electrode

m_{B_c} : mass of a capacitor-type electrode (= non-faradaic electrode)

2.0.5. Storable energy

E_1 : amount of energy stored in a single capacitor electrode with an aqueous electrolyte

E_s : amount of energy stored in a symmetric capacitor with an aqueous electrolyte

E_{as} : amount of energy stored in an asymmetric capacitor with an aqueous electrolyte

E_b : amount of energy stored in the battery-type electrode of an asymmetric capacitor with an aqueous electrolyte

E_c : amount of energy stored in the capacitor-type electrode of an asymmetric capacitor with an aqueous electrolyte

E_{o_1} : amount of energy stored in a single capacitor electrode with an organic electrolyte

$E_{o_{as}}$: amount of energy stored in an asymmetric capacitor with an organic electrolyte

E_{o_b} : amount of energy stored in the battery-type electrode of an asymmetric capacitor with organic electrolyte

E_{o_c} : amount of energy stored in the capacitor-type electrode of an asymmetric capacitor with organic electrolyte

E_B : amount of energy stored in the BatCap system

E_{B_B} : amount of energy stored in the BatCap electrode of the BatCap system

$E_{B_{Bb}}$: amount of energy stored in the battery-type component of the BatCap electrode

$E_{B_{Bc}}$: amount of energy stored in the capacitor-type component of the BatCap electrode

E_{B_c} : amount of energy stored in the capacitor-type electrode of the BatCap system

2.0.6. Energy density

ED_1 : specific energy density for a single capacitor electrode in an aqueous electrolyte

ED_s : specific energy density for a symmetric capacitor in an aqueous electrolyte

ED_{as}: specific energy density for an asymmetric capacitor in an aqueous electrolyte

ED_{o_1}: specific energy density for a single capacitor electrode in an organic electrolyte

ED_B: specific energy density for the BatCap system

2.0.7. Power density

PD₁: specific power density for a single capacitor electrode in an aqueous electrolyte

PD_s: specific power density for a symmetric capacitor in an aqueous electrolyte

PD_{as}: specific power density for an asymmetric capacitor in the an aqueous electrolyte

PD_{o_1}: specific energy density for a single capacitor electrode in the an organic electrolyte

PD_B: specific energy density for the BatCap system

2.0.8. Ratio factor

k₁: mass ratio factor of a battery-type electrode ($k_1 = m_b/m_{as}$, $0 < k_1 < 1$)

k₂: potential range ratio factor of a battery-type electrode and the BatCap electrode

($k_2 = \Delta V_b / \Delta V_{max}$, in an aqueous electrolyte or $k_2 = \Delta V_{o_b} / \Delta V_{o_{max}}$ in an organic electrolyte, and $k_2 = \Delta V_{B_b} / \Delta V_{B_{max}}$ in the BatCap system $0 < k_2 < 1$)

k₂' : potential range ratio factor of battery component in the BatCap electrode

($k_2' = \Delta V_{B_Bb}/\Delta V_{B_B}$, in an organic electrolyte, $0 < k_2' < 1$)

k_3 : maximum working potential range ratio between an aqueous and an organic electrolytes

($k_3 = \Delta V_{\max}/\Delta V_{o_{\max}}$, $0 < k_3 < 1$)

k_4 : specific capacitance ratio between capacitor-type electrodes with aqueous and organic electrolyte ($q_{o_1}/m_{o_1}\Delta V_{o_{\max}} = k_4 \cdot q_1/m_1\Delta V_{\max}$, $0 < k_4 < 1$)

k_5 : storable electrical charge ratio of a capacitor-type component in the BatCap electrode

($k_5 = q_{B_Bc}/q_{B_B}$, $0 < k_5 \ll 1$)

2.0.9. Storable energy-influencing factor

K_{BM} : Battery-type material-related coefficient ($K_M = (1+k_1)(1-k_2^2)$)

K_E : Electrolyte-related coefficient ($K_E = k_4/k_3^2$)

K_{BC} : BatCap-related coefficient ($K_{BC} = (1-k_2k_5+2k_2k_2'k_5)/(1+k_2)$)

2.1. Introduction

Enhancing renewable and sustainable energy has been one of the most important issues not only for governments but also for science and engineering societies around the world due to the rapidly fading fossil energy resources and acute environmental pollution with sudden climate change. Combined with studies seeking to generate energy from clean sources such as solar or wind power, efficient energy storage systems have been studied to solve the energy

crisis. Batteries and electrochemical capacitors are typical energy storage devices with electrochemistry capable of storing the electrical energy which is the most useful environmentally friendly energy. In spite of the tremendous effort, we are facing a challenge to enhance the electrochemical performance of both batteries and electrochemical capacitors, due to the increasing requirements for better electrical devices, such as electrical vehicles, high-performance portable devices, and smartphones. Therefore, the most significant key advance of the future is to develop an advanced energy storage system [1-3].

There are two general approaches to this challenge: performance-enhancing strategies for batteries with high energy density with low charge/discharge rates and a strategy to create an electrochemical capacitor which shows great cycle stability and a high power density with a low energy density. In the effort to enhance the high rate capability of batteries, various approaches have been adapted to increase the amount of storable energy for electrochemical capacitors by controlling the electrolyte and working potential range [4].

The introduction of an organic electrolyte into an electrochemical capacitor is one suitable strategy to improve the low energy density by increasing the working potential range of the system [5]. This approach is effective, because the energy density of an electrochemical capacitor electrode is proportional to the squared value of the working potential range. Another approach is to apply asymmetric electrodes in electrochemical capacitor with battery- and supercapacitor-type electrodes in a single system. Battery-type electrode in the

system is available to increase the open-circuit voltage and maintain the reactive potential, thus increasing the energy density.

Recently, a new approach to develop an advanced energy storage device, called the BatCap system, was introduced [6, 7]. This system showed improved electrochemical performance compared to typical electrochemical capacitors via the hybridization of battery-capacitor materials in a single electrode. In this chapter, the theoretical aspects of the BatCap system are discussed in a comparison between this new system and typical electrochemical capacitors, followed by an electrochemical performance plot of various results from previous studies with calculated and reported values. For comparison, it is assumed that the same materials are applied in the theoretical calculation.

2.2. Theoretical comparison of typical capacitor systems

2.2.1. A symmetric capacitor system and an asymmetric capacitor system with aqueous electrolyte

Electrochemical capacitor systems, also called supercapacitors, a typical energy storage device, can be classified according to the symmetry of the electrodes and the solvent of the electrolyte. There are traditionally two types of electrodes: the electric double-layer capacitor (EDLC) type electrode and the pseudocapacitor-type electrode: these have activated porous carbonaceous materials (AC) and various metal oxides [8]. The EDLC-type electrode and the pseudocapacitor-type electrode, which store electrochemical energy using electrostatic force (non-faradaic reaction) and a redox reaction (faradaic reaction), respectively, can be fabricated and operated as an electrochemical capacitor in the symmetric mode or the asymmetric mode. For the electrolyte, there are mainly two types applied in electrochemical capacitors: an aqueous electrolyte and a non-aqueous (organic) electrolyte. As mentioned above, because the electrode material and electrolyte directly influence the performance of the energy storage device, i.e., the power density and the energy density, classification of the electrochemical capacitor system can be appropriately determined by symmetry of the electrode with the material type and the applied electrolyte.

A symmetric capacitor system using an aqueous solution as the electrolyte is the traditional and widely used electrochemical system. Both the negative and

positive electrodes are made of the same electrode material, hence the classification as the symmetric mode. Also, various aqueous solutions containing highly ionic-conductive ions can be used as the electrolyte, such as HCl, KOH, and H₂SO₄ solutions [9]. A symmetric capacitor system using an aqueous electrolyte is schematically illustrated as the potential profile for the charging state with a single electrode system in Figure 2.1, which is useful to compare and discuss the amount of energy stored in each capacitor system. Both capacitor-type electrodes have a proportional relationship between the amount of charge and potential difference of counter electrodes, as shown in Figure 2.1. The capacitance of the electrode is an intrinsic property of the electrode material related to the applied electrolyte. This parameter, denoted here as capacitance C, is defined as the amount of charge, q, stored in the electrode material per potential difference, ΔV. Therefore, C is the slope of the line in the q-ΔV profile of Figure 2.1, which is calculated using the following equation:

$$C = \frac{q}{\Delta V} \text{ (F g}^{-1}\text{)} \text{ or } q = C\Delta V \quad (2.1)$$

The amount of electrochemical energy, E, is determined by the integration of the stored charge over the electrostatic potential difference, representing the energy of each charge. Hence, E is equal to the value of the q-ΔV plot area in Figure 2.1, calculated with the following equation:

$$E = \frac{1}{2}q\Delta V = \frac{1}{2}C\Delta V^2 \text{ (W)} \quad (2.2)$$

The specific energy density, ED, refers to the storable electrochemical energy per unit mass of the electrode and unit time, as defined by

$$ED = \frac{1}{2} \frac{q\Delta V}{m} \cdot \frac{1}{3600s} = \frac{1}{2} \frac{C\Delta V^2}{m} \cdot \frac{1}{3600s} \text{ (Wh g}^{-1}\text{)} \quad (2.3)$$

where m is the mass of the electrode and 3600 s is 1 hr.

When a single capacitor-type electrode stores electrochemical energy in an aqueous electrolyte with a maximum working potential range of ΔV_{\max} , the capacitance of the single capacitor-type electrode, C_1 , is calculated by the equation, $C_1 = q_1 / \Delta V_{\max}$, with q_1 as the storable charge for a single capacitor electrode with an aqueous electrolyte, as shown in Figure 2.1A. Also, E_1 and ED_1 , which are amount of electrochemical energy and the specific energy density of a single capacitor-type electrode with an aqueous electrolyte, respectively, are determined by the following equation:

$$E_1 = \frac{1}{2}q_1\Delta V_{\max} \quad (2.4)$$

$$ED_1 = \frac{1}{2} \frac{q_1\Delta V_{\max}}{m_1} \cdot \frac{1}{3600s} \quad (2.5)$$

Here, m_1 represents the mass of a single capacitor-type electrode.

The symmetric capacitor system with the aqueous electrolyte shown in Figure 2.1B has both negative and positive electrodes using a single capacitor-type electrode. Assuming that a symmetric capacitor system with an aqueous electrolyte contains same the electrode material and electrolyte as the single capacitor-type electrode in Figure 2.1A, the specific capacitance of both systems will have the same value.

Moreover, the electrochemical energy stored in this symmetric capacitor system, E_s , is determined by

$$E_s = \frac{1}{2} \cdot q_s \Delta V_{\max} = \frac{1}{2} \cdot \frac{1}{2} q_1 \Delta V_{\max} \quad (2.6)$$

when q_s represents the amount of charge stored in both the electrodes and the entire symmetric capacitor system. The same amount of charge is simultaneously stored both inside and outside of each electrode surfaces through an increase of the potential difference to ΔV_{\max} owing to the identical capacitance values with a single capacitor-type electrode. Therefore, the total storable charge for the symmetric capacitor system with an aqueous electrolyte, q_s , will be $1/2 \cdot q_1$. Also, the entire capacitance of this symmetric capacitor system, C_s , is determined as half of C_1 ; that is $C_s = 1/2 \cdot C_1$; in Figure 2.1B.

Consequently, the specific energy density of the symmetric capacitor system can be calculated as using the following equation:

$$ED_s = \frac{1}{2} \cdot \frac{1}{2} \frac{q_1 \Delta V_{\max}}{m_s} \cdot \frac{1}{3600s} = \frac{1}{4} \frac{q_1 \Delta V_{\max}}{m_s} \cdot \frac{1}{3600s} \quad (2.7)$$

where m_s is the total mass of the symmetric capacitor system consisting of the same capacitor-type electrodes. Because each electrode can store an amount of charge equal to only half of q_1 , the mass of each electrode will be $1/2 \cdot m_1$ such that $m_s = 1/2 \cdot m_1 + 1/2 \cdot m_1 = m_1$.

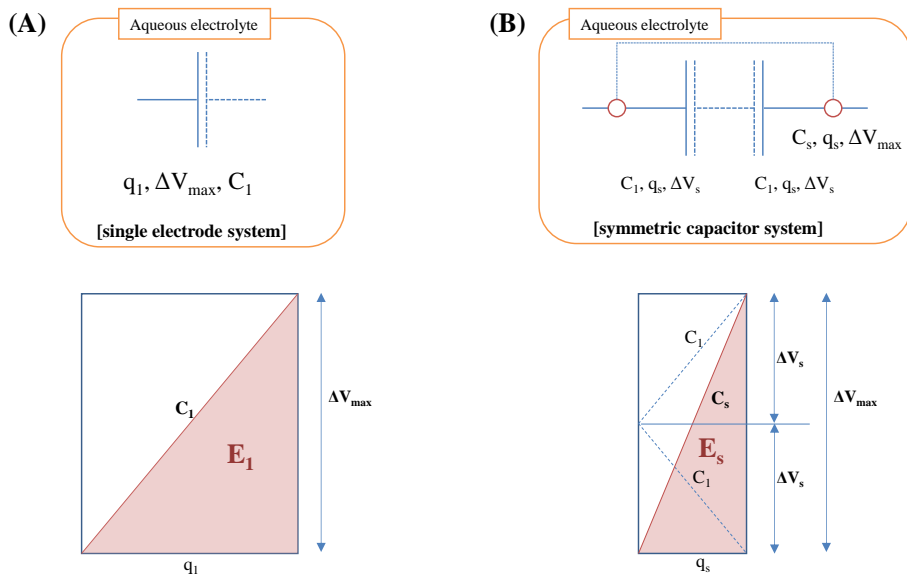


Figure 2.1. Schematic representation of (A) single electrode system and (B) a symmetric capacitor system with an aqueous electrolyte according to the charge-potential profiles.

In contrast to the symmetric electrode system, an asymmetric capacitor system is fabricated using different types of negative and positive capacitor-type electrodes. Such a system is defined as the asymmetric mode. In fact, in spite of the equal electrodes in the system, negative and positive electrodes have different charge storage capabilities due to the stronger adsorption force of the electrolyte-anion than that of the electrolyte-cation during the charge process as the electrostatic potential increases. This phenomenon led to an asymmetric capacitor system using the same capacitor-type electrode but with a different mass in previous research or in commercialized products regarding the charge balance between the negative and positive electrodes [10-12]. However, here we consider an asymmetric capacitor system with an aqueous electrolyte (Figure 2.2) consisting of different types of electrodes, i.e., a capacitor-type electrode and a battery-type electrode, with a wholly different electrochemical reaction mechanism. For the battery-type electrode in this asymmetric capacitor system, the potential remains constant, as shown in the example V_b in Figure 2.2, during the charging of the electrochemical energy due to the redox reaction on the surface of the battery-type electrode following the Nernst equation. Therefore, it is essential to use a higher working potential combined with a capacitor-type electrode at the initial stage of the charging process, as shown in Figure 2.2, resulting in an increase of the storable amount of energy compared to a symmetric capacitor system. Moreover, the total capacitance of the asymmetric capacitor system cannot available to be defined due to the constant electrochemical potential value of the battery-type electrode, in contrast with

the symmetric capacitor system. It is assumed that the redox reaction of the battery-type electrode, which shows lower kinetics than the electrostatic charge storage of a capacitor-type electrode in an actual system, is fast enough to operate as the counter electrode of a capacitor-type electrode. We also assume that this asymmetric capacitor system applies the same aqueous electrolyte and capacitor-type electrode used in the aforementioned symmetric capacitor system with an aqueous electrolyte. Therefore, the electrochemical energy stored in this asymmetric capacitor system, E_{as} , is given as

$$E_{as} = q_{as}\Delta V_b + \frac{1}{2}q_{as}\Delta V_c \quad (2.8)$$

when q_{as} is the amount of charge stored in both the electrodes and the asymmetric capacitor system; and ΔV_b and ΔV_c are the working potential range of the battery- and the capacitor-type electrode, respectively. Because the total mass of the asymmetric capacitor system with an aqueous electrolyte is the sum of m_b , the mass of the battery-type electrode, and the m_c , mass of the capacitor-type electrode, we can derive the specific energy density of the asymmetric capacitor system with an aqueous electrolyte, ED_{as} , as follows:

$$\begin{aligned} ED_{as} &= \frac{E_b + E_c}{m_b + m_c} \cdot \frac{1}{3600s} = \frac{q_{as}\Delta V_b + \frac{1}{2}q_{as}\Delta V_c}{m_b + m_c} \cdot \frac{1}{3600s} \\ &= \frac{q_{as}}{m_{as}} \cdot \left(\Delta V_b + \frac{1}{2}\Delta V_c \right) \cdot \frac{1}{3600s} \end{aligned} \quad (2.9)$$

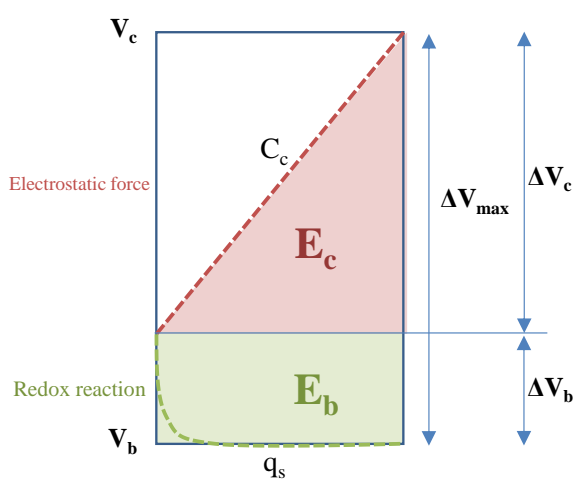
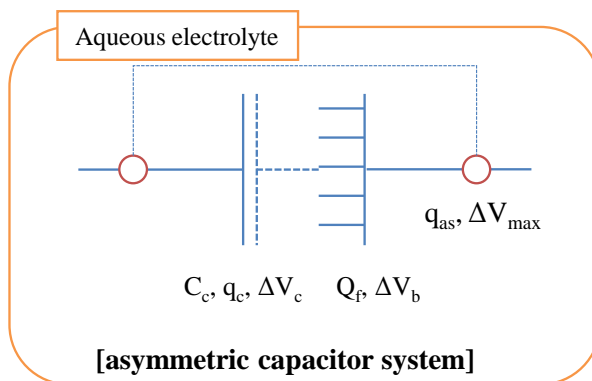


Figure 2.2. Schematic representation of an asymmetric capacitor system with an aqueous electrolyte according to the charge-potential profile

These equations for the specific capacities can be regenerated to consider the performance relative to a symmetric capacitor system with an aqueous electrolyte using the mass and working potential range ratio factors of the battery-type electrode, k_1 and k_2 , respectively:

$$\begin{aligned}
 k_1 &= \frac{m_b}{m_{as}} \text{ or } m_b = k_1 m_{as} \quad (0 < k_1 < 1) \\
 k_2 &= \frac{\Delta V_b}{\Delta V_{\max}} \text{ or } \Delta V_b = k_2 \Delta V_{\max} \quad (0 < k_2 < 1)
 \end{aligned}
 \tag{2.10}$$

Therefore, ED_{as} is rearranged as the following equation with detailed calculations given in Appendix 2.5.1:

$$\begin{aligned}
 ED_{as} &= \frac{q_{as}}{m_{as}} \bullet \left(\Delta V_b + \frac{1}{2} \Delta V_c \right) \bullet \frac{1}{3600s} \\
 &= \frac{q_{as} \Delta V_{\max}}{m_c} \bullet (1 - k_1) \bullet \frac{1}{2} (1 + k_2) \bullet \frac{1}{3600s} \\
 &= (1 - k_1) (1 - k_2^2) \bullet \frac{1}{2} \frac{q_1 \Delta V_{\max}}{m_1} \bullet \frac{1}{3600s}
 \end{aligned}
 \tag{2.11}$$

According to equation 2.7 and 2.11, the specific energy density of symmetric and asymmetric capacitor systems with an aqueous electrolyte, respectively ED_{as} and ED_s , can be compared in terms of the battery-type material-related coefficient, K_{BM} , depending on the ratio factors of k_1 and k_2 :

$$K_{BM} = (1 - k_1)(1 - k_2^2)$$

$$ED_{as} = K_{BM} \cdot \frac{1}{2} \frac{q_1 \Delta V_{max}}{m_1} \cdot \frac{1}{3600s} \quad (2.12)$$

Figure 2.3A shows the plot of K_{BM} as a function of k_1 and k_2 . Also, the plane for $K_{MB}=1/2$ is illustrated in Figure 2.3B to compare the specific energy densities, ED_s and ED_{as} . According to equation 2.12, the smaller the values of k_1 and k_2 are, the higher K_{BM} will be. It is also obvious that k_1 has more of an effect on the value of K_{BM} than k_2 due to the substitution of square value of k_2 in the equation for K_{MB} .

As shown in equation 2.7, K_{BM} for a symmetric capacitor system with an aqueous electrolyte is $1/2$, therefore, ED_{as} is higher than E_s when the value of K_{BM} is higher than $1/2$, viz. as in the following condition:

$$k_2 < \sqrt{\frac{2k_1 - 1}{2k_1 - 2}} \quad (2.13)$$

demonstrated in Figure 2.3B. Particularly, k_1 should be lower than 0.5 and k_2 should be lower than $1/2^{0.5}$ for a value of K_{BM} higher than $1/2$; that is, the mass of a battery-type electrode should be lower than half of the total mass of the system and the working potential range of the battery-type electrode cannot exceed $1/2^{0.5}$ of the total working potential range for an aqueous electrolyte in an asymmetric capacitor system.

Thus, if an asymmetric capacitor system contains a battery-type electrode with an appropriate mass and working potential range, the asymmetric capacitor system has the advantage of being able to store more electrochemical energy compared to a symmetric capacitor system with an aqueous electrolyte.

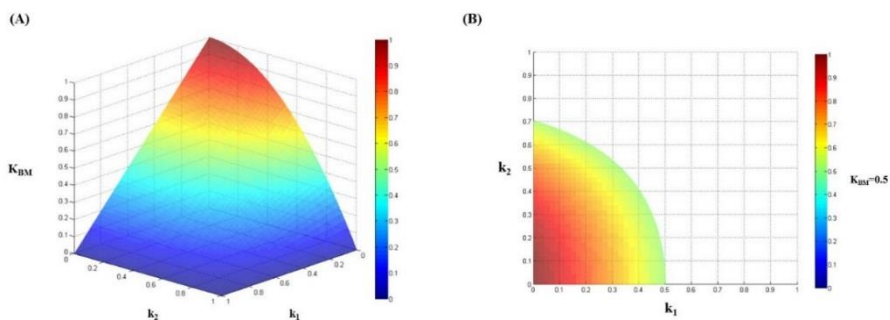


Figure 2.3. (A) Plot of the value of the battery-type material-related coefficient, K_{BM} , as a function of the mass and working potential range ratio factors of the battery-type electrode, k_1 and k_2 , respectively. (B) Plot of $K_{BM}=1/2$.

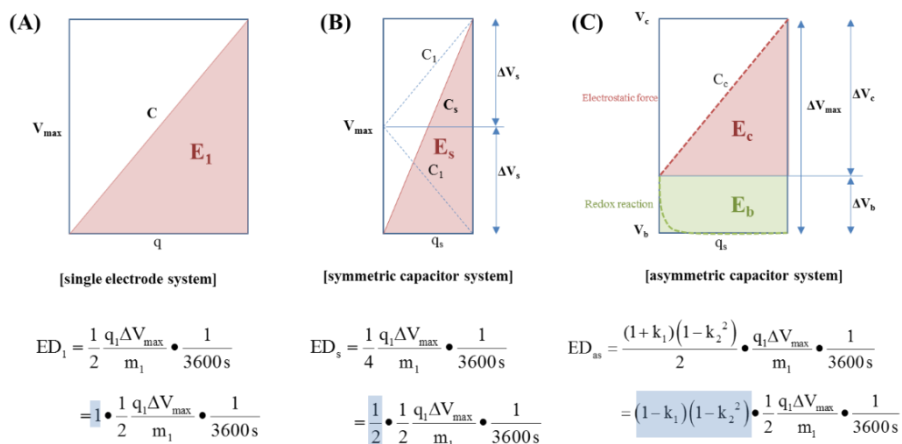


Figure 2.4. Comparison of various capacitor systems using an aqueous electrolyte.

In summary, we can typically consider the EDs of three different types of capacitor system as shown in Figure 2.4. A single electrode system cannot be operated without a counter electrode, as shown in Figure 2.4A, and this can be the standard for a comparison of various electrode systems. As shown in Figure 2.4 and by equation 2.12, the specific energy density of each electrode system can be described by the multiplication of ED_1 by K_{BM} , as highlighted by the blue squares in Figure 2.4.

For the specific maximum power density, PD, on the same assumption used in the ED calculation, the PD for each capacitor system with an aqueous electrolyte can be determined by the following equations:

$$\begin{aligned}
 PD_1 &= \frac{I_{\max} \Delta V_{\max}}{m_1} \\
 PD_s &= \frac{I_{\max} \Delta V_{\max}}{m_s} = PD_1 \\
 PD_{as} &= \frac{I_{\max} \Delta V_{\max}}{m_{as}} = \left(\frac{1-k_1}{1-k_2} \right) \bullet PD_1
 \end{aligned}
 \tag{2.14}$$

Here, I_{\max} is the maximum current for each electrode, PD_1 is the PD for a single electrode system, PD_s is the PD for the symmetric capacitor system, and PD_{as} is the PD for the asymmetric capacitor system with an aqueous electrolyte. Then, PD_{as} can be higher than PD_s under the condition of $k_1 < k_2$.

Thus, according to equations 2.13 and 2.14, we can predict the specified condition of better electrochemical performance for the asymmetric capacitor

system as compared to the symmetric capacitor system with an aqueous electrolyte. Assuming that k_1 and k_2 are in the condition illustrated in Figure 2.5, both ED_{as} and PD_{as} of the asymmetric capacitor system will be higher than those of the symmetric capacitor system. These theoretical analyses clearly demonstrate that the asymmetric capacitor system give the advantage of better electrochemical performance compared to the symmetric capacitor system with an aqueous electrolyte.

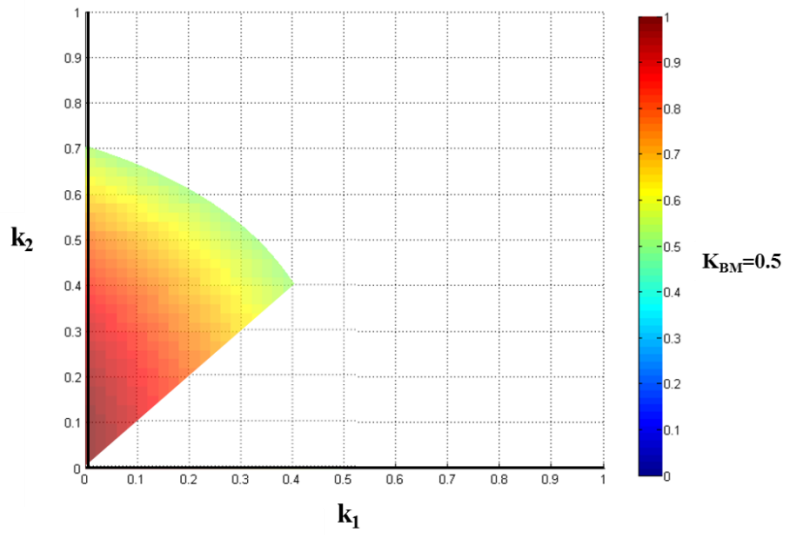


Figure 2.5. Plot of the condition for higher values of ED_{as} and PD_{as} compared to the simultaneous values of ED_s and PD_s

2.2.2. A symmetric capacitor system and an asymmetric capacitor system with an organic electrolyte

One of the effective approaches to enhance the ED and PD of an electrochemical capacitor system is to employ an organic solvent as the electrolyte [5]. An aqueous electrolyte can generally be operated under a maximum potential difference, ΔV_{\max} , of 1.2 V due to the electric decomposition of the water into oxygen and hydrogen gas. This water splitting phenomenon governs the limit of ED and PD for both symmetric and asymmetric capacitor systems using aqueous electrolyte. On the other hand, a proper organic electrolyte in an electrochemical capacitor system can increase the working potential range such that it exceeds that of water, for example over 4 V for Li-ion salt-containing organic solvents that are widely used in LIBs [13, 14]. Because a higher working potential range is one of the effective ways to enhance the ED and PD, there have been various studies regarding the use of an organic electrolyte in the electrochemical capacitor combined with an asymmetric capacitor system [15-19]. Figure 2.6 illustrates an asymmetric capacitor system with an organic electrolyte using the potential profile of the charging state with a single electrode system, which mostly resembles the profile of an asymmetric capacitor system with an aqueous electrolyte except for working potential range in Figure 2.2. As shown in Figure 2.6A, the capacitance of a single electrode with an organic electrolyte, $C_{o,1}$, can be obtained by the equation, $C_{o,1}=q_{o,1}/\Delta V_{o,\max}$, where $q_{o,1}$ is the storable charges for a single capacitor electrode with an organic electrolyte and $\Delta V_{o,\max}$, is the

maximum working potential range of the organic electrolyte in the system. Therefore, E_{o_1} , the amount of electrochemical energy of a single capacitor-type electrode with an organic electrolyte, is derived by the following equation:

$$E_{o_1} = \frac{1}{2} q_{o_1} \Delta V_{o_{\max}} \quad (2.15)$$

Assuming both the single electrodes of the aqueous electrolyte applied system and the organic electrolyte applied system are identical in the comparison of the electrochemical performance, the specific energy density of this single electrode with an organic electrolyte, ED_{o_1} , will be calculated as

$$ED_{o_1} = \frac{1}{2} \frac{q_{o_1} \Delta V_{o_{\max}}}{m_1} \cdot \frac{1}{3600s} \quad (2.16)$$

due to same mass of the electrode in Figures 2.2A and 2.6A.

Figure 2.6B represents the charge-potential profile for the asymmetric capacitor system combining a capacitor-type electrode and a battery-type electrode with an organic electrolyte, where $q_{o_{as}}$ is amount of charges stored in both electrodes, V_{o_c} is the maximum working potential of the capacitor-type electrode, and V_{o_b} is the redox reaction potential of the battery-type electrode in the organic electrolyte. It is assumed that the capacitor-type of electrode in this asymmetric capacitor system is identical to the electrode in the asymmetric capacitor system

with the aqueous electrolyte. Considering the storable charge of the entire system (q_{o_as}) and each electrode (q_{o_b} and q_{o_c}), they should have the same charge-balance value for the different types of electrodes in the system; that is, $q_{o_as}=q_{o_b}=q_{o_c}$.

The energy stored in the asymmetric capacitor system with an organic electrolyte in Figure 2.6B, E_{o_as} , is given as

$$E_{o_as} = q_{o_as} \Delta V_{o_b} + \frac{1}{2} q_{o_as} \Delta V_{o_c} \quad (2.17)$$

where ΔV_{o_b} and ΔV_{o_c} are the working potential range of the battery- and the capacitor-type electrode, respectively. Hence, the specific energy density of this system, ED_{o_as} , can be calculated by following the equation:

$$ED_{o_as} = \frac{q_{o_as} \Delta V_{o_b} + \frac{1}{2} q_{o_as} \Delta V_{o_c}}{m_{o_b} + m_{o_c}} \cdot \frac{1}{3600s} = \frac{q_{o_as}}{m_{o_as}} \cdot \left(\Delta V_{o_b} + \frac{1}{2} \Delta V_{o_c} \right) \cdot \frac{1}{3600s} \quad (2.18)$$

Here, m_{o_b} , m_{o_c} , and m_{o_as} are the mass of the battery-type electrode, capacitor-type electrode, and sum of these masses, respectively. Also, as mentioned earlier as regards the recalculation of equation 2.11 for ED_{as} , this equation for ED_{o_as} can be regenerated by equation 2.19, of which detailed calculations are shown in Appendix 2.5.2:

$$ED_{o_{-as}} = \frac{(1-k_1)(1-k_2^2)}{2} \cdot \frac{q_o \Delta V_{o_{-max}}}{m_{o_{-1}}} \cdot \frac{1}{3600s} = K_{BM} \cdot \frac{1}{2} \frac{q_o \Delta V_{o_{-max}}}{m_{o_{-1}}} \cdot \frac{1}{3600s} \quad (2.19)$$

The ratio factors, k_1 and k_2 , for the organic electrolyte as used here are calculated as follows:

$$k_1 = \frac{m_{o_{-b}}}{m_{o_{-as}}} \text{ or } m_{o_{-b}} = k_{o_{-1}} m_{o_{-as}} \quad (0 < k_1 < 1)$$

$$k_2 = \frac{\Delta V_{o_{-b}}}{\Delta V_{o_{-max}}} \text{ or } \Delta V_{o_{-b}} = k_2 \Delta V_{o_{-max}} \quad (0 < k_2 < 1) \quad (2.20)$$

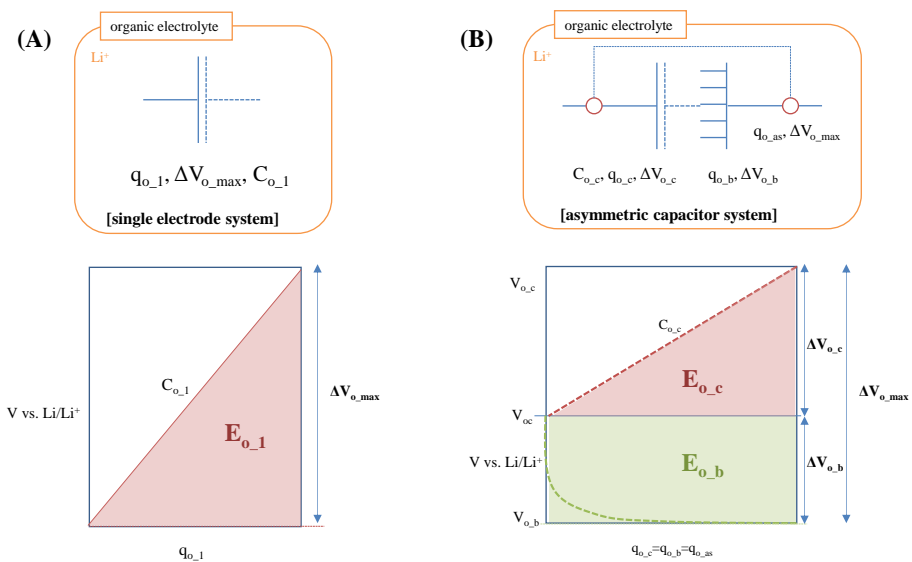


Figure 2.6. Schematic representation of (A) a single electrode system and (B) an asymmetric capacitor system with an organic electrolyte according to the charge-potential profiles

Considering the maximum specific power density of the asymmetric capacitor system with an organic electrolyte, PD_{o_as} , it is derived by equation 2.21, showing a good degree of similarity with PD_{as} .

$$PD_{o_as} = \frac{I_{o_max} \Delta V_{o_max}}{m_{o_as}} = \left(\frac{1-k_1}{1-k_2} \right) \bullet PD_{o_1} \quad (2.21)$$

To compare the electrochemical performances of asymmetric capacitor systems using an aqueous and an organic electrolyte, Figure 2.7 represents the charge-potential profiles of each asymmetric capacitor system with an applied electrolyte. Assuming both asymmetric capacitor systems in Figure 2.7 are designed with same types of capacitor-type electrode but with a different electrolyte, ED_{o_as} in equation 2.19 can be reorganized as

$$\begin{aligned} ED_{o_as} &= \frac{(1-k_1)(1-k_2^2)}{2} \bullet \frac{q_o \Delta V_{o_max}}{m_{o_1}} \bullet \frac{1}{3600s} \\ &= \frac{k_4}{k_3^2} \bullet (1-k_1)(1-k_2^2) \bullet \frac{1}{2} \frac{q_1 \Delta V_{max}}{m_1} \bullet \frac{1}{3600s} \quad (2.22) \\ &= \frac{k_4}{k_3^2} \bullet K_{BM} \bullet \frac{1}{2} \frac{q_1 \Delta V_{max}}{m_1} \bullet \frac{1}{3600s} \end{aligned}$$

where k_3 is the ratio of the maximum working potential range between the aqueous and organic electrolytes and k_4 is the ratio of the specific capacitance between the capacitor-type electrodes in the aqueous and organic electrolyte:

$$\begin{aligned}
k_3 &= \frac{\Delta V_{\max}}{\Delta V_{o_{-}\max}} \quad \text{or} \quad \Delta V_{\max} = k_3 \Delta V_{o_{-}\max} \quad (0 < k_3 < 1, \quad k_3 \cong 0.3 \text{ for Li}^+ \text{ ion}) \\
k_4 &= \frac{C_{o_{-}1} / m_{o_{-}1}}{C_1 / m_1} = \frac{q_{o_{-}1} / m_{o_{-}1} \Delta V_{o_{-}\max}}{q_1 / m_1 \Delta V_{\max}} \quad \text{or} \\
\frac{q_{o_{-}1}}{m_{o_{-}1} \Delta V_{o_{-}\max}} &= k_4 \frac{q_1}{m_1 \Delta V_{\max}} \quad (k_4 < 1, \quad k_4 \cong 0.5 \text{ for Li}^+ \text{ ion})
\end{aligned} \tag{2.23}$$

Because k_3 and k_4 are influenced by the type of applied electrolyte, k_4/k_3^2 can be defined in terms of an electrolyte-related coefficient, K_E , which can be substituted into the equation for $ED_{o_{-}\text{as}}$ as follows:

$$\begin{aligned}
ED_{o_{-}\text{as}} &= \frac{k_4}{k_3^2} \cdot (1 - k_1)(1 - k_2^2) \cdot \frac{1}{2} \frac{q_1 \Delta V_{\max}}{m_1} \cdot \frac{1}{3600 \text{ s}} \\
&= K_E \cdot K_{\text{BM}} \cdot \frac{1}{2} \frac{q_1 \Delta V_{\max}}{m_1} \cdot \frac{1}{3600 \text{ s}}
\end{aligned} \tag{2.24}$$

Hence, when the K_E value is higher than 1 in Figure 2.7B (shown in blue), an organic electrolyte improves the specific energy density of the electrochemical system more compared to an aqueous electrolyte. Generally, the working potential range of the organic electrolyte containing Li-ion salt is about 3 times higher than that of the aqueous electrolyte. Also, typical capacitor-type electrode materials, such as AC, show higher specific capacitances in an aqueous electrolyte by more than twofold compared to an organic electrolyte. That is, if we assume an asymmetric capacitor system with an aqueous and

organic electrolyte consisting of identical components with the same mass ratio and potential range ratio of the battery-type electrode, i.e., the same k_1 and k_2 values, ED_{o_as} can be approximately 4-6 times higher than ED_{as} .

Hence, as the above discussion attests, it is clear that a combination of an asymmetric capacitor system and an organic electrolyte is advantageous for improving electrochemical performance of an electrochemical capacitor, in good agreement with the results of numerous previous studies [9, 17, 18].

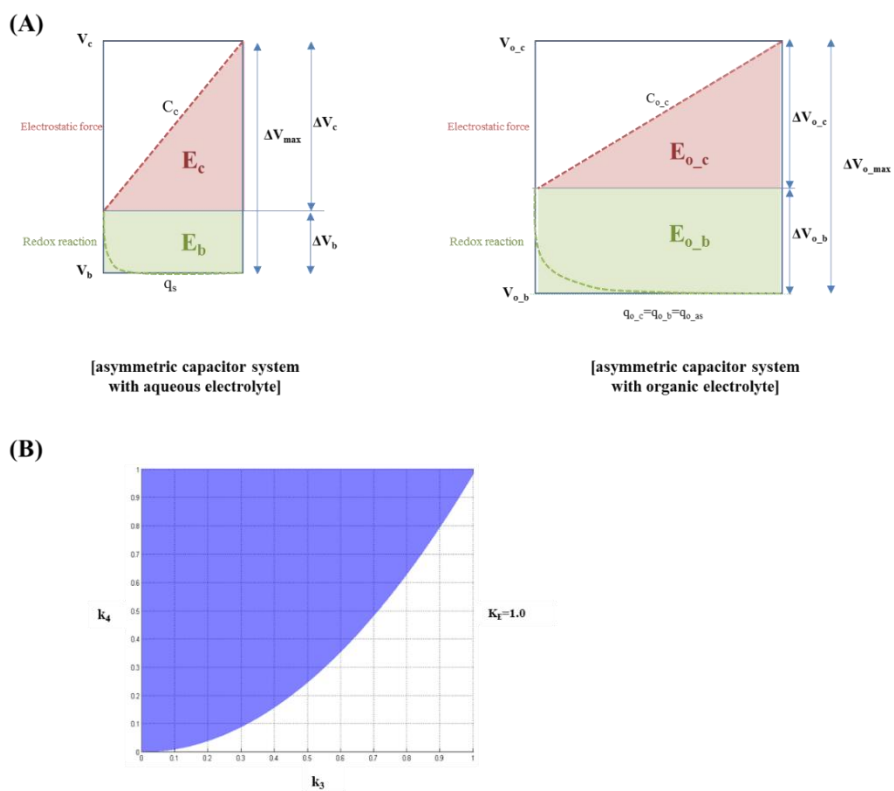


Figure 2.7. (A) Schematic representation of asymmetric capacitor systems containing an aqueous electrolyte and an organic electrolyte according to the charge-potential profiles. (B) Plot of the specified condition $K_E > 1$ as a function of k_3 and k_4

2.3. New concept of an electrode system: BatCap electrode

2.3.1. Concept of the BatCap electrode

As highlighted in the previous section, an asymmetric capacitor system combined with an organic electrolyte is a theoretically effective strategy to enhance the electrochemical performance of an electrochemical capacitor. However, it is very difficult to utilize the overall specific energy density of a typical battery-type electrode, such as graphite or metal oxide [20, 21], due to the redox reaction kinetics being too low in the asymmetric capacitor system. This property can degrade the energy storage ability of the electrochemical device during the fast charge/discharge process, that is, with a lower specific energy density at a higher specific power density. Hence, except for the higher initial power density and higher energy density at low charge/discharge rates, a general asymmetric capacitor system is not useful in an actual application, not only with an aqueous electrolyte but also with an organic electrolyte. This drawback requires a more advanced electrode which can improve the low charge transfer kinetics and redox reaction of a battery-type electrode.

There are several approaches to achieve this objective involving the introduction of a highly conductive material in a battery-type electrode [22-26]. Carbonaceous materials, which are widely used as anode materials in LIBs, are utilized as the negative electrode in an asymmetric capacitor system with a Li-ion salt-containing organic solvent due to the intrinsically high conductivity and good cycle stability [20, 27, 28]. However, the poor Li-ion transfer kinetics of carbonaceous materials at a high charge/discharge rate limits the

electrochemical performance with a high power density. Moreover, TiO_2 - and $\text{Li}_4\text{Ti}_5\text{O}_{12}$ -based anode materials for LIBs are other candidates that can be utilized in asymmetric capacitors with an organic electrolyte due to great cycle stability akin to that of a supercapacitor with zero-strain on during the charge/discharge process in spite of their insulating nature [29-31]. Therefore, modifications of these battery-type electrode materials have been conducted by means of metal doping, using a composite with a high conductive material, or through carbon coating methods to increase the low electronic conductivity [32-34]. Moreover, morphology control can be combined with the aforementioned strategies by enhancing of the contact probability, such as with a 1D or 3D network nanostructures [35, 36]. In spite of the various approaches, there are unsolved additional problems, such as the lower specific energy density of the battery-type electrode due to an unreactive component.

The BatCap electrode is a new-concept proposed here to overcome aforementioned problems. It is the hybridization of the battery component and the capacitor component in a single electrode [6, 7]. In contrast to the simple mixing method of the two components, it can use the energy storage properties of both the battery component and the capacitor component simultaneously, which can be illustrated in a charge-potential plot. Also, proper hybridization of the two different types of components can improve the poor electrochemical reaction kinetics of the battery component at high rates. Herein, we will provide a theoretical approach to realization of the BatCap electrode in an effort to understand operating mechanism of this new-concept of electrode. This is

followed by comparisons with typical electrochemical capacitor systems. Also, the proper structure with ideal conditions for the BatCap electrode will be proposed to enhance the electrochemical performance of this energy storage device.

2.3.2. Theoretical study of the BatCap electrode

As shown in the previous section in the discussion of typical electrochemical capacitors, the charge-potential plot is an effective illustration with which to study the nature of an electrochemical capacitor system. For an intuitive comparison, we will consider the BatCap electrode system containing a typical capacitor-type electrode and a BatCap electrode, as shown in Figure 2.8. The essential characteristic of the BatCap electrode is the synergistic hybridization of battery and capacitor components in a single electrode which can store electrochemical energy in each mechanism. In detail, the capacitor component is charged by electrostatic force in the initial state until the electrode potential attains the redox reaction potential of the battery component in the BatCap electrode. The amount of charge stored in this state is denoted as q_{B_Bc1} in Figure 2.8. Then, the battery component is charged by the redox reaction while maintaining the redox reaction potential of the BatCap electrode, V_{B_Bb} , until the component reaches a full-charge state, with the amount of charge denoted as q_{B_Bb} . After the full charge of the battery component, the capacitor component is charged again to the maximum potential of the BatCap electrode, V_{B_B} , storing the charge, denoted as q_{B_Bc2} , on the surface of the component.

Therefore, in Figure 2.8, the following equations can be defined through the aforementioned energy storage mechanism of the BatCap electrode with a typical capacitor-type electrode as a counter electrode:

$$\begin{aligned}
 q_B &= q_{B_c} = q_{B_B} = q_{B_Bb} + q_{B_Bc} \\
 &= q_{B_Bb} + (q_{B_Bc1} + q_{B_Bc2}) \\
 &= C_{B_c} \Delta V_{B_c}
 \end{aligned} \tag{2.25}$$

Here, q_B denotes the total charge amount, q_{B_c} is the amount of charge for the capacitor-type electrode, q_{B_B} is the amount of charge for the BatCap electrode, and C_{B_c} denotes the capacitance of the capacitor-type electrode in the BatCap system. The maximum working potential range of each electrode and components will be calculated as

$$\begin{aligned}
 \Delta V_{B_max} &= \Delta V_{B_c} + \Delta V_{B_B} \\
 &= \Delta V_{B_c} + (\Delta V_{B_Bb} + \Delta V_{B_Bc})
 \end{aligned} \tag{2.26}$$

where ΔV_{B_max} , ΔV_{B_c} , ΔV_{B_B} , ΔV_{B_Bb} , and ΔV_{B_Bc} are the maximum working potential range for the entire system, the capacitor-type electrode, the BatCap electrode, the battery-type component in the BatCap electrode, and the capacitor component in the BatCap electrode in the BatCap system, respectively. Assuming that the organic electrolyte and the capacitor-type electrode are identical in the BatCap and asymmetric capacitor systems for comparison, the

relationship between the maximum working potential ranges can be derived by equation 2.27:

$$\begin{aligned}\Delta V_{B_max} &= \Delta V_{o_max} \\ \Delta V_{B_c} &= \Delta V_{o_c}\end{aligned}\tag{2.27}$$

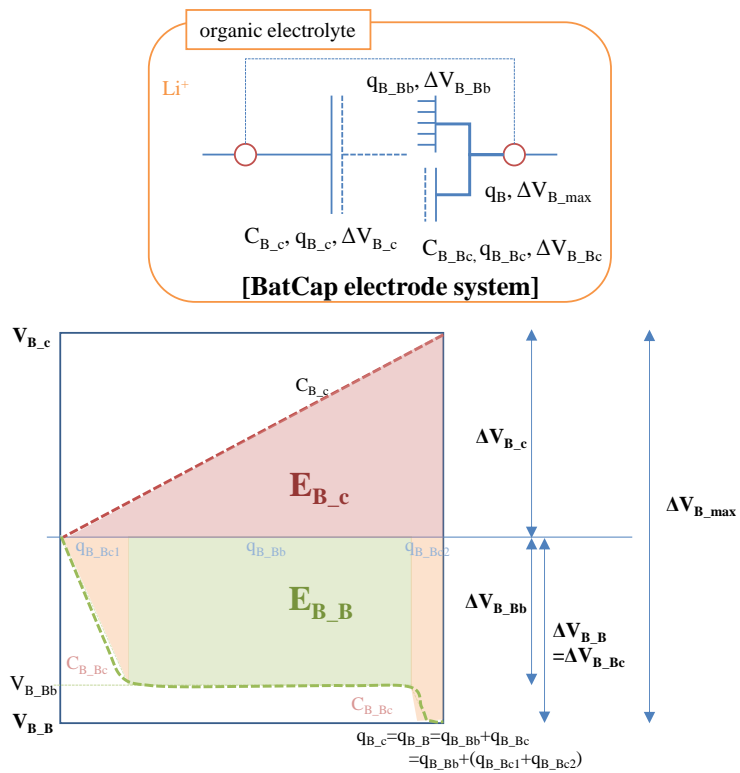


Figure 2.8. Schematic representation of the BatCap electrode system with an organic electrolyte according to the charge-potential profile

Also, the specific capacitances of the capacitor-type electrodes in both systems are identical, as follows:

$$\frac{C_{B_c}}{m_{B_c}} = \frac{C_{o_c}}{m_{o_c}} \quad (2.28)$$

By applying these assumption, the amount of energy stored in this new concept electrode system, E_B , can be obtained by the sum of the amounts of electrochemical energy stored in the capacitor-type electrode, E_{B_c} , and the BatCap electrode, E_{B_B} , in the BatCap system. This is done by equation 2.29, as illustrated in Figure 2.9:

$$\begin{aligned} E_B &= E_{B_c} + E_{B_B} \\ &= E_{B_c} + (E_{B_Bc} + E_{B_Bb}) \\ &= \frac{1}{2}q_{B_c}\Delta V_{B_c} + \left(\frac{1}{2}q_{B_Bc}\Delta V_{B_Bc} + q_{B_Bb}\Delta V_{B_Bb} \right) \end{aligned} \quad (2.29)$$

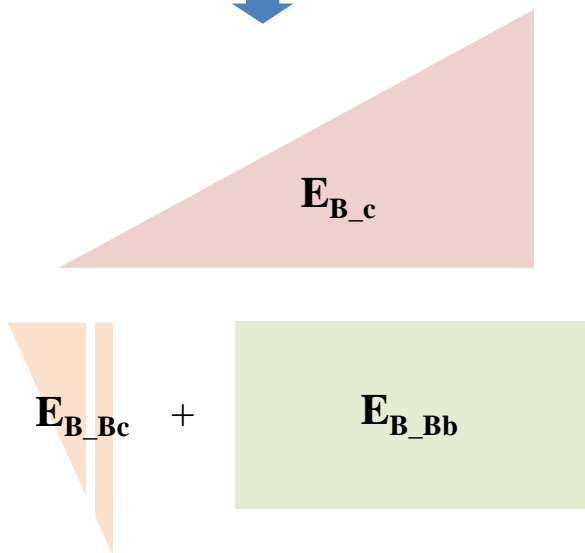
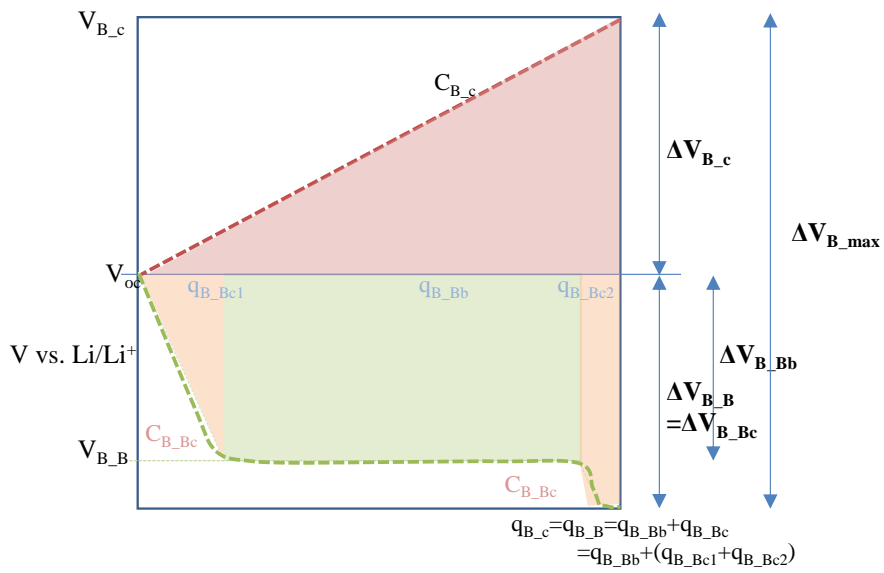


Figure 2.9. Scheme of the storable energy of the BatCap system.

Hence, the specific energy density of this system, ED_B , can be calculated by

$$ED_B = \frac{\frac{1}{2}q_{B_c}\Delta V_{B_c} + \left(\frac{1}{2}q_{B_c}\Delta V_{B_c} + q_{B_b}\Delta V_{B_b}\right)}{m_{B_c} + m_{B_B}} \bullet \frac{1}{3600s} \quad (2.30)$$

where m_{B_c} and m_{B_B} are the mass of the capacitor-type electrode and the BatCap electrode, respectively. The maximum specific power density of the BatCap system with organic electrolyte, PD_B , can be obtained by equation 2.31, similar to PD_{as} :

$$PD_B = \frac{I_{B_max} \Delta V_{B_max}}{m_B} = \left(\frac{1-k_1}{1-k_2}\right) \bullet PD_{o-1} \quad (2.31)$$

In this equation, I_{B_max} is the maximum current of each electrode, m_B is the total mass of the BatCap system electrodes, and $\Delta V_{B_max}=\Delta V_{B_c}$ due to the use of the same organic electrolyte in each electrode system. Thus, if the k_1 and k_2 values are identical in the asymmetric capacitor system and the BatCap system with an organic electrolyte, the maximum specific power densities of each electrode system will be equal, according to equation 2.31.

Meanwhile, ED_B can be rearranged as equation 2.32, with detail of the calculation given in Appendix 2.5.3:

$$\begin{aligned}
ED_B &= \frac{\frac{1}{2}q_{B_c}\Delta V_{B_c} + \left(\frac{1}{2}q_{B_c}\Delta V_{B_c} + q_{B_b}\Delta V_{B_b}\right)}{m_{B_c} + m_{B_B}} \cdot \frac{1}{3600s} \\
&= (1 - k_2 k_5 + 2k_2 k_2' k_5)(1 - k_1) \cdot \frac{1}{2} \frac{q_B \Delta V_{B_max}}{m_{B_c}} \cdot \frac{1}{3600s} \\
&= (1 - k_2 k_5 + 2k_2 k_2' k_5) \cdot (1 - k_1)(1 - k_2) \cdot \frac{1}{2} \frac{q_{o_b} \Delta V_{o_max}}{m_{o_1}} \cdot \frac{1}{3600s} \\
&= \left(\frac{1 - k_2 k_5 + 2k_2 k_2' k_5}{1 + k_2}\right) \cdot K_{BM} \cdot \frac{1}{2} \frac{q_{o_b} \Delta V_{o_max}}{m_{o_1}} \cdot \frac{1}{3600s}
\end{aligned} \tag{2.32}$$

These equations use the ratio factors of k_1 and k_2 in the BatCap system, as introduced in the previous section, and as shown in equation 2.33. In addition, k_2 represents the ratio of the maximum potential range of the BatCap electrode in the system. The potential range ratio factor of the battery component in the BatCap electrode, k_2' , and the stored charge ratio of the capacitor component in the BatCap electrode, k_5 , are defined by equation 2.34 to reflect the characteristics of the BatCap electrode as regards the electrochemical performance:

$$\begin{aligned}
k_1 &= \frac{m_{B_B}}{m_B} \text{ or } m_{B_B} = k_1 m_{B_B} \quad (0 < k_1 < 1) \\
k_2 &= \frac{\Delta V_{B_B}}{\Delta V_{B_max}} \text{ or } \Delta V_{B_B} = k_2 \Delta V_{o_max} \quad (0 < k_2 < 1)
\end{aligned} \tag{2.33}$$

$$\begin{aligned}
k_2' &= \frac{\Delta V_{B_Bb}}{\Delta V_{B_B}} \text{ or } \Delta V_{B_Bb} = k_2' \Delta V_{B_B} \quad (0 < k_2' < 1) \\
k_5 &= \frac{q_{B_Bc}}{q_B} \text{ or } q_{B_Bc} = k_5 q_B \quad (0 < k_5 < 1)
\end{aligned} \tag{2.34}$$

Because k_2' and k_5 are related to the components in the BatCap electrode, $(1 - k_2 k_5 + 2k_2 k_2' k_5)/(1 + k_2)$ can be defined in terms of the BatCap-related coefficient, K_{BC} , which can be substituted into the equation for ED_B with K_E and K_{BM} as follows for comparison:

$$\begin{aligned}
 ED_B &= \left(\frac{1 - k_2 k_5 + 2k_2 k_2' k_5}{1 + k_2} \right) \cdot K_{BM} \cdot \frac{1}{2} \frac{q_{o,b} \Delta V_{o,max}}{m_{o,1}} \cdot \frac{1}{3600s} \\
 &= \left(\frac{1 - k_2 k_5 + 2k_2 k_2' k_5}{1 + k_2} \right) \cdot \frac{k_4}{k_3^2} \cdot K_{BM} \cdot \frac{1}{2} \frac{q_1 \Delta V_{max}}{m_1} \cdot \frac{1}{3600s} \quad (2.35) \\
 &= K_{BC} \cdot K_E \cdot K_{BM} \cdot \frac{1}{2} \frac{q_1 \Delta V_{max}}{m_1} \cdot \frac{1}{3600s} \\
 &= K_{BC} \cdot ED_{as}
 \end{aligned}$$

Therefore, it is possible to compare the energy storage capacity of each electrode system using the specific energy density parameters, ED_B and ED_{as} , which are related to K_{BC} with the aforementioned assumptions. In detail, k_2 affects both coefficients; therefore, k_2 should be simultaneously considered with k_2' and k_5 to calculate K_{BC} , as illustrated in Figure 2.10. According to the calculation, the values of the K_{BC} in various conditions are under 1, indicating that E_{BC} cannot higher than E_{as} when they operate on the same capacitor-type electrode, battery component, and organic electrolyte with ideal charge transfer kinetics and redox reaction, as we mentioned before.

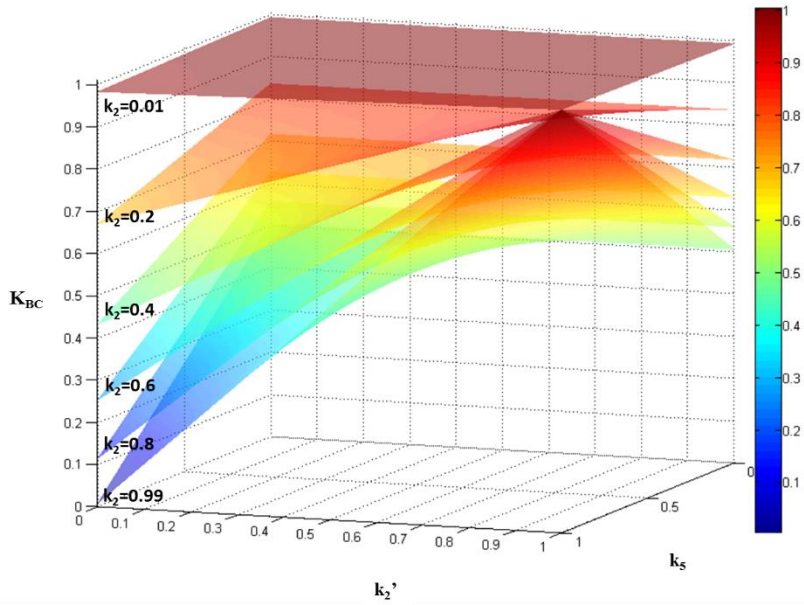


Figure 2.10. Plot of the value of the BatCap-related coefficient, K_{BC} , as a function of the working potential range ratio factors (k_2 and k_2') and storable electrical charge ratio factor of the capacitor component (k_5) in the BatCap electrode

In a real system, as mentioned before, the deterioration of the electrochemical performance can arise in electrochemical capacitor systems due to poor electron transport in the electrode, a poor charge transfer reaction on the surface of the electrode, and slow mass transfer in the electrolyte. Generally, the redox reaction for electron transfer is the rate-determining step in the electrochemical capacitor containing battery component, such as an asymmetric capacitor system or BatCap system. If both systems consist of the same type of battery component, electron and electrolyte transport will be the comparative rate-determining step. At a high charge/discharge rate, the amount of storable charge of the battery component, q_{o_b} or q_B , will be lower than that in the ideal state, resulting in a decrease of the specific energy density of each system.

Except for the mass transfer problem in the electrolyte, which can be partially prevailed by increase of salt-ion in the electrolyte [37], the BatCap system has advantage at a high power density due to the structural characteristics of the system compared to those of a typical asymmetric capacitor system with an organic electrolyte, as shown in Figure 2.6B. In detail, the capacitor component, which can also store electrochemical energy by electrostatic force, enhances the electron transport to the battery component in the BatCap system, causing a better charge transfer reaction at a high rate.

From these theoretical approaches, we can simply estimate the ED of each system with several approximations, i.e., the use of the same types of battery and capacitor components with the same electrodes in every systems. If we assume that the capacitor-type material is typical AC, the aqueous electrolyte

is the KOH aqueous solution with $\Delta V_{as} = 1.2$ V, and the organic electrolyte is 1M LiPF₆ in the ethylene carbonate/diethyl carbonate (EC/DEC) solvent with $\Delta V_{o_as} = \Delta V_B = 3.5$ V with a very fast charge transfer in each system, the approximate ED of each system can be calculated by $ED_B = 0.5 \sim 1 ED_{o_as} = 2 \sim 6 ED_{as}$.

Table 2.1. Theoretical equations to describe the electrochemical performance of each system.

Energy storage systems	Specific energy density	Specific power density
Symmetric capacitor system with aqueous electrolyte	$ED_s = \frac{1}{2} \cdot \frac{1}{2} \cdot \frac{q_1 \Delta V_{\max}}{m_s} \cdot \frac{1}{3600s}$ $= \frac{1}{4} \cdot \frac{q_1 \Delta V_{\max}}{m_s} \cdot \frac{1}{3600s}$	$PD_s = \frac{I_{\max} \Delta V_{\max}}{m_s} = PD_1$
Asymmetric capacitor system with aqueous electrolyte	$ED_{as} = \frac{q_{as}}{m_{as}} \cdot \left(\Delta V_b + \frac{1}{2} \Delta V_c \right) \cdot \frac{1}{3600s}$ $= \frac{q_{as} \Delta V_{\max}}{m_c} \cdot (1 - k_1) \cdot \frac{1}{2} (1 + k_2) \cdot \frac{1}{3600s}$ $= K_{BM} \cdot \frac{1}{2} \cdot \frac{q_1 \Delta V_{\max}}{m_1} \cdot \frac{1}{3600s}$	$PD_{as} = \frac{I_{\max} \Delta V_{\max}}{m_{as}}$ $= \left(\frac{1 - k_1}{1 - k_2} \right) \cdot PD_1$
Asymmetric capacitor system with organic electrolyte	$ED_{o_{-as}} = \frac{(1 - k_1)(1 - k_2^2)}{2} \cdot \frac{q_o \Delta V_{o_{-max}}}{m_{o_{-1}}} \cdot \frac{1}{3600s}$ $= \frac{k_4}{k_3^2} \cdot (1 - k_1)(1 - k_2^2) \cdot \frac{1}{2} \cdot \frac{q_1 \Delta V_{\max}}{m_1} \cdot \frac{1}{3600s}$ $= K_E \cdot K_{BM} \cdot \frac{1}{2} \cdot \frac{q_1 \Delta V_{\max}}{m_1} \cdot \frac{1}{3600s}$	$PD_{o_{-as}} = \frac{I_{o_{-max}} \Delta V_{o_{-max}}}{m_{o_{-as}}}$ $= \left(\frac{1 - k_1}{1 - k_2} \right) \cdot PD_{o_{-1}}$
BatCap system with organic electrolyte	$ED_B = \frac{\frac{1}{2} q_{B_{-c}} \Delta V_{B_{-c}} + \left(\frac{1}{2} q_{B_{-c}} \Delta V_{B_{-c}} + q_{B_{-b}} \Delta V_{B_{-b}} \right)}{m_{B_{-c}} + m_{B_{-B}}} \cdot \frac{1}{3600s}$ $= \left(\frac{1 - k_2 k_5 + 2k_2 k_5}{1 + k_2} \right) \cdot K_{BM} \cdot \frac{1}{2} \cdot \frac{q_{o_{-b}} \Delta V_{o_{-max}}}{m_{o_{-1}}} \cdot \frac{1}{3600s}$ $= K_{BC} \cdot K_E \cdot K_{BM} \cdot \frac{1}{2} \cdot \frac{q_1 \Delta V_{\max}}{m_1} \cdot \frac{1}{3600s}$	$PD_B = \frac{I_{B_{-max}} \Delta V_{B_{-max}}}{m_B}$ $= \left(\frac{1 - k_1}{1 - k_2} \right) \cdot PD_{o_{-1}}$

2.3.3. Conditions of the electrode material for the BatCap system

This hybridization strategy of the battery and capacitor component into a single electrode can realize the aforementioned advantages compared to the previously discussed traditional electrode with the following proper conditions:

1. Both the battery and capacitor components should be homogeneously hybridized to operate as a single electrode, which is the most important indicative difference with a simple mixing of a highly conductive material and a battery component in a single electrode. If they exist as the independent component in the electrode, the working potential will be directly increased in the charge state without the charging of the battery component due to the very fast kinetics of the conductive material, capacitor component.
2. Capacitor component should be not only highly electronic-conductive but also available to store the electrochemical energy by electrostatic force in the organic electrolyte. One of the important characteristics of the BatCap electrode is the charge-storable capacitor component in the electrode. From this point of view, carbonaceous materials are most effective candidate as the capacitor component in the BatCap system due to high conductivity and charge-storable property in the organic electrolyte [38-40]. In the case of RuO_2 or MnO_2 , which are typical faradaic supercapacitor materials, they cannot operate as the faradaic

capacitor component in an organic electrolyte. Also, various metals such as Fe, Pt, Cu, or Al, which are highly conductive materials, are not appropriate active material as the capacitor component due to their very low surface areas and lack of a charge storage ability with an organic electrolyte.

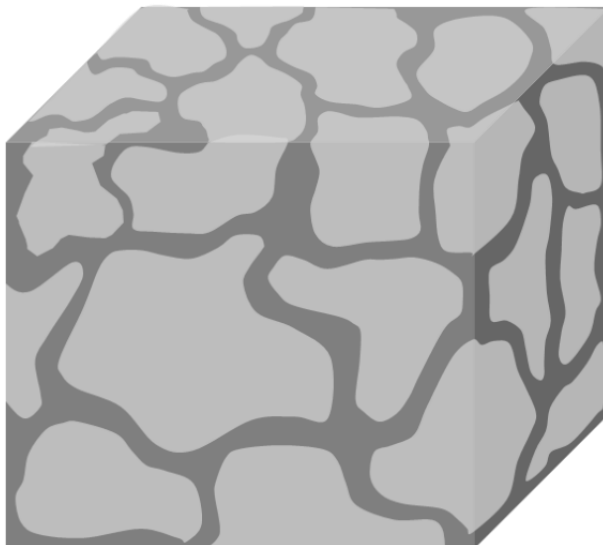
3. The BatCap electrode material should have a high surface area with an open porous structure for high energy density from the capacitor component and good ionic conductivity, respectively. The pore size should ensure a nanosized porous structure which can be penetrated by the organic electrolyte. Generally, the size of the organic electrolyte is in the range 2-5 nm in diameter. Also, a 3D network structure is beneficial to enhance the electron transport while retaining the ionic conductivity in this hybrid material.

Figure 2.11A schematically illustrates the ideal morphological structure for the BatCap electrode material which can satisfy the above-mentioned conditions. This ideal structure hybridized with a battery and capacitor component contains open pores on the surface of the material. This concept is similar to the habitat of the “moisture ant” colonies of which can be found in water-damaged area, in the rotting wood of fallen trees, in tree stumps, and in houses in natural area, as shown in Figure 2.11B.

The electrochemical performance of the BatCap electrode material is based on the hybridization and surrounding characteristics of both components. Therefore, a proper morphological structure consisting of proper components

is the key factor to actualize the potential of the BatCap electrode material compared to typical, traditional electrode materials.

(A)



(B)



Figure 2.11. (A) Ideal structure of the BatCap electrode material which resembles (B) the “moisture ant” habitat [41].

2.3.4. Comparison of an asymmetric capacitor and the BatCap electrode system

As in equation 2.35, in terms of ED, an asymmetric capacitor system is better than the BatCap system with an organic electrolyte in an ideal situation. However, as also mentioned earlier, ED_{o_as} can be limited under high-rate circumstances due to the poor redox reaction kinetics, leading to the better electrochemical performance of the BatCap system. Here, we consider the previously reported results in the literature [9] for an asymmetric capacitor system and the BatCap system, as listed and illustrated in Table 2.2 and Figure 2.12, respectively.

There have been several outstanding reports of asymmetric capacitor systems using various active materials as the counter electrode for AC. Examples include MnO_2 [42, 43], NiO [44], $Li_2Mn_4O_9$ [45], $LiTi_2(PO_4)_3$ [46] with an aqueous electrolyte and graphite [18], $Li_4Ti_5O_{12}$ [14], and TiO_2 [17] with an organic electrolyte. As mentioned above, the research trend in previous studies of the electrochemical capacitors focused on an increase of the energy density, leading to the introduction of asymmetric electrodes and organic electrolytes. As shown in Figure 2.12, these approaches are successful to enhance the specific energy density of AC//AC symmetric capacitors under 10 Wh kg^{-1} . These results can be estimated through a theoretical consideration while applying asymmetric electrodes and an organic electrolyte in section 2.3.2, of which the results are shown in the blue and green regions in Figure 2.12. Meanwhile, the BatCap system cannot theoretically store more electrochemical

energy than an asymmetric capacitor system with organic electrolyte, as shown in Figure 2.10. However, as shown in Figure 2.12 in red, the new electrode, the BatCap system, indicates a better specific energy density at a high rate in an actual system. This result clearly shows the advantage of the BatCap system with hybridization of the battery-capacitor component in a single electrode. In spite of the intrinsically low specific energy density of the BatCap electrode, the synergetic effects from hybridization improve the charge transfer kinetics of the battery component, thus improving the high rate capability, of which influences can be described in terms of the practical coefficient; K_R , as explained in Appendix 2.5.4. Also, at a very low power density, the BatCap system operates as a typical battery with a high ED, indicating the dual-functionality of this system.

Table 2.2. Summary of various electrochemical capacitor systems

Negative electrode material	Positive electrode material	Electrolyte	working potential (V)	Energy Density (Wh kg ⁻¹)	Power Density (W kg ⁻¹)	Ref.
Asymmetric electrode system with aqueous electrolyte						
AC	Amorphous MnO ₂	KCl/H ₂ O	2.0	9.6	2.7	[47]
AC	Amorphous MnO ₂	K ₂ SO ₄ /H ₂ O	2.2	6.3	3.6	[48]
AC	Amorphous MnO ₂	K ₂ SO ₄ /H ₂ O	2.2	5.8	6.3	[49]
AC	Amorphous MnO ₂	K ₂ SO ₄ /H ₂ O	2.0	3.3	5.6	[12]
AC	MnO ₂ nanorods	Na ₂ SO ₄ or K ₂ SO ₄ /H ₂ O	1.8	5.7	0.7	[51]
AC	MnO ₂	Ba(NO ₃) ₂ /H ₂ O	2.0	5.4	13.0	[50]
AC	Mesoporous MnO ₂	KOH/H ₂ O	1.8	10.4	0.1	[51]
AC	Nano-structured MnO ₂	K ₂ SO ₄ /H ₂ O	1.8	5.7	0.7	[52]
AC	MnO ₂	LiOH /H ₂ O	1.8	6.8	0.3	[53]
AC	K-doped MnO ₂	K ₂ SO ₄ /H ₂ O	1.8	5.9	0.7	[54]
AC	PbSO ₄ /PbO ₂	H ₂ SO ₄ /H ₂ O	2.2	18.0	100.0	[55]
AC	V ₂ O ₅ ·0.6H ₂ O	K ₂ SO ₄ /H ₂ O	1.8	9.7	2.0	[56]
AC	Co(OH) ₂ nano-flakes	KOH/H ₂ O	1.6	8.6	0.8	[57]
AC	Co,Al hydroxide	KOH/H ₂ O	1.6	5.6	0.1	[58]
AC	Ni,Zn,Co oxide /hydroxide	KOH/H ₂ O	1.5	13.9	1.0	[59]
AC	RuO ₂ /TiO ₂ nanotubes	KOH/H ₂ O	1.4	3.4	0.4	[60]
AC	Li ₂ Mn ₄ O ₉	Li ₂ SO ₄ /H ₂ O	1.4	5.0	0.5	[45]
AC	Nano-structured MnO ₂	LiOH /H ₂ O	1.8	6.7	0.9	[53]
LiTi ₂ (PO ₄) ₃	AC	Li ₂ SO ₄ /H ₂ O	1.4	8.0	0.3	[46]
Asymmetric electrode system with organic electrolyte						
Graphite	AC	LiPF ₆ /EC:DMC	4.5	34.6	3.3	[18]
Non-graphitizable carbon	AC	LiPF ₆ /EC:DEC	3.5	25.0	0.3	[61]
Nano-structured Li ₄ Ti ₅ O ₁₂	AC	LiBF ₄ /AN	3.0	11.0	4.0	[14]
Li ₄ Ti ₅ O ₁₂ /CNF	AC	LiBF ₄ /PC	2.8	13.3	2.8	[62]
CNF	LiCoPO ₄	LiClO ₄ /EC:PC	2.0	3.7	0.3	[63]

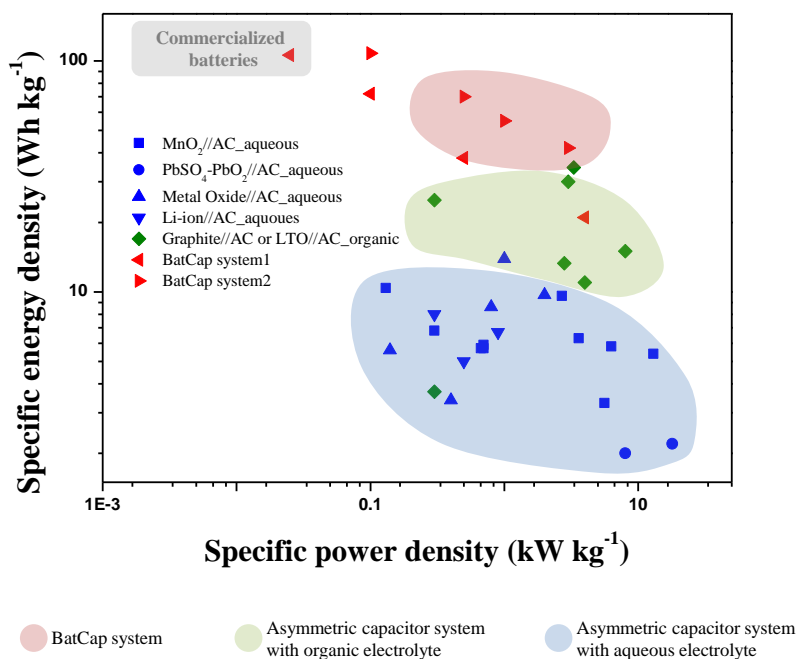


Figure 2.12. Specific power density-specific energy density plot of typical commercialized batteries (grey region), an asymmetric capacitor system with an aqueous electrolyte (blue region), an asymmetric capacitor system with an organic electrolyte (green region), and the BatCap system (red region) using various electrode materials

2.4. Conclusions

We successively derived the theoretical equations for ED and PD for various electrochemical capacitor systems which can be classified according to the symmetry of the electrodes and the type of the electrolyte. These calculations clearly show that the introduction of an asymmetric electrode and an organic electrolyte is effective to enhance the electrochemical performance of an electrochemical capacitor. Also, ED and PD approximations are possible in each system with the information of the working potential range and mass ratio of the electrode in the system, which can decrease the experimental trial-and-error process to find the optimum fabrication condition of the system.

Moreover, the BatCap system, a newly proposed energy storage system, is theoretically considered by the modeling and calculation of ED and PD under specified conditions. The BatCap electrode, consisting of a battery and capacitor component in a single electrode, is designed to overcome the poor electrochemical reaction kinetics of the asymmetric capacitor system. Also, we suggest the ideal structure of the BatCap electrode material to maximize the electrochemical performance, which is similar to the habitat of the moisture ant in nature.

Through the calculation of ED and PD combined with component conditions, we can theoretically compare the electrochemical performance between the BatCap system and typical electrochemical capacitors. In spite of the lower theoretical values of ED, the BatCap system indicates the better electrochemical performance than that of a typical capacitor in an actual system.

This comparison clearly illustrates the advantage of the BatCap system, caused by the synergetic hybridization of the battery and capacitor components under the proper conditions. In conclusion, the BatCap system is an effective approach to enhance electrochemical capacitors, achieving an increase in ED with a high PD.

2.5. Appendix

A. 2.5.1. Calculation of the specific energy density for an asymmetric capacitor system with an aqueous electrolyte

Each ratio factor is defined for the calculation of the specific energy density for an asymmetric capacitor system using an aqueous electrolyte, as follows:

$$\begin{aligned}m_b &= k_1 m_{as} \quad (k_1 < 1) \\m_c &= m_{as} - m_b = m_{as} (1 - k_1) \\ \Delta V_b &= k_2 \Delta V_{max} \quad (k_2 < 1) \\ \Delta V_c &= \Delta V_{max} - \Delta V_b \\ &= \Delta V_{max} (1 - k_2)\end{aligned} \quad (2.A1)$$

Also, in the approximation of this system, both of the capacitor-type electrodes of the symmetric and asymmetric electrode systems consist of same type of material. Therefore, the specific capacitance of each electrode is identical, as follows:

$$\frac{q_{as}}{m_c \Delta V_c} = \frac{q_1}{m_s \Delta V_{max}} \quad (2.A2)$$

Detail calculation pertaining to the specific energy density for an asymmetric capacitor system with an aqueous electrolyte is shown in equation 2.A3

$$\begin{aligned}
ED_{as} &= \frac{E_b + E_c}{m_b + m_c} = \frac{q_{as}\Delta V_b + \frac{1}{2}q_{as}\Delta V_c}{m_b + m_c} = \frac{q_{as}}{m_{as}} \bullet \left(\Delta V_b + \frac{1}{2}\Delta V_c \right) \\
&= \frac{q_{as}}{m_c} \bullet (1 - k_1) \bullet \left(\Delta V_b + \frac{1}{2}\Delta V_c \right) \\
&= \frac{q_{as}}{m_c} \bullet (1 - k_1) \bullet \left(k_2\Delta V_{\max} + \frac{1}{2}(1 - k_2)\Delta V_{\max} \right) \\
&= \frac{q_{as}\Delta V_{\max}}{m_c} \bullet (1 - k_1) \bullet \left(\frac{1}{2} + \frac{1}{2}k_2 \right) \\
&= \frac{q_{as}\Delta V_{\max}}{m_c} \bullet (1 - k_1) \bullet \frac{1}{2}(1 + k_2) \\
&= \frac{q_1\Delta V_{\max}}{m_1} \bullet (1 - k_2) \bullet (1 - k_1) \frac{1}{2}(1 + k_2) \\
&= \frac{(1 - k_1)(1 - k_2^2)}{2} \bullet \frac{q_1\Delta V_{\max}}{m_1}
\end{aligned} \tag{2.A3}$$

A. 2.5.2. Calculation of the specific energy density for an asymmetric capacitor system with an organic electrolyte

As in the aqueous electrolyte containing system, the ratio factors (2.A4) and specific capacitance (2.A5) of an asymmetric capacitor system with an organic electrolyte can be defined and calculated by the following equations:

$$m_{o_f} = k_1 m (k_1 < 1)$$

$$\begin{aligned} \Delta V_{o_f} &= k_2 \Delta V_{o_max} (k_2 < 1) \\ \Delta V_{o_c} &= \Delta V_{o_max} - \Delta V_{o_f} \\ &= \Delta V_{o_max} (1 - k_2) \end{aligned} \quad (2.A4)$$

$$\frac{q_{o_as}}{m_{o_c} \Delta V_{o_c}} = \frac{q_o}{m_{o_1} \Delta V_{o_max}} \quad (2.A5)$$

Therefore, the specific energy density of this system can be obtained by equation 2.A6, which has a similar form of ED_{as} to that in equation 2.A3.

$$\begin{aligned}
ED_{o_as} &= \frac{q_{o_as} \Delta V_{o_b} + \frac{1}{2} q_{o_as} \Delta V_{o_c}}{m_{o_b} + m_{o_c}} \\
&= \frac{q_{o_as}}{m_{o_c}} \bullet (1 - k_1) \bullet \left(\Delta V_{o_b} + \frac{1}{2} \Delta V_{o_c} \right) \\
&= \frac{q_{o_as} \Delta V_{o_max}}{m_{o_c}} \bullet (1 - k_1) \bullet \left(\frac{1}{2} + \frac{1}{2} k_2 \right) \\
&= \frac{(1 - k_1)(1 - k_2^2)}{2} \bullet \frac{q_o \Delta V_{o_max}}{m_{o_1}}
\end{aligned} \tag{2.A6}$$

A. 2.5.3. Calculation of the specific energy density for the BatCap system with an organic electrolyte

Ratio factors to simplify the ED_B are defined by equation 2.A7. For the BatCap electrode, k_2' and k_5 are additionally defined in equation 2.A8 to reflect the characteristics of the BatCap electrode in the system.

$$m_{B_B} = k_1 m_B (k_1 < 1)$$

$$\Delta V_{B_B} = k_2 \Delta V_{B_max} (k_2 < 1) \quad (2.A7)$$

$$\begin{aligned} \Delta V_{B_c} &= \Delta V_{B_max} - \Delta V_{B_B} \\ &= \Delta V_{B_max} (1 - k_2) \end{aligned}$$

$$\Delta V_{B_Bb} = k_2' \Delta V_{B_B} (k_2' < 1)$$

$$q_{B_Bc} + q_{B_b} = q_B = q_{B_c}$$

$$q_{B_Bc} = k_5 q_B (k_5 < 1) \quad (2.A8)$$

$$\begin{aligned} \therefore \frac{1}{2} q_{B_Bc} + k_2' q_{B_Bb} \\ = q_B \left(\frac{1}{2} - \frac{1}{2} k_5 + k_2' k_5 \right) \end{aligned}$$

Using the previous defined factors, ED_B can be calculated via the following equation with the previously defined ratio factors.

$$\begin{aligned}
ED_B &= \frac{\frac{1}{2}q_{B_c}\Delta V_{B_c} + \left(\frac{1}{2}q_{B_c}\Delta V_{B_c} + q_{B_b}\Delta V_{B_b}\right)}{m_{B_c} + m_{B_B}} \\
&= \frac{\frac{1}{2}(1-k_2)q_{B_c}\Delta V_{B_max} + \Delta V_{B_B} \left(\frac{1}{2}q_{B_c} + k_2q_{B_b}\right)}{m_B} \\
&= \frac{\frac{1}{2}(1-k_2)q_B\Delta V_{B_max} + k_2\Delta V_{B_max} \bullet q_B \left(\frac{1}{2} - \frac{1}{2}k_5 + k_2k_5\right)}{m_B} \tag{2.A9} \\
&= \frac{q_B\Delta V_{B_max} \left(\frac{1}{2}(1-k_2) + k_2 \left(\frac{1}{2} - \frac{1}{2}k_5 + k_2k_5\right)\right)}{m_B} \\
&= \frac{q_B\Delta V_{B_max}}{m_{B_c}} \bullet \frac{1}{2}(1-k_1)(1-k_2k_5 + 2k_2k_2k_5) \\
&= \frac{q_{o_b}\Delta V_{o_max}}{m_{o_1}} \bullet \frac{1}{2}(1-k_2)(1-k_1)(1-k_2k_5 + 2k_2k_2k_5)
\end{aligned}$$

A. 2.5.4. Consideration of the practical values pertaining to the electrochemical performance of the energy storage systems

Compared with theoretical values of the electrochemical performances of energy storage devices, as simulated and calculated in the previous sections in this paper, the practical values are influenced by the three additional parameters of the mass transfer in the electrolyte, the charge transfer on the surface of the electrode, and the charge transport behavior in the electrode [37]. First, mass transfer can be described by the ion flux near the interface between the electrode and the electrolyte, as shown in equation 2.A10:

$$J_{\text{ion}} = |z_i| F u_i C_i \frac{d\Phi}{dx} \quad (2.A10)$$

Here, z_i is the charge of the ions, F is the Faraday constant, u_i is the mobility of the ions, C is the concentration of ions, and Φ is the potential difference between the electrodes. Also, the charge transfer reaction on the surface of the electrode can be calculated by equation 2.A11:

$$i_0 = \frac{-RT}{nFR_{\text{ct}}} = nFAk_0C \cdot \exp(-\alpha nF\eta) \quad (2.A11)$$

where R_{ct} is the charge transfer resistance on the surface of the electrode, k_0 is the reaction constant, α is a symmetric parameter ($=1/2$), and η is the over-potential). Moreover, the charge transport in the electrode can be described using the electronic conductivity for a negative charge and the charge transfer time for each ion for a positive charge, as shown in equation 2.A12:

$$\begin{aligned} \kappa &= F \Sigma |z_e| u_e c_e \\ T &= \frac{d_i^2}{\alpha^2 D_i} \end{aligned} \quad (2.A12)$$

In this equation, κ is the electronic conductivity, z_e is the transferred charge number, u_e is the mobility of the electron, C_e is the concentration of electrons, d_i is the diffusion path, α is the number of available vacant interstitial sites in the active material lattice, and D_i is the diffusion coefficient of the ion.

These parameters can be calculated from practical analytic values, for example the electronic conductivity; however, a reverse operation to derive the practical power and energy densities from the parameters is not possible, as these parameters affect the practical values in a complex manner with a combination of a variety of properties of the material, such as the shape, size, and/or surface area.

2.6. References

- [1] P. Simon, Y. Gogotsi, *Nature Materials*, 7 (2008) 845-854.
- [2] F. Cheng, J. Liang, Z. Tao, J. Chen, *Adv Mater*, 23 (2011) 1695-1715.
- [3] R. Marom, S.F. Amalraj, N. Leifer, D. Jacob, D. Aurbach, *Journal of Materials Chemistry*, 21 (2011) 9938-9954.
- [4] J.B. Goodenough, Y. Kim, *Chemistry of Materials*, 22 (2010) 587-603.
- [5] W.G. Pell, B.E. Conway, *Journal of Power Sources*, 136 (2004) 334-345.
- [6] H.S. Choi, T. Kim, J.H. Im, C.R. Park, *Nanotechnology*, 22 (2011) 405402.
- [7] H.S. Choi, J.H. Im, T. Kim, J.H. Park, C.R. Park, *Journal of Materials Chemistry*, 22 (2012) 16986-16993.
- [8] B.E. Conway, *Electrochemical Supercapacitors—Scientific Fundamentals and Technological Applications*, Kluwer, New York, 1999.
- [9] D. Cericola, R. Kotz, *Electrochimica Acta*, 72 (2012) 1-17.
- [10] E. Frackowiak, V. Khomenko, K. Jurewicz, K. Lota, F. Béguin, *Journal of Power Sources*, 153 (2006) 413-418.
- [11] V. Khomenko, E. Raymundo-Piñero, F. Béguin, *Journal of Power Sources*, 153 (2006) 183-190.
- [12] T. Brousse, P.-L. Taberna, O. Crosnier, R. Dugas, P. Guillemet, Y. Scudeller, Y. Zhou, F. Favier, D. Bélanger, P. Simon, *Journal of Power Sources*, 173 (2007) 633-641.
- [13] A. Du Pasquier, A. Laforgue, P. Simon, G.G. Amatucci, J.-F. Fauvarque, *Journal of The Electrochemical Society*, 149 (2002) A302.

- [14] A. Du Pasquier, I. Plitz, S. Menocal, G. Amatucci, *Journal of Power Sources*, 115 (2003) 171-178.
- [15] J.P. Zheng, *Journal of The Electrochemical Society*, 150 (2003) A484-A492.
- [16] A. Du Pasquier, A. Laforgue, P. Simon, *Journal of Power Sources*, 125 (2004) 95-102.
- [17] T. Brousse, R. Marchand, P.-L. Taberna, P. Simon, *Journal of Power Sources*, 158 (2006) 571-577.
- [18] V. Khomenko, E. Raymundo-Piñero, F. Béguin, *Journal of Power Sources*, 177 (2008) 643-651.
- [19] Z. Chen, V. Augustyn, J. Wen, Y. Zhang, M. Shen, B. Dunn, Y. Lu, *Adv Mater*, 23 (2011) 791-795.
- [20] Y.-C. Chang, H.-J. Sohn, *Journal of The Electrochemical Society*, 147 (2000) 50-58.
- [21] Y.S. Han, J.Y. Lee, *Electrochimica Acta*, 48 (2003) 1073-1079.
- [22] J. Shu, *Electrochimica Acta*, 54 (2009) 2869-2876.
- [23] N. Zhu, W. Liu, M. Xue, Z. Xie, D. Zhao, M. Zhang, J. Chen, T. Cao, *Electrochimica Acta*, 55 (2010) 5813-5818.
- [24] R. Cai, X. Yu, X.Q. Liu, Z.P. Shao, *Journal of Power Sources*, 195 (2010) 8244-8250.
- [25] N.D. He, B.S. Wang, J.J. Huang, *Journal of Solid State Electrochemistry*, 14 (2010) 1241-1246.
- [26] X. Li, M. Qu, Z. Yu, *Solid State Ionics*, 181 (2010) 635-639.

- [27] M. Wakihara, *Materials Science & Engineering R-Reports*, 33 (2001) 109-134.
- [28] A.S. Arico, P. Bruce, B. Scrosati, J.M. Tarascon, W. van Schalkwijk, *Nat Mater*, 4 (2005) 366-377.
- [29] S.W. Lee, N. Yabuuchi, B.M. Gallant, S. Chen, B.-S. Kim, P.T. Hammond, Y. Shao-Horn, *Nat Nano*, 5 (2010) 531-537.
- [30] A.S. Prakash, P. Manikandan, K. Ramesha, M. Sathiya, J.M. Tarascon, A.K. Shukla, *Chemistry of Materials*, 22 (2010) 2857-2863.
- [31] T. Yuan, X. Yu, R. Cai, Y. Zhou, Z. Shao, *Journal of Power Sources*, 195 (2010) 4997-5004.
- [32] S.-Y. Lee, J.H. Park, P. Park, J.H. Kim, S. Ahn, K.-J. Lee, H.-D. Lee, J.-S. Park, D.-H. Kim, Y.U. Jeong, *Journal of Solid State Electrochemistry*, 14 (2009) 951-956.
- [33] J.S. Chen, X.W. Lou, *Electrochemistry Communications*, 11 (2009) 2332-2335.
- [34] K.S. Park, A. Benayad, D.J. Kang, S.G. Doo, *Journal of the American Chemical Society*, 130 (2008) 14930-+.
- [35] Y.F. Tang, L. Yang, Z. Qiu, J.S. Huang, *Electrochemistry Communications*, 10 (2008) 1513-1516.
- [36] Y. Yu, C.-H. Chen, Y. Shi, *Advanced Materials*, 19 (2007) 993-997.
- [37] A.J. Bard, L.R. Faulkner, *Electrochemical Methods : Fundamentals and Applications*, second ed., John Wiley & Sons, Inc., Austin, 2001.

- [38] Z. Fan, J. Yan, L. Zhi, Q. Zhang, T. Wei, J. Feng, M. Zhang, W. Qian, F. Wei, *Advanced Materials*, 9999 (2010) NA.
- [39] K. V. E. Frackowiak, F. Beguin, *Electrochimica Acta*, 50 (2005) 2499-2506.
- [40] G. Zhao, T. Wen, C. Chen, X. Wang, *RSC Advances*, 2 (2012) 9286-9303.
- [41] C. Li, Z. Yu, S. Fang, H. Wang, Y. Gui, J. Xu, R. Chen, *Journal of Alloys and Compounds*, 475 (2009) 718-722.
- [42] C.C. Hu, T.W. Tsou, *Electrochimica Acta*, 47 (2002) 3523-3532.
- [43] C.C. Hu, T.W. Tsou, *Electrochemistry Communications*, 4 (2002) 105-109.
- [44] V. Ganesh, S. Pitchumani, V. Lakshminarayanan, *Journal of Power Sources*, 158 (2006) 1523-1532.
- [45] Y.J. Hao, Q.Y. Lai, L. Wang, X.Y. Xu, H.Y. Chu, *Synthetic Metals*, 160 (2010) 669-674.
- [46] J.-Y. Luo, Y.-Y. Xia, *Journal of Power Sources*, 186 (2009) 224-227.
- [47] M.S. Hong, S.H. Lee, S.W. Kim, *Electrochemical and Solid State Letters*, 5 (2002) A227-A230.
- [48] T. Brousse, M. Toupin, D. Belanger, *Journal of The Electrochemical Society*, 151 (2004) A614-A622.
- [49] T. Cottineau, M. Toupin, T. Delahaye, T. Brousse, D. Belanger, *Applied Physics a-Materials Science & Processing*, 82 (2006) 599-606.
- [50] C. Xu, H. Du, B. Li, F. Kang, Y. Zeng, *Journal of The Electrochemical Society*, 156 (2009) A435-A441.

- [51] Z. Sun, K.Y. Liu, H.F. Zhang, A.S. Li, X.C. Xu, *Wuli Huaxue Xuebao/Acta Physico - Chimica Sinica*, 25 (2009) 1991-1997.
- [52] Q. Qu, P. Zhang, B. Wang, Y. Chen, S. Tian, Y. Wu, R. Holze, *The Journal of Physical Chemistry C*, 113 (2009) 14020-14027.
- [53] A. Yuan, X. Wang, Y. Wang, J. Hu, *Energy Conversion and Management*, 51 (2010) 2588-2594.
- [54] Q. Qu, L. Li, S. Tian, W. Guo, Y. Wu, R. Holze, *Journal of Power Sources*, 195 (2010) 2789-2794.
- [55] S.A. Kazaryan, S.N. Razumov, S.V. Litvinenko, G.G. Kharisov, V.I. Kogan, *Journal of The Electrochemical Society*, 153 (2006) A1655-A1671.
- [56] Q.T. Qu, Y. Shi, L.L. Li, W.L. Guo, Y.P. Wu, H.P. Zhang, S.Y. Guan, R. Holze, *Electrochemistry Communications*, 11 (2009) 1325-1328.
- [57] L.-B. Kong, M. Liu, J.-W. Lang, Y.-C. Luo, L. Kang, *Journal of The Electrochemical Society*, 156 (2009) A1000-A1004.
- [58] Y.G. Wang, L. Cheng, Y.Y. Xia, *Journal of Power Sources*, 153 (2006) 191-196.
- [59] H. Wang, Q. Gao, J. Hu, *Journal of Power Sources*, 195 (2010) 3017-3024.
- [60] Y.G. Wang, Z.D. Wang, Y.Y. Xia, *Electrochimica Acta*, 50 (2005) 5641-5646.
- [61] H. Konno, T. Kasashima, K. Azumi, *Journal of Power Sources*, 191 (2009) 623-627.
- [62] K. Naoi, S. Ishimoto, Y. Isobe, S. Aoyagi, *Journal of Power Sources*, 195 (2010) 6250-6254.

[63] R. Vasanthi, D. Kalpana, N.G. Renganathan, *Journal of Solid State Electrochemistry*, 12 (2008) 961-969.

Part III

Negative electrodes for the BatCap system

Chapter 3. Preparation and Electrochemical Performance of Hyper-networked Li₄Ti₅O₁₂/Carbon Hybrid Nanofiber Sheets for a Negative Electrode of the BatCap System

3.1. Introduction

As the demand for electric vehicles (EVs) and hybrid EVs (HEVs) increases due to their lower environmental impact, high-performance energy storage devices become extremely important [1-5]. However, neither LIBs nor supercapacitors, which are currently considered as the best electrochemical energy storage devices, can meet the needs of practical applications [6-9]. One approach that could potentially resolve these shortcomings is to develop a new energy device based on a hybridization of the concept of a LIB that can generate high energy density and a supercapacitor that has high power density. In fact, there have already been a few works to create such a hybrid energy storage devices by combining the electrode system of one type of energy storage device with that of the other type of energy storage device, viz. by adopting one kind for the negative electrode and the other kind for the positive electrode among various kinds of electrodes [10-20]. In recent years, intensive efforts have been devoted to hybridizing a faradaical battery-type electrode and a non-faradaical rechargeable capacitor-type electrode, which is usually called ‘hybrid capacitor’

or ‘asymmetric capacitor’ [10, 11, 13, 17]. Especially, so-called non-aqueous asymmetric capacitors, which have battery-type negative electrode utilizing a Li-ion intercalation and a capacitor-type positive electrode showing an electrical double layer capacitance (EDLC) in an organic solvent as an electrolyte have been reported to exhibit high-performance energy storage [12, 13, 16, 17]. In the case of the negative electrode for this energy storage system, fast charge/discharge capability with long term cycle stability in the Li-ion intercalation process is one of the most important properties to balance with the positive electrode, which has good cycle stability along with high charge/discharge rate capability [15]. Carbonaceous materials that have been widely used as negative electrodes in LIBs can be used as the negative electrode in the asymmetric capacitor because of their high energy density and good cycle stability [14, 18-20]. However, it is difficult to maintain the capacitance in high charge/discharge rate conditions, because of poor Li-ion transfer kinetics from the lithiation mechanism in the carbonaceous materials. On the other hand, $\text{Li}_4\text{Ti}_5\text{O}_{12}$ - and TiO_2 -based materials have been reported to be good candidate materials for the negative electrode because of their fast charge/discharge capability without volume expansion, resulting in high cycle stability [6, 7, 15, 21-23]. Improving the low electronic conductivity ($10^{-12} \text{ S cm}^{-1}$) and increasing the specific capacity of Li-ions in the $\text{Li}_4\text{Ti}_5\text{O}_{12}$ - and TiO_2 -based materials may provide a breakthrough in the area of negative electrodes for use in hybrid energy storage devices. One effective approach to overcoming this disadvantage is to hybridize $\text{Li}_4\text{Ti}_5\text{O}_{12}$ - and TiO_2 -based materials with a highly

conductive material, as is used in metal doping or carbon coating strategies [24-31]. Additionally, control over the morphology has been widely studied as a means for enhancing the low electronic conductivity of these materials [32-36]. 1D nanostructures provide a morphology that enhances the electronic kinetics due to the higher probability of contact [34]. Several 1D nanostructured materials have been considered as promising candidates for use in high-power energy storage devices.

Having considered the abovementioned situation, we aimed herein at developing a high-performance negative electrode for the BatCap, whereby a hybrid nanofiber web composed of $\text{Li}_4\text{Ti}_5\text{O}_{12}$ /N-enriched carbon (denoted LTO/C-HNS) and an activated carbon are used for the negative and positive electrodes, respectively. Compared to other battery-type faradaic electrodes of the conventional asymmetric capacitors, the newly prepared LTO/C-HNS hybrid composite electrode itself contains both faradaically rechargeable battery-type component viz. $\text{Li}_4\text{Ti}_5\text{O}_{12}$ and non-faradaically rechargeable capacitor-type component viz. N-enriched carbon. It is therefore a good advantage of this new hybrid composite electrode to store more charges than the conventional single component electrode. The new term, BatCap, was adopted herein to discern the presently suggested hybrid energy storage system from earlier hybrid and/or asymmetric ones. A combination of morphology-controlled 1-D structure and hybridization with carbon enhanced the electron-transport kinetics by a continuous conductive electron pathway. Further, the N-enriched carbons in the hyper-networked LTO/C-HNS, which were prepared

using vapor polymerization of polypyrrole followed by carbonization, contributed to increasing the energy density via additional EDLC to the electrochemical capacitance of $\text{Li}_4\text{Ti}_5\text{O}_{12}$.

3.2. Experimental

3.2.1. Reagents and chemicals

Lithium hydroxide (Aldrich, 98%), titanium(IV) bis(ammonium-lactato)dihydroxide solution (Aldrich, 50 wt% in H₂O), ammonium persulfate (Aldrich, 98%), polyvinylpyrrolidone (PVP) (Aldrich, Mw = 1300 k), acetic acid (Daejung Chemical Co.), and pyrrole monomer (Aldrich, 98%) were used without further purification.

3.2.2. Synthesis of LTO/C-HNS

As shown in Figure 3.1, hyper-networked Li₄Ti₅O₁₂/carbon hybrid nanofiber sheets were synthesized using electrospinning and vapor polymerization techniques followed by heat treatment. Typically, 3 g of aqueous precursors for Li₄Ti₅O₁₂ containing lithium hydroxide and titanium(IV) bis(ammonium-lactato)dihydroxide solution with Li:Ti = 4:5 by moles and 1 g of ammonium persulfate as oxidant for vapor polymerization of polypyrrole (PPy) were blended with 5 ml of 20 wt% polyvinylpyrrolidone (PVP) aqueous solution with 0.5 ml of acetic acid for electrospinning. This solution was electrospun on aluminum foil as the electrode with 25 kV of voltage bias, with a distance of 25 cm between the metal needle and the electrode. After transferring the electrospun hyper-networked nanofiber sheets (denoted HNS) to a beaker, pyrrole monomer (without any type of purification) as the carbon precursor was polymerized on the surface of the electrospun nanofiber sheets via a vapor

polymerization technique for 30 min. Then, the PPy-coated nanofiber sheet (PPy-HNS) was heat treated to make LTO/C-HNS in a tube furnace at 800 °C (denoted as LTO/C-HNS for 6 h after preheat treatment at 400 °C for 1 h under a N₂ atmosphere).

3.2.3. Characterization of LTO/C-HNS

Various techniques were used to characterize the synthesized LTO/C-HNS. Microstructural and morphology analyses were performed using X-ray diffractometry (XRD) (D8 Advance, Bruker) with standard procedures [37, 38], Raman spectroscopy (HORIABA Jobin Yvon, T64000) with a He–Ne laser ($\lambda = 632.8$ nm), field emission scanning electron microscopy (FE-SEM) (JSM-6700F, JEOL), and high resolution transmission electron microscopy (HR-TEM) (F20, Tecnai) operating at 200 kV. A four-point probe conductivity meter (CMT-1000N, AIT) was used to measure the electronic conductivity, and thermogravimetric analysis (TGA) (SDT Q600, TA) was used to determine the proportion of carbon material in the prepared sample. Also, Micromeritics ASAP 2020 static volumetric gas adsorption instrument was used to measure the nitrogen adsorption isotherms of the prepared sample at liquid nitrogen temperature (77 K) using ultrahigh purity grade (99.999 %) gas.

3.2.4. Electrochemical tests of LTO/C-HNS

The electrochemical performance of the LTO/C-HNS was tested on a battery cyclers (WBCS3000, WonATech) in a glove box filled with Ar gas (Korea

Kiyon). The electrodes of each synthesized sample, which were used as the working electrodes in the half-cell performance test and as the negative electrodes in the electrochemical performance test, were prepared with 80 wt% of active materials, 10 wt% of carbon black as conductive material, and 10 wt% of polyvinylidene (PVDF) as binder. To evaluate the half-cell performances of each sample, the 2032 coin-type half cells were assembled in a glove box with a lithium-metal reference electrode, Celgard 2320 microporous membrane, and working electrodes with 1 M LiPF₆ in a mixture of ethylene carbonate (EC)/diethyl carbonate (DEC) (1:1 by volume ratio, Cheil Industry Inc.) as electrolyte. The half-cell performances of the LTO/C-HNS series for LIBs were carried out with various charge/discharge rates in the potential range from 0 to 2.5 V vs. Li/Li⁺ using the constant-current mode. On the other hand, the negative electrode performance of LTO/C-HNS for the hybrid BatCap system was tested with a two-electrode system using commercial activated carbon (AC) (SX Ultra, Norit) as the positive electrode, the as-prepared negative electrode, and the same electrolyte as was used in the half-cell performance test. The positive electrodes based on the AC were prepared with 90 wt% of active materials and 10 wt% of PVDF as binder. The electrochemical characteristics of the negative electrode in the hybrid BatCap system were determined by CV and the galvanostatic charge/discharge test. Also, an AC//AC symmetric capacitor was assembled using the same fabrication process as for the hybrid BatCap system to compare the electrochemical performance with the LTO/C-HNS//AC hybrid BatCap system.

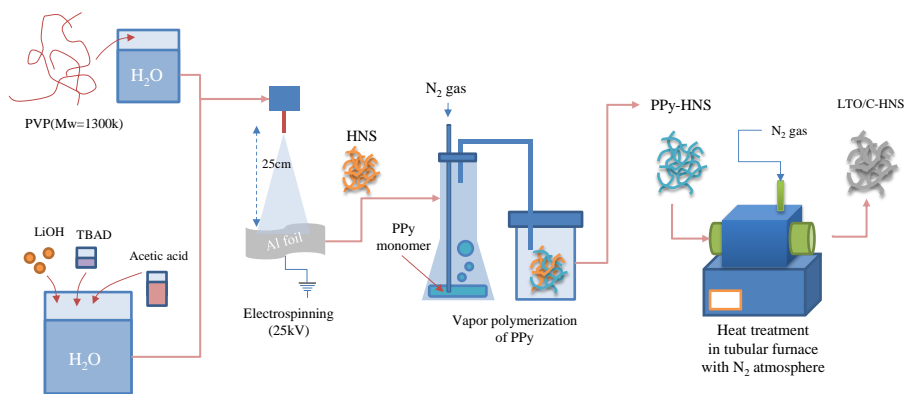


Figure 3.1. Schematic illustration for synthesis of PPy-HNS via electrospinning and vapor polymerization techniques.

3.3. Results and discussion

3.3.1. Morphological, microstructural, and surface characteristics of the LTO/C-HNS series

Figure 3.2 shows typical FE-SEM micrographs of electrospun HNS, pyrrole vapor polymerized PPy-HNS, and LTO/C-HNS after heat treatment of PPy-HNS. As can be seen in Figure 3.2A, the electrospun fibers were about 200 nm in diameter with a smooth surface and longitudinally continuous morphology. After vapor polymerization of PPy, the diameter of the PPy-HNS was slightly increased by about 10–20 nm because of polymerized PPy on the surface of the electrospun HNS, while the smooth surface and continuous morphology were maintained.

According to Figure 3.2C, the diameters of the LTO/C-HNS are about 200–250 nm with well-developed and largely maintained 1-D fibrillar structure after heat treatment compared with PPy-HNS in Figure 3.2B. In particular, hyper-networked structure of LTO/C-HNS can improve the charge transfer kinetics for the high rate of charge/discharge process because of the continuous electron pathway.

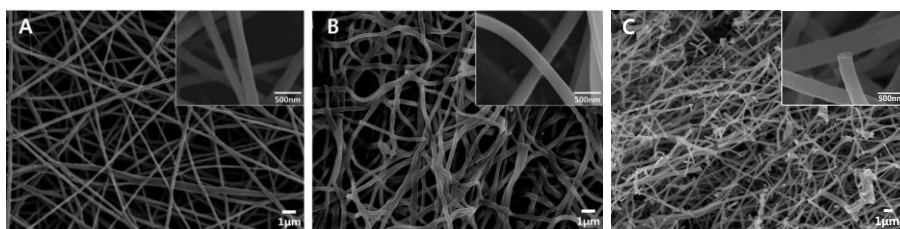


Figure 3.2. (A) FE-SEM micrographs of electrospun HNS. (B) pyrrole vapor polymerized PPy-HNS. (C) LTO/C-HNS after heat treatment of PPy-HNS. The insets show a magnified image of each sample.

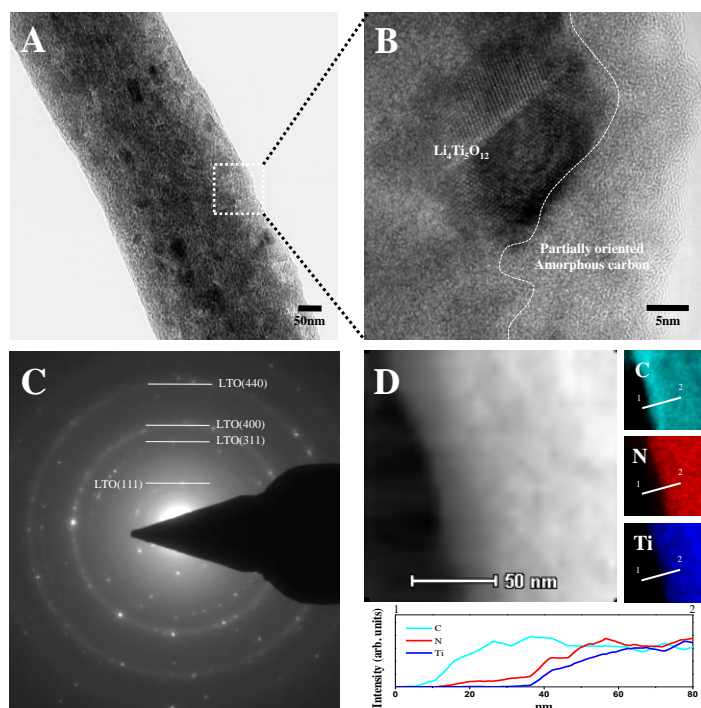


Figure 3.3. (A) HR-TEM micrograph of LTO/C-HNS, (B) a magnified image of the surface region, and (C) SAED pattern of (B). (D) Typical STEM and EDS images of the LTO/C-HNS surface. The inset graphs of (D) indicate the positions of the line scanning profiles from the EDS images for each atom.

Figure 3.3 shows HR-TEM images of LTO/C-HNS with selected-area electron diffraction (SAED) pattern, scanning transmission electron microscopy (STEM), and energy dispersive spectroscopy (EDS) images of the surface region. The low-magnification TEM image in Figure 3.3A shows the morphology of the well-developed 1-D fibrillar structure formed by polycrystalline $\text{Li}_4\text{Ti}_5\text{O}_{12}$ in the N-enriched carbon matrix. Indeed, small intensity differences between the central region and the surface region in the low-magnification TEM image indicate the development of a partial LTO/C core-shell structure, i.e., a meso core-shell structure. The meso core-shell structures, developed by vapor polymerization of PPy followed by heat treatment, are readily seen in the high-magnification image in Figure 3.3B and in the STEM image in Figure 3.3D. Moreover, the intensity line profiles from the EDS results for the LTO/C-HNS samples indicate that the N-enriched carbon layers from the PPy layer coated on the electrospun nanofibers were retained after heat treatment, with a thickness of 35 nm.

The SAED pattern of the sample, shown in Figure 3.3C, displays five circles that are characteristics of a polycrystalline material, as shown in Figure 3.3A, as well as some point-like spots. These five circles correspond to the reflections of the (111), (311), (400), and (440) lattice planes with interlayer d-spacing of 18.528, 35.578, 43.673, and 63.959 nm, respectively. This result agreed well with the formation of $\text{Li}_4\text{Ti}_5\text{O}_{12}$ after heat treatment, which corresponded to the XRD pattern of the sample. Figure 3.4 also indicates that the LTO/C-HNS

sample is composed mainly of $\text{Li}_4\text{Ti}_5\text{O}_{12}$ phase with trace amount of rutile TiO_2 impurity.

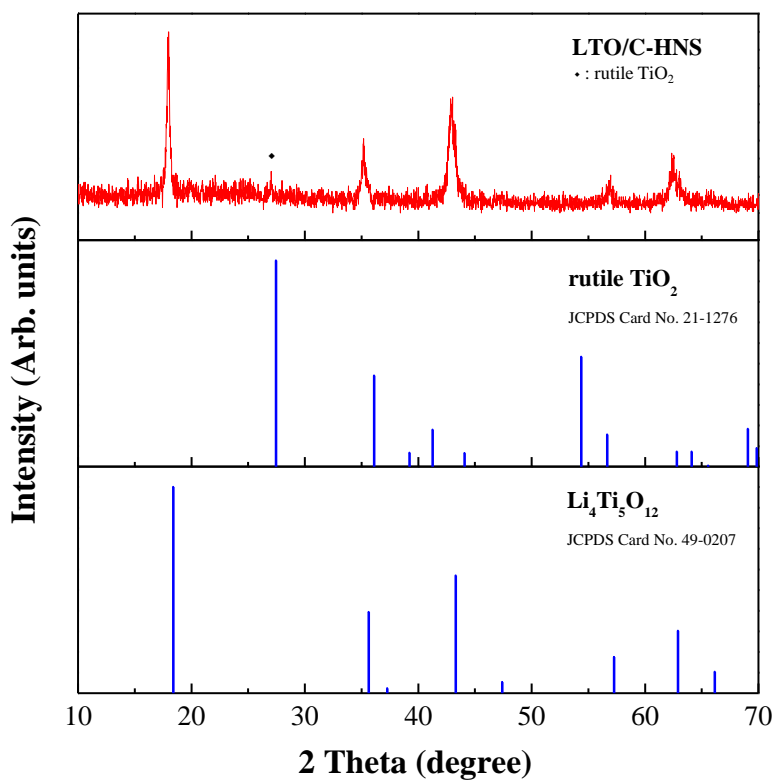


Figure 3.4. X-ray diffractogram of LTO/C-HNS (top) together with JCPDF data for rutile (middle; Card No. 21-1276), and typical Li₄Ti₅O₁₂ (bottom; Card No. 49-0207). Diamond symbol indicates the presence of trace amount of rutile TiO₂ impurity.

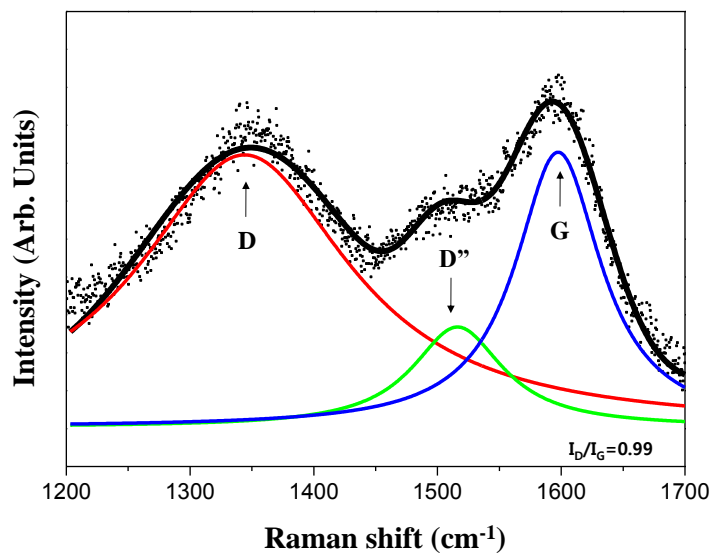


Figure 3.5. Raman spectra of LTO/C-HNS. The solid lines are the superposition of the D, D'' , and G bands, shown in red, green, and blue, respectively, fitted by a Lorentzian fitting procedure

Table 3.1. D, D'' , and G peak parameters, and R of the Raman spectra for LTO/C-HNS

LTO/C-HNS1000			
	D	D''	G
Wave number (cm ⁻¹)	1344	1516	1597
Band width (cm ⁻¹)	206	89	84
$R = I_D/I_G$	0.99		

Figure 3.5 shows Raman spectra result of the LTO/C-HNS in the Raman shift range from 1200 to 1700 cm^{-1} , which indicate the crystalline perfection of the carbonaceous materials. The best fitted curves were obtained using a Lorentzian fitting procedure with three superposed band at around 1360 cm^{-1} , 1520 cm^{-1} , and 1590 cm^{-1} , which are the D band from less ordered carbons, the D' band from amorphous sp^2 -bonded carbons or reactive intermediate carbons, and the G band from highly ordered carbons [39, 40]. The fitting results of Figure 3.5 are summarized in Table 3.1. Similar to the results of previous work for PPy-based carbon materials [39-43], there are fewer differences in the peak positions of each peak compared with other carbonaceous materials [44-50]. The relative intensity of the D peak to the G peak, denoted as $R = I_D/I_G$, is about 0.99, which is higher than 0.86 of the R -value of graphite. The R -value varies with the degree of graphitization and alignment of the graphitic planes; specifically, a lower R -value indicates a higher amount of sp^2 -bonding carbon atoms on the surface of the sample. Therefore, the higher R -value represents the less developed graphitic carbon structure viz. disordered carbon on the LTO/C-HNS surface [40]. Because of the high electronic conductivity of graphitic carbon, about 10^2 S cm^{-1} [44], it is possible to assume that sample with the high R -value have the low electronic conductivity. The electronic conductivity of the LTO/C-HNS measured using four-point probe conductivity meter is $6.61 \times 10^{-5} \text{ S cm}^{-1}$, which indicates that most of carbon phase on the surface of the LTO/C-HNS is amorphous structure. This is a good

correspondence with powder XRD pattern that there is no peak appearance around at $2\theta = 25^\circ$ from (002) plane of the graphitic carbon.

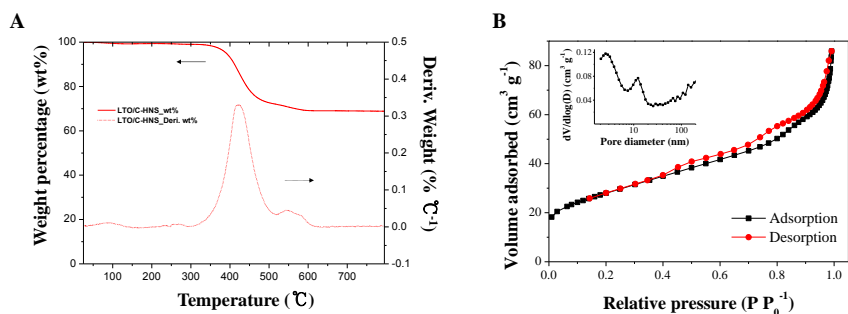


Figure 3.6. (A) Thermogravimetric analysis (TGA) of the LTO/C-HNS. Solid line: thermogravimetric curve, dotted line: differential thermogravimetric curve. (B) Nitrogen adsorption/desorption isotherms at 77 K of the LTO/C-HNS (Inset : Pore size distribution of the product, analyzed using the BJH equation.)

Table 3.2. Pore characteristics determined from the nitrogen adsorption isotherm at 77 K of the LTO/C-HNS.

Sample	BET SSA ^a (m ² g ⁻¹)	Langmuir SSA ^b (m ² g ⁻¹)	Average pore diameter (nm)	Total pore volume at 0.98 of relative pressure (cm ³ g ⁻¹)
LTO/C-HNS	99.69	136.95	6.39	0.12

^a SSA, specific surface area, determined by the BET equation.

^b Determined by the Langmuir equation

The carbonaceous material proportion in the sample is about 32 wt%, which value was estimated from thermogravimetric analysis under air up to 800 °C in Figure 3.6A. Also, table 3.2 which summarizes the result of the nitrogen adsorption/desorption isotherms analysis for the LTO/C-HNS indicates that the sample has relatively high BET surface area of approximately 100 m² g⁻¹ and most of pores are mesopores in range of 2-20 nm, which arise from N-enriched carbon component contributing on the capacitive storage. These results show that not only morphology control of the hyper-networked structure with conductive element, which can establish a continuous electron pathway, but also LTO/C hybridization, which can improve the storable charge from lithiation/delithiation of Li₄Ti₅O₁₂ and EDLC of the carbon, helps to improve the power density and energy density, simultaneously.

3.3.2. Electrochemical performance of the LTO/C-HNS series

The electrochemical performance of LTO/C-HNS over the range 0–2.5 V vs. Li/Li⁺, as a negative electrode in LIBs, is shown in Figure 3.7. The potential profile of the sample during the 20th cycle with a 100 mA g⁻¹ charge/discharge rate is shown in the inset image. The reversible specific capacities of the sample at the various charge/discharge rates were 255, 202, 177, 152, and 122 mAh g⁻¹ at 100, 500, 1000, 2000, and 4000 mA g⁻¹, respectively.

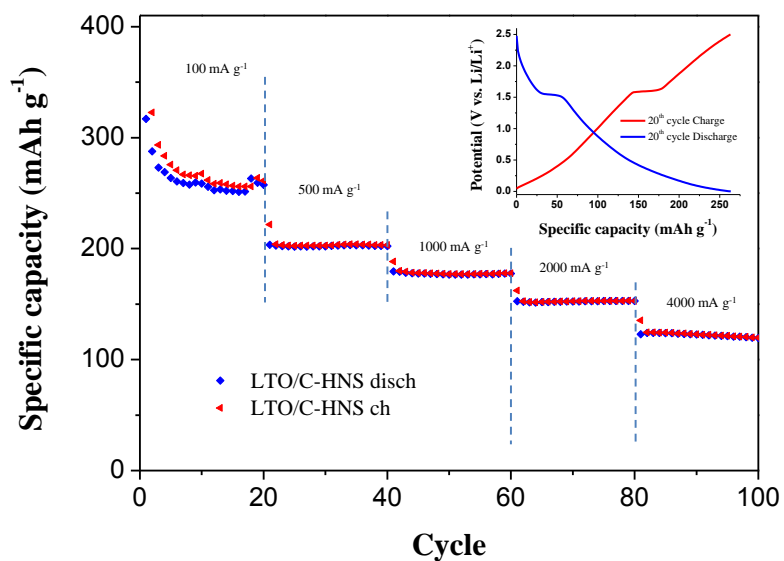


Figure 3.7. Cycle performances of the LTO/C-HNS at various charge/discharge rates. The inset shows the potential profiles at a charge/discharge rate of 100 mA g⁻¹.

At a low charge/discharge rate of 100 mA g^{-1} , LTO/C-HNS yielded a Coulombic efficiency that was low compared with that obtained at higher charge/discharge rates due to the irreversible specific capacity of the amorphous phase carbonaceous materials in the LTO/C-HNS during the lithiation process [51]. According to the potential profile during the 20th cycle at 100 mA g^{-1} , shown in the inset in Figure 3.7, the sample clearly displayed a charge/discharge curve with a small slope due to the presence of a partially oriented amorphous carbon phase formed from the carbonized PPy. A plateau at $1.5 \text{ V vs. Li/Li}^+$ in the middle of the charge/discharge curve corresponded to the charge/discharge process of $\text{Li}_4\text{Ti}_5\text{O}_{12}$ in the LTO/C-HNS.

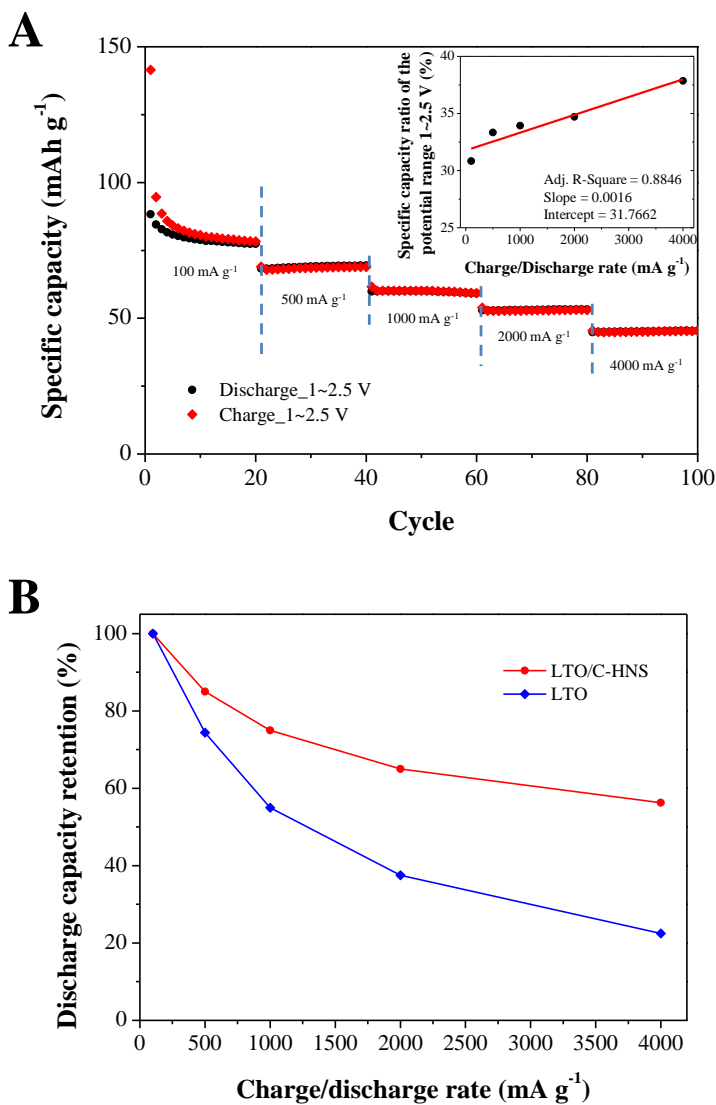


Figure 3.8. (A) Cycle performances of LTO/C-HNS in the range of 1–2.5 V vs. Li/Li⁺ (Inset : specific capacity ratio over the potential range 1–2.5 V vs. Li/Li⁺ at various charge/discharge rates.) and (B) discharge capacity retention at each charge/discharge rate for LTO/C-HNS and commercial LTO (supported from Umicore Korea).

Figure 3.8A represents the cycle performances of LTO/C-HNS over the range 1–2.5 V, which compare the specific capacity at various charge/discharge rates to estimate the capacity ratio of the $\text{Li}_4\text{Ti}_5\text{O}_{12}$ phase in the LTO/C-HNS composite. Reversible specific capacities at each charge/discharge rate are 80, 68, 60, 52, and 45 mAh g^{-1} at 100, 500, 1000, 2000, and 4000 mA g^{-1} , respectively. The values of the specific capacity ratio in the potential range 1–2.5 V were estimated using the results of Figures 3.8A and 3.7. In particular, the $\text{Li}_4\text{Ti}_5\text{O}_{12}$ phase displayed a charge/discharge reaction around 1.55 V vs. Li/Li^+ [52]. Therefore, it was reasonable to estimate the capacity due to the $\text{Li}_4\text{Ti}_5\text{O}_{12}$ phase in the sample using the specific capacity measured over the range 1–2.5 V. The specific capacity ratio over the potential range 1–2.5 V, which can be calculated using $\text{Capacity}_{1-2.5\text{V}}/\text{Capacity}_{0-2.5\text{V}}$, shows a linear dependence on the charge/discharge rate in the inset of Figure 3.8A. Further, Figure 3.8B shows that LTO/C-HNS has better discharge capacity retention ratio than commercial LTO, particularly with increasing charge/discharge rate. Therefore, the $\text{Li}_4\text{Ti}_5\text{O}_{12}$ phase in the LTO/C-HNS maintained a higher rate capability and a better electrochemical performance compared with typical $\text{Li}_4\text{Ti}_5\text{O}_{12}$ due to the presence of the carbonaceous phase on the surface of the sample.

As the charge/discharge rate increased beyond the low rate regime, LTO/C-HNS yielded an excellent capacity retention compared with that of typical $\text{Li}_4\text{Ti}_5\text{O}_{12}$, with over 95% retention after 20 cycles. However, the specific capacity tended to decrease as the charge/discharge rate increased. The capacity

ratio of the $\text{Li}_4\text{Ti}_5\text{O}_{12}$ phase in the LTO/C-HNS composite depended linearly on the charge/discharge rate, as shown in Figure 3.8, which indicated that the electrochemical performance of the $\text{Li}_4\text{Ti}_5\text{O}_{12}$ phase in LTO/C-HNS was better than that of the pure- $\text{Li}_4\text{Ti}_5\text{O}_{12}$ sample at high charge/discharge rates. In principle, particularly at high charge/discharge rates, the electron transport kinetics determines the extent of the charge transfer reaction that achieves energy storage in a lithium ion battery [53, 54]. Accordingly, the presence of an amorphous carbon phase coated on the surface of the $\text{Li}_4\text{Ti}_5\text{O}_{12}$ phase nanosheet enhanced the electron transport kinetics with additional capacity at high charge/discharge rates simultaneously, which corresponded well with the higher electronic conductivity of the LTO/C-HNS compared with that of typical $\text{Li}_4\text{Ti}_5\text{O}_{12}$, as determined using a four-point probe conductivity meter.

The half-cell performance results suggested that the $\text{Li}_4\text{Ti}_5\text{O}_{12}$ /carbon hybridized material with a hyper-networked structure enhanced the capabilities at high charge/discharge rates. The LTO/C-HNS material may be used as a negative electrode in hybrid BatCap systems because of their novel electrochemical performances at high charge/discharge rates.

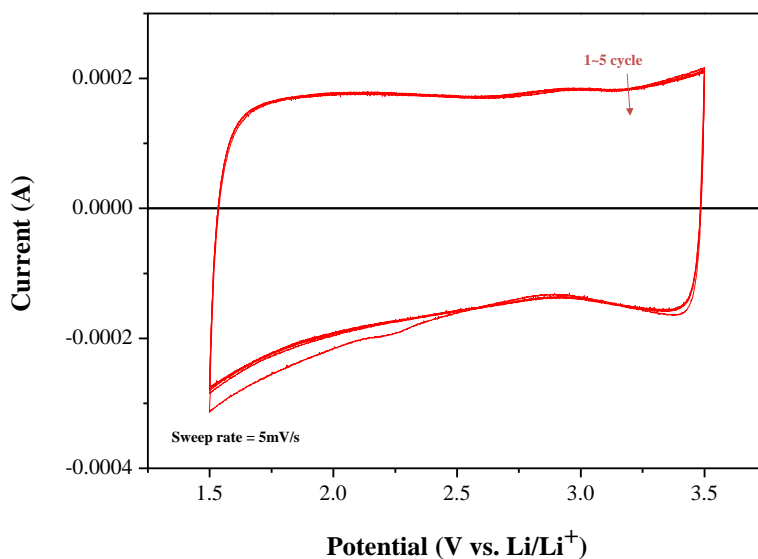


Figure 3.9. The CV of AC at a 5 mV s^{-1} sweep rate.

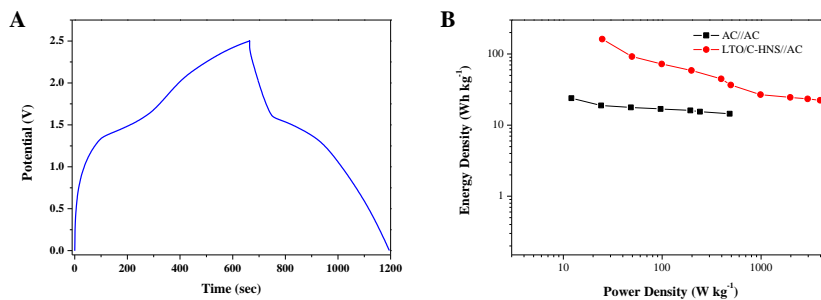


Figure 3.10. Galvanostatic charge/discharge graph of the LTO/C-HNS//AC hybrid BatCap system at C/3 rate (A) and the Ragone plot of the LTO/C-HNS//AC hybrid BatCap system and AC//AC symmetric capacitor at various charge/discharge rates in the working potential range 0–2.5 V (B).

The cyclic voltammogram (CV) of activated carbon (denoted as AC) with the Li salt-based organic electrolyte (1 M LiPF₆ in EC/DEC) was investigated at a sweep rate of 5 mV s⁻¹ using AC as the positive electrode in the hybrid BatCap system (Figure 3.9). A solid electrolyte interface (SEI) layer formed at low applied potentials, which closed the open pores on the surface of the AC, limiting the approach of Li-ions in the electrolyte. The electrolyte decomposed at high applied potentials, which caused irreversible specific capacity loss [18]. Therefore, the CV test was investigated in the range 1.5–3.5 V vs. Li/Li⁺ to prevent the above-mentioned side reactions. The resulting curve yielded a typical rectangular shape related to that of the common AC from electrical double layer capacitance (denoted as EDLC) by a rotational mirror symmetry operation. The calculated capacitance of the AC from the CV result was 71 F g⁻¹, which provided a specific capacity of 39.1 mAh g⁻¹ at a working potential of 1.5–3.5 V vs. Li/Li⁺.

On the other hand, a full cell test as the hybrid BatCap system using LTO/C-HNS as the negative electrode and AC as the positive electrode was associated with various charge/discharge rates in the range of 1.5–3.5 V. From the specific capacity information in Figure 3.9, the mass of each electrode was controlled as $m_{\text{positive}}/m_{\text{negative}} = 4$, because the high energy density of the hybrid energy storage device can be generated through the balance of exchanged charge between positive and negative electrodes [15, 18, 23]. Figure 3.10A shows the galvanostatic charge/discharge graph of the LTO/C-HNS//AC hybrid BatCap system at C/3 rate in the cell potential range 0–2.5 V. In the early state of the

charge/discharge process, the charge/discharge curve of the negative electrode indicates a linear slope-shaped tendency because of the EDLC of the carbon species in the LTO/C-HNS sample. Then, around 1.5 V vs. Li/Li⁺, there is a plateau region on the charge/discharge curve of the negative electrode from the Li⁺ ion lithiation/delithiation reaction in the Li₄Ti₅O₁₂ species. This result suggests that hybridization of carbon with Li₄Ti₅O₁₂ can enhance the energy density compared with a single Li₄Ti₅O₁₂ as the negative electrode in the BatCap system because of the additional EDLC from the carbon species.

The Ragone plots in Figure 3.10B summarize the electrochemical performance of the LTO/C-HNS//AC hybrid BatCap system and AC//AC symmetric capacitor at various charge/discharge rates in the working potential range 0–2.5 V. Since the LTO/C-HNS//AC BatCap system is operating based on a combined energy storage mechanism for a battery and an EDLC, as indeed supported by the combined profile of charge/discharge of a battery and an EDLC as shown in Figure 3.10B, it is not easy to estimate the electrochemical performance of this BatCap system using conventional equations for the batteries or supercapacitors. In a typical battery system, the potential of electrochemical redox reaction remains at a fixed value during charge/discharge process. The energy density can therefore be estimated by the product of the state of charge, Q, and the working potential, V, per mass of active material. On the other hand, the energy density of a typical EDLC based supercapacitor can be calculated by the equation of (1/2)QV, because the state of charge is proportional to the working potential [55]. Therefore, the energy densities of the hybrid BatCap

system can be estimated by integrating the area of Q-V graph in discharge process followed by the unit conversion to Wh kg⁻¹ [46]. In the case of the power density (PD), the maximum power density can be calculated by the equation, $PD_{\max}=V_{\max}I$, in which V_{\max} is max working potential and charge/discharge current, I. However, the maximum power density calculated from this simple equation tends to over-estimate the actually available power of the concerned energy storage device. So, we considered the energy efficiency, i.e. the fraction of the net energy transferred from a device to the surrounding except for the energy loss by heat generation. The maximum power density can then be estimated from the equation of $PD_{\max}=V_{\max}^2/4R=V_{\max}I/2$ [18, 56].

At 50 W kg⁻¹ of low power density, the energy density is 91 Wh kg⁻¹ and 17 Wh kg⁻¹ for the LTO/C-HNS//AC hybrid BatCap system and AC//AC symmetric electrode system, respectively. At a high charge/discharge rate, for example about 4000 W kg⁻¹ of power density, the energy density of the hybrid BatCap system is maintained at 22 Wh kg⁻¹, which is much higher value compared with 14 Wh kg⁻¹ at 500 W kg⁻¹ for the symmetric electrode system. In addition, on a comparison with literature value of approximately 10 Wh kg⁻¹ at 1000 W kg⁻¹ for a typical hybrid capacitor [57] which consists of Li₄Ti₅O₁₂ as a negative electrode and carbon as a positive electrode, these results indicate that there is a synergistic effects between Li₄Ti₅O₁₂ and N-enriched carbon components.

3.4. Conclusions

LTO/C-HNS hybrid materials were successfully synthesized via electrospinning and vapor polymerization of PPy followed by heat treatment at various temperatures to produce a new type of hybrid energy storage device, the hybrid BatCap system. Half-cell performance test results using the LTO/C-HNS series yielded an enhanced specific capacity and a high charge/discharge rate capability due to improved electronic conductivity, especially in the case of LTO/C-HNS. The hybrid BatCap system was fabricated with AC as positive electrode and LTO/C-HNS as negative electrode including a battery-type component (LTO) and a capacitor-type component (Carbon), simultaneously. The hybrid BatCap system showed energy densities that ranged from 91 Wh kg⁻¹ to 17 Wh kg⁻¹ over a power density range of 50–4000 W kg⁻¹. This performance range was comparable to that achieved by the fast charge/discharge LIBs and high-energy storage supercapacitors. These findings indicate that the hybrid BatCap system may provide clues to producing energy storage systems [52] with superior performance for electrical vehicles.

3.5. References

- [1] A.S. Arico, P. Bruce, B. Scrosati, J.M. Tarascon, W. Van Schalkwijk, *Nat Mater*, 4 (2005) 366-377.
- [2] J.M. Tarascon, M. Armand, *Nature*, 414 (2001) 359-367.
- [3] H. Li, Z. Wang, L. Chen, X. Huang, *Advanced Materials*, 21 (2009) 4593-4607.
- [4] J.B. Goodenough, Y. Kim, *Chemistry of Materials*, 22 (2009) 587-603.
- [5] H.G. Cho, Y.J. Kim, Y.-E. Sung, C.R. Park, *Electrochim Acta*, 53 (2007) 944-950.
- [6] A.D. Pasquier, I. Plitz, J. Gural, S. Menocal, G. Amatucci, *Journal of Power Sources*, 113 (2003) 62-71.
- [7] A.D. Pasquier, I. Plitz, J. Gural, S. Menocal, G. Amatucci, *Journal of Power Sources*, 136 (2004) 160-170.
- [8] V.L. Pushparaj, M.M. Shaijumon, A. Kumar, S. Murugesan, L. Ci, R. Vajtai, R.J. Linhardt, O. Nalamasu, P.M. Ajayan, *Proceedings of the National Academy of Sciences*, 104 (2007) 13574-13577.
- [9] H.S. Choi, J.G. Lee, H.Y. Lee, S.W. Kim, C.R. Park, *Electrochim Acta*, 56 (2010) 790-796.
- [10] G.G. Amatucci, F. Badway, A.D. Pasquier, T. Zheng, *Journal of The Electrochemical Society*, 148 (2001) A930-A939.
- [11] A.D. Pasquier, I. Plitz, S. Menocal, G. Amatucci, *Journal of Power Sources*, 115 (2003) 171-178.
- [12] W.G. Pell, B.E. Conway, *Journal of Power Sources*, 136 (2004) 334-345.

- [13] S. Nohara, A.A. Toshihide, H. Wada, N. Furukawa, H. Inoue, N. Sugoh, H. Iwasaki, C. Iwakura, *Journal of Power Sources*, 157 (2006) 605-609.
- [14] G.X. Wang, B.L. Zhang, Z.L. Yu, M.Z. Qu, *Solid State Ionics*, 176 (2005) 1169-1174.
- [15] T. Brousse, R. Marchand, P.L. Taberna, P. Simon, *J Power Sources*, 158 (2006) 571-577.
- [16] H.Q. Li, Y. Zou, Y.Y. Xia, *Electrochim Acta*, 52 (2007) 2153-2157.
- [17] M. Mastragostino, F. Soavi, *Journal of Power Sources*, 174 (2007) 89-93.
- [18] V. Khomenko, E. Raymundo-Piñero, F. Béguin, *J Power Sources*, 177 (2008) 643-651.
- [19] Y.Y. Liang, H.L. Li, X.G. Zhang, *Mat Sci Eng a-Struct*, 473 (2008) 317-322.
- [20] R. Vasanthi, D. Kalpana, N.G. Renganathan, *J Solid State Electr*, 12 (2008) 961-969.
- [21] X. Hu, Z. Deng, J. Suo, Z. Pan, *Journal of Power Sources*, 187 (2009) 635-639.
- [22] S.W. Lee, N. Yabuuchi, B.M. Gallant, S. Chen, B.S. Kim, P.T. Hammond, Y. Shao-Horn, *Nat Nanotechnol*, 5 (2010) 531-537.
- [23] K. Naoi, S. Ishimoto, Y. Isobe, S. Aoyagi, *Journal of Power Sources*, 195 (2010) 6250-6254.
- [24] S.H. Huang, Z.Y. Wen, X.J. Zhu, Z.H. Gu, *Electrochemistry Communications*, 6 (2004) 1093-1097.
- [25] Y.J. Hao, Q.Y. Lai, J.Z. Lu, X.Y. Ji, *Ionics*, 13 (2007) 369-373.

- [26] L. Cheng, X.L. Li, H.J. Liu, H.M. Xiong, P.W. Zhang, Y.Y. Xia, *Journal of the Electrochemical Society*, 154 (2007) A692-A697.
- [27] P. Kubiak, A. Garcia, M. Womes, L. Aldon, J. Olivier-Fourcade, P.E. Lippens, J.C. Jumas, *Journal of Power Sources*, 119 (2003) 626-630.
- [28] J. Shu, *Electrochim Acta*, 54 (2009) 2869-2876.
- [29] N. Zhu, W. Liu, M. Xue, Z. Xie, D. Zhao, M. Zhang, J. Chen, T. Cao, *Electrochim Acta*, 55 (2010) 5813-5818.
- [30] N. He, B. Wang, J. Huang, *J Solid State Electr*, 14 (2010) 1241-1246.
- [31] X. Li, M. Qu, Z. Yu, *Solid State Ionics*, 181 (2010) 635-639.
- [32] Y.F. Tang, L. Yang, Z. Qiu, J.S. Huang, *Electrochemistry Communications*, 10 (2008) 1513-1516.
- [33] Y. Tang, L. Yang, S. Fang, Z. Qiu, *Electrochim Acta*, 54 (2009) 6244-6249.
- [34] S.C. Lee, S.M. Lee, J.W. Lee, J.B. Lee, S.M. Lee, S.S. Han, H.C. Lee, H.J. Kim, *The Journal of Physical Chemistry C*, 113 (2009) 18420-18423.
- [35] J.Z. Chen, L. Yang, S.H. Fang, Y.F. Tang, *Electrochim Acta*, 55 (2010) 6596-6600.
- [36] J. Li, Z. Tang, Z. Zhang, *Electrochemistry Communications*, 7 (2005) 894-899.
- [37] S.H. Gihm, C.R. Park, *Carbon*, 44 (2006) 1016-1019.
- [38] N. Iwashita, C.R. Park, H. Fujimoto, M. Shiraishi, M. Inagaki, *Carbon*, 42 (2004) 701-714.
- [39] L. Zou, R. Lv, F. Kang, L. Gan, W. Shen, *J Power Sources*, 184 (2008) 566-569.

- [40] T. Vergunst, F. Kapteijn, J.A. Moulijn, *Carbon*, 40 (2002) 1891-1902.
- [41] C.-C. Han, J.-T. Lee, R.-W. Yang, H. Chang, C.-H. Han, *Chemistry of Materials*, 11 (1999) 1806-1813.
- [42] A.B. Fuertes, T.A. Centeno, *Journal of Materials Chemistry*, 15 (2005) 1079-1083.
- [43] P.F. Fulvio, M. Jaroniec, C. Liang, S. Dai, *The Journal of Physical Chemistry C*, 112 (2008) 13126-13133.
- [44] F. Tuinstra, J.L. Koenig, *The Journal of Chemical Physics*, 53 (1970) 1126-1130.
- [45] J. Robertson, *Advances in Physics*, 35 (1986) 317 - 374.
- [46] M. Endo, C. Kim, T. Karaki, T. Kasai, M.J. Matthews, S.D.M. Brown, M.S. Dresselhaus, T. Tamaki, Y. Nishimura, *Carbon*, 36 (1998) 1633-1641.
- [47] F.J. Maldonado-Hódar, C. Moreno-Castilla, J. Rivera-Utrilla, Y. Hanzawa, Y. Yamada, *Langmuir*, 16 (2000) 4367-4373.
- [48] Y. Wang, S. Serrano, J.J. Santiago-Avilés, *Synthetic Metals*, 138 (2003) 423-427.
- [49] Y.Z. Jin, C. Gao, W.K. Hsu, Y. Zhu, A. Huczko, M. Bystrzejewski, M. Roe, C.Y. Lee, S. Acquah, H. Kroto, D.R.M. Walton, *Carbon*, 43 (2005) 1944-1953.
- [50] M.M. Titirici, A. Thomas, M. Antonietti, *Advanced Functional Materials*, 17 (2007) 1010-1018.
- [51] S.R. Mukai, T. Hasegawa, M. Takagi, H. Tamon, *Carbon*, 42 (2004) 837-842.

- [52] K. Zaghbi, M. Simoneau, M. Armand, M. Gauthier, *J Power Sources*, 82 (1999) 300-305.
- [53] S.-S. Kim, Y. Kadoma, H. Ikuta, Y. Uchimoto, M. Wakihara, *Electrochemical and Solid-State Letters*, 4 (2001) A109-A112.
- [54] Y.P. Wu, E. Rahm, R. Holze, *Journal of Power Sources*, 114 (2003) 228-236.
- [55] B.E. Conway, *Electrochemical Supercapacitors—Scientific Fundamentals and Technological Applications*, Kluwer, New York, 1999.
- [56] A. Burke, M. Miller, *Journal of Power Sources*, 196 (2011) 514-522.
- [57] A. Du Pasquier, I. Plitz, S. Menocal, G. Amatucci, *J Power Sources*, 115 (2003) 171-178.

Chapter 4. Preparation and Electrochemical Performance of $\text{Li}_4\text{Ti}_5\text{O}_{12}$ -activated carbon hybrid nanotubes for a Negative Electrode of the BatCap System

4.1. Introduction

In view of the global energy crisis, the problems of resource exhaustion, climate change, and environmental pollution have accelerated the transition in the energy industry from an oil-based economy to an electricity-based economy. The current focus of national policies directed toward energy production is to promote the utilization of alternative energy resources [1-3]. The harnessing of non-pollutive energy resources, including solar energy, geothermal energy, wind, wave, is on the rise, and it is universally recognized that effective energy management systems must be evaluated in an effort to address the imbalances between energy supply and demand. Special attention has been paid to the development of electric vehicles that can switch to the utilization of combustion engines due to the lower environmental impact of such technologies. High-performance energy storage devices that simultaneously collect high power and energy densities, while displaying cycle stability have become extremely important [4-7].

Lithium-ion batteries (LIBs) and supercapacitors are currently considered to be the energy storage devices that are most suitable for converting electrical energy into chemical energy. However, typical LIBs and supercapacitors cannot meet the need of practical applications which demand high-performance energy storage device [8-10]. LIBs are commonly used to store larger amount of electrochemical energy relative supercapacitors, meaning that LIBs indicate a high energy density. On the contrary, supercapacitors are more appropriate energy storage devices than LIBs in the context of high-powered electric systems due to their higher power density and stable power generation properties. Therefore, several studies have been focused on the development of high rate capability to enhance the LIBs for use in high-performance electrical devices. Especially, because one of the most important limiting factors for the high-rate power generation of LIBs is slow charge transfer, many research efforts have been geared toward enhancing the charge transfer speed with material morphology control [11-14], composite with high-electrical conductive material [15-19], etc. On the other hand, several supercapacitor designs have tried to introduce effective methods for increasing the capacitance to enhance the storable electrochemical energy. Typically, most material designs that have been proposed to improve supercapacitors have focused on higher surface area [20, 21], larger working potential window [22-26], use of faradaic reaction with specified metal oxide [27-29], etc., because energy densities are based on the capacitance and working potential window [30, 31]. Asymmetric electrode systems consisting of different electrode types have been

proposed as advanced supercapacitors because they offer improved energy densities due to the differences in the redox potential of each electrode material. Recently, a new approach to energy storage devices has been proposed, involving the hybridization of LIBs and supercapacitors, described by Amatucci et al. [8, 9, 32] as a hybrid supercapacitor. The proposed cell design consists of a Li^+ ion-active negative and electrochemical double layer capacitance (EDLC) positive electrodes immersed in a Li salt containing an organic solvent. Hybridization of battery and supercapacitor electrodes combined with organic electrolyte results in the storage of a larger energy due to the wide working potential window of the organic electrolyte and the steady redox reaction potential of the battery-type negative electrode. Basically, good cycle performance of hybrid supercapacitor can be depressed by poor cycle stability of battery-type electrode relative to EDLC-type electrode. Therefore, most important properties of negative electrode in the hybrid supercapacitor are long-term cycling stability, rapid charge and discharge, and a higher energy density compared with activated carbon, for example $\text{Li}_4\text{Ti}_5\text{O}_{12}$ [31]. Following their first clever proposal were reports of using Brookite (TiO_2) [31], graphite [33], $\text{Li}_4\text{Ti}_5\text{O}_{12}$ /MWCNT composite [34], as battery-type negative electrode that can satisfy the conditions mentioned above in the presence of an activated carbon supercapacitor-type positive electrode.

The present work examines advanced battery-supercapacitor hybrid energy storage device, the BatCap system, developed through hybridization of battery-type electrode material and supercapacitor-type electrode material at a single

negative electrode [35]. We developed $\text{Li}_4\text{Ti}_5\text{O}_{12}/\text{AC}$ (LTO/AC) hybrid nanotubes as negative electrodes for the BatCap system using electrospinning techniques, an *in-situ* TiO_2 sol-gel reaction combined with hydrothermal reaction to synthesize $\text{Li}_4\text{Ti}_5\text{O}_{12}$, and, finally, heat treatment. The battery-supercapacitor hybridized electrodes could be charged and discharged via faradaic and non-faradaic mechanism as the step process, thereby increasing the amount of energy that could be stored with a high rate. This complementary electrode system required large surface area of AC part to enable the faradaic mechanism, and better charge transfer properties with high electrical conductivity and short ion diffusion length for non-faradaic mechanism. Therefore, we attempted to implement a carbon activation process and synthesize 1D-tubular morphological structure. The material characteristics and electrochemical performances of the LTO/AC hybrid nanotubes as negative electrodes in the BatCap system were investigated using a variety of analytic methods and electrochemical tests.

4.2. Experimental Section

4.2.1. Reagents and chemicals

Polyvinyl alcohol (PVA) (Acros, average $M_w=88,000$), lithium ethoxide (LiEox) (Aldrich), lithium chloride (LiCl) (Aldrich), titanium isopropoxide (TIPP) (Aldrich), activated carbon (SX ultra, Norit), and isopropylalcohol (IPA) (Daejung, Korea) were purchased and used without further purification.

4.2.2. Synthesis of LTO/AC hybrid nanotubes

We prepared the LTO/AC hybrid nanotubes via two steps [36]. PVA was electrospun on the aluminum foil followed by an *in-situ* TiO_2 sol-gel reaction on the surface of the electrospun PVA nanofibers. PVA was dissolved in deionized water for 3 hrs with stirring at 70 °C to prepare the 7 wt% PVA aqueous solution. This solution was then transferred to a syringe connected to a metal needle and electrospun at a 1 mL hr^{-1} feeding rate into a bath filled with a 0.02 M TIPP/IPA solution to synthesize the TiO_2 -coated PVA nanofibers (TCP-NF) via an *in-situ* sol-gel reaction. The second stage involved the hydrothermal reaction of TCP-NF in the LiEox/LiCl/IPA solution followed by heat treatment to prepare the LTO/AC hybrid nanotubes. First, LiEox was dissolved in the 0.01 M LiCl/IPA solution during 30 min of stirring to yield the Li precursor for the phase transition from TiO_2 to $\text{Li}_4\text{Ti}_5\text{O}_{12}$. TCP-NFs were moved into the 100 mL of Teflon-lined stainless autoclave containing the LiEox/LiCl/IPA solution. The hydrothermal reaction was carried out at 150 °C

over 72 hrs, and the product was washed with IPA several times to eliminate the unreacted precursors. Finally, the prepared sample was heat-treated in a tubular furnace at 800 °C for 3 hrs under a N₂ atmosphere and 5 min under an air atmosphere to activate the PVA-derived carbonaceous phase in the composite.

4.2.3. Characterization of LTO/AC hybrid nanotubes

Microstructural and morphological analysis of the prepared materials was performed using X-ray diffractometry (XRD, D8 Advance, Bruker) with standard procedures [37-39], field-emission scanning electron microscopy (FE-SEM, JSM-6700F, JEOL), and transmission electron microscopy (TEM, JEM-2010, JEOL) operating at 200 kV. Thermogravimetric analysis (TGA, SDT Q600, TA) was carried out to determine the proportion of carbonaceous phase in the composite. X-ray photoelectron spectroscopy (XPS; AXIS-HSi, KRATOS) was employed to study the surface characteristics of the product. A Micromeritics ASAP 2020 static volumetric gas adsorption instrument was performed to measure the nitrogen adsorption isotherms of the composite at liquid N₂ temperature using ultrahigh purity grade (99.9999%).

4.2.4. Electrochemical tests of LTO/AC hybrid nanotubes

The electrochemical performances of the LTO/AC hybrid nanotubes were tested using a battery cycler (WBCS3000, WonATech) in an Ar-filled glove box (Korea Kiyon). The electrodes of the LTO/AC hybrid nanotubes were prepared

using 80 wt% active material, 10 wt% carbon black, and 10 wt% polyvinylidene (PVDF) as the working electrodes in the half-cell performance tests and as the negative electrodes in the electrochemical performance tests. The anodic performances of the LTO/AC hybrid nanotubes were tested by assembling 2032 coin-type half-cells with lithium-metal as the reference electrode, Celgard 2400 as the separator, and a 1 M LiPF_6 solution in a mixture of ethylene carbonate (EC)/diethyl carbonate (DEC) (1:1 by volume ratio, Cheil Industry Inc.) as the electrolyte in the glove box. The electrochemical performances of the half-cell comprising LTO/AC hybrid nanotubes were tested at various charge/discharge rates in the potential range 1.0-2.5 V vs. Li/Li^+ in the constant-current mode. An electrochemical impedance spectroscopy (EIS) study was carried out using a multi-channel potentiostat generator (VMP3, Biologic). Comparable half-cells containing commercialized $\text{Li}_4\text{Ti}_5\text{O}_{12}$ as the active material were assembled and tested under the exact same experimental conditions to compare the electrochemical performance with those of the LTO/AC hybrid nanotubes. Moreover, negative electrode performances of the LTO/AC hybrid nanotubes in the BatCap system were carried out using a three-electrode system with commercialized AC (SX Ultra, Norit) as the positive electrode, lithium-metal as the reference electrode, and as-prepared negative electrode. The positive AC electrode was prepared using an 80 wt% active material and 20 wt% PVDF as the binder. The electrochemical performances of the negative electrode in the BatCap system were investigated by cyclic voltammetry (CV) using a coin-type half-cell and galvanostatic charge/discharge test with a LTO/AC hybrid

nanotubes//AC hybrid BatCap system. The AC//AC symmetric supercapacitor system was fabricated using same full-cell preparation process, and was tested to compare the electrochemical characteristics with those of the LTO/AC hybrid nanotubes//AC BatCap system.

4.3. Results and Discussion

4.3.1. Microstructural and morphological characteristics of LTO/AC hybrid nanotubes

The microstructure and crystal structure of the LTO/AC hybrid nanotubes were analyzed using XRD yielding the results shown in Figure 4.1A with a diffraction peak typical of the $\text{Li}_4\text{Ti}_5\text{O}_{12}$ phase (space group: Fd3m, JCPDS card No.49-0207) in Figure 4.1B. The cell parameter calculated from the XRD peaks for the LTO/AC hybrid nanotubes was $a=0.8369$ nm, which agreed well with the theoretical value of $a=0.8357$ nm. These results also corresponded to the properties of the synthesized $\text{Li}_4\text{Ti}_5\text{O}_{12}$ phase in the LTO/AC hybrid nanotubes after preparation. The carbonaceous material in the LTO/AC hybrid nanotubes displayed an amorphous phase that could not be detected in the XRD measurements.

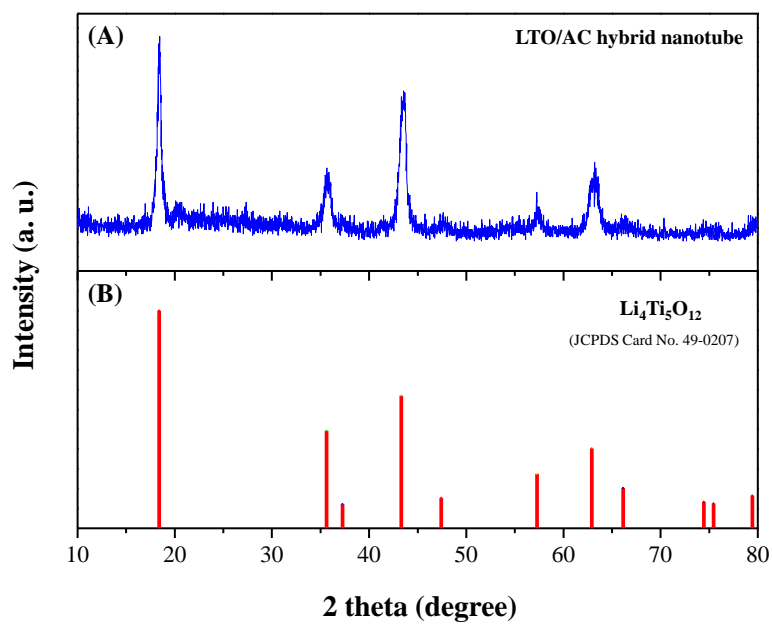


Figure 4.1. XRD patterns of the (A) LTO/AC hybrid nanotubes and (B) typical $\text{Li}_4\text{Ti}_5\text{O}_{12}$ phase.

The morphology of the LTO/AC hybrid nanotubes was investigated by FE-SEM and TEM imaging. SEM images, shown in Figure 4.2A, clearly indicated that 1D morphology caused by electrospinning procedure was well maintained after the hydrothermal reaction and heat treatment. The 1D-shaped LTO/AC hybrid nanotubes were about 250 nm in diameter. Figure 4.2B shows a magnified image of the LTO/AC hybrid nanotubes, revealing evidence for the tubular structure formed by decomposition of the TiO₂-coated PVA phase in the TiO₂-coated PVA nanofibers (TCP-NF) under the *in situ* sol-gel reaction [36]. In addition, the porous morphology on the surface of the LTO/AC hybrid nanotubes could be readily observed. The PVA phase is one of the promising precursors for activated carbon via an appropriate dehydrating agent and activation process [40-42]. In this study, we impregnated LiCl into the TCP-NF as the dehydrating agent in the hydrothermal reaction process, followed by air-assisted surface activation during the heat treatment procedure [43]. 1D-tubular morphologies with porous surface structures were clearly revealed in the TEM analysis results. Figure 4.2C shows the TEM analysis of the LTO/AC hybrid nanotubes, and a high-magnification image of the surface region is indicated in Figure 4.2D. These results present the obvious 1D-tubular structure of the LTO/AC hybrid nanotubes, in good agreement with the SEM analysis result. Furthermore, the high-magnification image of the surface region, shown in Figure 4.2D, indicated the presence of morphological characteristics typical of AC materials, as reported previously [40, 44]. The carbonaceous materials in the LTO/AC hybrid nanotubes with an activated phase enhanced the electron

transport kinetics due to relatively higher electronic conductivity compared with $\text{Li}_4\text{Ti}_5\text{O}_{12}$ phase in the composite. Also, the activated phase with a large surface area can present additional sites for electrochemical energy as the EDLC.

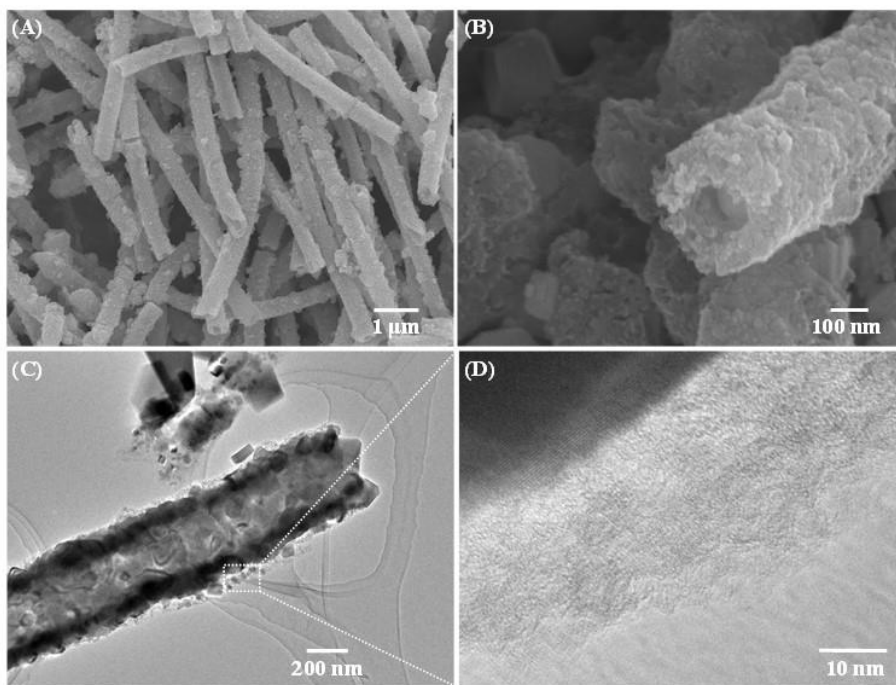


Figure 4.2. FE-SEM micrographs of (A) LTO/AC hybrid nanotubes with (B) a magnified image and TEM micrograph of (C) the LTO/AC hybrid nanotubes and (D) a magnified image of the surface region.

TGA was carried out to calculate the weight ratio of the lithium titanium oxide phase in the LTO/AC hybrid nanotubes and the LTO/C hybrid nanotubes, as shown in Figure 4.3. These values contributed to the evaluation of the specific surface area of a carbonaceous phase in a composite according to the BET analysis, as shown in Figure 4.4. The samples were heated from 25°C to 800°C at a heating rate of 5°C min⁻¹ under an air flow rate of 100 mL min⁻¹. The residual weight after calcination of each sample is listed in Table 4.1, which indicate that the proportion of carbonaceous materials in the composite was about 21.1 wt%.

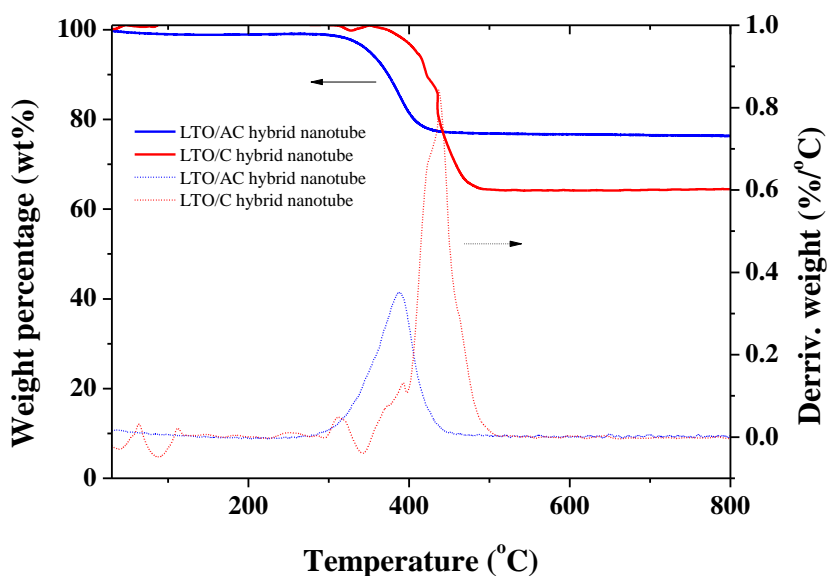


Figure 4.3. The thermogravimetric analysis (TGA) of the LTO/C-HNS. The solid line indicates the thermogravimetric curve and the dotted line indicates the differential thermogravimetric curve.

Table 4.1. Residual weight ratios of the LTO/C-HNS series after TGA measurements.

Sample	LTO/AC hybrid nanotubes	LTO/C hybrid nanotubes
Residual weight ratio [wt%]	78.86	64.28

4.3.2. Surface characteristics of LTO/AC hybrid nanotubes

Nitrogen adsorption isotherm analysis was performed to characterize the surface textures of the LTO/AC hybrid nanotubes, as shown in Figure 4.4. The similar surface characterizations were conducted on the $\text{Li}_4\text{Ti}_5\text{O}_{12}$ /Carbon (LTO/C) hybrid nanotubes, which were prepared using same procedure of the LTO/AC hybrid nanotubes except activation process, and LTO/AC hybrid nanotubes after heat treatment in the air atmosphere at 800 °C, denoted as air-LTO/AC hybrid nanotubes. The surface characterization results are summarized in Table 4.2 to figure out the effects of the activation process on the surface area. Table 4.2 also lists estimates of the surface area of the carbonaceous phase in the LTO/AC hybrid nanotubes. The BET specific surface area (BET SSA) of carbonaceous material can be estimated as BET SSA divided by mass of carbonaceous phase due to no BET SSA of air-LTO/AC hybrid nanotubes. Table 4.2 reveals that the BET SSA of the LTO/AC hybrid nanotubes is about $158 \text{ m}^2 \text{ g}^{-1}$ much higher than that of the LTO/C hybrid nanotubes, despite the lower amount of carbonaceous phase present in the sample. These results indicated that activation process effectively increased the surface area of the LTO/AC hybrid nanotubes, thereby providing additional EDLC on the negative electrode. Also, the BET SSA of the carbonaceous phase in the LTO/AC hybrid nanotubes was calculated using the thermogravimetric analysis (TGA) results in Table 4.2, which indicates the similar values to the previous reports for PVA-derived AC materials [43, 45, 46].

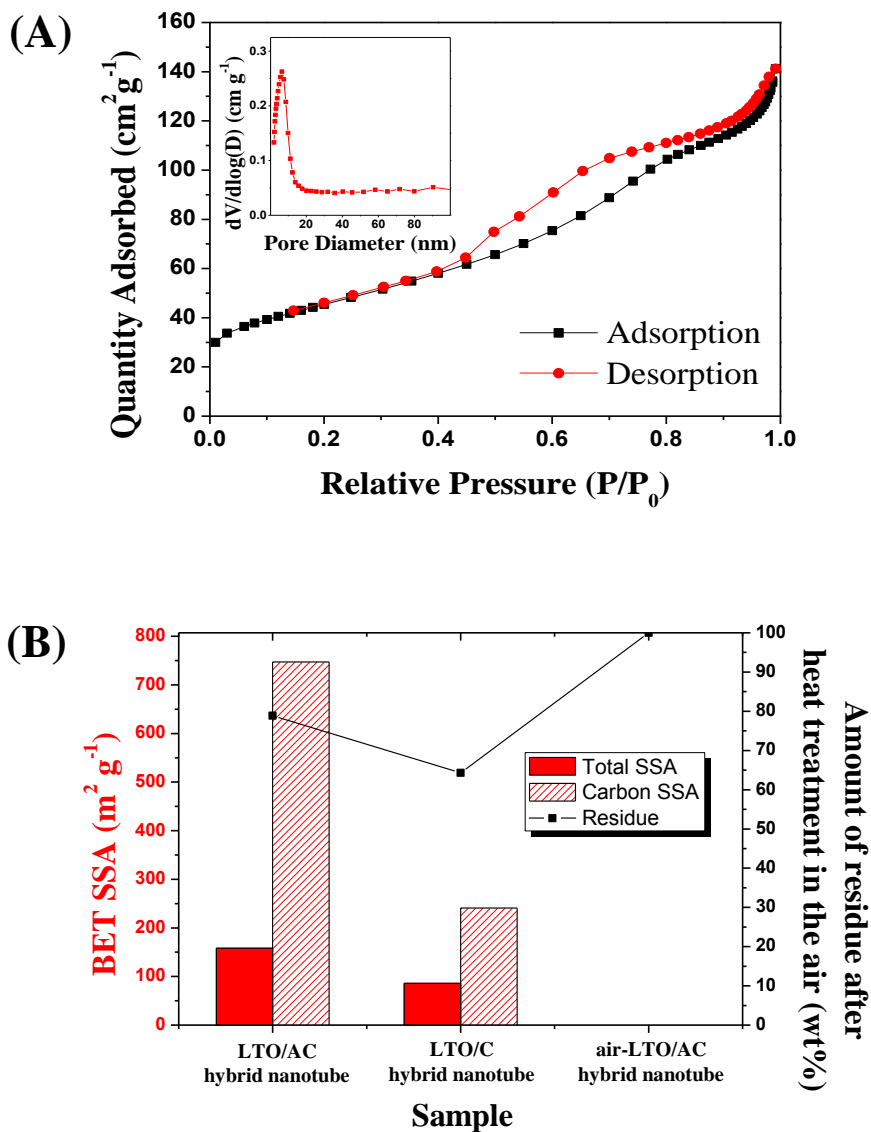


Figure 4.4. (A) Nitrogen adsorption isotherms at 77K of the LTO/AC hybrid nanotubes with the inset showing the pore size distribution and (B) a comparison of the BET specific surface area and amount of residue remaining after heat treatment under ambient conditions.

Table 4.2. Pore characteristics determined from the nitrogen adsorption isotherm at 77 K of the LTO/AC hybrid nanotubes, LTO/C hybrid nanotubes, and air-heat treated LTO/AC hybrid nanotubes.

Sample	BET SSA ^{a)} $[\text{m}^2 \text{g}^{-1}]$	Langmuir SSA ^{b)} $[\text{m}^2 \text{g}^{-1}]$	Average pore diameter [nm]	Total pore volume at 0.98 of relative pressure $[\text{cm}^3 \text{g}^{-1}]$	BET SSA of carbonaceous phase ^{c)} $[\text{m}^2 \text{g}^{-1}]$
LTO/AC hybrid nanotubes	158	220	5.23	0.21	747
LTO/C hybrid nanotubes	86	119	4.27	0.08	240
air-LTO/AC hybrid nanotubes	0	0	.	.	.

^{a)} SSA, specific surface area, determined by the BET equation.

^{b)} Determined by the Langmuir equation.

^{c)} BET specific surface area of the carbonaceous phases in the sample were calculated as the BET specific surface areas divided by mass of the carbonaceous phase in the sample based on TGA analysis.

Raman spectroscopy and XPS were performed to obtain information about the surface chemical characteristics of the LTO/AC hybrid nanotubes. Figure 4.5 shows the Raman spectrum of the LTO/AC hybrid nanotubes in the Raman shift range from 900 to 1900 cm^{-1} , which represent the crystalline perfection of the carbonaceous materials. The curve fit was obtained using a Gaussian fitting procedure with four superimposed Raman shift peaks at 1171, 1337, 1507, and 1604 cm^{-1} . Peak 1 at position 1171 cm^{-1} arose from the sp^3 -rich phase of the amorphous carbon [47, 48], peak 2 at position 1337 cm^{-1} (D band) arose from highly disordered graphitic structure [35, 49], peak 3 at position 1337 cm^{-1} arose from the semicircle ring stretch vibration of benzene [50], and peak 4 at position 1337 cm^{-1} (G band) arose from the sp^2 stretch vibration contribution from the benzene moiety [35, 49]. The curve deconvolution results are summarized in Table 4.3, in which the values are similar to the results of typical amorphous carbon materials, especially the existence of peak 1 and peak 3 due to the sp^3 -rich phase and the C-H bond vibrations, respectively [47]. This is in good agreement with the XRD analysis results, as shown in Figure 4.1, in that no peak was observed around $2\theta = 25^\circ$ from the (002) plane of the graphite. Also, the relative intensity of peak 2 (D band) to peak 4 (G band), of which the value can be denoted as $R = I_{\text{peak2}}/I_{\text{peak4}}$ and which varies with the degree of graphitization and the alignment of the graphitic planes [48], was about 1.25. This value is lower than typical R value for graphite, indicating the presence of a less-developed graphitic carbon structure on the surfaces of the LTO/AC hybrid nanotubes.

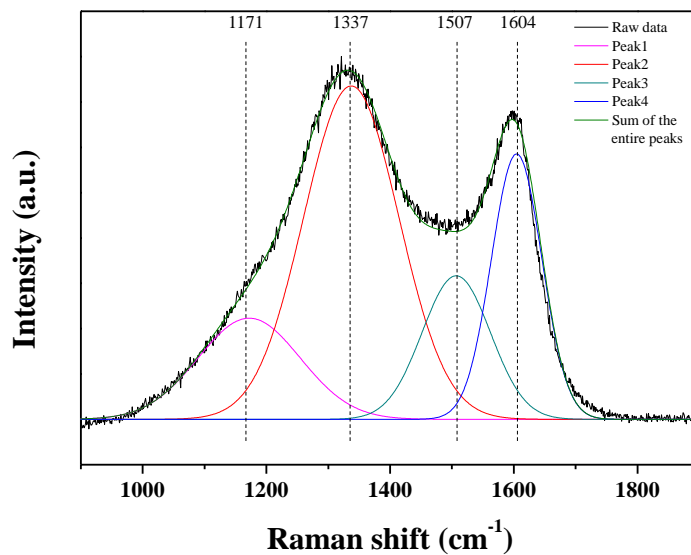


Figure 4.5. Raman spectrum and curve fitting result for the LTO/AC hybrid nanotubes. Four peaks with peak maxima at 1171, 1337, 1507, and 1604 cm^{-1} were required for the curve description of the Raman spectrum.

Table 4.3. Deconvolution of the Raman spectrum of the LTO/AC hybrid nanotubes, as shown in Figure 4.5.

Peak	Position [cm^{-1}]	Area [Area %]	Intensity	FWHM [cm^{-1}]	$R=I_{\text{peak2}}/I_{\text{peak4}}$
Peak1	1171.8	115543.1 (15.8)	557.8	165.5	1.25
Peak2	1337.4	354979.2 (48.7)	1838.0	154.2	
Peak3	1507.1	109485.1 (15.0)	791.1	110.5	
Peak4	1604.8	149527.2 (20.5)	1463.2	81.6	

Figure 4.6 shows the XPS spectra of the LTO/AC hybrid nanotubes, which provides useful information for various functional groups on the composite surfaces. The survey XPS spectrum in Figure 4.6A includes the clearly observed peaks corresponding to Li1s, Ti2p, and O1s due to the $\text{Li}_4\text{Ti}_5\text{O}_{12}$ phase and C1s due to the activated carbonaceous materials in the LTO/AC hybrid nanotubes. The inset of Figure 4.6A shows that the Ti2p level consisted of a single doublet due to spin-orbit splitting composed of two symmetric peaks at 464.02 eV and 458.26 eV for the $\text{P}_{1/2}$ and $\text{P}_{3/2}$ lines, respectively. These results supported the presence of only Ti^{4+} in the $\text{Li}_4\text{Ti}_5\text{O}_{12}$ phase of the composite [51-53] indicating that the $\text{Li}_4\text{Ti}_5\text{O}_{12}$ phase was well synthesized after the preparation procedure for the LTO/AC hybrid nanotubes. Figure 4.6B shows the C1s spectra of the LTO/AC hybrid nanotubes. The peaks were deconvoluted using a Lorentzian-Gaussian mixed function. The information and the peak parameters are summarized in Table 4.4. As shown in Figure 4.6B, the C1s spectrum of the LTO/AC hybrid nanotubes mainly consisted of three peaks at binding energies of 284.55, 286.70, and 288.43 eV, which corresponded to the non-functionalized graphitic carbon (C- sp^2 and/or - sp^3 bondings), the C-O of ether/hydroxyl groups, and the COO of the carboxyl/lactone groups, respectively [43, 45, 46]. These results indicated the absence of a carbon peak corresponding to the carbonyl/quinone groups through the LiCl-assisted air-activation process for PVA. Also, the element data, normalized by the area ratio of each peak in Table 4.4, shows that graphitic carbon clearly provided the most dominant carbon structure, at about 78% in the LTO/AC hybrid nanotubes, due

to the use of the LiCl-assisted air-activation process. These results indicated the well-prepared $\text{Li}_4\text{Ti}_5\text{O}_{12}$ phase and graphitic carbon as the most dominant carbon structures in the LTO/AC hybrid nanotubes.

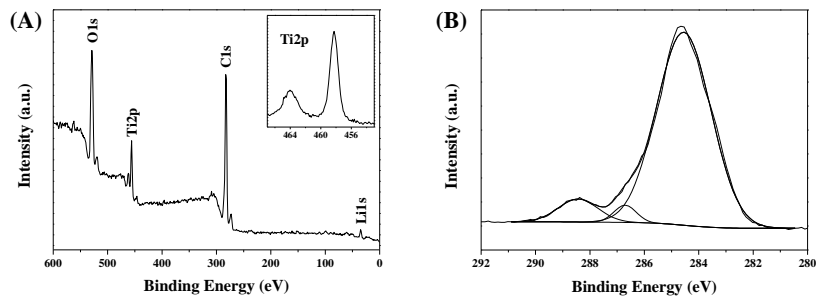


Figure 4.6. XPS survey spectrum with the inset showing the Ti2p region (A) and the C1s region (B) of the LTO/AC hybrid nanotubes.

Table 4.4. C1s peak deconvolution of the XPS spectrum in the LTO/AC hybrid nanotubes, as shown in Figure 4.6B.

Sample	Element	Peak position [eV]	Relative amount of element [Area %]
LTO/AC hybrid nanotubes	C-C and/or C=C	284.55	89.0
	C-O	286.70	3.3
	COO	288.43	7.7

4.3.3. Electrochemical performances of LTO/AC hybrid nanotubes

We electrochemically characterized the LTO/AC hybrid nanotubes as the anode for LIBs using half-cell performance tests at different charge/discharge rates in the potential range 1.0-2.5 V vs. Li/Li⁺. The anodic performance of the LTO/AC hybrid nanotubes is displayed in Figure 4.7A, and differential capacity vs. cell potential curve is shown in the inset image. At a 100 mA g⁻¹ of charge/discharge rate, the LTO/AC hybrid nanotubes exhibited a specific capacity of 128 mAh g⁻¹. This value approached the theoretical value of 131 mAh g⁻¹ for the Li₄Ti₅O₁₂ phase, which accounted for about 79 wt% of the LTO/AC hybrid nanotubes. The potential value of charge and discharge reaction for the composite sample were 1.59 V and 1.52 V vs. Li/Li⁺ at 100 mA g⁻¹, respectively, which are typical potential values for Li₄Ti₅O₁₂ as the anode in LIBs. These results indicated that Li₄Ti₅O₁₂ phase functioned well as the anode in the LTO/AC hybrid nanotubes similar to the pure Li₄Ti₅O₁₂.

The specific capacities at 500, 1000, 2000, and 4000 mA g⁻¹ were found to be 107, 104, 92, and 84 mAh g⁻¹, respectively, indicating an enhanced rapid charge/discharge rate for the LTO/AC hybrid nanotubes. Details are provided in Figure 4.7B, which indicates the discharge capacities of the LTO/AC hybrid nanotubes and pure Li₄Ti₅O₁₂ retained at various charge/discharge rates. The values were calculated as the values of discharge capacity ratio at each charge/discharge rate compared with the discharge capacity at 100 mA g⁻¹. As the charge/discharge rate increased beyond the low value regime, the LTO/AC

hybrid nanotubes yielded an excellent retained discharge capacity exceeding 67% at 4000 mA g⁻¹ much higher than the value of the pure Li₄Ti₅O₁₂, 14%. Figure 4.8 shows the cycle performance of the LTO/C hybrid nanotube at various charge/discharge rates as the anode of LIBs. Also, a comparison of the discharge capacity between LTO/AC hybrid nanotubes and LTO/C hybrid nanotubes is displayed in the inset. This indicates that the discharge capacity of the LTO/AC hybrid nanotubes is better than that of the LTO/C hybrid nanotubes at each charge/discharge rate, which illustrates that the porosity and high surface area of the LTO/AC hybrid nanotubes help to enhance the electrochemical performance due to the better charge transport kinetics.

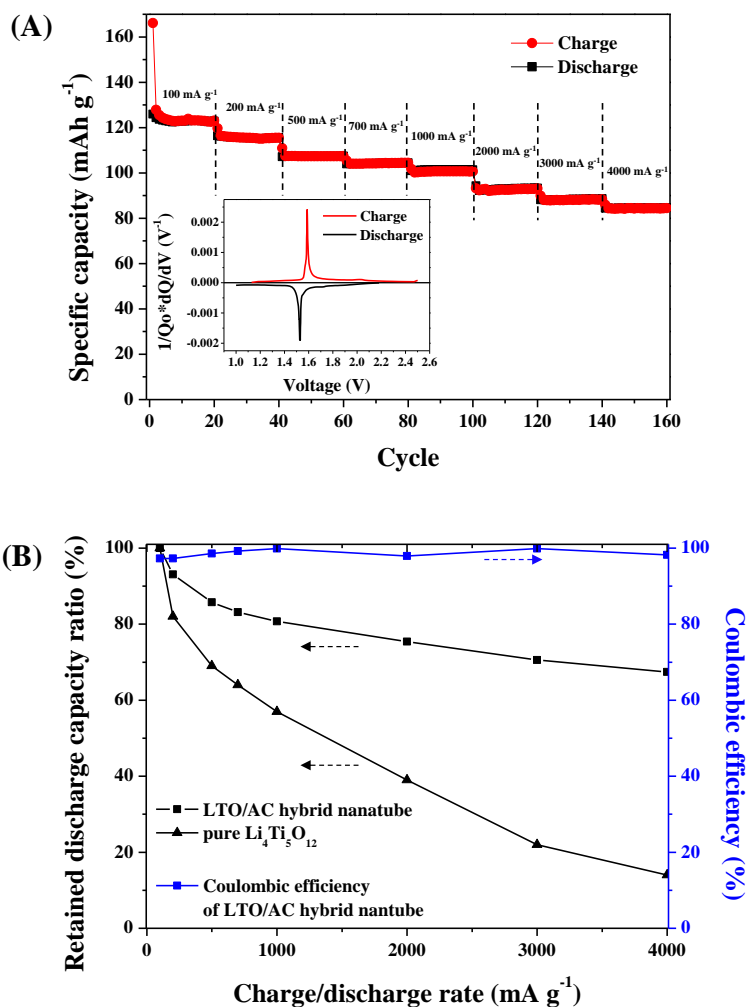


Figure 4.7. (A) Cycle performances of the LTO/AC hybrid nanotubes at various charge/discharge rates. The inset shows the differential capacity vs. cell potential curve at a charge/discharge rate of 100 mA g⁻¹ during the second cycle. (B) Retained discharge capacity ratio of the LTO/AC hybrid nanotubes and the pure Li₄Ti₅O₁₂, and Coulombic efficiencies at various charge/discharge rates of the LTO/AC hybrid nanotubes.

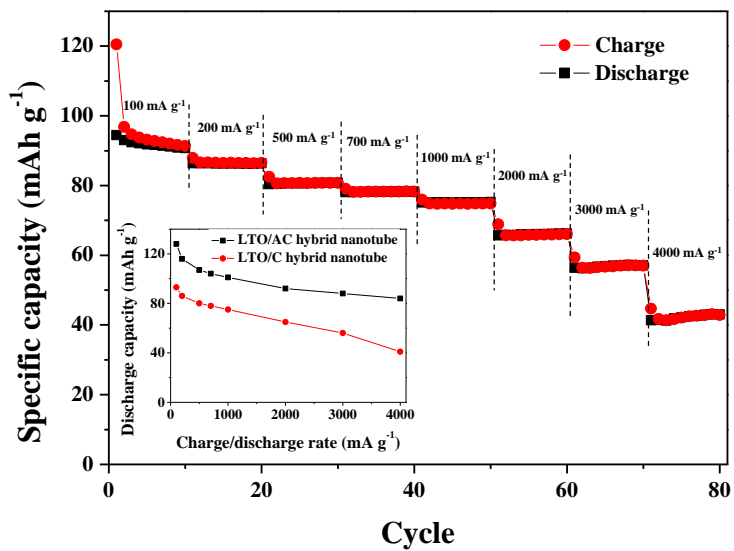


Figure 4.8. Cycle performances of the LTO/C hybrid nanotubes at various charge/discharge rates in the potential range 1.0-2.5 V vs. Li/Li⁺. The inset shows the discharge capacity of the LTO/AC hybrid nanotubes and LTO/C hybrid nanotubes at various charge/discharge rates.

We also performed the impedance analysis of the samples to understand the charge transfer kinetics in depth depending on the morphological controlled nanostructure and the hybridized electro-conducting phase in the composite. AC impedance data for the LTO/AC hybrid nanotubes and pure $\text{Li}_4\text{Ti}_5\text{O}_{12}$ half-cells were compared over the frequency range 100 kHz-10 mHz under an open circuit after preliminary equilibration. The Nyquist plots and analytic values of the samples are shown in Figure 4.9 and Table 4.6. The resistance values were normalized by multiplying mass of the active material of each sample to attain a fair comparison [54]. Also, these analytic spectra were fitted using a simple modified Randles–Ershler equivalent circuit [55] as shown in Figure 4.10 and the related parameters were calculated based on the impedance results listed in Table 4.5. Figure 4.10 indicates the equivalent circuit, where W is the Warburg impedance, CPE_L and CPE_C are the constant phase elements representing the imperfective double layer capacitance of $\text{Li}_4\text{Ti}_5\text{O}_{12}$ and activated carbon components under the applied potential, respectively, R_e is the electrolyte solution resistance, and R_{CT} is charge transfer resistance. According to Table 4.5 of summary for simulated plot in Figure 4.10 using equivalent circuit, specific capacitance of battery component, $\text{Li}_4\text{Ti}_5\text{O}_{12}$, and capacitor component, activated carbon, can be estimated as 0.0254 and 35.0698 F g^{-1} , respectively, based on the mass of each component. Also, CPE exponent value of CPE_C (α_C), which indicates perfection of capacitor, is higher than that of CPE_L (α_L). From these analytic results, it is clearly shown that activated carbon operates as the

capacitor component in the LTO/AC hybrid nanotube with 35.0698 of specific capacitance.

The electrolyte solution resistance (R_e) was evaluated based on the impedance intercept on the Z-real axis in Figure 4.9. Furthermore, the charge transfer and Li^+ ion diffusion kinetics were estimated based on the semicircle in the high-middle frequency range and the oblique line of the low frequency range, respectively. The charge transfer resistance at the active material/electrolyte interface (R_{CT}) was evaluated based on the right-hand side intercept impedance intercept on the Z-real axis of the semicircle. The Li^+ ion diffusion coefficient, abbreviated D_{Li^+} , was calculated using the following equation [56-58]:

$$D_{\text{Li}^+}^{1/2} = \frac{RT}{2^{1/2} n^2 F^2 A} \times \frac{1}{\sigma C_{\text{Li}^+}} \quad (1)$$

where R is the gas constant ($R = 8.314 \text{ J mol}^{-1} \text{ K}^{-1}$), T is the working temperature, n is the number of electrons in the reaction, F is the Faradaic constant ($F = 96500 \text{ C mol}^{-1}$), A is the active surface area, and C_{Li^+} is the molar concentration of Li in an electrode active material. The Warburg impedance coefficient, denoted σ , may be obtained from the slope of R_{ct} vs. $\omega^{-1/2}$ (ω : angular frequency) in the medium frequency range. Also, the values of the exchange current density, abbreviated i_0 , in Table 4.6 were calculated from the following equation [57].

$$i_0 = \frac{RT}{nFAR_{ct}} \quad (2)$$

The exchange current density of the LTO/AC hybrid nanotubes was higher than that of $\text{Li}_4\text{Ti}_5\text{O}_{12}$, however, the D_{Li^+} of the LTO/AC hybrid nanotubes ($9.48 \times$

$10^{-9} \text{ cm}^2 \text{ s}^{-1}$) was one order of magnitude higher than the value for the pure $\text{Li}_4\text{Ti}_5\text{O}_{12}$ ($2.37 \times 10^{-10} \text{ cm}^2 \text{ s}^{-1}$) suggesting that the charge transfer reaction of the LTO/AC hybrid nanotubes was significantly better than the pure $\text{Li}_4\text{Ti}_5\text{O}_{12}$, resulting in a good agreement at faster frequency responses, as shown in Figure 4.11 and in previous publications studying the high-rate capability of the $\text{Li}_4\text{Ti}_5\text{O}_{12}$ /carbonaceous material hybrid [57].

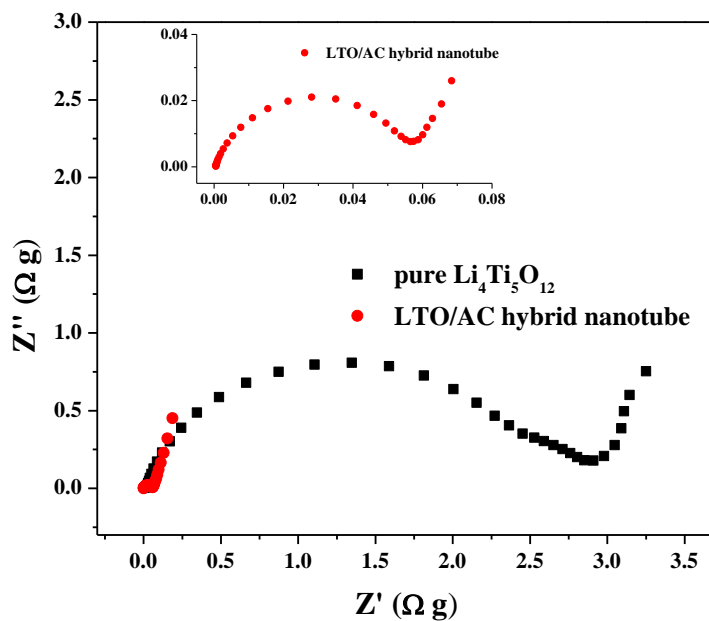


Figure 4.9. Nyquist impedance spectra of the LTO/AC hybrid nanotubes and pure $\text{Li}_4\text{Ti}_5\text{O}_{12}$. A magnified view of the high frequency region for the LTO/AC hybrid nanotubes is provided in the inset.

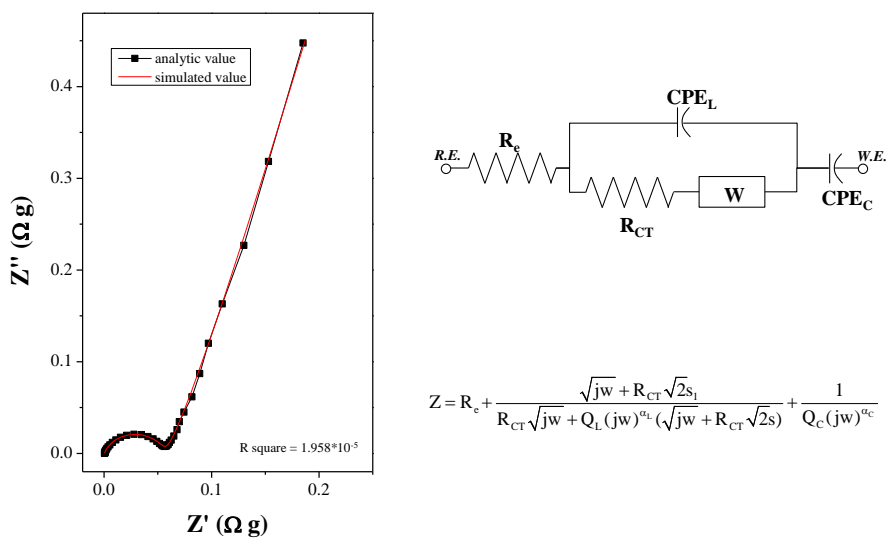


Figure 4.10. Experimental and simulated plots for AC impedance spectra of the LTO/AC hybrid nanotubes with equivalent circuit and simulated impedance equation.

Table 4.5. Summary for equivalent circuit with impedance equation from AC impedance spectra of LTO/AC hybrid in Figure 4.10.

	R_e [Ω]	R_{CT} [Ω]	s [$\Omega \cdot s^{-0.5}$]	Q_L [$F \cdot s^{1/\alpha_L}$]	α_L	Q_C [$F \cdot s^{1/\alpha_C}$]	α_C
LTO/AC hybrid nanotube	3.2	433	90	$1.03 \cdot 10^{-6}$	0.81	$3.45 \cdot 10^{-3}$	0.898

Table 4.6. Impedance parameters and Li^+ ion diffusion coefficient calculated from the impedance spectra of the LTO/AC hybrid nanotubes and pure $Li_4Ti_5O_{12}$.

Sample	R_e [Ω g]	R_{CT} [Ω g]	i_0 [$mA\ cm^{-2}$]	D_{Li^+} [$cm^2\ s^{-1}$]
LTO/AC hybrid nanotubes	5.089×10^{-4}	0.058	0.263	9.48×10^{-10}
Pure $Li_4Ti_5O_{12}$	3.067×10^{-2}	2.632	0.717	2.37×10^{-9}

The rapid power generation performance of the LTO/AC hybrid nanotubes compared with the pure $\text{Li}_4\text{Ti}_5\text{O}_{12}$ was also demonstrated by comparing the normalized capacitance with the frequency response of each sample in Figure 4.11. The results indicated that the capacitance dropped to 50% of its maximum value ($f_{0.5}$). The LTO/AC hybrid nanotubes apparently provided a faster frequency response for $f_{0.5}=0.6$ Hz than the pure $\text{Li}_4\text{Ti}_5\text{O}_{12}$ of $f_{0.5}=0.9$ Hz, which results agrees well with the values of D_{Li^+} provided in Table 4.5 with the high rates [59].

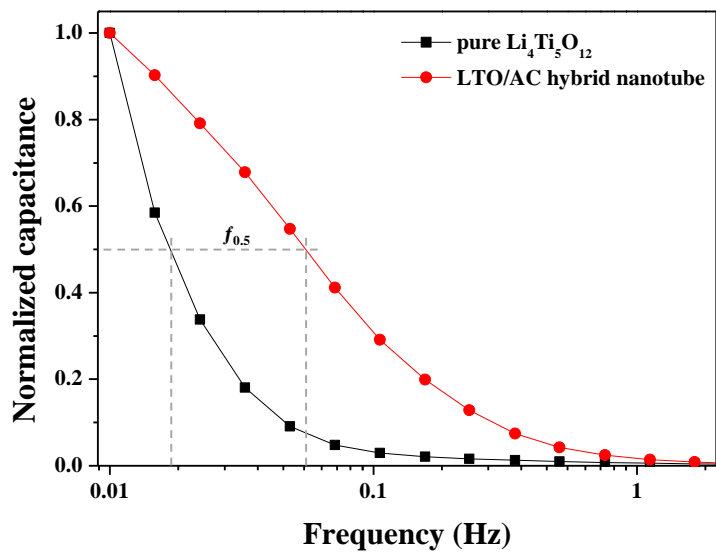


Figure 4.11. Normalized capacitance and frequency response for the LTO/AC hybrid nanotubes and pure $\text{Li}_4\text{Ti}_5\text{O}_{12}$ half-cells.

As can be seen in the results, it is noteworthy that the LTO/AC hybrid nanotubes provided better anodic performance at high charge/discharge rates with a great Coulombic efficiency close to 100%. Collectively, these results suggest that morphological control over the nanosized 1D-tubular structures and PVA-derived activated carbonaceous phases of the LTO/AC hybrid nanotubes provide effective control over the electrochemical performance when used as the anode in LIBs at high rates. Particularly, 1D-tubular structure enhances the accessibility of the electrolytes to the active material surface resulting in better Li-ion transport kinetics. Accordingly, the presence of the PVA-derived activated carbonaceous phase in the 1D-tubular composite improved the electron transport kinetics, which determined the extent of the charge transfer reaction at high charge/discharge rates [35]. The significantly enhanced electrochemical performances at high rate were attributed to better charge transport kinetics and can potentialize the use of LTO/AC hybrid nanotubes not only for the high-power LIBs but also in the BatCap system.

The cyclic voltammograms (CVs) of the activated carbon (SX Ultra, denoted as AC) in various potential ranges were measured at a sweep rate of 5 mV s^{-1} with the Li salt-based organic electrolyte (1 M LiPF_6 in EC/DEC) to use AC as the positive electrode in the hybrid BatCap system (Figure 4.12). The resulting curve yielded a typical rectangular shape related to the curve shape for common AC from electrical double layer capacitance (EDLC) by a rotational mirror symmetry operation in the potential range 2.0-4.0 V vs. Li/Li^+ . The CV results of the AC indicated that an a solid electrolyte interface (SEI) layer, which

closed the open pores on the surface of the AC, thereby limiting the approach of Li^+ ions in the electrolyte, could be formed at applied potentials below 2.0 V vs. Li/Li^+ . Besides, the electrolyte decomposition on the surfaces of the AC could be prevented at potentials up to 4.0 V vs. Li/Li^+ of the applied potentials, which caused irreversible specific capacity [33]. Therefore, the CV test results indicated that AC is an appropriate active material for use in the hybrid BatCap system at a potential range of 2.0-4.0 V vs. Li/Li^+ . The calculated capacitance of the AC based on the CV result was 69 F g^{-1} , which provided a specific capacity of 46 mAh g^{-1} at a working potential of 2–4 V vs. Li/Li^+ .

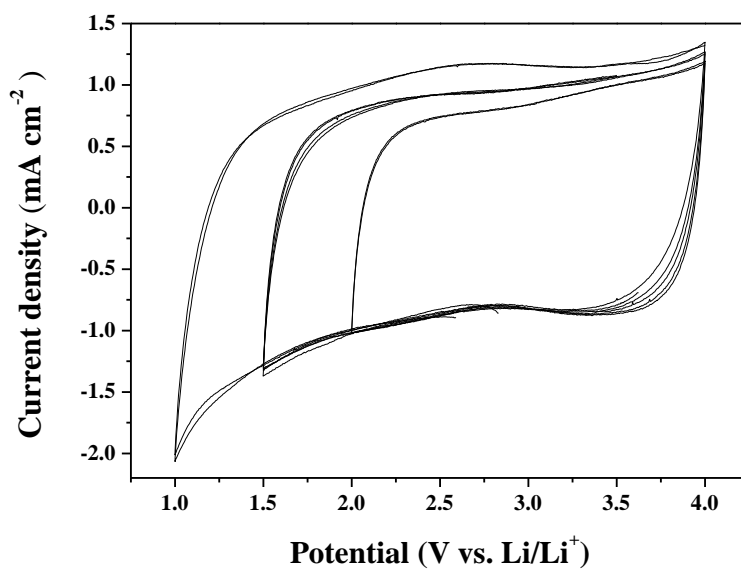


Figure 4.12. The CV of AC at a 5 mV s⁻¹ sweep rate over various potential ranges from 1 to 4 V vs. Li/Li⁺.

The LTO/AC hybrid nanotubes were also subjected to cycling over a potential range of 0.5-3.5 V of potential range at a variety of charge/discharge rates in an effort to evaluate the electrochemical performances as a negative electrode with AC as a positive electrode in the BatCap system. The mass of each electrode was fixed at $m_{\text{positive}}/m_{\text{negative}} = 3$ to fabricate the full-cell from the specific capacity information about the AC, as shown in Figure 4.12, because the highest energy density of the hybrid energy storage device can be generated through a balance of the exchanged charge between the positive and negative electrodes [31, 33, 34].

Figure 4.13 illustrates the galvanostatic charge/discharge curves of the LTO/AC hybrid nanotubes//AC hybrid BatCap system with separated potential profiles for each electrode and full-cell. In the early state, the full-cell potential plot demonstrated the slow decrease in the curve-shaped slope because of a plateau region at the negative electrode (the red-colored potential profile) from the Li^+ ion lithiation/delithiation reaction in the $\text{Li}_4\text{Ti}_5\text{O}_{12}$ species around 1.5 V vs. Li/Li^+ . Then, the linear slope of the full-cell potential profile indicated a linear plot with a higher slope than was observed for the early state due to the end of the plateau region of the negative electrode above 2.2 V in the full-cell potential range. The negative electrode potential profile for the LTO/AC hybrid nanotubes//AC hybrid BatCap system, the shape of which is differed substantially from the profile shapes of the pure $\text{Li}_4\text{Ti}_5\text{O}_{12}$ or general activated carbon, could be explained in terms of the energy storage mechanism unlike typical symmetric capacitors. The AC part of the LTO/AC hybrid nanotubes

could be operated as the EDLC until the negative electrode potential reached the faradaic reaction-available potential of $\text{Li}_4\text{Ti}_5\text{O}_{12}$. The faradaic redox reaction potential around 1.5 V vs. Li/Li^+ showed that the $\text{Li}_4\text{Ti}_5\text{O}_{12}$ material could be charged or discharged as a battery material, indicating the potential to store a higher energy density than typical EDLC material, followed by another energy density increase from EDLC material in the composite after a full faradaic redox reaction of $\text{Li}_4\text{Ti}_5\text{O}_{12}$ part. The potential range of the LTO/AC hybrid nanotubes was controlled over 0.7 V vs. Li/Li^+ to prevent the formation of solid electrolyte interface (SEI) layers that could disturb the charge transfer kinetics. The potential profile of the positive AC electrode in the hybrid BatCap system was nearly linear over the entire charge/discharge potential range up to around 4.0 V vs. Li/Li^+ . This result was typical of EDLC electrode, indicating good agreement with the CV curve presented in Figure 4.12.

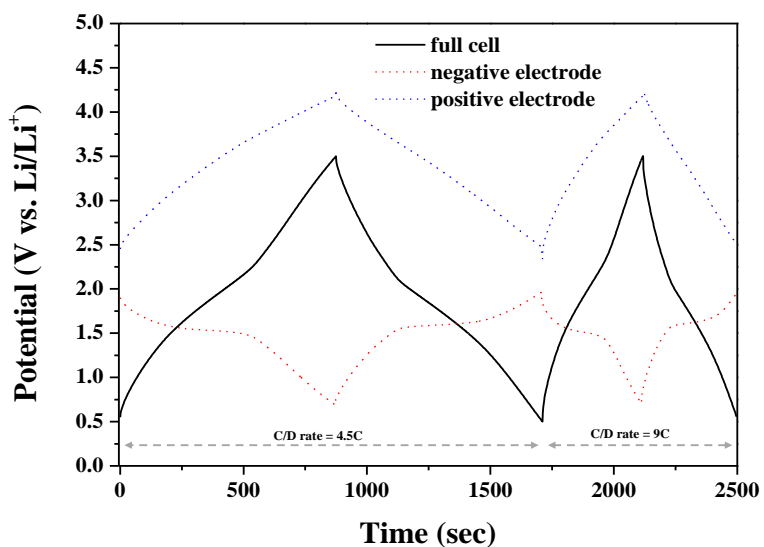


Figure 4.13. Galvanostatic charge/discharge plot for the LTO/AC hybrid nanotubes//AC hybrid BatCap system at a 4.5 C rate and a 9 C rate in the working potential range of 0.5-3.5 V. The black-colored potential profile indicates the full-cell, the red-colored potential profile indicates the negative electrode of the LTO/AC hybrid nanotubes, and the blue-colored potential profile indicates the positive AC electrode.

The Ragone plot in Figure 4.14 was obtained from charge/discharge measurements of the LTO/AC hybrid nanotubes//AC hybrid BatCap system and the AC//AC symmetric capacitor system at a variety of power densities based on the total mass of both electrodes. The plot summarizes the electrochemical performances of each energy storage system. The LTO/AC hybrid nanotubes//AC hybrid BatCap system operated using a combination of an energy storage mechanism for a battery and an EDLC, as supported by the combined charge/discharge potential profile of a battery and an EDLC, as illustrated in Figure 4.13. It was not appropriate, therefore, to estimate the electrochemical performance of this hybrid BatCap system using conventional equations for either batteries or supercapacitors. In a typical battery system, the energy density can be calculated based on the product of the state of charge, Q , and the working potential, V , per mass of active material, due to the fixed potential value of the electrochemical redox reaction during the charge/discharge process. Otherwise, the energy density of a typical EDLC based on a supercapacitor can be estimated using the equation $(1/2)QV$, because Q value is proportional to the working potential. Therefore, the energy densities of the hybrid BatCap system could be calculated by integrating the Q - V graph area during the discharge process, followed by unit conversion to Wh kg^{-1} . The maximum power density (PD) could be estimated using the equation, $PD_{\text{max}}=V_{\text{max}}I$, in which V_{max} is the max working potential and charge/discharge current, I . However, the maximum power density calculated using this typical equation tended to over-estimate the power of the concerned energy storage

device that was actually available. The energy efficiency, i.e. the fraction of the total energy transferred from a device to the surrounding except for the energy lost due to heat generation, was calculated. The maximum power density could then be estimated using the equation $PD_{\max} = V_{\max}^2 / 4R = V_{\max} I / 2$ [33, 35].

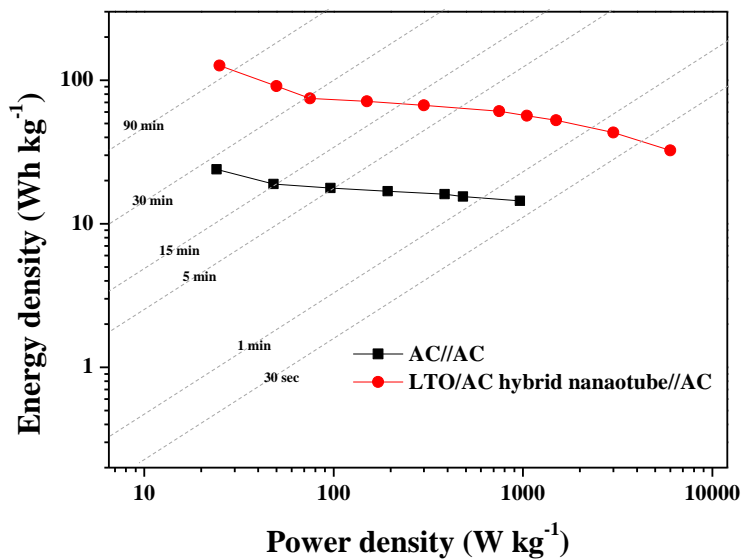


Figure 4.14. Ragone plot for the LTO/AC hybrid nanotubes//AC hybrid BatCap system and the AC//AC symmetric capacitor at various charge/discharge rates in the working potential range of 0.5-3.5 V. The data were calculated based on the total mass of both electrodes.

As demonstrated in the Ragone plot in Figure 4.14, the energy densities at a low power density, 50 W kg^{-1} , for the LTO/AC hybrid nanotubes//AC hybrid BatCap system and the AC//AC symmetric capacitor system are about 90 and 18 Wh kg^{-1} , respectively. The practical specific energy density of the LTO/AC hybrid nanotube//AC hybrid BatCap system can be expected to be close to 40 Wh kg^{-1} , as the practical large batteries generally contain an electrode material mass of about 35-40 wt% of the total mass of the system, of which the value is 5-10 times higher than that of EDLCs using acid or alkaline aqueous solution. At a high power density of 6000 W kg^{-1} , the LTO/AC hybrid nanotubes hybrid BatCap system exhibited 32 Wh kg^{-1} of energy density against only 14 Wh kg^{-1} for the AC//AC symmetric capacitor system even at a much lower power density, 1000 W kg^{-1} . These specific energy density values for the hybrid BatCap system reveal synergistic effects relative to the literature values for typical commercialized LIBs (about 10 Wh kg^{-1} at 1000 W kg^{-1}), EDLCs (about 5 Wh kg^{-1} at 5000 W kg^{-1}) or hybrid capacitors (about 15 Wh kg^{-1} at 1000 W kg^{-1}) consisting of pure $\text{Li}_4\text{Ti}_5\text{O}_{12}$ and AC in each electrode.

The results shown in Figure 4.14 reveal that control over the 1D-tubular morphology of the composite with AC improved the electrical conductivity and shortened the ion diffusion length. Additionally, $\text{Li}_4\text{Ti}_5\text{O}_{12}$ -AC hybridization, which provided a higher storable charge from the EDLC of the AC and lithiation/delithiation of $\text{Li}_4\text{Ti}_5\text{O}_{12}$, simultaneously affected the improvements in the power and energy densities.

4.4. Conclusion

A synthetic technique for the *in-situ* sol-gel reaction was combined with electrospinning, hydrothermal reaction, and heat treatment to successfully prepare LTO/AC hybrid nanotubes that can potentially enable advanced energy storage device, such as the hybrid BatCap system, which includes both battery component and capacitor component in a single electrode. The LTO/AC hybrid nanotubes contributed 67 % of the capacity ratio at 4000 mA g⁻¹ of charge/discharge rate in the half-cell performance test. These results indicated excellent high power generation rate compared with the pure Li₄Ti₅O₁₂, due to the better charge transfer kinetics, as shown by the impedance analysis results. The hybrid BatCap system was fabricated using the LTO/AC hybrid nanotubes as the negative electrode and AC as the positive electrode. The energy densities of the LTO/AC hybrid nanotubes//AC hybrid BatCap system were in the range 90-32 Wh kg⁻¹ over the power densities from 50 to 6000 W kg⁻¹. These values permitted the envisioning of hybrid BatCap system using LTO/AC hybrid nanotubes for the negative electrode with superior charge storage for high-performance-required application.

4.5. Appendix

To illustrate the difference of BatCap system compared to typical battery-electrode//capacitor-electrode asymmetric capacitor and battery and capacitor components simple mixing//capacitor-electrode asymmetric capacitor, electrochemical performance tests for LTO//AC asymmetric capacitor and LTO-AC simple mixing//AC asymmetric capacitor were conducted at a variety of charge/discharge rates.

First of all, LTO-AC simple mixing electrode was fabricated and tested as the half-cell to show the effects of hybridization of LTO/AC hybrid nanotube. As indicated in Figure 4.A1A, LTO-AC simple mixing electrode was prepared using simply mixed 80 wt% of $\text{Li}_4\text{Ti}_5\text{O}_{12}$ (Sud Chemie, Germany) and 20 wt% of activated carbon (SX ultra, Norit) as the active material with same weight ratio of binder and conductive material compared to LTO/AC hybrid nanotube electrode. Figure 4.A2A and B illustrate cycle stability and charge/discharge profiles of LTO-AC simple mixing electrode in the potential range from 1.0 to 2.5 V vs. Li/Li^+ at various charge/discharge rates, respectively. At a low charge/discharge for rate, LTO-AC simple mixing electrode shows typical specific capacity of $\text{Li}_4\text{Ti}_5\text{O}_{12}$, such as about 150 mAh g^{-1} of specific capacity based on the $\text{Li}_4\text{Ti}_5\text{O}_{12}$ component. On the other hand, electrochemical performance of the LTO-AC simple mixing electrode is deteriorated at a high rate circumstance compared to LTO/AC hybrid nanotube in Figure 4.8. These results show that simply mixed state of LTO and AC in the electrode is not available to generate the synergetic effects on the charge transfer kinetics at a

high rate. It is a good agreement with charge/discharge potential profiles in Figure 4.A1C. The margin between charge and discharge plateaus for LTO component is proportionally increased with charge/discharge rate, which reflects increase of polarity of LTO-AC simple mixing electrode due to poor charge transfer kinetics. Also, charge/discharge plateaus are almost disappeared and linear slope of profiles are emerged over 3000 mA g^{-1} of high rate.

Electrochemical performances of the half-cell for LTO, LTO-AC simple mixing, and LTO/AC hybrid nanotube are illustrated in Figure 4.A2 as the discharge capacity decay in comparison with capacity at 100 mA g^{-1} of charge/discharge rate. It is clearly shown that simple mixing of activated carbon with $\text{Li}_4\text{Ti}_5\text{O}_{12}$ is more effective on the electrochemical performance than pure $\text{Li}_4\text{Ti}_5\text{O}_{12}$, however, it is difficult to expect the synergetic effects on the charge transfer kinetics with simple mixing method compared to LTO/AC hybrid nanotube.

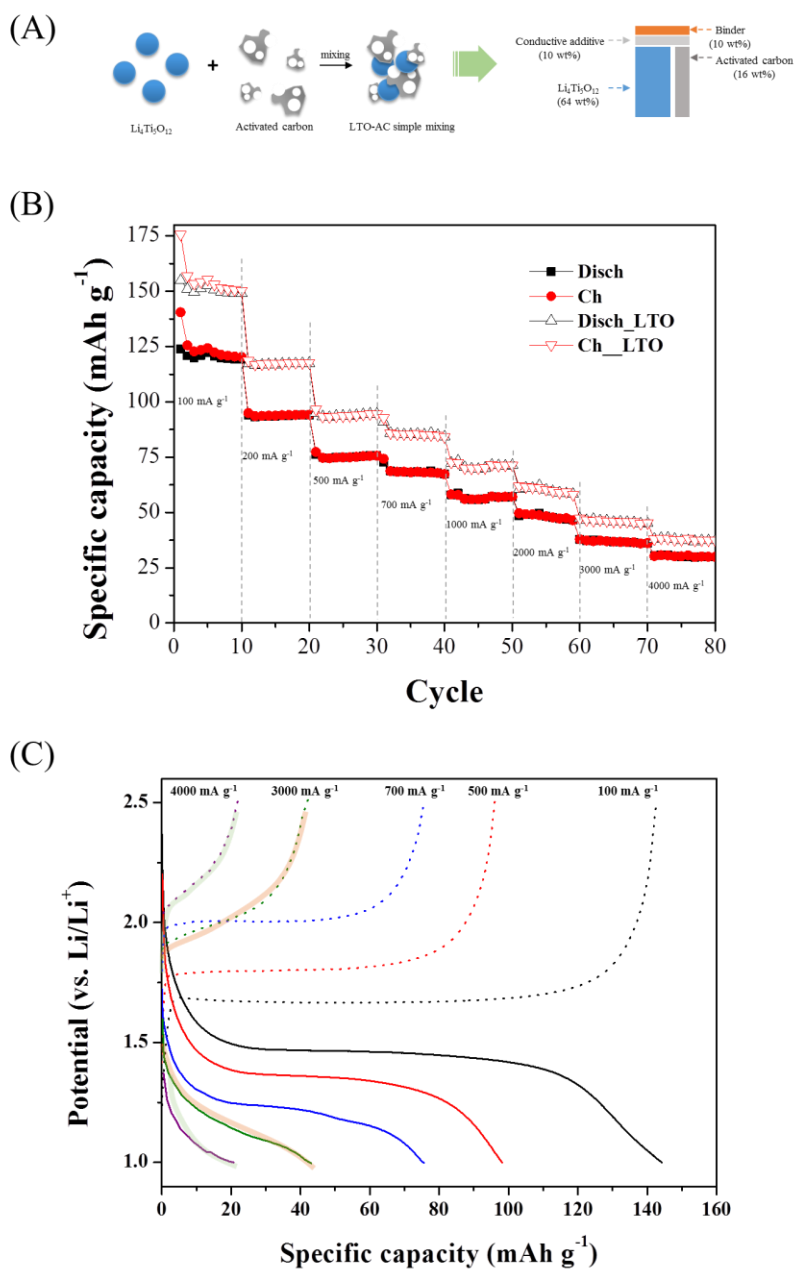


Figure 4.A1. (A) Scheme of LTO-AC simple mixing electrode. (B) Cycle stability and (C) charge/discharge profiles of LTO-AC simple mixing electrode in the half-cell test at various charge/discharge rates

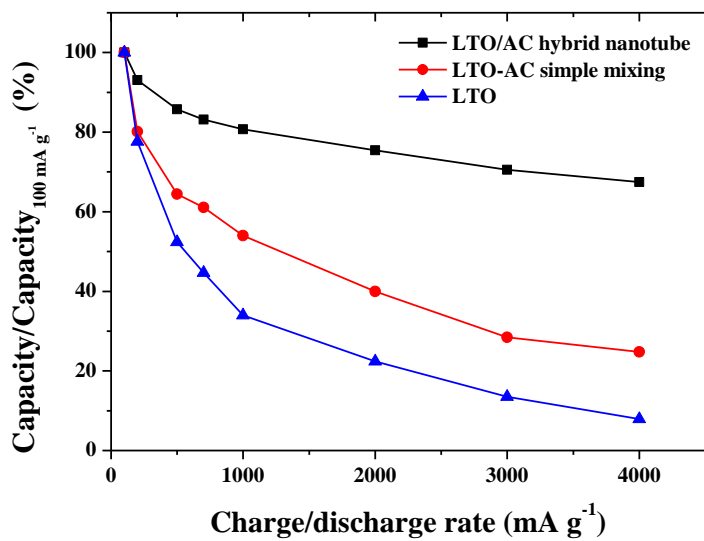


Figure 4.A2. Cycle stability comparison of LTO, LTO-AC simple mixing, and LTO/AC hybrid nanotube electrode in the half-cell test at various charge/discharge rates.

LTO//AC asymmetric capacitor and LTO-AC simple mixing//AC asymmetric capacitor were fabricated and tested to compare electrochemical performances with the LTO/AC hybrid nanotube//AC BatCap system. Figure 4.A3 shows scheme of LTO//AC asymmetric capacitor with theoretical charge/discharge potential profile and charge/discharge potential profile of LTO//AC asymmetric capacitor at low and high rates in the potential range from 0.0 to 3.0 V. Potential profile of negative electrode indicates typical constant value at 1.6 V vs. Li/Li⁺ with small margin between charge and discharge process at a low rate. When the charge/discharge rate increase to 18 C of the high rate, margin is drastically increased due to polarization of LTO from poor charge transfer kinetics at a high rate.

On the other hand, charge/discharge potential profile of LTO-AC simple mixing//AC asymmetric capacitor is illustrated in Figure 4.A4 with scheme and theoretical charge/discharge potential profile. Because battery component, Li₄Ti₅O₁₂, and capacitor component, activated carbon, are simply mixed without any chemical bonding such as covalent bond in the electrode, electrons are moved into both of components which of potential can be determined by sum of potential for the battery and capacitor component. Hence, potential of negative electrode can be estimated as slowly increasing and decreasing shape illustrated in the theoretical potential profile in Figure 4.A4A. In the experimental results for LTO-AC simple mixing//AC asymmetric capacitor, polarization of the LTO in the electrode is obviously shown not only at a low charge/discharge rate but also at a high charge/discharge rate. Also, potential

of the negative electrode is drastically ascended in the discharge process indicating poor charge transfer kinetics. Therefore, from this result, simply mixed battery and capacitor components is not available to give synergetic performance improvement to each other, which is manifest difference with the BatCap system.

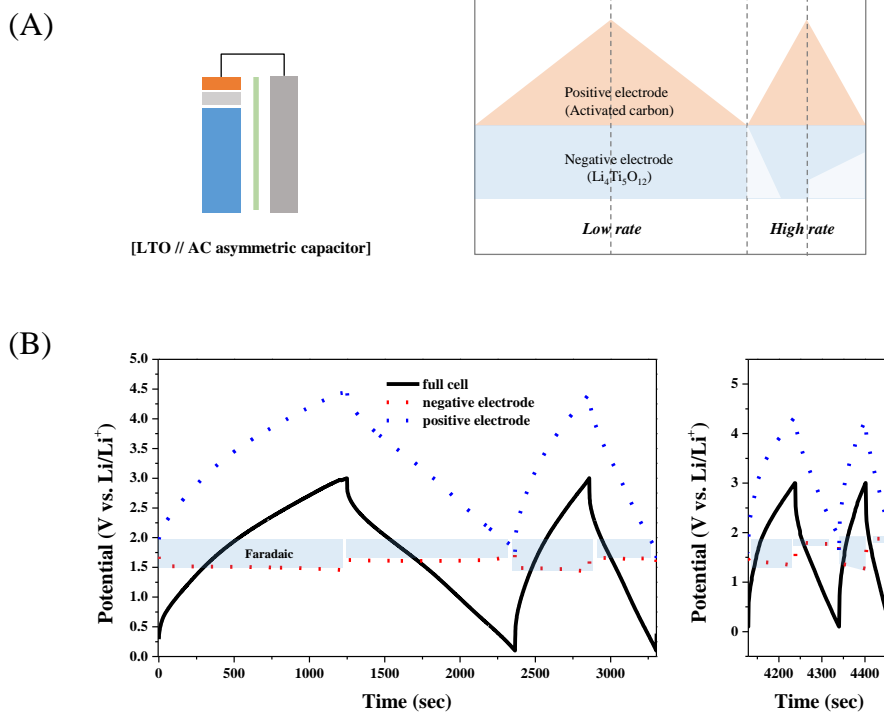
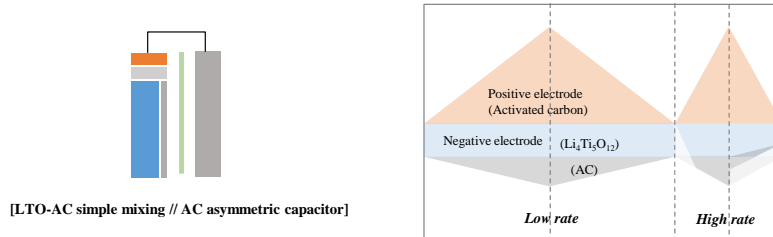


Figure 4.A3. (A) Scheme of LTO//AC asymmetric capacitor with theoretical charge/discharge potential profile and (B) charge/discharge potential profile of LTO//AC asymmetric capacitor at low (left side) and high (right side) rates.

(A)



(B)

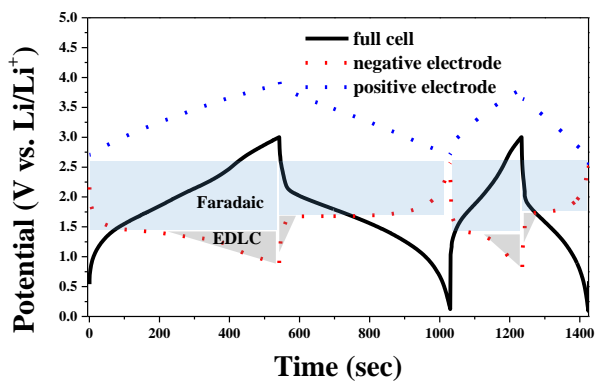


Figure 4.A4. (A) Scheme of LTO-AC simple mixing//AC asymmetric capacitor with theoretical charge/discharge potential profile and (B) charge/discharge potential profile of LTO-AC simple mixing//AC asymmetric capacitor at low and high rates.

Figure 4.A5 indicates Ragone plot for the AC//AC symmetric capacitor, LTO/AC hybrid nanotubes//AC hybrid BatCap system, LTO//AC asymmetric capacitor, and LTO-AC simple mixing//AC asymmetric capacitor at various charge/discharge rates. In a low power density range, LTO//AC asymmetric capacitor showed the highest specific energy density because of large amount of $\text{Li}_4\text{Ti}_5\text{O}_{12}$ component in the negative electrode. Moreover, LTO-AC simple mixing//AC asymmetric capacitor and LTO/AC hybrid nanotube//AC BatCap indicated almost similar value of specific energy density due to similar ratio of $\text{Li}_4\text{Ti}_5\text{O}_{12}$ component in the electrode. On the contrary, specific energy density of LTO//AC asymmetric capacitor is rapidly deteriorated at a high power density range due to poor charge transfer kinetics which is already revealed in Figure 4.A3. Also, LTO/AC hybrid nanotube//AC BatCap shows better electrochemical performance than LTO-AC simple mixing//AC asymmetric capacitor at a high power density range, which clearly indicates the synergetic effects of battery and capacitor components with hybridization on the charge transfer kinetics compared to the simply mixed components. Therefore, BatCap system with battery and capacitor components hybridization is valid strategy to enhance the electrochemical performance to improve the typical capacitors.

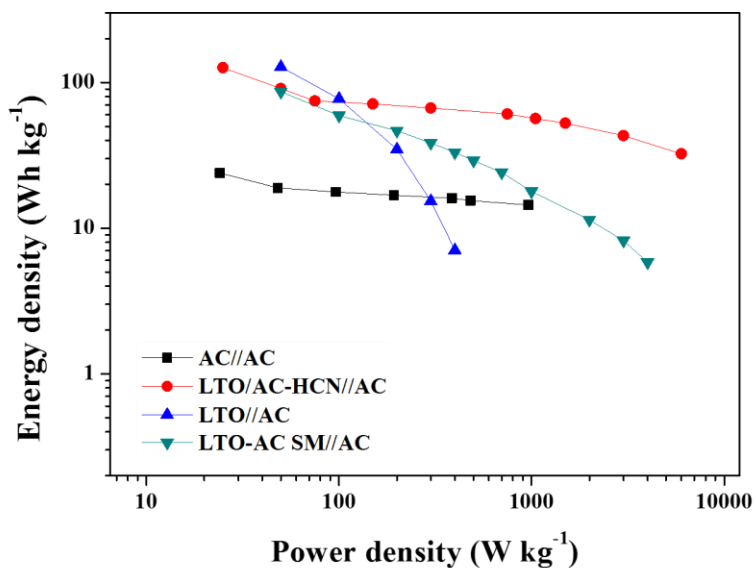


Figure 4.A5. Ragone plot for the AC//AC symmetric capacitor, LTO/AC hybrid nanotubes//AC hybrid BatCap system, LTO//AC asymmetric capacitor, and LTO-AC simple mixing//AC asymmetric capacitor at various charge/discharge rates. The data were calculated based on the total mass of both electrodes.

4.6. References

- [1] J.M. Tarascon, M. Armand, *Nature*, 414 (2001) 359-367.
- [2] A.S. Arico, P. Bruce, B. Scrosati, J.M. Tarascon, W. Van Schalkwijk, *Nature Materials*, 4 (2005) 366-377.
- [3] R. Marom, S.F. Amalraj, N. Leifer, D. Jacob, D. Aurbach, *Journal of Materials Chemistry*, 21 (2011) 9938-9954.
- [4] P. Simon, Y. Gogotsi, *Nature Materials*, 7 (2008) 845-854.
- [5] J.B. Goodenough, Y. Kim, *Chemistry of Materials*, 22 (2009) 587-603.
- [6] H. Li, Z. Wang, L. Chen, X. Huang, *Advanced Materials*, 21 (2009) 4593-4607.
- [7] F. Cheng, J. Liang, Z. Tao, J. Chen, *Advanced Materials*, 23 (2011) 1695-1715.
- [8] A. Du Pasquier, I. Plitz, S. Menocal, G. Amatucci, *Journal of Power Sources*, 115 (2003) 171-178.
- [9] A.D. Pasquier, I. Plitz, J. Gural, S. Menocal, G. Amatucci, *Journal of Power Sources*, 136 (2004) 160-170.
- [10] V.L. Pushparaj, M.M. Shaijumon, A. Kumar, S. Murugesan, L. Ci, R. Vajtai, R.J. Linhardt, O. Nalamasu, P.M. Ajayan, *Proceedings of the National Academy of Sciences*, 104 (2007) 13574-13577.
- [11] Y.F. Tang, L. Yang, Z. Qiu, J.S. Huang, *Electrochemistry Communications*, 10 (2008) 1513-1516.
- [12] S.C. Lee, S.M. Lee, J.W. Lee, J.B. Lee, S.M. Lee, S.S. Han, H.C. Lee, H.J. Kim, *The Journal of Physical Chemistry C*, 113 (2009) 18420-18423.

- [13] Y. Tang, L. Yang, S. Fang, Z. Qiu, *Electrochimica Acta*, 54 (2009) 6244-6249.
- [14] J.Z. Chen, L. Yang, S.H. Fang, Y.F. Tang, *Electrochimica Acta*, 55 (2010) 6596-6600.
- [15] J. Shu, *Electrochimica Acta*, 54 (2009) 2869-2876.
- [16] R. Cai, X. Yu, X. Liu, Z. Shao, *Journal of Power Sources*, 195 (2010) 8244-8250.
- [17] N. He, B. Wang, J. Huang, *Journal of Solid State Electrochemistry*, 14 (2010) 1241-1246.
- [18] X. Li, M. Qu, Z. Yu, *Solid State Ionics*, 181 (2010) 635-639.
- [19] N. Zhu, W. Liu, M. Xue, Z. Xie, D. Zhao, M. Zhang, J. Chen, T. Cao, *Electrochimica Acta*, 55 (2010) 5813-5818.
- [20] Z. Chen, V. Augustyn, J. Wen, Y. Zhang, M. Shen, B. Dunn, Y. Lu, *Advanced Materials*, 23 (2010) 791-795.
- [21] K. Zhang, B.T. Ang, L.L. Zhang, X.S. Zhao, J. Wu, *Journal of Materials Chemistry*, 21 (2011) 2663-2670.
- [22] H.Y. Lee, J.B. Goodenough, *Journal of Solid State Chemistry*, 144 (1999) 220-223.
- [23] A. Yuan, Q. Zhang, *Electrochemistry Communications*, 8 (2006) 1173-1178.
- [24] T. Aida, I. Murayama, K. Yamada, M. Morita, *Journal of Power Sources*, 166 (2007) 462-470.

- [25] Y.Y. Liang, H.L. Li, X.G. Zhang, *Materials Science and Engineering a-Structural Materials Properties Microstructure and Processing*, 473 (2008) 317-322.
- [26] Z. Fan, J. Yan, L. Zhi, Q. Zhang, T. Wei, J. Feng, M. Zhang, W. Qian, F. Wei, *Advanced Materials*, 22 (2010) 3723-3728.
- [27] Y.-G. Wang, Z.-D. Wang, Y.-Y. Xia, *Electrochimica Acta*, 50 (2005) 5641-5646.
- [28] K.-W. Nam, C.-W. Lee, X.-Q. Yang, B.W. Cho, W.-S. Yoon, K.-B. Kim, *Journal of Power Sources*, 188 (2009) 323-331.
- [29] F. Ataherian, N.-L. Wu, *Electrochemistry Communications*, 13 (2011) 1264-1267.
- [30] W.G. Pell, B.E. Conway, *Journal of Power Sources*, 136 (2004) 334-345.
- [31] T. Brousse, R. Marchand, P.L. Taberna, P. Simon, *Journal of Power Sources*, 158 (2006) 571-577.
- [32] G.G. Amatucci, F. Badway, A.D. Pasquier, T. Zheng, *Journal of The Electrochemical Society*, 148 (2001) A930-A939.
- [33] V. Khomenko, E. Raymundo-Piñero, F. Béguin, *Journal of Power Sources*, 177 (2008) 643-651.
- [34] K. Naoi, S. Ishimoto, Y. Isobe, S. Aoyagi, *Journal of Power Sources*, 195 (2010) 6250-6254.
- [35] H.S. Choi, T. Kim, J.H. Im, C.R. Park, *Nanotechnology*, 22 (2011).
- [36] I. Ji Hyuk, Y. Seung Jae, Y. Chang Hun, P. Chong Rae, *Nanotechnology*, 23 (2012) 035604.

- [37] N. Iwashita, C.R. Park, H. Fujimoto, M. Shiraishi, M. Inagaki, *Carbon*, 42 (2004) 701-714.
- [38] S.H. Gihm, C.R. Park, *Carbon*, 44 (2006) 1016-1019.
- [39] H.S. Choi, J.G. Lee, H.Y. Lee, S.W. Kim, C.R. Park, *Electrochimica Acta*, 56 (2010) 790-796.
- [40] T. Morishita, Y. Soneda, T. Tsumura, M. Inagaki, *Carbon*, 44 (2006) 2360-2367.
- [41] Y.J. Hwang, S.K. Jeong, K.S. Nahm, J.S. Shin, A. Manuel Stephan, *Journal of Physics and Chemistry of Solids*, 68 (2007) 182-188.
- [42] M. Sathishkumar, K. Vijayaraghavan, A.R. Binupriya, A.M. Stephan, J.G. Choi, S.E. Yun, *Journal of Colloid and Interface Science*, 320 (2008) 22-29.
- [43] S.-J. Zhang, H.-Q. Yu, H.-M. Feng, *Carbon*, 44 (2006) 2059-2068.
- [44] U.K. Fatema, A.J. Uddin, K. Uemura, Y. Gotoh, *Textile Research Journal*, 81 (2011) 659-672.
- [45] Z. Yue, C.L. Mangun, *J. Economy, Carbon*, 42 (2004) 1973-1982.
- [46] S.-J. Zhang, H.-M. Feng, J.-P. Wang, H.-Q. Yu, *Journal of Colloid and Interface Science*, 321 (2008) 96-102.
- [47] R.J. Nemanich, J.T. Glass, G. Lucovsky, R.E. Shroder, *Journal of Vacuum Science & Technology a-Vacuum Surfaces and Films*, 6 (1988) 1783-1787.
- [48] R.E. Shroder, R.J. Nemanich, J.T. Glass, *Physical Review B*, 41 (1990) 3738-3745.
- [49] M.A. Tamor, W.C. Vassell, *Journal of Applied Physics*, 76 (1994) 3823-3830.

- [50] N. Colthup, L. Daly, S. Wiberley, Introduction to Infrared and Raman Spectroscopy, Academic, New York, 1975.
- [51] Y. Zhao, G. Liu, L. Liu, Z. Jiang, Journal of Solid State Electrochemistry, 13 (2009) 705-711.
- [52] J. Haetge, P. Hartmann, K. Brezesinski, J. Janek, T. Brezesinski, Chemistry of Materials, 23 (2011) 4384-4393.
- [53] H.-G. Jung, S.-T. Myung, C.S. Yoon, S.-B. Son, K.H. Oh, K. Amine, B. Scrosati, Y.-K. Sun, Energy & Environmental Science, 4 (2011) 1345-1351.
- [54] E. Kang, Y.S. Jung, G.-H. Kim, J. Chun, U. Wiesner, A.C. Dillon, J.K. Kim, J. Lee, Advanced Functional Materials, 21 (2011) 4349-4357.
- [55] K. Dokko, M. Mohamedi, M. Umeda, I. Uchida, Journal of The Electrochemical Society, 150 (2003) A425-A429.
- [56] Y. Li, H. Zhao, Z. Tian, W. Qiu, X. Li, Rare Metals, 27 (2008) 165-169.
- [57] H. Bai, C. Li, X. Wang, G. Shi, The Journal of Physical Chemistry C, 115 (2011) 5545-5551.
- [58] M. Shi, Z. Chen, J. Sun, Cement and Concrete Research, 29 (1999) 1111-1115.
- [59] L. Wei, M. Sevilla, A.B. Fuertes, R. Mokaya, G. Yushin, Advanced Energy Materials, 1 (2011) 356-361.

Part IV

Positive electrodes for the BatCap system

Chapter 5. Preparation and Electrochemical Performance of Sulfur-Carbon Nanosheet Hybrids via a Solid Solvothermal Reaction for a Positive Electrode of the BatCap System

5.1. Introduction

BatCap system is one of the acceptable candidates as the advanced energy storage system to alternate the typical electrochemical devices such as batteries and supercapacitors [1]. Compared to recently studied materials on the battery-type negative electrode, currently commercialized LiCoO_2 and LiFePO_4 show a low specific capacity under 180 mAh g^{-1} as the cathode material for LIBs, requiring new approach for the battery-type positive electrode material to enhance the performance of for the BatCap system or asymmetric capacitor. This issue also includes their extremely high cost and the toxicity of the precursors and production processes, despite of their success in the portable electronic devices market [2, 3]. Elemental sulfur is a well-known potential candidate to alternate the present cathode materials because it is inexpensive, plentiful in nature, and has the highest theoretical capacity of 1672 mAh g^{-1} [4-6], which gives the opportunity to use the sulfur-related material as the positive electrode material for the BatCap system. Unfortunately, pristine elemental sulfur is not possible to use directly in the positive electrode for electrochemical

devices due to its insulating nature and the on account of the dissolution of the polysulfides (Li_2S_n , $4 \leq n \leq 8$) into the electrolyte, a process known as the “shuttle reaction” [6-8]. These problems cause imperfect utilization of the active material due to the low electron conductivity and poor cycle stability caused by the loss of the active material.

Various approaches have been studied to overcome aforementioned problems in recent years, such as electrolyte control[9-11], using a composite with highly conductive materials [12-17], and introducing template materials for the confinement of the sulfur [6, 18-20]. In particular, mesoporous carbonaceous materials are commonly used as a sulfur-containing template to overcome the abovementioned problems [5, 21-25]. Mesoporous carbonaceous materials combined with sulfur enable facile charge transfer of both electrons and the electrolyte owing to the creation of a conductive electron pathway and due to their opened-porous structure. Also, mesoporous carbonaceous materials effectively work as a template for the sulfur, allowing excellent contact due to their very large surface area and ordered structure in which dissolved polysulfide can be confined, preventing “shuttle reaction”. On the other hand, there have been several different attempts to enhance the cycle stability of the sulfur-containing electrodes by controlling the electrochemical reaction in order to prevent dissoluble polysulfide production with a composite containing a conductive polymer such as polyacrylonitrile or polypyrrole [4, 26-28].

Herein, we report a unique strategy to introduce the new potentiality of the sulfur as the positive electrode material through *in-situ* sulfur-carbon nanosheet

hybridization. Sulfur-carbon nanosheet hybrids (denoted as SCNHs) are successfully synthesized in a single-step solid solvothermal reaction to enable a simple, mass-production process [29-31] compared to the previously reported methods for sulfur-carbonaceous material composite such as the graphene-sulfur composite which uses reduced graphite oxide. The sulfur components in the SCNHs are controlled by means of hybridization with carbon nanosheet using a solid solvothermal reaction, giving them a beneficial effect for the enhancement of the electrochemical performance and an advantageous form of nanosheet morphology for better electron and ion conductivity. The charge transfer reaction of the SCNH is improved through the use of a carbon component resulting in the enhancement of the electrical and morphological properties. Using carbon nanosheet components and with proper control of the chemical-state of the sulfur, the electrochemical performance of the SCNH is enhanced compared to that of elemental sulfur. Also, SCNH//AC BatCap, which of SCNH is fabricated as the positive electrode in the full cell, indicated better electrochemical performance than that of AC//AC symmetric capacitor.

5.2. Experimental

5.2.1. Reagents and chemicals

Tetrachloroethylene (TCE; Aldrich), sulfur (Aldrich), sodium (Aldrich), hydrogen chloride (HCl; Deajung, Korea), and ethanol (Deajung, Korea) were purchased and used without any further treatment.

5.2.2. Synthesis of SCNH

TCE (0.55 ml, 0.0054 mol) was mixed with sulfur (0.69 g, 0.0217 mol) and sodium (0.50 g, 0.0217 mol) in a 30 ml stainless steel autoclave under an argon gas atmosphere to prevent any side reaction. The solvothermal reaction was carried out at 300 °C for 12 hrs in argon (Ar), and was then naturally cooled to room temperature. The product was sequentially washed and filtered with 50 wt% HCl solution, deionized water, and ethanol several times. After the washing procedure, the products, SCNHs, were dried in a vacuum oven at 80 °C overnight before further characterization processes were carried out.

5.2.3. Characterizations of SCNH

A field-emission scanning electron microscope (FE-SEM; JSM-6700F, JEOL) and a transmission electron microscope (TEM; JEM-2010, JEOL) were utilized to investigate the morphologies of the SCNHs. Powder X-ray diffraction (XRD) was carried out using a D8 Advance diffractometer (Bruker) to analyze the microstructure of the product in the reflection mode of Ni-filtered $\text{CuK}\alpha$

radiation ($\lambda=0.154184$ nm) with standard procedure.[14] Raman spectroscopy was performed on a RAMANplus confocal laser Raman microscope (Nanophoton) using 532 and 785 nm laser wavelengths to investigate the surface chemical structure of the product. X-ray photoelectron spectroscopy (XPS; AXIS-HSi, KRATOS) was also employed to study the surface characteristics of the product and elemental sulfur. Thermogravimetric analysis (TGA; SDT Q600, TA) and SEM/energy dispersive X-ray spectroscopy (SEM/EDS) were conducted to determine the proportion of the sulfur element in the product.

5.2.4. Electrochemical tests of SCNH

The electrochemical performances of the SCNH were investigated using a battery cycler (WBCS3000, WonATech) as the 2032 coin-type half-cell in the Ar-filled glove box (Korea Kiyon). The working electrode in the half-cell was prepared using polyvinylidene (15 wt%), carbon black (15 wt%), and active material (70 wt%) with Li metal as the reference electrode and Celgard 2400 as the separator. The electrolyte in the cell was constructed using lithium trifluoromethanesulfonate (1M) in a tetraethylene glycol dimethyl ether/1,3-dioxolane (1:1 of molar ratio) solution. Cyclic voltammetry (CV) and cycle performance tests (constant-current mode) of the SCNHs were carried out using the fabricated half-cell in the potential range 1.5-3.5 V vs. Li/Li⁺. An electrochemical impedance spectroscopy (EIS) study was conducted with a multi-channel potentiostat generator (VMP3, Bio-Logic). The 2032 coin-type

half-cell for the elemental sulfur was fabricated using the correspondent process of the SCNHs half-cell for comparison. Also, electrochemical characteristics as the positive electrode for the BatCap system was conducted by full cell test with commercialized activated carbon (AC) (SX Ultra, Norit) as the negative electrode.

5.3. Results and discussion

5.3.1. Microstructural and morphological characteristics of SCNH

The synthesis of the SCNHs was successively acquired by means of a single-step solid solvothermal reaction using TCE as the carbon precursor, sodium as the reductant, and elemental sulfur as the sulfur precursor. During the formation of the carbon nanosheet through low-temperature reduction of TCE at 300 °C with sodium, melted elemental sulfur was homogeneously hybridized with carbon without interfering with the nanosheet formation process. As shown in Figures 5.1A and 5.1B, the 2D morphology of the SCNHs was well prepared after the solid solvothermal reaction. This is similar with the morphology of the carbon nanosheets (CNs) synthesized using the same procedure without sulfur precursor. Figure 5.2 shows morphological characteristics of the CNs using FE-SEM and TEM analyses. The morphology of the CNs prepared by solid solvothermal reaction is similar with the morphology of the SCNHs which are synthesized using almost same procedure containing sulfur precursor in Figure 5.1. These results confirm that sulfur-carbon hybridization is available without morphology change in the preparation of the SCNHs using a single-step solid solvothermal reaction. This morphology is advantageous for good electronic and ionic conductivity owing to the high surface area of the nanosheet structure. The TEM images in Figures 5.1C and 5.1D clearly exhibit a well-developed thin layer of carbon nanosheet with a crumpled structure. Moreover, this

crumpled morphological characteristic of the SCNHs can help prevent the restacking problem which easily arises during the preparation of reduced graphite oxide-used composite without further treatment [33, 34].

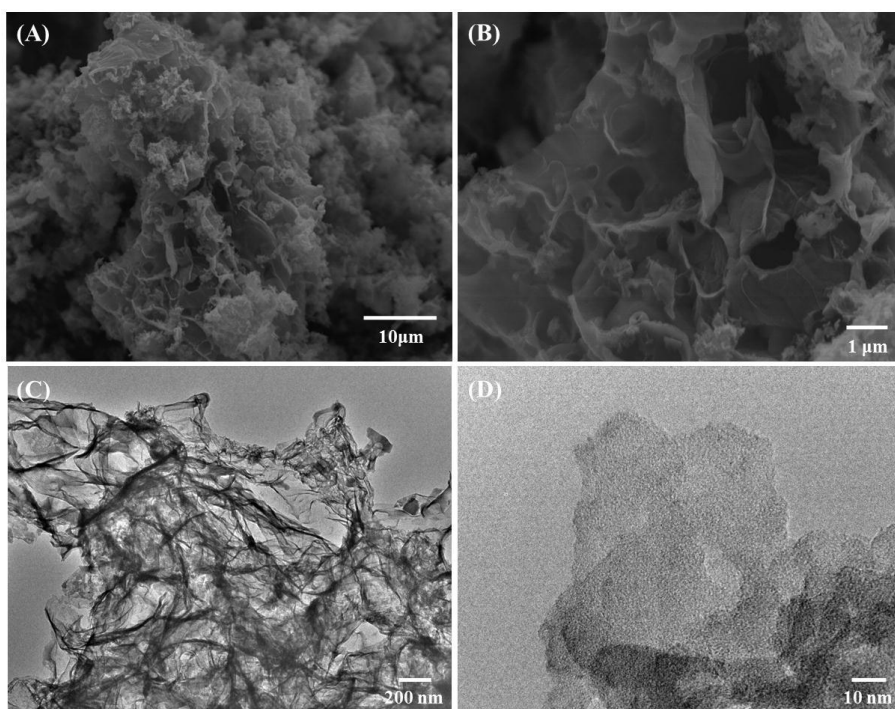


Figure 5.1. FE-SEM images of the SCNHs under (A) low and (B) high magnification. (C) TEM and (D) HR-TEM images of the SCNH showing crumpled carbon nanosheet.

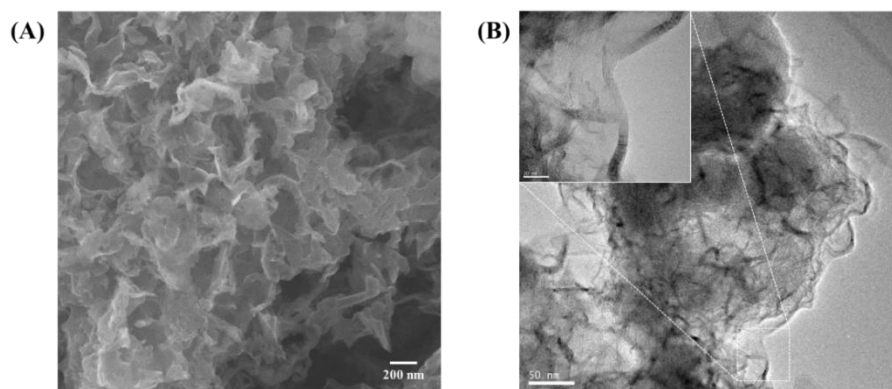


Figure 5.2. FE-SEM image (A) and TEM images (B) of the CNs showing crumpled carbon nanosheet.

The EDS mapping analysis of the SCNHs shown in Figure 5.3A indicates that the sulfur element in the hybrids was uniformly embedded in the carbon nanosheet after the solid solvothermal reaction. The sulfur content in the SCNHs existed homogeneously in the composite at a level of about 50 wt%, as summarized in Table 5.1. This value is similar to that of the sulfur ratio, as calculated by the TGA result. The well embedded elemental sulfur affects the crystal structure of the hybrid, as shown in the powder XRD pattern of the SCNHs in Figure 5. 3B. Based on the XRD pattern of the elemental sulfur and CNs, the hybrids containing crystal sulfur with an amorphous structure of carbon nanosheet exhibited a broad peak of the diffraction pattern of around 25 °. Also, there was no additional peak from the carbon sulfide residue which cannot serve as an active material for the battery component in the BatCap system. As a result, the well-embedded sulfur in the hybrids with the crystal structure after the solid solvothermal reaction is feasible for use as the electrochemical active component.

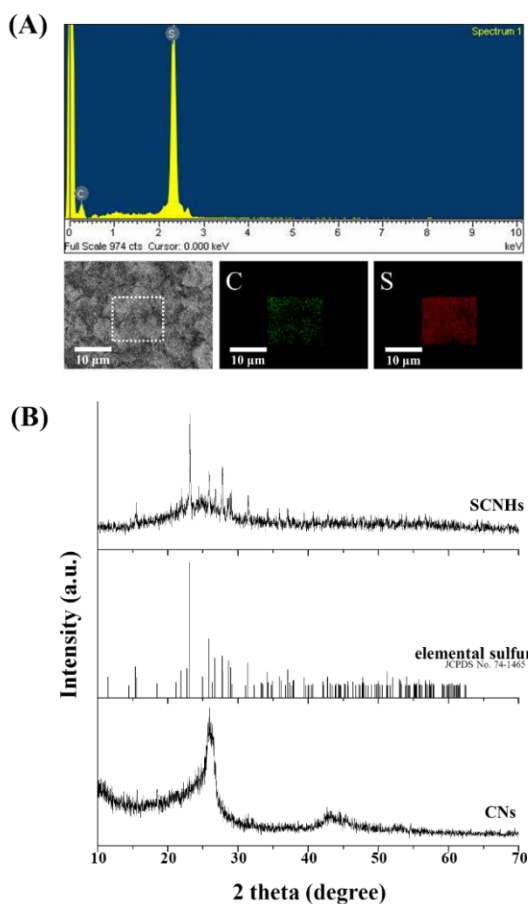


Figure 5.3. (A) EDS mapping analysis results of the SCNHs for elements of carbon (green) and sulfur (red). (B) Powder XRD patterns of the SCNHs (above), elemental sulfur (middle), and the CNs (bottom).

Table 5.1. Component distribution analysis results by EDS.

Element	Weight%
C	50.23
S	49.77

5.3.2. Surface characteristics of SCNH

The surface characteristics of the SCNHs were analyzed using XPS and Raman spectroscopy. Figure 5.4A indicates the survey XPS spectra with magnified views of the carbon (C1s) and sulfur (S2p) peaks in the insets. The C1s peak from the carbon nanosheet indicates a single curve corresponding to a C=C or C-C bond at a binding energy of 284.59 eV. This result confirms the absence of a chemical reaction between the sulfur and carbon in the SCNHs after the solid solvothermal reaction. In the case of sulfur, the S2p peak can be deconvoluted into two peaks at 165.12 (S2p_{1/2}) and 163.92 eV (S2p_{3/2}). These are slightly lower values compared to typical peaks of elemental sulfur (chemical shift: -0.60 eV of the S2p_{3/2} peak in Figure 5.4A), thus indicating the chemical shift of the sulfur in the SCNHs due to higher electronegativity (2.58) of the sulfur than that of the carbon (2.55) [6, 35, 36]. That is, sulfur atoms will slightly pull the valence electrons of the adjacent carbon atoms, resulting in a less tightly held core electrons by the positively charged sulfur nucleus as a result of more electrostatic-screening by the valence electrons.

The Raman spectrum in Figure 5.4B also exhibits a typical sulfur peak at 497 cm⁻¹ [37]. Moreover, there is no peak in the Raman shift range of around 600-800 cm⁻¹ from the C-S chemical bond [38, 39], which is in good agreement with the XPS analysis result for the sulfur. A broad peak situated between 1100 and 1700 cm⁻¹ arose, most likely due to the amorphous carbon with C=C or C-C bonds in the SCNHs [40] with good agreement of the XRD result in Figure 5.3B. The amorphous phase of the carbon in the SCNHs is different from that

of other typical carbonaceous materials synthesized by a solid solvothermal reaction using a carbon-chlorine precursor under a similar condition [29, 41, 42] resulting in the interference of the sulfur elements during the production of the carbon nanosheet. These results of the surface characteristics of SCNHs clearly exhibit that sulfur and carbon were present as independent elements without chemical bonds, in spite of the chemical-state change of the sulfur contents during the hybridization process with carbon due to difference of electronegativity, as shown in XPS result. The sulfur contents in the SCNHs showing similar chemical-state of sulfur in the high-n lithium polysulfide of Li_2S_n can affect the electrochemical reaction when applied as the positive electrode and cathode in the BatCap system and LiS batteries, respectively.

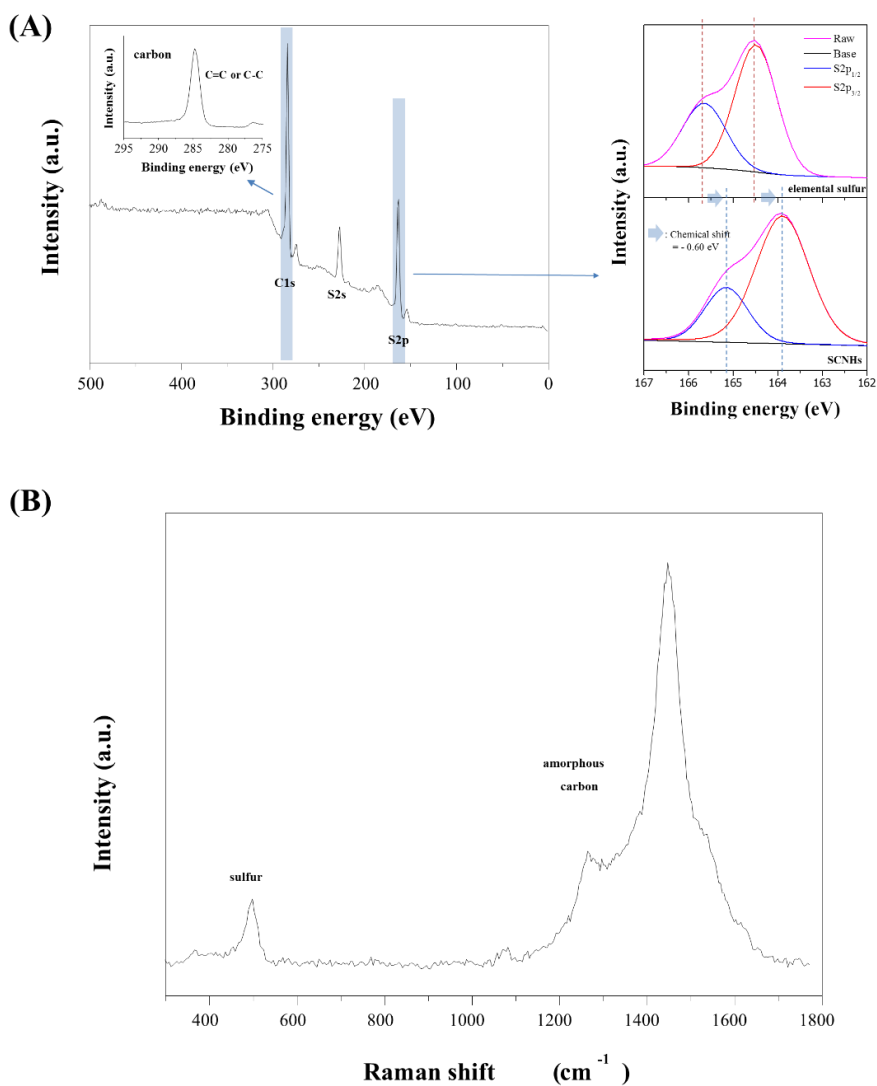


Figure 5.4. XPS (A) and Raman (B) spectrum of the SCNHS. The inset of (A) depicts a magnified view of the the carbon, and a magnified spectrum on the left of (A) indicates XPS of elemental sulfur (top) and SCNHS (bottom). Blue arrow is the amount of chemical shift after hybridization of sulfur and carbon

5.3.3. Electrochemical performance of SCNH

To analyze the electrochemical performance of the SCNHs as the positive material for the BatCap system, cyclic voltammetry and charge/discharge performance tests at various rates were conducted using Li/electrolyte/SCNHs cells. As shown in Figure 5.5A, there are two cathodic reaction peaks for the SCNHs at 2.4 and 1.8 V, which were slightly shifted to higher value compared to those when elemental sulfur was used. The cathodic peak at 2.4 V arose due to the electrochemical reaction of soluble polysulfide Li_2S_n , $4 \leq n \leq 8$, while the peak at 1.8 V is from the formation of dissoluble polysulfide of Li_2S_n , $n \leq 4$. [5, 43, 44] The intensity of the peak at 1.8 V is stronger than that of the peak at 2.4 V, indicating the opposite tendency of the elemental sulfur. These results can be also observed in the researches of the nitrogen-doped carbon/sulfur composite materials for LiS batteries containing higher electronegativity atoms, nitrogen (3.04). [4, 8, 27]

In contrast, the cyclic voltammogram of the elemental sulfur shows a major cathodic peak at 2.45 V corresponding to the formation of soluble polysulfide causing the shuttle reaction in the LiS batteries. Furthermore, the lower potential difference between the cathodic and anodic peaks of the SCNHs indicates the lower polarization compared to that of the elemental sulfur, thus presenting better charge transfer kinetics. Therefore, these results indicate that sulfur element in SCNHs can be hybridized with carbon content using a solid solvothermal reaction, which can cause better cycle stability of the sulfur in the hybrid. Moreover, the carbon nanosheets in the hybrids enhance the charge

transfer kinetics during the electrochemical reaction due to improved electrical properties.

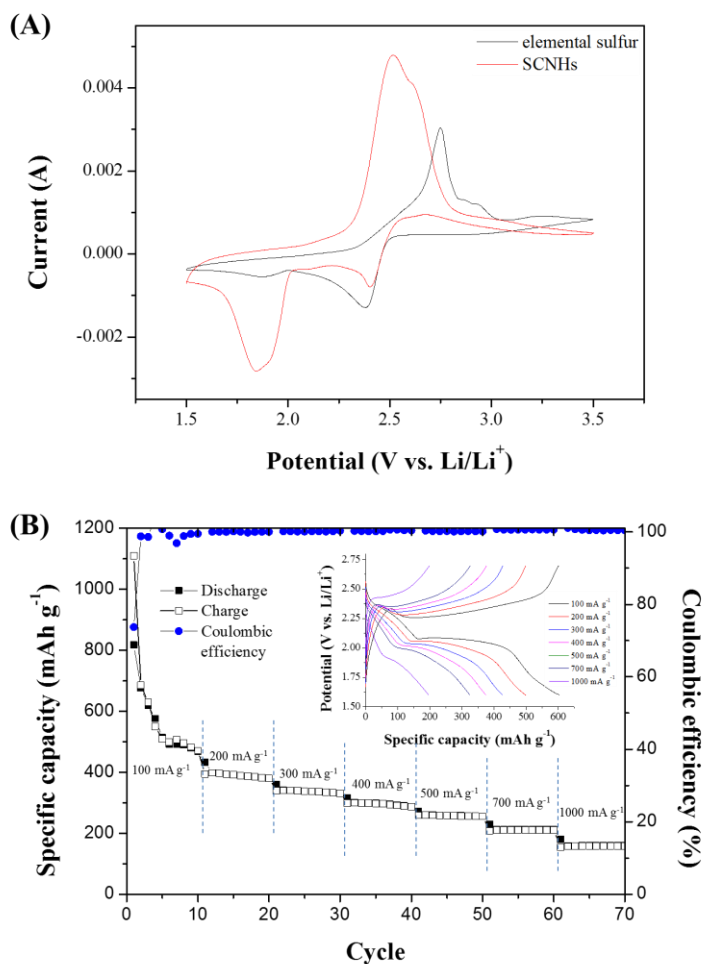


Figure 5.5. Electrochemical characterization of the SCNHs: (A) cyclic voltammetry of SCNHs and elemental sulfur in the second cycle at a sweep rate of 5 mV s^{-1} , and (B) cycle performance test results of the SCNHs at various charge/discharge rates. Specific capacities are calculated based on the sulfur mass. Inset of (B) depicts potential profiles of the SCNHs at various charge/discharge rates.

Figure 5.5B displays the cycle performance results with inset of charge/discharge potential profiles of the SCNHs at various charge/discharge rates. The specific capacity of SCNHs is about 810 mAh g^{-1} at 100 mA g^{-1} , which represents about 50 % of the overall usage based on the theoretical capacity of the sulfur. The reversible specific capacities of the hybrids are close to 510, 270, and 180 mAh g^{-1} at charge/discharge rates of 100, 500, and 1000 mA g^{-1} , respectively. Also, Coulombic efficiency of the SCNHs indicates nearly 100 % as compared to the use of typical sulfur, exhibiting a retained capacity of the SCNHs of over 35 % with a higher charge/discharge rate by tenfold. This result also indicates that the carbon nanosheet in SCNHs, containing homogeneously embedded sulfur, improves the electron and ion transport due to the better electronic conductivity and enhanced ion accessibility.

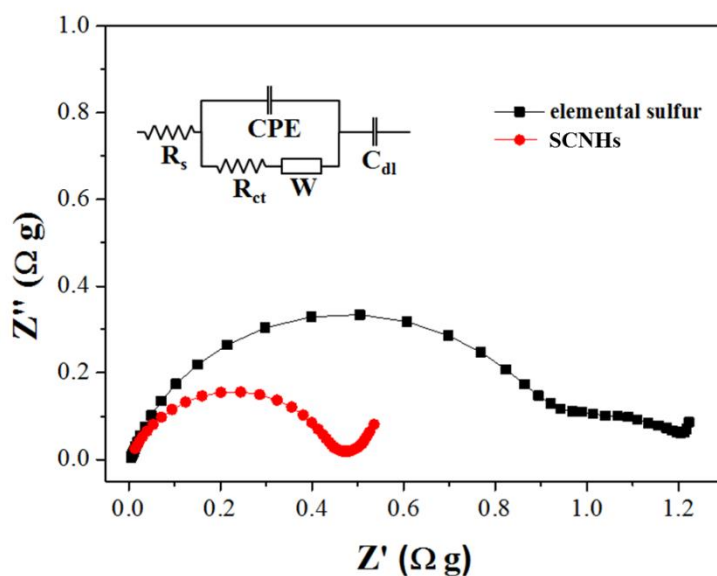


Figure 5.6. Nyquist impedance spectra of the SCNHS and pure sulfur. The inset shows the equivalent circuit evaluated based on the AC impedance spectra of the SCNHS and pure sulfur.

Table 5.2. Impedance parameters and Li^+ ion diffusion coefficient calculated from the impedance spectra of the SCNHS and pure sulfur.

Sample	R_s [$\Omega \text{ g}$]	R_{ct} [$\Omega \text{ g}$]	i_0 [mA cm^{-2}]	D_{Li^+} [$\text{cm}^2 \text{ s}^{-1}$]
SCNHS	0.14×10^{-3}	0.46	7.03×10^{-4}	1.10×10^{-10}
pure sulfur	5.83×10^{-3}	1.02	4.03×10^{-4}	2.81×10^{-11}

The Nyquist impedance spectra of the SCNHs and pure sulfur are illustrated in Figure 5.6. The AC impedance analysis spectra were fitted using a simple modified Randles–Ershler equivalent circuit[1] as shown in the inset, where W is the Waburg impedance, CPE is the constant phase element representing the double layer capacitance, and C_{dl} is the insertion capacitance under the applied potential. Also, the related parameters were calculated based on the impedance results, which are listed in Table 5.2.

The electrolyte solution resistance (R_s) and the charge transfer resistance at the active material/electrolyte interface (R_{ct}) were evaluated based on the left-hand and right-hand side impedance intercepts on the Z -real axis of the semicircle in the high-middle frequency range, respectively. The Li^+ ion diffusion kinetics was estimated based on the oblique line of the low frequency range, which is the Li^+ ion diffusion coefficient (D_{Li^+}) calculated by the following equation[45, 46]:

$$D_{Li^+}^{1/2} = \frac{RT}{2^{1/2} n^2 F^2 A} \times \frac{1}{\sigma C_{Li^+}} \quad (1)$$

where R is the gas constant ($R = 8.314 \text{ J mol}^{-1} \text{ K}^{-1}$), T is the working temperature, n is the number of electrons in the reaction, F is the Faradaic constant ($F = 96500 \text{ C mol}^{-1}$), A is the active surface area, and C_{Li^+} is the molar concentration of Li in an electrode active material. The Waburg impedance coefficient (σ) can be calculated from the slope of R_{ct} vs. $\omega^{1/2}$ (ω : angular frequency) in the medium

frequency range. Also, the values of the exchange current density (i_0) in Table 5.2 were estimated using the following equation.

$$i_0 = \frac{RT}{nFAR_{ct}} \quad (2)$$

It can be clearly seen that both the charge transfer resistance (R_{ct}) and the resistance of electrolyte (R_s) of the SCNHs were smaller than the corresponding values of the elemental sulfur. Furthermore, the SCNHs indicated the higher Li^+ ion diffusion coefficient (D_{Li^+}) and exchange current density (i_0) values compared to that of the elemental sulfur, suggesting the significantly better charge transfer reaction of the SCNHs than the elemental sulfur. Accordingly, the SCNHs can provide better cycle performance at high charge/discharge rates with excellent Coulombic efficiency close to 100% is due to the confined electrochemical reaction of dissolvable polysulfide, resulting in a low specific capacity and improved charge transfer kinetics.

Figure 5.7 illustrates the galvanostatic charge/discharge curves and Ragone plot of the AC//SCNHs BatCap system with separated potential profiles for each electrode and full-cell in the potential range of 0.1-1.8 V. The mass ratio of each electrode was controlled as $m_{\text{negative}}/m_{\text{positive}} = 4$ to balance the exchanged charges between the negative electrode, AC, and positive electrode, SCNHs. As shown in Figure 5.7A, curve-shaped slope was demonstrated in the early state of charge process for the full-cell potential plot due to a plateau region at

the positive electrode around 2.3 V vs. Li/Li⁺. Then, linear slope of full-cell potential profile was observed after charging of the positive electrode which was indicated on the potential profile for the SCNHs electrode. In the discharge process, curve-shaped slope followed by linear slope was revealed at the slightly higher full-cell potential state due to discharge process of the positive electrode around 2.3 V vs. Li/Li⁺. Negative electrode of this BatCap system, AC, illustrated the linear shape of typical potential profile for EDLC in the charge/discharge process. These results confirmed that AC//SCNHs can be operated as the BatCap system.

Ragone plot in Figure 5.7B indicates the electrochemical performance of the BatCap system consisting of AC//SCNHs. Energy densities at a variety of power densities were estimated by integrating the Q-V graph area during the discharge process based on the total mass of active materials of both negative and positive electrodes. Power densities were calculated using the equation, $PD_{\max} = V_{\max}I$, in which V_{\max} is the max working potential and charge/discharge current, I. As demonstrated in the Ragone plot, the energy density at a low power density, 100 W kg⁻¹, was obtained as 73 Wh kg⁻¹, which value is comparable with the typical AC//AC symmetric capacitor system of about 15 Wh kg⁻¹. In the middle of the Ragone plot for the BatCap system, energy density was rapidly decreased around 500 W kg⁻¹ of power density, because carbon nanosheets working as the capacitor-type material in the SCNHs were not enough conductive to tremendously enhance the energy density. On the other hand, AC//SCNHs BatCap system exhibited 14 Wh kg⁻¹ of energy density at a

high power density of 4000 W kg^{-1} , which is higher than that of AC//AC symmetric capacitor system of 10 Wh kg^{-1} .

These results shows that BatCap system fabricated with AC and SCNHs has enhanced electrochemical performances compared to the typical AC//AC symmetric capacitor system.

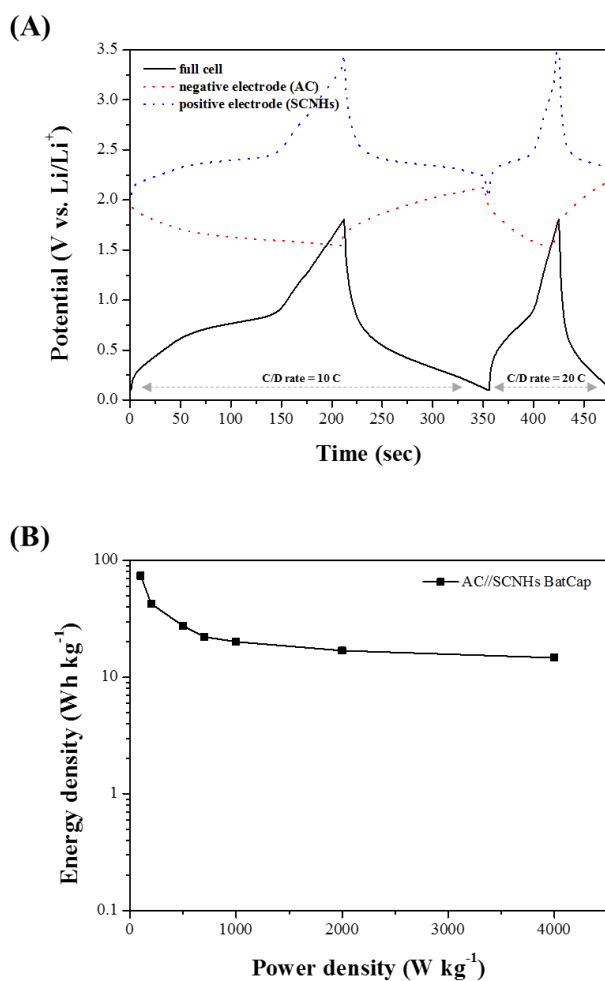


Figure 5.7. (A) Galvanostatic charge/discharge plot for the AC//SCNH BatCap system at a 10 C rate and a 20 C rate in the working potential range of 0.1-1.8 V. The black-colored potential profile indicates the full-cell, the blue-colored potential profile indicates the positive electrode of the AC//SCNH, and the red-colored potential profile indicates the negative AC electrode. (B) Ragone plot for the AC//SCNH BatCap system at various charge/discharge rates in the working potential range of 0.1-1.8 V. The data were calculated based on the total mass of both electrodes.

5.4. Conclusion

A unique sulfur-carbon hybrid was prepared simply by a single-step solid solvothermal reaction without any further additional treatment. The synthesized SCNHs contained chemical-state-controlled sulfur resulting in the hybridization with carbon without chemical bond. The CV results demonstrated that the major electrochemical reaction was confined during the production of dissoluble polysulfide at a cathodic potential of 1.8 V. This particular and controlled electrochemical reaction of SCNHs enhanced the cycle performance with excellent Coulombic efficiency even at a high charge/discharge rate of 1000 mA g⁻¹. The specific capacity of the hybrid was about 810 mAh g⁻¹ at a rate of 100 mA g⁻¹, which is lower compared to theoretical capacity of elemental sulfur due to better charge transfer kinetics from 2D carbon nanosheet-sulfur hybridization using solid-solvothermal reaction. Also, SCNH//AC BatCap full-cell showed improved electrochemical performance compared to AC//AC symmetric capacitor system. These results permit the envisioning of hybridization of sulfur and carbon using a solid solvothermal reaction for high-performance LiS batteries, leading to the remarkably unique approach as compared to typical composite strategies using mesoporous carbon as the template.

5.5. References

- [1] H.S. Choi, J.H. Im, T. Kim, J.H. Park, C.R. Park, *Journal of Materials Chemistry*, 22 (2012) 16986-16993.
- [2] M. Armand, J.M. Tarascon, *Nature*, 451 (2008) 652-657.
- [3] C. Barchasz, J.-C. Leprêtre, F. Alloin, S. Patoux, *Journal of Power Sources*, 199 (2012) 322-330.
- [4] J. Wang, J. Yang, C. Wan, K. Du, J. Xie, N. Xu, *Advanced Functional Materials*, 13 (2003) 487-492.
- [5] X. Ji, K.T. Lee, L.F. Nazar, *Nature Materials*, 8 (2009) 500-506.
- [6] X. Yang, J. Zhu, L. Qiu, D. Li, *Advanced Materials*, 23 (2011) 2833-2838.
- [7] J.R. Akridge, Y.V. Mikhaylik, N. White, *Solid State Ionics*, 175 (2004) 243-245.
- [8] J. Guo, Y. Xu, C. Wang, *Nano Letters*, 11 (2011) 4288-4294.
- [9] Y. Yang, G. Yu, J.J. Cha, H. Wu, M. Vosgueritchian, Y. Yao, Z. Bao, Y. Cui, *ACS Nano*, 5 (2011) 9187-9193.
- [10] H.-S. Ryu, H.-J. Ahn, K.-W. Kim, J.-H. Ahn, K.-K. Cho, T.-H. Nam, J.-U. Kim, G.-B. Cho, *Journal of Power Sources*, 163 (2006) 201-206.
- [11] J.H. Shin, E.J. Cairns, *Journal of The Electrochemical Society*, 155 (2008) A368-A373.
- [12] S.S. Zhang, *Electrochimica Acta*, 70 (2012) 344-348.
- [13] X. He, W. Pu, J. Ren, L. Wang, J. Wang, C. Jiang, C. Wan, *Electrochimica Acta*, 52 (2007) 7372-7376.

- [14] Y. Cao, X. Li, I.A. Aksay, J. Lemmon, Z. Nie, Z. Yang, J. Liu, *Physical Chemistry Chemical Physics*, 13 (2011) 7660-7665.
- [15] J.-Z. Wang, L. Lu, M. Choucair, J.A. Stride, X. Xu, H.-K. Liu, *Journal of Power Sources*, 196 (2011) 7030-7034.
- [16] W. Ahn, K.-B. Kim, K.-N. Jung, K.-H. Shin, C.-S. Jin, *Journal of Power Sources*, 202 (2012) 394-399.
- [17] M.-S. Park, J.-S. Yu, K.J. Kim, G. Jeong, J.-H. Kim, Y.-N. Jo, U. Hwang, S. Kang, T. Woo, Y.-J. Kim, *Physical Chemistry Chemical Physics*, 14 (2012) 6796-6804.
- [18] M. Rao, X. Song, H. Liao, E.J. Cairns, *Electrochimica Acta*, 65 (2012) 228-233.
- [19] N. Jayaprakash, J. Shen, S.S. Moganty, A. Corona, L.A. Archer, *Angewandte Chemie International Edition*, 50 (2011) 5904-5908.
- [20] G. Zheng, Y. Yang, J.J. Cha, S.S. Hong, Y. Cui, *Nano Letters*, 11 (2011) 4462-4467.
- [21] L. Xiao, Y. Cao, J. Xiao, B. Schwenzer, M.H. Engelhard, L.V. Saraf, Z. Nie, G.J. Exarhos, J. Liu, *Advanced Materials*, 24 (2012) 1176-1181.
- [22] J. Wang, S.Y. Chew, Z.W. Zhao, S. Ashraf, D. Wexler, J. Chen, S.H. Ng, S.L. Chou, H.K. Liu, *Carbon*, 46 (2008) 229-235.
- [23] Y. Zhao, G. Liu, L. Liu, Z. Jiang, *Journal of Solid State Electrochemistry*, 13 (2009) 705-711.
- [24] C. Liang, N.J. Dudney, J.Y. Howe, *Chemistry of Materials*, 21 (2009) 4724-4730.

- [25] G. He, X. Ji, L. Nazar, *Energy & Environmental Science*, 4 (2011) 2878-2883.
- [26] H.-G. Jung, S.-T. Myung, C.S. Yoon, S.-B. Son, K.H. Oh, K. Amine, B. Scrosati, Y.-K. Sun, *Energy & Environmental Science*, 4 (2011) 1345-1351.
- [27] X. Liang, Z. Wen, Y. Liu, H. Zhang, L. Huang, J. Jin, *Journal of Power Sources*, 196 (2011) 3655-3658.
- [28] M. Sun, S. Zhang, T. Jiang, L. Zhang, J. Yu, *Electrochemistry Communications*, 10 (2008) 1819-1822.
- [29] X. Liang, Y. Liu, Z. Wen, L. Huang, X. Wang, H. Zhang, *Journal of Power Sources*, 196 (2011) 6951-6955.
- [30] X. Liang, Z. Wen, Y. Liu, X. Wang, H. Zhang, H.M.W. Lezhi, *Solid State Ionics*, 192 (2011) 347-350.
- [31] Q. Kuang, S.-Y. Xie, Z.-Y. Jiang, X.-H. Zhang, Z.-X. Xie, R.-B. Huang, L.-S. Zheng, *Carbon*, 42 (2004) 1737-1741.
- [32] M. Choucair, P. Thordarson, J.A. Stride, *Nat Nano*, 4 (2009) 30-33.
- [33] D. Deng, X. Pan, L. Yu, Y. Cui, Y. Jiang, J. Qi, W.-X. Li, Q. Fu, X. Ma, Q. Xue, G. Sun, X. Bao, *Chemistry of Materials*, 23 (2011) 1188-1193.
- [34] C. Zhang, H.B. Wu, C. Yuan, Z. Guo, X.W. Lou, *Angew Chem Int Ed Engl*, 51 (2012) 9592-9595.
- [35] D. Kim, S.J. Yang, Y.S. Kim, H. Jung, C.R. Park, *Carbon*, 50 (2012) 3229-3232.
- [36] S.J. Yang, T. Kim, H. Jung, C.R. Park, *Carbon*, 53 (2013) 73-80.

- [37] V. Toniazzo, C. Mustin, J.M. Portal, B. Humbert, R. Benoit, R. Erre, *Applied Surface Science*, 143 (1999) 229-237.
- [38] I. Seo, S.W. Martin, *RSC Advances*, 1 (2011) 511-517.
- [39] D.-W. Wang, G. Zhou, F. Li, K.-H. Wu, G.Q. Lu, H.-M. Cheng, I.R. Gentle, *Physical Chemistry Chemical Physics*, 14 (2012) 8703-8710.
- [40] W.H. Smith, G.E. Leroi, *The Journal of Chemical Physics*, 45 (1966) 1778-1783.
- [41] H.E. Van Wart, A. Lewis, H.A. Scheraga, F.D. Saeva, *Proceedings of the National Academy of Sciences*, 70 (1973) 2619-2623.
- [42] J. Filik, I.M. Lane, P.W. May, S.R.J. Pearce, K.R. Hallam, *Diamond and Related Materials*, 13 (2004) 1377-1384.
- [43] Y. Jiang, Y. Wu, S. Zhang, C. Xu, W. Yu, Y. Xie, Y. Qian, *Journal of the American Chemical Society*, 122 (2000) 12383-12384.
- [44] G. Hu, D. Ma, M. Cheng, L. Liu, X. Bao, *Chemical Communications*, (2002) 1948-1949.
- [45] D. Marmorstein, T.H. Yu, K.A. Striebel, F.R. McLarnon, J. Hou, E.J. Cairns, *Journal of Power Sources*, 89 (2000) 219-226.
- [46] X. Liang, Z. Wen, Y. Liu, H. Zhang, J. Jin, M. Wu, X. Wu, *Journal of Power Sources*, 206 (2012) 409-413.
- [47] M. Shi, Z. Chen, J. Sun, *Cement and Concrete Research*, 29 (1999) 1111-1115.
- [48] Y. Li, H. Zhao, Z. Tian, W. Qiu, X. Li, *Rare Metals*, 27 (2008) 165-169.

Chapter 6. Preparation and Electrochemical Performance of a Graphene/CNT-Sulfur Hybrid Aerogel via a One-step Hydrothermal Reaction for a Positive Electrode of the BatCap System

6.1. Introduction

The demand for high-performance and clean energy storage device is increasing sharply owing to the development of applications such as portable electronic devices and electric vehicles, both of which are currently available [1]. Moreover, electrical energy generation from clean sources, such as solar, ocean waves, and geothermal energy, require energy storage devices for better efficiency of renewable energy. Therefore, it is extremely important to find the next generation of energy storage device which can meet the high energy density requirements at a high power density [2-4]. In spite of the great contribution of lithium ion batteries (LIBs) and supercapacitors as general energy storage devices on the progress of our life over the past two decade, more advanced energy storage devices are required with improved energy and power densities for the longer cycle life. LIBs are already widely used in a variety of applications due to their higher energy densities compared to typical energy storage devices. On the other hand, supercapacitors have the advantage of a high power density with great cycle stability. Therefore, most studies have

focused on an increase of the power density and improved cycle stability for LIBs and an increase of the energy density for supercapacitors [2, 5]. Meanwhile, another approach is the hybridization of LIBs and supercapacitors to make up for the weak points of each energy storage device, introducing electrode asymmetry and an organic electrolyte [6-9]. The BatCap system is one such alternative energy storage device for typical LIBs and supercapacitors, working by means of battery-supercapacitor hybridization [10]. However, it is rarely required to enhance the both the negative and positive electrode of the BatCap system as an alternate to typical energy storage devices.

Sulfur has been widely researched as a cathode material for LIBs due to its high specific capacity compared to general commercialized metal oxides [11-13]. Also, it is one of the candidates for a positive electrode material for the BatCap system. For the utilization of sulfur in the BatCap system, the cycle stability should be initially guaranteed through hybridization with the capacitor component.

To overcome the poor cycle stability due to the intrinsic insulating property and the lithium polysulfide dissolution problem, which can be called the “shuttle reaction”, mesoporous carbon has been introduced to enhance the electronic conductivity and to prevent the shuttle reaction with a confinement effect [14, 15]. Also, several different carbonaceous materials, including hollow carbon spheres, CNTs or graphene [11, 16-19], have been studied for similar purposes as the mesoporous carbon. However, these approaches have the lower device specific capacities, because carbonaceous additives for better cycle stability

occupy a high ratio of weight without activity as a cathode or a positive electrode material. Therefore, most research on the specific capacity was based on the sulfur weight to show the cycle performance of the products, though it was not effective to indicate the specific capacity of an actual device containing a current collector, binder, and conductive additives.

In this chapter, we develop a free-standing graphene/CNT-sulfur hybrid (denoted as GCSH) aerogel as a positive electrode for the BatCap system through a facile one-step fabrication process using a hydrothermal reaction. The aerogel structure is very advantageous as an electrode material for the BatCap system, with its battery and capacitor components in a single electrode, as mentioned in the chapter 2, which is similar to the habitat of the moisture ant. We successively prepared 3D interconnected and open porous networks consisting of graphene, MWCNT, and sulfur by means of the self-assembly of graphite oxide by the reduction process of a hydrothermal reaction which comes from the decrease of the repulsion force between each graphite oxide layer. Na_2S was introduced as the multi-functional agent to reduce graphite oxide and to dissolve sulfur in the water, which permits a suitably embedded battery component, sulfur clusters, in the 3D graphene/CNT hybrid structure. Also, this morphological characteristic is helpful to confine the lithium polysulfide, thus restraining the shuttle reaction of the sulfur. The graphene served not only as a capacitor component but also as a conductive additive combined with CNTs to enhance the insulating properties of the battery component, i.e., sulfur. Hence, the prepared free-standing graphene/CNT-sulfur hybrid aerogel can be operated

alone without a current collector, binder, and conductive additives causing an increase of the real device specific capacity, which is advantageous compared to typical mesoporous carbon-sulfur composite materials.

6.2. Experimental

6.2.1. Reagents and chemicals

Graphite (powder, <150 μm ; Aldrich), multi-walled carbon nanotubes (MWCNTs, CM250; Hanwha Chemical, Co), sulfur (Aldrich), sodium sulfide (Na_2S ; Aldrich), commercialized activated carbon (AC) (SX Ultra, Norit) ,and hydrogen chloride (HCl; Deajung, Korea) were purchased and utilized without any further treatment.

6.2.2. Synthesis of the GCSH aerogel

Graphite oxide (denoted as GO) was prepared using a modified Hummers' method [20-22] followed by neutralization and a drying process on PTFE dishes. The MWCNTs were oxidized with a mixed acid (mixture of 14.2 M HNO_3 , 75 ml and concentrated H_2SO_4 , 225 ml) followed by neutralization and a vacuum-drying process for purification and surface functionalization. In a typical synthetic process, 0.75 ml of a 1 mg ml^{-1} MWCNT aqueous suspension and 3 ml of a 5 mg ml^{-1} GO aqueous suspension were homogeneously mixed with ultrasonication for 6 hrs. Then, 1.5 ml of a 200mM $\text{Na}_2\text{S/S}$ aqueous solution (molar ratio=1:1) was quickly added as a reducing agent and sulfur precursor into the GO/MWCNT homogeneous suspension stored in a 20 ml vial. A hydrothermal reaction of this reaction vessel was carried out in a 90 $^\circ\text{C}$ -preset oven for 6 hrs to fabricate the self-assembled free-standing 3D-hydrogel structure. Next, 10 ml of a 5 M HCl aqueous solution was added into the

reaction vessel to remove Na₂S from the hydrogel followed by washing for neutralization. Finally, the prepared hydrogel was freeze-dried into a free-standing GCSH aerogel for further characterizations and electrochemical performance tests. The same procedure was utilized to synthesize a free-standing graphene-sulfur hybrid (GSH) aerogel without MWCNTs for comparison.

6.2.3. Characterization of the GCSH aerogel

An optical digital camera was used to obtain optical images of the product. Field-emission scanning electron microscopy (FE-SEM; JSM6700F instrument, JEOL) and high-resolution transmitted scanning electron microscopy (HR-TEM; JEM3000F instrument with an acceleration voltage of 200 kV, JEOL) were used to analyze the morphological characteristics of the product. Powder X-ray diffraction (XRD) studies were carried out using an X-ray diffractometer (D8 Advanced, Bruker) equipped with a Ni-filtered Cu-K α radiation source ($\lambda = 0.154184$ nm) to analyze the microstructure of the product. A thermogravimetric analysis (TGA, SDT Q600, TA) was carried out to determine the proportion of the sulfur in the product. An elemental analysis (EA) was conducted using Flash2000 (CE Instrument) on the product. X-ray photoelectron spectroscopy (XPS; AXIS-HSi, KRATOS) was also employed to study the surface characteristics of the product. A Micromeritics ASAP 2020 static volumetric gas adsorption instrument was utilized to measure the N₂ adsorption isotherms of the composite at liquid N₂ temperature using ultrahigh

purity grade (99.9999%) gas. Prior to the sorption analysis, the product (30 mg) in the analysis chamber was subjected to a vacuum of 10^{-5} Torr at 60 °C for 12 h to remove any impurities without sulfur dissolution.

6.2.4. Electrochemical tests of the GCSH aerogel

Electrochemical measurements including cyclic voltammetry (CV), a half-cell test, and a full-cell test of the products were carried out using a battery cycler (WBCS3000, WonATech) in an Ar-filled glove box (Korea Kiyon) using 2032 coin-type cells. The electrodes of the free-standing GCSH aerogel consisted of only the product without a current collector, binder, or conductive agent; these were used as a working electrode in the half-cell test and as a positive electrode in the full-cell BatCap test with Li metal as a reference electrode and Celgard 2400 as the separator. A negative electrode was fabricated using 10 wt% of polytetrafluoroethylene for the binder and 90 wt% of commercialized AC as the active material in the full-cell test. The electrolyte in the cell was constructed with lithium trifluoromethanesulfonate (1M) in a tetraethylene glycol dimethyl ether/1,3-dioxolane (1:1 of molar ratio) solution.

6.3. Results and Discussion

6.3.1. Microstructural and morphological characteristics of the GCSH aerogel

In a typical preparation process, a mixture of 5 ml of GO/CNT suspension and Na₂S/S solution was sealed in a convection oven at 90 °C without stirring for the hydrothermal reaction followed by a HCl solution treatment and neutralization. As illustrated in Figure 1A, a 3D monolith hydrogel containing sulfur was assembled without any further treatment. This floated on the surface of the water. Na₂S is a multi-functional agent in this preparation, serving not only as a reductant for GO and MWCNT but also as a sulfur-dissolving agent for water forming polysulfide solution, as described by the reaction process: $\text{Na}_2\text{S} + x\text{S} + \text{H}_2\text{O} \rightarrow \text{Na}_2\text{S}_{x+1} + \text{H}_2\text{O}$ [18]. The hydrogel formation mechanism for the GOs or CNTs is related to the decrease of the repulsion force between the GOs or CNTs via a hydrothermal reaction [23], a pH control [24, 25], or through the use of a reducing agent such as various transition metal ions (Fe, Mg, Ca, Cu, or Cr) [26, 27] or vitamin C [28]. Hence, it is clear that Na₂S is an effective agent to form the self-assembled 3D monolith shape of the structure using the GO/CNT suspension by a hydrothermal reaction. Also, the monolith shape is well maintained after the free-drying process resulting in the free-standing GCSH aerogel shown in Figure 1B. The shape of the monolith is dependent on the shape of the reactor [27]; that is, the shape of the GCSH aerogel can be controlled using a proper shape of the reactor. The density of the

product was calculated as 0.78 kg m^{-2} , which is comparable to that of a typical graphene aerogel. Furthermore, the high density is directly related to the porous structure, leading to good electrolyte accessibility for an electrochemical energy storage device. Also, the aerogel structure of the product is suitable for the mechanical properties, as shown in Figure 6.1C, testing the load-bearing capacity of the GCSH aerogel. The shape of the product was sustained after weight loading with a weight 3880 times heavier than the product. Hence, it is clear that the GCSH aerogel can be used as a free-standing electrode by itself without another agent such as a binder or a current collector for mechanical complementary, which is one of the important advantages of the product.

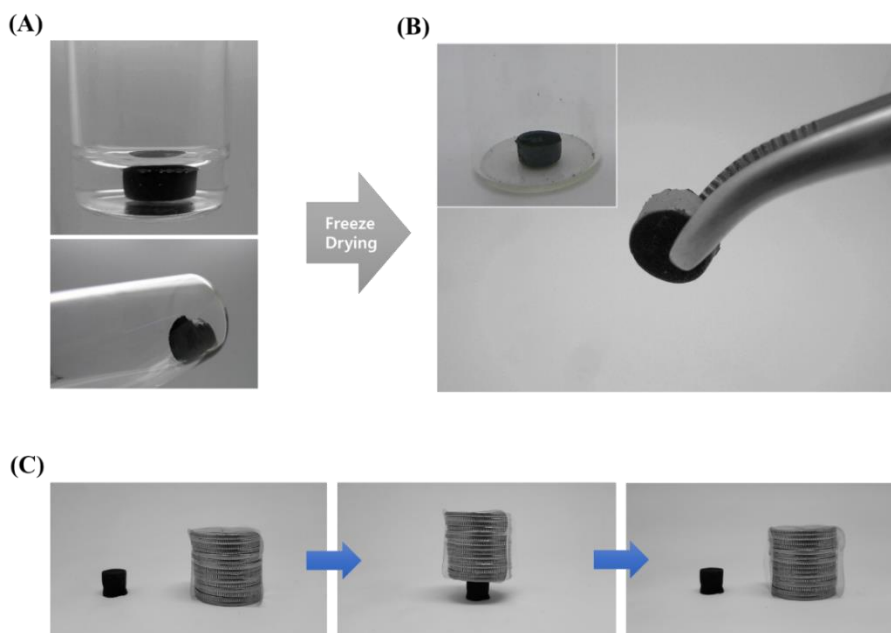


Figure 6.1. Photographs of (A) a free-standing GCSH hydrogel after the hydrothermal reaction, (B) a free-standing GCSH aerogel after the freeze-drying process of the hydrogel, and (C) load-bearing capacity of the free-standing GCSH aerogel.

Figure 6.2 indicates the morphological properties of the free-standing GCSH aerogel as obtained by the SEM and TEM analysis. As shown in Figure 6.2(A) of the surface of the product, an open porous structure of the aerogel is achieved by means of the hydrothermal reaction without a graphene-layer or CNT aggregation, which is advantageous for the both electron and electrolyte transport kinetics. The pore size on the surface of the GCSH aerogel is in the range of 2~5 μm . Also, as shown in Figure 6.2B, CNTs were well settled [29, 30] inside of the product, which improve the mechanical properties and electronic conductivity on 2D graphene structures [29, 30].

One important advantage of the present preparation process is that it is an easy and one-step synthetic process without an additional treatment of sulfur insertion into the product, e.g., a melting and adsorption process of sulfur over 110 $^{\circ}\text{C}$. As shown in Figure 6.3A, sulfur is well impregnated into the aerogel at a ratio of 19.1 wt% (Table 6.1). This result is a good agreement with the sulfur weight ratio of 21 wt% as calculated from TGA result in Figure 6.3B and 21.6 wt% obtained by EA in Table 6.1. Also, it clearly confirms that the water-dissolving agent for sulfur, Na_2S , is effectively eliminated after the HCl treatment and the washing process. Therefore, the Na_2S -assisted hydrothermal reaction can be considered as an appropriate means of sulfur impregnation in a graphene/CNT-hybridized aerogel via the aforementioned one-step process.

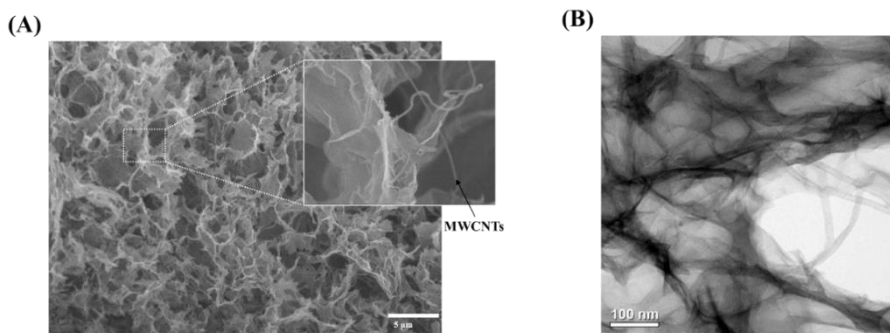


Figure 6.2. (A) FE-SEM image with the inset showing a high-resolution image and (B) a HR-TEM image of the free-standing GCSH aerogel

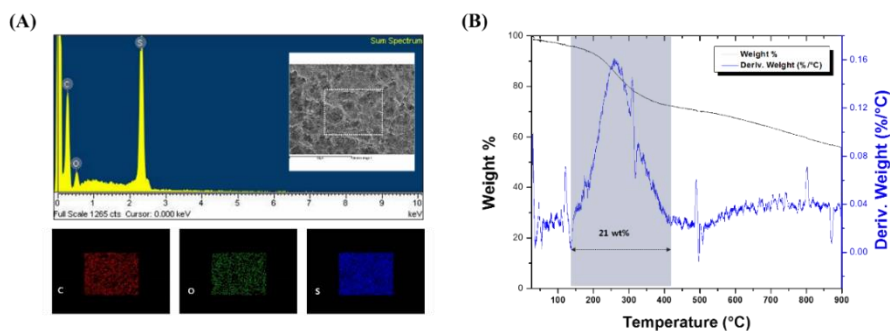


Figure 6.3. (A) EDS analysis and (B) TGA results of the free-standing GCHS aerogel

Table 6.1. EDS analysis and EA results for each element of the GCHS aerogel

Element	Carbon	Oxygen	Sulfur
wt% from EDS	69.9	11.0	19.1
wt% from EA	62.4	11.4	21.6

Figure 6.4 illustrates the XRD pattern of the free-standing GCSH aerogel with patterns of the GSH aerogel and GO for comparison. The XRD pattern of GO prepared by a modified Hummer's method for graphite reveal oxidized sheets with a (002) peak at $2\theta = 12.5^\circ$ indicating d value of 0.708 nm. After the hydrothermal reaction, all of the diffraction peaks of the (002) plane for the GCSH and GSH aerogels were shifted to the position of $2\theta = 24.5^\circ$. There was a similar pattern of GCSH compared to GSH due to the superimposed CNT diffraction peak at this position. These results indicate that GO sheets were successively reduced by the Na_2S -assisted hydrothermal reaction resulting in the formation of a 3D free-standing monolith. Also, this clearly shows that the repulsion force between each GO sheet was decreased to form the aerogel structure, in spite of the remaining oxygen on the surface of the GO, as analyzed in the EDS result shown in Figure 6.3. On the other hand, it was not possible to find any diffraction peak from the sulfur in the products. This result exhibits the well-impregnated sulfur clusters through the simple one-step synthetic process without the formation of large sulfur particles, which can be helpful to enhance the electrochemical reaction due to the larger surface area than typical micro-sized sulfur. Also, there was no peak noted from Na_2S which is a good agreement with the EDS result of the product.

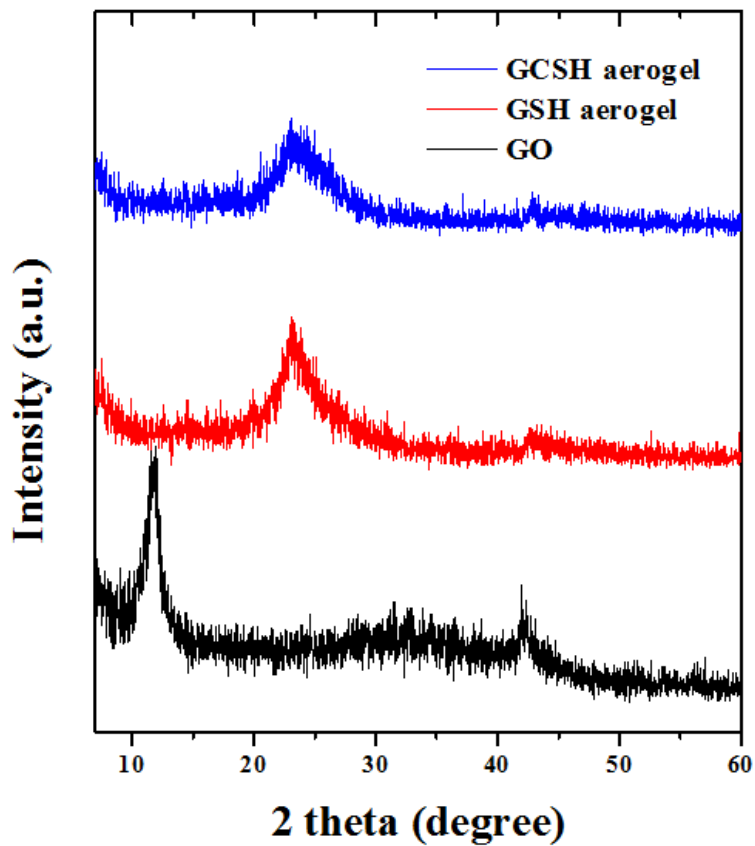


Figure 6.4. Powder XRD spectrum of free-standing GCSH aerogel, GSH aerogel, and pristine GO.

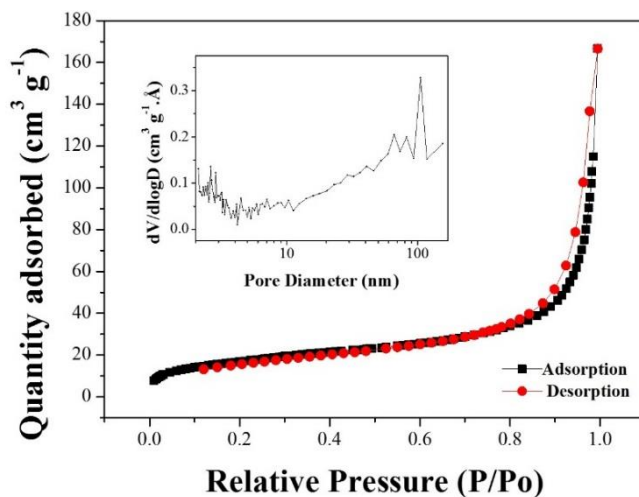
6.3.2. Surface characteristics of the GCSH aerogel

A nitrogen adsorption isotherm analysis was carried out to characterize the surface textures of the free-standing GCSH aerogel, as demonstrated in Figure 6.5A and summarized in Table 6.2. To eliminate the residual water and other solvents in the pores of the product, a pre-activation process was conducted at 80 °C for 6 hrs; this which temperature is sufficiently lower than the melting temperature of the sulfur element. The BET specific surface area (BET SSA) of the GCSH aerogel is about 62.45 m² g⁻¹ with an average pore diameter of 11.38 nm. This value is lower than typical graphene- or carbon-based aerogels of 100-1000 m² g⁻¹ [1], owing the sulfur impregnated into the pores of the GCSH aerogel. In comparison with sulfur-impregnated mesoporous carbon [15], however, the GCSH aerogel indicates a higher surface area with a larger pore volume, which is responsible for the better electrolyte accessibility to the active material. Also, the value of the average pore diameter exhibits the mesoporous structure of the product resulting from the sulfur impregnation into the pores and reflecting the large size of open porous structure of the aerogel on the surface of the product, corresponding to the surface morphology shown in Figure 6.2A.

Figure 6.5B exhibits the XPS spectra of the GCSH aerogel to provide information pertaining to the various functional groups on the surface. The survey of the XPS spectrum of the GCSH aerogel shows the clearly observable peaks corresponding to C1s, O1s, and S2p. The peaks were deconvoluted using a Lorentzian-Gaussian mixed function and peak parameters. This information

is summarized in Table 6.3. As shown in Figure 6.5B, the magnified XPS spectra for the C1s and O1s exhibit the partially reduced graphene and CNTs due to reductant of Na₂S, which is in good agreement with the XRD result in Figure 6.4. In the case of the peak for S2p, the existence of sulfur is noted in the GCSH aerogel with deconvoluted peaks at 163.6 and 164.8 eV for S2p_{3/2} and S2p_{1/2}, respectively, values which are shifted slightly lower than that of elemental sulfur due to the electrostatic-screening effect caused by the adjacent carbon atoms.

(A)



(B)

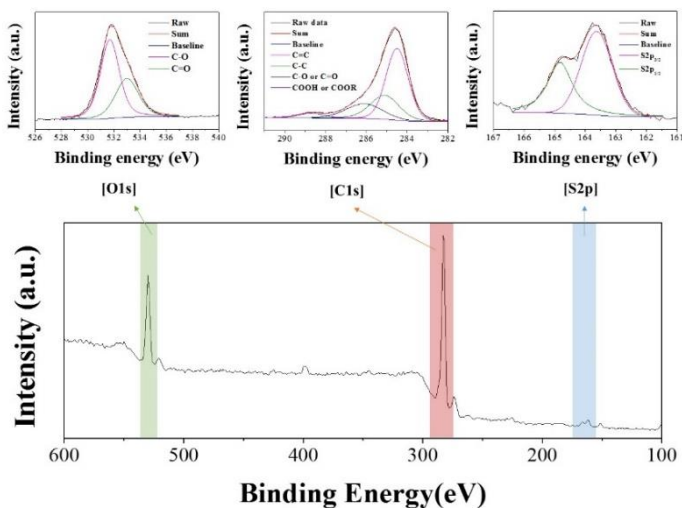


Figure 6.5. (A) Nitrogen adsorption isotherms at 77 K of the GCSH aerogel with the inset showing the pore size distribution, and (B) XPS survey spectrum with magnified images of the C1s, O1s, and S2p regions

Table 6.2. Pore characteristics determined from the nitrogen adsorption isotherm at 77 K of the GCSH aerogel

Product	BET SSA ^a (m ² g ⁻¹)	Langmuir SSA ^b (m ² g ⁻¹)	Average pore diameter (nm)	Total pore volume at a relative pressure of 0.98 [cm ³ g ⁻¹]
GCSH aerogel	62.45	87.14	11.38	0.17

a SSA, specific surface area, determined by the BET equation.

b Determined by the Langmuir equation.

Table 6.3. Peak deconvolutions of the XPS spectra for the GCSH aerogel, as shown in Figure 6.5B

	Functional group	Peak position (eV)	Area (ratio)	FWHM
Carbon	C=C (sp ² bonding)	284.492	10400.69 (0.53)	1.28
	C-C (sp ³ bonding)	285.1	4825.37 (0.25)	1.66
	C-O or C=O (ether/hydroxyl group)	286.1	3590.44 (0.18)	2.10
	COOH (carboxyl/lactone group)	288.7	776.33 (0.03)	1.52
Oxygen	C=O	531.6	20136.85 (0.63)	1.71
	C-O	532.9	11847.25 (0.37)	2.08
Sulfur	S2p _{3/2}	163.6	2021.28 (0.59)	1.19
	S2p _{1/2}	164.8	1390.69 (0.41)	0.96

6.3.3. Electrochemical performance of the GCSH aerogel

To evaluate the electrochemical performance of GCSH aerogel as the positive material for the BatCap system, 2032-type coin cells were fabricated as the half-cell using Li metal as a counter and reference electrode without any kind of current collector, binder, and conducting additives. Figure 6.6A shows the potential profiles of GCSH aerogel at different charge/discharge rates. Also, the cycle performances of the GCSH and GSH aerogels at a variety charge/discharge rates to demonstrate the effect of CNTs in the aerogel to the kinetics of the electrode in the inset. The charge/discharge potential profiles of both slow (100 mA g^{-1}) and fast (500 mA g^{-1}) rates reveal the typical two plateaus of a sulfur as cathode material for LiS batteries, corresponding to the formation of electrolyte-soluble polysulfides (Li_2S_n , $4 \leq n \leq 8$) at 2.3 V and electrolyte-insoluble polysulfides (Li_2S_n , $1 \leq n \leq 4$) at 2.1 V. Also, flat plateau for 2.1 V exhibits the uniformly formed Li_2S with little kinetic barriers. In addition, specific capacity decay for increase of current density from 100 mA g^{-1} to 500 mA g^{-1} after 5 cycle is under 10 %, indicating enhanced kinetics of the GCSH aerogel electrode [16]. Also, specific capacities of the GCSH aerogel were 882, 610, 464, and 290 mAh g^{-1} at 100, 200, 500, and 1000 mA g^{-1} of charge/discharge rates, which are averagely 45 % higher values than those of GSH aerogel, as demonstrated in the inset. This could be attributed to the confinement effect and improved charge transport kinetics by structural characteristics of the aerogel consisting of graphene and CNTs with open porous structure.

Figure 6.6B indicates capacity comparison between GCSH aerogel and mesoporous carbon-sulfur (denoted as MPC-S) composite was conducted at 100 mA g⁻¹ of charge/discharge rate in the inset. Entire specific capacities were calculated with total mass of the electrode, called 'electrode capacity', to avoid capacity over-estimation by the calculation based on the only mass of sulfur in the electrode. GCSH aerogel has much better electrode capacity than MPC-S composite over two times higher with comparable cycle stability in the inset of Figure 6.6B.

This result clearly shows that GCSH aerogel structure has enough mechanical and charge transfer properties to work as the positive electrode for BatCap system without any additives, such as current collector, binder, and conducting material which are generally required for typical materials. Also, it is obvious that CNTs gives better charge transport kinetics on the GCSH aerogel structure for high-rate capability.

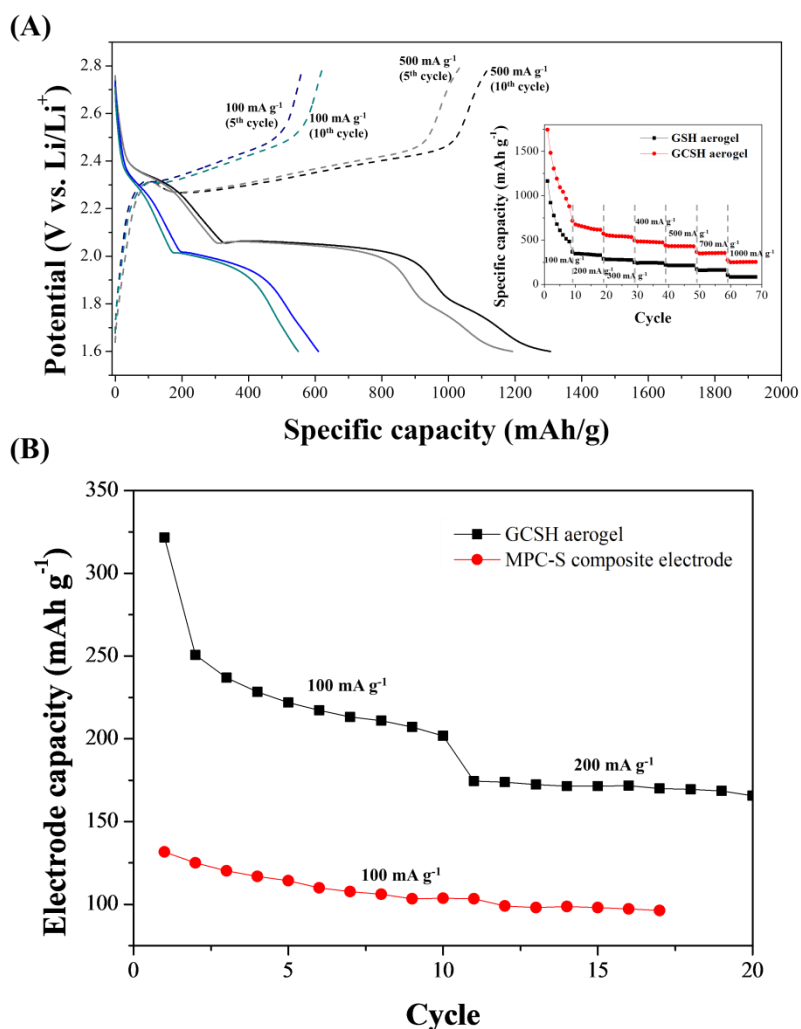


Figure 6.6. (A) Charge/discharge potential profile of GCSH aerogel at 100 and 500 mA g⁻¹ after 5 cycle (Inset: cycle performances of GCSH aerogel and GSH aerogel at a variety charge/discharge rates based on the mas of the sulfur in the products.) (B) Cycle performances of GCSH aerogel and MPC-S composite at 100 mA g⁻¹. Specific capacities were calculated based on the total mass of each electrode.

The galvanostatic charge/discharge curves and Ragone plot of the AC//GCSH aerogel BatCap system are illustrated in Figure 6.7 with separated potential profiles for each electrode and full-cell in the potential range of 0.1-2.5 V. The electrodes mass ratio was controlled as $m_{\text{negative}}/m_{\text{positive}} = 8$ to balance the exchanged charges between each electrode for maximizing chargeable electrochemical energy. For comparison, energy densities and power densities of the AC//GCSH aerogel BatCap system and AC//AC symmetric capacitor system were estimated by the values based on the total mass of both electrodes including current collector, active material, binder, and conducting additives. As shown in Figure 6.7A, the full-cell potential for early state of charge process exhibited curve-shaped slope resulting from a plateau region of the positive electrode potential around 2.3 V vs. Li/Li⁺, for the charge of a sulfur component in the GCSH aerogel. Then, linear slope of full-cell potential profile was followed to the end of charge state indicating charge of a graphene/CNT components and AC in the positive and negative electrodes, respectively. In the discharge process, shape of the potential profiles for each electrode were almost symmetry of the charge process. This result clearly demonstrated that GCSH aerogel was operated as the BatCap electrode which consists of battery and capacitor component.

The Ragone plot indicates electrochemical performances for AC//GCSH aerogel BatCap system and AC//AC symmetric capacitor system, which are electrode energy and power densities. Energy densities of AC//GCSH aerogel BatCap are much higher than that of AC//AC symmetric capacitor at the both

low and high power densities, which corresponded to 21 and 20 Wh kg⁻¹ at 322 and 938 W kg⁻¹, respectively, as demonstrated in Figure 6.7B. From these results, it is obviously clear that GCSH aerogel is advantageous electrochemical active material for the positive electrode of the BatCap system due to well hybridized battery and capacitor components and open porous aerogel structure which are undoubtedly responsible for the better electronic and ionic conductivities with enhanced charge transfer kinetics.

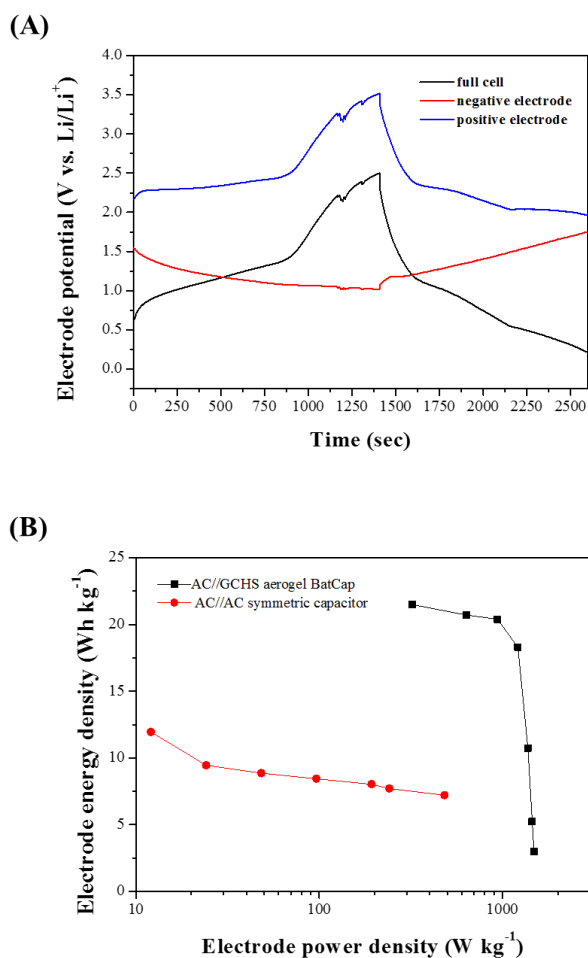


Figure 6.7. (A) Galvanostatic charge/discharge plot for the AC//GCSH aerogel BatCap system at a 2/3 C rate in the working potential range of 0.1-2.5 V. The black-colored potential profile indicates the full-cell, the blue-colored potential profile indicates the positive electrode of the AC//GCSH aerogel, and the red-colored potential profile indicates the negative AC electrode. (B) Ragone plot for the AC//GCSH aerogel BatCap system at various charge/discharge rates in the working potential range of 0.1-2.5 V. The data were calculated based on the total mass of both electrodes.

6.4. Conclusion

In summary, we report that novel self-assembled graphene/CNT hybrid aerogel containing sulfur with interconnected 3D networks, effectively induced by simple and one-step hydrothermal reaction with Na_2S as the reducing and sulfur-dissolving agent. The 3D open porous structure composed of highly electrical conductive components of graphene and CNT was successively prepared with well impregnated sulfur in the hybrid, which was advantageous on the better ion and electron kinetics for electrochemical reaction of the sulfur as positive electrode material for the BatCap system. Also, free-standing monolith shape potentialized no use of current collector, binder, and conducting agent which are not available to work as active material reducing specific rechargeable energy of the entire device. Hence, half-cell performance test result for the free-standing GCSH aerogel indicated enhanced device specific capacity as cathode of LIBs, over two times higher compared to that of typical mesoporous carbon-sulfur composite. In addition, electrochemical performance of the product as a positive electrode in the full-cell was improved due to proper morphology and material characteristics of the components, that is, graphene operated as effective capacitor component with assistance of CNT on better electron kinetics and sulfur worked as high-performance battery component with enhanced cycle stability. These finding indicate that the free-standing GCSH aerogel have potential as the positive electrode for the BatCap system which can alternate the typical electrochemical energy storage devices such as LIBs or supercapacitors.

6.5. References

- [1] N.-S. Choi, Z. Chen, S.A. Freunberger, X. Ji, Y.-K. Sun, K. Amine, G. Yushin, L.F. Nazar, J. Cho, P.G. Bruce, *Angewandte Chemie International Edition*, 51 (2012) 9994-10024.
- [2] M. Armand, J.M. Tarascon, *Nature*, 451 (2008) 652-657.
- [3] B.L. Ellis, K.T. Lee, L.F. Nazar, *Chemistry of Materials*, 22 (2010) 691-714.
- [4] F. Cheng, J. Liang, Z. Tao, J. Chen, *Adv. Mater.*, (2011) n/a-n/a.
- [5] P. Simon, Y. Gogotsi, *Nature Materials*, 7 (2008) 845-854.
- [6] A. Du Pasquier, A. Laforgue, P. Simon, G.G. Amatucci, J.-F. Fauvarque, *Journal of The Electrochemical Society*, 149 (2002) A302-A306.
- [7] A. Du Pasquier, I. Plitz, S. Menocal, G. Amatucci, *J. Power Sources*, 115 (2003) 171-178.
- [8] V. Khomenko, E. Raymundo-Piñero, F. Béguin, *J. Power Sources*, 177 (2008) 643-651.
- [9] Z. Fan, J. Yan, T. Wei, L. Zhi, G. Ning, T. Li, F. Wei, *Advanced Functional Materials*, 21 (2011) 2366-2375.
- [10] H.S. Choi, J.H. Im, T. Kim, J.H. Park, C.R. Park, *Journal of Materials Chemistry*, 22 (2012) 16986-16993.
- [11] J. Guo, Y. Xu, C. Wang, *Nano Lett.*, 11 (2011) 4288-4294.
- [12] Y. Yang, G. Yu, J.J. Cha, H. Wu, M. Vosgueritchian, Y. Yao, Z. Bao, Y. Cui, *ACS Nano*, 5 (2011) 9187-9193.
- [13] C. Zhang, H.B. Wu, C. Yuan, Z. Guo, X.W. Lou, *Angewandte Chemie International Edition*, (2012) n/a-n/a.

- [14] J. Wang, S.Y. Chew, Z.W. Zhao, S. Ashraf, D. Wexler, J. Chen, S.H. Ng, S.L. Chou, H.K. Liu, *Carbon*, 46 (2008) 229-235.
- [15] X. Ji, K.T. Lee, L.F. Nazar, *Nature Materials*, 8 (2009) 500-506.
- [16] G. Zheng, Y. Yang, J.J. Cha, S.S. Hong, Y. Cui, *Nano Lett.*, 11 (2011) 4462-4467.
- [17] Y. Fu, A. Manthiram, *RSC Advances*, 2 (2012) 5927-5929.
- [18] M. Rao, X. Song, H. Liao, E.J. Cairns, *Electrochimica Acta*, 65 (2012) 228-233.
- [19] F. Zhang, Y. Dong, Y. Huang, G. Huang, X. Zhang, L. Wang, *Journal of Physics: Conference Series*, 339 (2012) 012003.
- [20] W.S. Hummers, R.E. Offeman, *J Am Chem Soc*, 80 (1958) 1339-1339.
- [21] D.C. Marcano, D.V. Kosynkin, J.M. Berlin, A. Sinitskii, Z. Sun, A. Slesarev, L.B. Alemany, W. Lu, J.M. Tour, *ACS Nano*, 4 (2010) 4806-4814.
- [22] S.J. Yang, J.H. Kang, H. Jung, T. Kim, C.R. Park, *Journal of Materials Chemistry A*, (2013).
- [23] L. Zhang, G. Shi, *The Journal of Physical Chemistry C*, 115 (2011) 17206-17212.
- [24] H.-P. Cong, X.-C. Ren, P. Wang, S.-H. Yu, *ACS Nano*, 6 (2012) 2693-2703.
- [25] M.A. Worsley, S.O. Kucheyev, H.E. Mason, M.D. Merrill, B.P. Mayer, J. Lewicki, C.A. Valdez, M.E. Suss, M. Stadermann, P.J. Pauzauskie, J.H. Satcher, J. Biener, T.F. Baumann, *Chemical Communications*, 48 (2012) 8428-8430.
- [26] H. Bai, C. Li, X. Wang, G. Shi, *The Journal of Physical Chemistry C*, 115 (2011) 5545-5551.

- [27] W. Chen, L. Yan, *Nanoscale*, 3 (2011) 3132-3137.
- [28] X. Zhang, Z. Sui, B. Xu, S. Yue, Y. Luo, W. Zhan, B. Liu, *Journal of Materials Chemistry*, 21 (2011) 6494-6497.
- [29] D. Cai, M. Song, C. Xu, *Adv. Mater.*, 20 (2008) 1706-1709.
- [30] Z.-D. Huang, B. Zhang, R. Liang, Q.-B. Zheng, S.W. Oh, X.-Y. Lin, N. Yousefi, J.-K. Kim, *Carbon*, 50 (2012) 4239-4251.

Part V

Conclusions

Chapter 7. Conclusive remarks and outlook

High-performance energy storage device is one of the key factors for clean and renewable energy economy in the world. However, typical electrochemical energy storage devices, LIBs and supercapacitors, have not yet satisfied the demand of high energy and power density with good cycle stability. In spite of variety of approaches to overcome the lacks of LIBs and supercapacitor, these techniques could not meet the solution for performance trade-off problems in the general energy storage devices, such as energy density vs. power density and energy density vs. cycle stability. Hence, new generation energy storage device is requested to achieve high-performance dealing with global energy crisis.

Herein of thesis, we have introduced a new energy storage system, BatCap, which is a battery-capacitor hybridized electrochemical device. Through the theoretical modeling, performance of the BatCap could be calculated in accordance with component conditions. Also, theoretical and practical performance comparison was carried out with previously studied electrochemical devices, which indicated the advantages of the BatCap system due to battery and capacitor components hybridization in a single electrode. Following this theoretical discussion, ideal structure for the BatCap system was proposed to potentialize the improved electrochemical performance compared to the typical energy storage devices.

Through this theoretical approach for the BatCap system, design strategy of the BatCap electrode material is focused on the following conditions

- (1) Increase of K_{BM} coefficient by lower value of k_1 and k_2 factors from introducing high specific capacity battery component material to decrease m_B and ΔV_{B_B}
- (2) Increase of K_E coefficient by lower k_3 factor from use of organic electrolyte to increase ΔV_B and by higher k_4 factor from porous structure to satisfy $C_{aq}=C_{organic}$ of the capacitor component.
- (3) Increase of K_{BC} coefficient by higher k_2' and k_5 factors from proper charge/discharge potential and good cycle stability of battery component to increase ratio of ΔV_{B_Bb}

Therefore, $Li_4Ti_5O_{12}$ /carbon hybrid nanofiber sheets and $Li_4Ti_5O_{12}$ -activated carbon hybrid nanotubes were prepared, characterized and electrochemically tested as negative electrode materials for the BatCap system. On the other hand, sulfur-carbon nanosheet hybrids and graphene/CNT-sulfur hybrid aerogel were prepared, characterized and electrochemically tested as positive electrode materials for the BatCap system. From aforementioned results of electrochemical performance tests, it is clearly shown that electrochemical performances of the BatCap electrode materials were enhanced through increase of K-coefficients by control of the k-factors, which of K-coefficients are summarized in Table 7.1.

These processes illustrated that new concept of the BatCap system is effective strategy to find breakthrough for advanced energy storage device.

Table 7.1. Summaries of the K-coefficients for each BatCap electrode material.

Classification	References	Negative electrode	Positive electrode	K_{BM}	K_E	K_{BC}
organic / BatCap	Chap. 3	LTO/PVA	AC	0.505	7.55	0.491
organic / BatCap	Chap. 4	LTO/AC	AC	0.444	5.547	0.6
organic / BatCap	Chap. 5	AC	SCNH	0.558	2.465	0.635
organic / BatCap	Chap. 6	AC	GCSH aerogel	0.525	3.852	0.58

초록

에너지 저장 기술은, 화석연료의 사용에 의한 지구 온난화, 화석연료 자원의 고갈, 그리고 환경 오염으로 대표되는 에너지 위기를 해결하고, 스마트폰, 태블릿, 그리고 전기자동차와 같이 고성능을 요구하는 전자기기들의 발전에 대응하기 위한 매우 중요한 기술이다. 다양한 에너지 저장 시스템들 중에서, 전기화학 에너지 저장 매체는 화석연료에 기반하는 에너지 체계를 대체할 수 있는 효율적인 전기 에너지 저장 기술로써 많은 관심을 받고 있다. 지난 20 년간, 대표적인 전기화학 에너지 저장 매체인 리튬 이온 배터리와 슈퍼캐패시터에 관한 수많은 연구가 이루어져 왔으나, 새로운 관련 시장 및 산업계의 요구를 충족시키기 위해 좀 더 향상된 전기화학적 성능이 요구되고 있는 실정이다.

본 연구에서는, 고성능 에너지 저장 대안 기술로써, 새로운 개념의 에너지 저장 매체인 배트캡(BatCap)시스템을 제안하고자 한다. 배트캡 시스템은, 하나의 전극에 배터리와 캐패시터 구성요소가 복합화 되어 있는 열린 공극 구조의 배트캡 전극으로 구성되어 있으며, 이로 인하여 배터리와 캐패시터 구성요소에 의한 상승작용을 기대할 수 있다. 구체적으로, 배터리 구성요소의 뛰어난 전기화학 에너지 저장 능력과, 공극 구조와 캐패시터 구성요소에

의한 전하전달 속도 향상을 통해 배트캡 시스템의 전기화학적 성능이 향상될 수 있다. 이 연구의 목적은 첫째, 고성능 에너지 저장 대안 기술로서, 새로운 개념의 전기화학 에너지 저장 매체인 배트캡(BatCap)시스템을 제안하고, 둘째, 이에 대한 이론모델을 제안하면서 기존의 배터리-캐패시터 복합 시스템들과의 성능을 이론적으로 비교하였다. 나아가 셋째, 배트캡 시스템에 부합하는 음극 및 양극 물질 합성, 물성 분석, 전기화학적 성능을 분석함으로써, 배트캡 시스템의 대안 에너지 저장 시스템으로서의 가능성에 대해 고찰하고자 하였다.

1 부에서는 에너지 저장 매체에 대한 전반적인 소개를 통해 대표적인 에너지 저장 매체인 리튬 이차 배터리 및 슈퍼캐패시터에 대한 연구를 소개하고, 에너지 밀도-출력 밀도 간 성능 트레이드 오프(trade-off) 관점에서 이들 에너지 저장 매체들의 기술상황 및 과제들에 대해 분석하였으며, 이를 통해서 새로운 에너지 저장 매체인, 배트캡 시스템의 필요성에 대해 살폈다.

2 부에서는 다양한 에너지 저장 시스템들을 전극의 대칭성과 전해질의 종류를 기준으로 분류하고, 각각의 에너지 밀도 및 출력 밀도를 이론적으로 계산하였으며, 전기화학적 성능 비교를 위해 다양한 요소와 이들과 관련된 계수를 도입하여 시스템 구성 조건에 따른 성능에 대해 고찰하였다. 이를 통해서, 기존의 복합 전기화학

에너지 저장 매체에 비해, 배트캡이 상대적으로 향상된 전기화학적 성능을 가지는 것을 확인하였다.

3 부와 4 부에서는 각각 배트캡 시스템의 음극재 및 양극재를, 2 부에서 제시된 이론에 맞춰 설계하고 그 성능을 측정하였다. 그 결과 이론을 통해 예측한대로, 배트캡 시스템은 배터리와 슈퍼캐패시터의 시너지적 융합효과를 발휘하는 새로운 개념의 전기에너지 저장 시스템을 확인하였다.

결과적으로, 이 연구를 통해서 이론적 고찰을 바탕으로 기존의 전기화학 에너지 저장 장치를 대체할 수 있는 진보된 형태의 배트캡 시스템을 제시하고, 형상 조절 및 나노크기의 배터리 구성요소/캐패시터 구성요소의 복합화를 통해 이에 부합하는 배트캡 물질을 합성하였으며, 이를 통해 배트캡 시스템의 새로운 전기화학 에너지 저장 매체로서의 가능성을 확인할 수 있었다.

제시어: 전기화학; 배트캡 시스템; 리튬 이온 배터리; 슈퍼캐패시터;
비대칭 전극 시스템; 리튬 티타늄 산화물; 황; 그래핀; 탄소나노튜브
학번: 2007-22969